

AN INNOVATIVE PHYSICAL ACTIVATION METHOD FOR
PRODUCING MICROPOROUS-MESOPOROUS ACTIVATED CARBON
WITH HIGH POROUS PROPERTIES



A Thesis Submitted in Partial Fulfillment of the Requirements for the
Degree of Doctor of Philosophy in Mechanical and Process System Engineering
Suranaree University of Technology
Academic Year 2022

วิธีการกระตุ้นทางกายภาพแบบใหม่สำหรับการผลิตถ่านกัมมันต์ไมโครพอร์ส
และเมโซพอร์สที่มีคุณสมบัติความพรุนสูง



วิทยานิพนธ์นี้เป็นส่วนหนึ่งของการศึกษาตามหลักสูตรปริญญาวิศวกรรมศาสตรดุษฎีบัณฑิต
สาขาวิชาวิศวกรรมเครื่องกลและระบบกระบวนการ
มหาวิทยาลัยเทคโนโลยีสุรนารี
ปีการศึกษา 2565

AN INNOVATIVE PHYSICAL ACTIVATION METHOD FOR PRODUCING
MICROPOROUS-MESOPOROUS ACTIVATED CARBON WITH HIGH POROUS
PROPERTIES

Suranaree University of Technology has approved this thesis submitted in partial fulfillment of the requirements for the Degree of Doctor of Philosophy.

Thesis Examining Committee


.....
(Asst. Prof. Dr. Ratanawan Kiattikomol)
Chairperson


.....
(Assoc. Prof. Dr. Atichat Wongkoblap)
Member (Thesis Advisor)


.....
(Prof. Dr. Chaiyot Tangsathitkulchai)
Member (Thesis Co-Advisor)


.....
(Dr. Terasut Sookkumnerd)
Member


.....
(Dr. Supunnee Junpirom)
Member


.....
(Dr. Aroonsri Nuchitprasittichai)
Member


.....
(Assoc. Prof. Dr. Chatchai Jothityangkoon)
Vice Rector for Academic Affairs
and Quality Assurance


.....
(Assoc. Prof. Dr. Pornsiri Jongkol)
Dean of Institute of Engineering

ภาณุวัฒน์ ลอแท : วิธีการกระตุ้นทางกายภาพแบบใหม่สำหรับการผลิตถ่านกัมมันต์ไมโครพอร์สและเมโซพอร์สที่มีคุณสมบัติความพรุนสูง (AN INNOVATIVE PHYSICAL ACTIVATION METHOD FOR PRODUCING MICROPOROUS-MESOPOROUS ACTIVATED CARBON WITH HIGH POROUS PROPERTIES) อาจารย์ที่ปรึกษา : รองศาสตราจารย์ ดร. อติชาติ วงศ์กอบลาภ, 217 หน้า.

คำสำคัญ : วิธีการกระตุ้นใหม่เชิงกายภาพ; ถ่านกัมมันต์; การกระจายขนาดรูพรุน; เมล็ดลำไย; คาร์บอนเจด; ไมโครพอร์ส-เมโซพอร์สคาร์บอน; จลนพลศาสตร์ของแก๊สซีพีเคชั่น; การดูดซับ

วิทยานิพนธ์ฉบับนี้เสนอแนวทางใหม่ในการควบคุมรูพรุนขนาดกลางในถ่านกัมมันต์ที่เตรียมจากเมล็ดลำไยโดยใช้กระบวนการต่อเนื่องของการออกซิไดซ์ถ่านด้วยอากาศเพื่อสร้างหมู่ฟังก์ชันที่พื้นผิว การทำลายหมู่ฟังก์ชันด้วยความร้อน และ การกระตุ้นด้วยแก๊สคาร์บอนไดออกไซด์ ซึ่งเรียกว่าวิธี OTA การเตรียมถ่านกัมมันต์ด้วยเทคนิคนี้สามารถผลิตถ่านกัมมันต์ที่มีรูพรุนสูงและมีสัดส่วนของรูพรุนขนาดกลางที่สูงกว่าเมื่อเทียบกับวิธีการกระตุ้นทางกายภาพแบบสองขั้นตอน วิทยานิพนธ์ฉบับนี้ประกอบด้วยงานหลายส่วน ได้แก่ การเตรียมถ่านกัมมันต์ การศึกษาการดูดซับแก๊สและการพัฒนารูพรุนโดยใช้แบบจำลอง GCMC และ การประยุกต์ใช้ถ่านกัมมันต์ที่ผลิตได้ในกระบวนการดูดซับ

วิธี OTA ประกอบด้วยสามขั้นตอนต่อเนื่องกันคือ (1) การออกซิไดซ์ด้วยอากาศของไมโครพอร์สคาร์บอนเพื่อเพิ่มหมู่ฟังก์ชันบนพื้นผิวของคาร์บอน (2) การทำลายหมู่ฟังก์ชันด้วยความร้อนในบรรยากาศของแก๊สเฉื่อยที่อุณหภูมิสูง เพื่อทำลายพันธะเคมีของหมู่ฟังก์ชันนำไปสู่การเพิ่มจำนวนของอิเล็กตรอนอิสระซึ่งช่วยเพิ่มความว่องไวต่อการเกิดปฏิกิริยาแก๊สซีพีเคชั่นบนพื้นผิวของรูพรุนขนาดเล็กที่มีอยู่ก่อน และ (3) การกระตุ้นด้วยแก๊สคาร์บอนไดออกไซด์ของคาร์บอนที่ผ่านการบำบัดด้วยความร้อน เพื่อสร้างรูพรุนขนาดเล็กและรูพรุนขนาดกลางในปริมาณที่มากขึ้น การวิเคราะห์การพัฒนารูพรุนของถ่านกัมมันต์ที่เตรียมได้โดยใช้แบบจำลอง GCMC ที่มีข้อบกพร่องบนพื้นผิวคาร์บอนเผยให้เห็นว่าการใช้วิธี OTA ในการผลิตถ่านกัมมันต์จะช่วยเพิ่มรูพรุนขนาดกลางโดยการขยายรูพรุนขนาดเล็กซึ่งเป็นผลมาจากความว่องไวในการเกิดปฏิกิริยาของรูพรุนขนาดเล็กที่เพิ่มขึ้นสำหรับปฏิกิริยาแก๊สซีพีเคชั่น นอกจากนี้ยังได้ศึกษาเทคนิคที่คล้ายคลึงกันกับวิธี OTA โดยการออกซิไดซ์ถ่านเมล็ดลำไยล่วงหน้าก่อนที่จะกระตุ้นด้วยแก๊สคาร์บอนไดออกไซด์ซึ่งพบว่าเทคนิคนี้สามารถเพิ่มอัตราการเกิดปฏิกิริยาแก๊สซีพีเคชั่นของถ่านเมล็ดลำไยได้เป็นอย่างมากเมื่อเทียบกับถ่านที่ไม่ได้ผ่านออกซิไดซ์ด้วยอากาศ

ถ่านกัมมันต์ที่ผลิตจากวิธีการกระตุ้นทางกายภาพแบบสองขั้นตอนมีการกระจายตัวของขนาดรูพรุนส่วนใหญ่อยู่ในช่วงขนาด 0.65 ถึง 1.4 นาโนเมตร และ 3 ถึง 4 นาโนเมตร ในขณะที่

ถ่านกัมมันต์ที่ผลิตจากวิธี OTA มีการกระจายตัวของขนาดรูพรุนส่วนใหญ่อยู่ในช่วงขนาด 0.65 ถึง 1.4 นาโนเมตร และ 2 ถึง 3 นาโนเมตร จากการใช้งานถ่านกัมมันต์ในการศึกษาการดูดซับของเมทิลีนบลูออกจากสารละลาย พบว่าปริมาณเมทิลีนบลูที่ถูกดูดซับเพิ่มขึ้นตามระยะเวลาการดูดซับและพื้นที่ผิวของถ่านที่เพิ่มขึ้น ค่าการแพร่เชิงรูพรุนเฉลี่ยของถ่านที่เตรียมจากวิธี OTA มีค่าประมาณ 11.8×10^{-7} ตร. ซม./วินาที ซึ่งมีความมากกว่าถ่านที่เตรียมจากวิธีการกระตุ้นแบบสองขั้นตอนอย่างมีนัยสำคัญ ถ่านกัมมันต์ที่เตรียมจากวิธี OTA ซึ่งมีพื้นที่ผิวสูงสุดสามารถดูดซับเมทิลีนบลูได้สูงสุดประมาณ 1,000 มก./ก.

นอกจากนี้ยังมีการประยุกต์ใช้วิธี OTA กับคาร์บอนเจลเพื่อปรับปรุงคุณสมบัติรูพรุน จากการศึกษาพบว่าถ่านกัมมันต์ที่สังเคราะห์ด้วยวิธี OTA ช่วยปรับปรุงคุณสมบัติรูพรุนของคาร์บอนเจลให้สูงขึ้นมากเมื่อเปรียบเทียบกับถ่านกัมมันต์ที่เตรียมด้วยวิธีการกระตุ้นแบบดั้งเดิมภายใต้สภาวะการกระตุ้นเดียวกัน คุณสมบัติรูพรุนสูงสุดที่สังเคราะห์โดยใช้วิธี OTA ของปริมาตรรูพรุนขนาดเล็กคือ 1.19 ลบ.ซม./ก. ปริมาตรรูพรุนขนาดกลางคือ 1.81 ลบ.ซม./ก. และ พื้นที่ผิว 2,920 ตร.ม./ก. (การเผาไหม้ของคาร์บอน 72%) การเพิ่มคุณสมบัติรูพรุนของถ่านกัมมันต์ที่เตรียมโดยวิธี OTA นั้นเกิดจากผลของขั้นตอนการออกซิเดชันและการบำบัดด้วยความร้อนที่สามารถสร้างตำแหน่งการเกิดปฏิกิริยาได้เป็นจำนวนมากจึงนำไปสู่การพัฒนาคุณภาพรูพรุนตลอดกระบวนการการกระตุ้นด้วยแก๊สคาร์บอนไดออกไซด์ได้อย่างมีประสิทธิภาพ

มหาวิทยาลัยเทคโนโลยีสุรนารี

สาขาวิชาวิศวกรรมเคมี
ปีการศึกษา 2565

ลายมือชื่อนักศึกษา *สมิทธิพร*
ลายมือชื่ออาจารย์ที่ปรึกษา *สมิทธิพร*
ลายมือชื่ออาจารย์ที่ปรึกษาร่วม *สมิทธิพร*

PANUWAT LAWTAE : AN INNOVATIVE PHYSICAL ACTIVATION METHOD FOR PRODUCING MICROPOROUS-MESOPOROUS ACTIVATED CARBON WITH HIGH POROUS PROPERTIES. THESIS ADVISOR : ASSOC. PROF. ATICHAT WONGKOBLAP, Ph.D., 217 PP.

Keywords : Novel activation method; Activated carbon; Pore size distribution; Longan seed; Carbon gels; Microporous-mesoporous carbons; Gasification kinetics; Adsorption

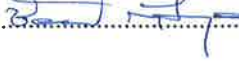
In this thesis, a new approach was proposed for controlling mesoporosity in activated carbon from longan seed by the consecutive process of carbon char oxidation with air to form surface functional groups, thermal destruction of the functional groups, and carbon activation with CO_2 , being called as the OTA method. The preparation technique was able to produce highly porous activated carbons with a higher proportion of mesopore volume, as compared to the conventional two-step activation method. This thesis work consisted of several tasks, including the preparation of activated carbon, the study of gas adsorption and pore development by GCMC simulation, and the applications of the produced activated carbons in adsorption processes.

The OTA method consisted of three consecutive steps: (1) air oxidation of an initial microporous carbon to introduce additional oxygen-containing functional groups, (2) thermal destruction of the existing functional groups in an inert atmosphere at a high temperature to disrupt the chemical bonds of those functional groups, leading to an increase in the number of unpaired electrons which enhances the reactivity of pre-existing micropore surfaces, and (3) activating the heat-treated carbon with CO_2 to create increasing amounts of both micropores and mesopores. The analysis of pore development in the prepared microporous-mesoporous activated carbon based on GCMC simulation and a surface defect model revealed that the use of the OTA method increased the mesopore volume by the widening of the reactive micropores by gasification reaction. By employing a similar technique to the OTA method, the pre-oxidation of longan-seed char prior to CO_2 activation could increase the gasification rate of the char substantially, as compared to the non-oxidized char.

Microporous and mesoporous activated carbons were produced from the longan fruit seeds by the conventional activation method and the OTA method, respectively. The analysis of pore size distributions in activated carbons via the GCMC simulation indicated that most pores consisted of micropores in the size range of 0.65–1.4 nm and mesopores in the size range of 3–4 nm, with mesopore volume concentrating in the smaller mesopore size range of 2–3 nm for the OTA-carbons. For the study on the removal of methylene blue (MB) from an aqueous solution, it was found that the amount of MB adsorbed increased with the increase in the adsorption time and the carbon surface area. The average pore diffusivity of the mesoporous-activated carbon was about an order of magnitude larger than that of the microporous-activated carbon, with a value of $11.8 \times 10^{-7} \text{ cm}^2/\text{s}$. The mesoporous-activated carbon produced by the OTA method having the highest surface area yielded the maximum MB adsorption capacity of about 1000 mg/g carbon.

The OTA method was used to improve the porous properties of mesoporous carbon produced from carbon gels. The findings showed that the activated carbons derived from the OTA procedure provided improved porous properties of activated carbon gels when compared with those prepared through the traditional activation method under the same activation conditions. Under the best preparation conditions, the maximum values of micropore volume, mesopore volume, and BET surface area achievable using the OTA method were $1.19 \text{ cm}^3/\text{g}$, $1.81 \text{ cm}^3/\text{g}$, and $2,920 \text{ m}^2/\text{g}$, respectively, at a 72% carbon burn-off. The large increase in the porous properties of activated carbon gels prepared by the OTA method was attributed to the incorporation of the oxidation and heat treatment steps that could produce a larger number of reaction sites, hence promoting pore development over the course of the gasification process.

School of Chemical Engineering
Academic Year 2022

Student's Signature 
Advisor's Signature 
Co-advisor's Signature 

ACKNOWLEDGEMENTS

First and foremost, I would like to express my deepest gratitude to my principal advisor, Prof. Dr. Chaiyot Tangsathitkulchai, for his kindness, immense knowledge, constructive questions, unwavering dedication, and motivation have been critical to my success. Without him, my Ph.D. career would not have been completed. I am also grateful to my co-advisor, Assoc. Prof. Dr. Atichat Wongkoblaph, for his warm encouragement, support, and valuable suggestions. My sincere appreciation also goes to Prof. Dr. Shin R. Mukai, who was a great supervisor during my research time at Hokkaido University, Sapporo, Japan. His kind assistance, collaboration, and valuable suggestions were invaluable to the completion of this thesis.

I would like to convey my gratitude to my thesis examination committee members, Dr. Aroonsri Nuchitprasittichai, Dr. Supunnee Junpirom, Dr. Terasut Sookkumnerd, and Asst. Prof. Dr. Ratanawan Kiattikomol, for their kind agreement to serve on my committees and for their valuable comments and suggestions.

My thanks go to the technical staff of the Center for Scientific and Technological Equipment, SUT, and in the Division of Applied Chemistry, Hokkaido Univ., especially, Mr. Saran Dokmaikun, the technical staff of the Chemical Engineering Laboratory, for their assistance. I would also like to thank Mrs. Amporn Ladnongkhun for her skillful secretarial work and assistance in dealing with the countless academic paperwork.

I gratefully thank my colleagues in the Carbon and Adsorption Research (CAR) group, Dr. Krittamet Phothong, Mr. Suravit Naksusuk, Mr. Tarathorn Limsiri, and Miss Prapatsorn Borisut for their helpful discussions, assistance, research contributions, and problem-solving in our laboratory. Additionally, I am grateful to Dr. Wittaya Julklang, Dr. Kanungnit Chawong, Miss Boonpradab Daengpradab, Miss Sunisa Singhawannurat, Miss Sujitra Doungsri, and Mr. Santisuk Hasin for their invaluable friendship, making memorable time, and creating a good atmosphere in our research rooms.

My thanks also extend to my colleagues at the Material Design and Engineering Laboratory, particularly Mr. Shintaroh Nagaishi, for their collaboration, guidance, helpfulness, and great friendship throughout my journey at Hokkaido University. I would also like to express my gratitude to Asst. Prof. Dr. Shinichiroh Iwamura for his invaluable assistance and contribution to the experimental data included in this thesis.

I gratefully acknowledge the funding sources from the National Research Council of Thailand (NRCT) and Thailand Research Fund (TRF) through the Royal Golden Jubilee Ph.D. program (RGJ-Ph.D.), batch number 20, grant number PHD/0057/2560, for sponsoring my study and support for research. All members and staff in RGJ-Ph.D. program are also appreciatively acknowledged.

Last but certainly not least, I would like to express my heartfelt appreciation to my parents and sisters for their unwavering support and dedication throughout my journey. I am forever grateful for their encouragement and love. My friends and my relatives also deserve my thanks. Thank you all for being a part of my life and for believing in me. I am truly blessed to have such wonderful people in my life. As I embark on the next phase of my career, I will carry your support with me always.

Panuwat Lawtae

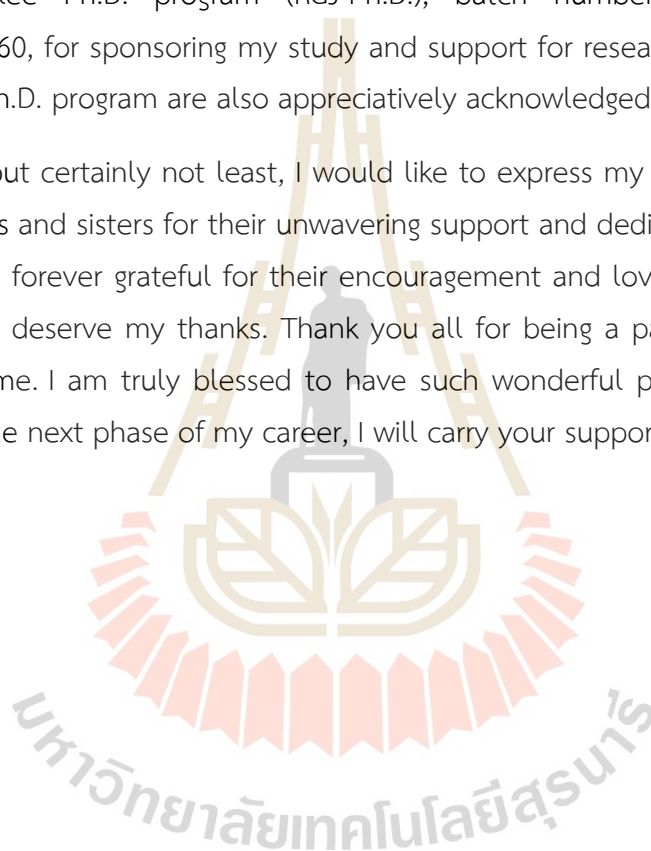


TABLE OF CONTENTS

	Page
ABSTRACT (THAI).....	I
ABSTRACT (ENGLISH).....	III
ACKNOWLEDGEMENTS.....	V
TABLE OF CONTENTS.....	VII
LIST OF TABLES.....	XII
LIST OF FIGURES.....	XV
SYMBOLS AND ABBREVIATIONS.....	XXI
CHAPTER	
I INTRODUCTION.....	1
1.1 Introduction to the Research.....	1
1.2 Scope and Limitation of the Research.....	5
1.3 Output of Research.....	6
1.4 Research Development.....	7
1.5 References.....	8
II THE CONSECUTIVE PROCESS OF AIR OXIDATION, THERMAL DESTRUCTION OF SURFACE FUNCTIONAL GROUPS, AND CARBON ACTIVATION (THE OTA METHOD).....	10
2.1 Abstract.....	10
2.2 Introduction.....	11
2.3 Experimental Procedure.....	13
2.3.1 Materials.....	13
2.3.2 Preparation of Char and Microporous Activated Carbon... 13	13
2.3.3 Preparation of Mesoporous Activated Carbon by the OTA Method.....	14
2.3.4 Raw Material Characterization.....	15

TABLE OF CONTENTS (Continued)

	Page
2.3.5 Porous Properties of the Prepared Activated Carbons	15
2.3.6 Surface Reactivity of Activated Carbon Towards CO ₂ Gasification Reaction	16
2.3.6 Surface Functional Groups of Activated Carbons	16
2.4 Results and Discussion	17
2.4.1 Thermal Decomposition Behavior of Longan Seed Precursor	17
2.4.2 Proximate and Ultimate Analyses of Longan Seed Precursor and Activated Carbon	18
2.4.3 N ₂ Isotherms of Prepared Activated Carbons.....	20
2.4.4 Porous Properties of Prepared Activated Carbons.....	22
2.4.5 On Mesopores Development by the OTA Method	28
2.4.6 Surface Functional Groups of Prepared Activated Carbons	31
2.4.7 Carbon Reactivity Towards CO ₂ Gasification.....	34
2.4.8 Pore size Distributions and Surface Morphology of Prepared Activated Carbons	39
2.5 Conclusions.....	43
2.6 References	44
III THE USE OF ACTIVATED CARBON FROM LONGAN SEED BIOMASS FOR INCREASING CAPACITY AND KINETICS OF METHYLENE BLUE ADSORPTION FROM AQUEOUS SOLUTION	50
3.1 Abstract.....	50
3.2 Introduction	51
3.3 Experimental Procedure.....	53
3.3.1 Materials.....	53
3.3.2 Preparation of Longan Seed Activated Carbons.....	54
3.3.3 Characterization of the Prepared Activated Carbons	55
3.3.4 Methylene Blue Adsorption.....	56

TABLE OF CONTENTS (Continued)

	Page
3.4 Adsorption Analysis.....	58
3.4.1 Adsorption Kinetic Models.....	58
3.4.2 Adsorption Isotherm Models.....	59
3.5 Results and Discussion.....	61
3.5.1 Characterization of the Prepared Activated Carbons.....	61
3.5.2 Adsorption Kinetics and Model Testing.....	64
3.5.3 Adsorption Isotherms and Model Testing.....	69
3.5.4 Effect of Adsorbent Dosage.....	76
3.5.5 Effect of Initial pH.....	77
3.5.6 Effect of Temperature and Adsorption Thermodynamics Study.....	78
3.6 Conclusions.....	82
3.7 References.....	83
IV ANALYSIS OF GAS ADSORPTION AND PORE DEVELOPMENT IN ACTIVATED CARBON BASED ON SURFACE DEFECT MODEL.....	93
4.1 Abstract.....	93
4.2 Introduction.....	94
4.3 Experimental Procedure.....	96
4.4 Simulation Model.....	97
4.4.1 Fluid-Fluid Models and the Interaction Energy (U_{FF}).....	97
4.4.2 Solid-Fluid (U_{SF}) Potential Model.....	98
4.4.3 The Computer Simulation for Determining Pore Size Distribution.....	100
4.5 Results and Discussion.....	102
4.5.1 N_2 Adsorption Isotherms.....	102
4.5.2 CO_2 Adsorption Isotherms.....	104
4.5.3 Adsorption Isotherms of the Perfective Surface.....	106
4.5.4 Effect of Defect Size.....	107
4.5.5 Effect of Defect Area.....	111

TABLE OF CONTENTS (Continued)

	Page
4.5.6	Analysis of N ₂ Adsorption Based on Isosteric Heat 113
4.5.7	The PSD Derived from N ₂ Adsorption Isotherms 114
4.5.8	The PSD Derived from CO ₂ Adsorption Isotherms 118
4.6	Conclusions..... 120
4.7	References 121
V	A SIMPLE PRE-OXIDATION TECHNIQUE FOR INCREASING CO₂ GASIFICATION RATES IN LONGAN-SEED CHARs 128
5.1	Abstract..... 128
5.2	Introduction 128
5.3	Experimental Procedure..... 131
5.3.1	Materials..... 131
5.3.2	Char Oxidation Preparation..... 131
5.3.3	Analysis of Surface Functional Groups 132
5.3.4	Gasification Kinetics 133
5.4	Gasification Kinetic Modelling 134
5.5	Results and Discussion 136
5.5.1	Surface Functional Groups of Prepared Carbons 136
5.5.2	Gasification Kinetic and Model Testing..... 141
5.6	Conclusions..... 153
5.7	References 154
VI	IMPROVING POROUS PROPERTIES OF ACTIVATED CARBON GEL BY THE OTA METHOD 157
6.1	Abstract..... 157
6.2	Introduction 158
6.3	Experimental Procedure..... 160
6.3.1	Materials..... 160
6.3.2	Carbon Gel Preparation 160
6.3.3	Activated Carbon Production 161
6.3.4	Characterization..... 162
6.4	Results and Discussion 163

TABLE OF CONTENTS (Continued)

	Page
6.4.1 Thermal Decomposition Behavior of Organic Xerogels ...	163
6.4.2 N ₂ Adsorption Isotherms of Prepared Activated Carbons	165
6.4.3 Porous Properties of Prepared Activated Carbons.....	166
6.4.4 The Effect of Porous Properties of the Initial Carbon Precursor	170
6.4.5 Role of Surface Functional Groups in the OTA Method..	176
6.4.6 Determination of Carbon Reactivity Towards CO ₂ Gasification.....	179
6.4.7 Electrochemical Performances	181
5.6 Conclusions.....	185
5.7 References	186
VII CONCLUSIONS AND RECOMMENDATIONS	192
7.1 Conclusions.....	192
7.2 Recommendations	196
APPENDIX	
APPENDIX A SUPPLEMENTARY INFORMATION	197
APPENDIX B LIST OF PUBLICATIONS	215
BIOGRAPHY	217

LIST OF TABLES

Table	Page
2.1	Proximate analysis of longan seed and some industrial biomass wastes 19
2.2	Proximate and ultimate analysis results of longan seed, Longan seed char, and activated carbons 20
2.3	Porous properties of activated carbons prepared by the two-step activation and the OTA method..... 24
2.4	Preparation of activated carbon by various methods for mesoporous activated carbon production 25
2.5	Empirical equations correlating porous properties of activated carbon (y) prepared by the two-step activation and the OTA methods as a function of % carbon burn-off (x) 27
2.6	Amounts of oxygen functional groups on activated carbon surfaces determined by the Boehm titration technique 34
2.7	Sample description for the CO ₂ gasification in TGA..... 34
2.8	The pore volume for the pore size distribution of longan seed-derived activated carbon 42
3.1	Experimental conditions for the study of batch MB adsorption by longan seed-based activated carbons 57
3.2	Porous properties of prepared activated carbons 63
3.3	Pore size distribution of prepared activated carbons 63
3.4	Point of zero charge and surface functional groups in activated carbons 63
3.5	Kinetic parameters of various adsorption kinetic models for MB adsorption by longan seed-activated carbons 66
3.6	Comparison of the kinetic parameter (k_2) of the pseudo-second-order model for various types of activated carbons..... 68
3.7	Parameters of adsorption isotherm equations for MB adsorption at 35°C by the prepared activated carbons..... 71

LIST OF TABLES (Continued)

Table		Page
3.8	The maximum adsorption capacity of methylene blue from solutions (q_m) by activated carbons prepared from various materials and activation methods.....	73
3.9	Thermodynamic parameters of the MB adsorption on longan seed activated carbon	81
4.1	Molecular parameters used in the GCMC simulation Computation	98
4.2	Porous properties and percent char burn-off of the tested activated carbon	103
4.3	Values of R^2 and $\% \Delta V$ for the best fitting of N_2 and CO_2 adsorption isotherms	113
4.4	Parameters used in the simulation for determining the PSD of the activated carbon derived from N_2 adsorption isotherms	116
4.5	Pore volume distributions in the activated carbon based on perfective and defective models derived from N_2 adsorption isotherms	117
4.6	The pore volume of the PSD in the activated carbon derived from CO_2 adsorption isotherms	119
5.1	Experimental conditions of oxidized char preparation.....	132
5.2	Gasification conditions of the carbon samples in TGA.....	133
5.3	The amount of surface functional groups in the char samples determined by Boehm titration.....	138
5.4	Effect of oxidation conditions on the porous properties of raw char and oxidized chars.....	139
5.5	The fitted parameters of gasification kinetic models for the carbon samples.....	145
5.6	Comparison of the activation energy from various types of precursors.....	148
6.1	Textural properties of mesoporous carbons prepared by the conventional method and the OTA method.....	169
6.2	Textural properties of mesoporous carbons prepared by the OTA method from precursors having different initial porous properties.....	172

LIST OF TABLES (Continued)

Table	Page
6.3	The calculated pore volume for each pore size range (NLDFT method)..... 175
6.4	Total amounts of CO ₂ , CO, and H ₂ desorbed from the samples..... 179
6.5	The amount of oxygen-containing functional groups of the samples 179



LIST OF FIGURES

Figure	Page
2.1	Typical residual weight (TG) and weight loss rate (DTG) for the non-isothermal pyrolysis in an N ₂ atmosphere of longan seed biomass..... 18
2.2	N ₂ adsorption isotherms of microporous activated carbons prepared by the two-step activation method and mesoporous activated carbons prepared by the OTA method at two activation temperatures of (a) 850°C and (b) 900 °C, while (c, d) show the corresponding isotherms at a low-pressure range ($P/P_0 < 0.1$) on a semi-log scale 22
2.3	Effect of carbon burn-off during CO ₂ activation step of longan seed biomass on the porous properties of activated carbons prepared by the two-step activation and the OTA methods, (a) BET surface area, (b) total pore volume, (c) micropore volume, and (d) mesopore volume 28
2.4	The model for mesopore development by the OTA method is represented schematically by the following steps, (a) the initial activated carbon contains a certain number of micropores (nos.1–9), (b) formation of oxygen functional groups on the surface of some original micropores (nos.1, 3, 5, 6) by air oxidation, (c) bond dissociation of the functional groups increases the surface reactivity of micropores (nos.1, 3, 5, 6) due to the increasing number of free radicals and unpaired electrons, and (d) formation of new mesopores (nos.1, 3, 5, 6) by enlargement as well as the formation of new micropores (nos.10–12) by CO ₂ gasification reaction 30
2.5	FTIR spectra of the derived activated carbon prepared by (a) the OTA method, including (1) the initial activated carbon (A850-60), (2) the air-oxidized carbon (A850-60-OX), (3) the heat treatment carbon (A850-60-HT), (4-6) the reactivated carbon (A850-60-1-3), and (b) by the two-step activation method for varying activation (60–240 min) 33

LIST OF FIGURES (Continued)

Figure	Page
2.6	TG curves for CO ₂ gasification of longan-seed activated carbons prepared by the two-step activation and the OTA methods for activation temperatures of (a) 850°C and (b) 900°C, and TG curves for A850-60 carbon showing, (c) the effect of heat treatment time at temperature of 950°C and (d) the effect of heat treatment temperature for the treatment time of 2 h..... 37
2.7	Effect of carbon conversion (a) on char reactivity (R_c) towards CO ₂ gasification of temperature 850°C and (b) 900°C, and the effect of (c) heat treatment time and (d) heat treatment temperature on the char reactivity... 38
2.8	Pore size distributions of longan seed-derived activated carbon prepared by (a) the two-step activation method and (b) the OTA method, as determined by the GCMC simulation 41
2.9	SEM micrographs of activated carbon prepared by the OTA method for (a) A850-60, (b) A850- 60-1, (c) A850-60-2, and (d) A850-60-3, with a magnification of 1K for (a1)–(d1) and 100K. for (a2)–(d2) 42
3.1	The determination of pH_{PZC} of (a) microporous activated carbon, and (b) mesoporous activated carbon from the intersection between the curve of $pH_{initial}$ vs pH_{final} and the straight line of $pH_{initial} = pH_{final}$ 56
3.2	SEM micrographs of (a) the microporous activated carbon of A2 (A850-180), and (b) the mesoporous activated carbon of A5 (A850-60-2), with a magnification of 1K for (a1–b1) and 100K for (a2–b2) 64
3.3	Kinetics of methylene blue adsorption on the prepared microporous and mesoporous activated carbons from the longan fruit seed 66
3.4	Effect of percent mesoporosity in activated carbons on the rate constant (k_2) of the pseudo-second-order kinetic model. The black circles represent the results from the present study and the white circles are those from other investigators (see references in Table 3.6) 69

LIST OF FIGURES (Continued)

Figure		Page
3.5	Adsorption isotherms at 35°C of MB dye on longan seed-activated carbons prepared by (a) the two-step activation method, and (b) the OTA method	71
3.6	Effect of BET surface area on monolayer capacity (q_m) of the Langmuir isotherm equation and K_F of the Freundlich equation.....	74
3.7	Effect of BET surface area on K_L of the Langmuir equation and K_R of the Redlich-Peterson equation.....	74
3.8	Correlation between BET surface area and the maximum MB adsorption capacity from the data in Table 3.8.....	75
3.9	Effect of BET surface area on the maximum MB adsorption capacity. The black circles represent results from the present study (A1–A6) and the white circles belong to previous investigations.....	75
3.10	The effect of carbon dosage on (a) MB adsorption capacity and (b) MB removal efficiency for microporous (A3) and mesoporous (A6) activated carbons ($C_0 = 300$ mg/L, $V = 25$ mL and $T = 35^\circ\text{C}$).....	77
3.11	Effect of the initial solution pH on the removal efficiency of MB by the mesoporous activated carbon (A6), with $C_0 = 400$ mg/L, carbon dosage = 0.8 g/L and $T = 35^\circ\text{C}$	78
3.12	Effect of temperature on isotherms of MB adsorption by the mesoporous activated carbon (A6).....	79
3.13	The plot of $\ln(K_d)$ versus $1/T$ for MB adsorption onto mesoporous activated carbon (A6).....	81
4.1	Solid configuration of one graphene layer with percentage defects of 30% and the effective radius (R_c) of (a) 0.246 nm, (b) 0.492 nm, and (c) 0.615 nm. The black spheres represent carbon atoms of the graphene layer and the spaces represent the defect area.....	100
4.2	N_2 adsorption isotherms at 77 K of the three samples of microporous-mesoporous activated carbon (AC1, AC2, and AC3).....	103

LIST OF FIGURES (Continued)

Figure	Page
4.3	CO ₂ adsorption isotherms at 273 K for (a) excess adsorption capacity and (b) absolute adsorbed amount in a microporous-mesoporous activated carbon 106
4.4	Simulated adsorption isotherms of (a) N ₂ at 77 K and (b) CO ₂ at 273 K in carbon slit pores 107
4.5	Simulated adsorption isotherms of N ₂ at 77 K in carbon slit pores with 30% defects of the effective radius at (a) 0.246 nm and (b) 0.492 nm 109
4.6	Snapshots of N ₂ adsorption at 77 K in pore width of 2 nm at various adsorption pressure on the defective surface with R _c of (a) 0.246 nm, (b) 0.492 nm, and (c) 0.615 nm..... 110
4.7	Comparison of experimental and simulated adsorption isotherms for 30% defective area with various R _c of (a) 0.246 nm, (b) 0.492 nm, and (c) 0.615 nm..... 110
4.8	Snapshots of N ₂ at 77 K in pore width of 0.70 nm at 1 Pa on the carbon surface with the effective radius of 0.492 nm at percentage defects varying from 0 to 45%..... 112
4.9	Adsorption isotherms of N ₂ in 1.0 nm pores on the different percentages of defects (0–45%) with the effective radius of 0.492 nm..... 112
4.10	Isosteric heat as a function of loading for N ₂ adsorption in 1.10 nm pore at 77 K on (a) perfective surface, (b) defective surface 114
4.11	PSD for AC1, AC2, and AC3 derived from the perfective surface (left) and the defective surface models (right) as determined by the adsorption isotherms of N ₂ at 77 K..... 116
4.12	Comparison of simulated and experimental adsorption isotherms of (a) N ₂ at 77 K and (b) CO ₂ at 273 K 117
4.13	PSD for AC1, AC2, and AC3 calculated based on the adsorption isotherms of CO ₂ at 273 K..... 119
5.1	Effects of oxidation time and temperature on the char weight loss..... 137

LIST OF FIGURES (Continued)

Figure	Page
5.2	The effects of oxidation temperature and time on the amounts of (a) acidic groups and (b) basic groups 139
5.3	Isotherms of CO ₂ adsorption at 0°C by the raw char and oxidized chars, (a) effect of oxidation temperature and (b) effect of oxidation time for chars oxidized at 300°C..... 140
5.4	The FTIR spectra of the raw char and the oxidized chars at different oxidation temperatures 141
5.5	Typical TGA curves showing the weight loss vs time for CO ₂ gasification at (a) 850°C (b) 900°C, and (c) 950°C of the raw char and the oxidized chars (oxidation temperatures of 250–300°C for 24h)..... 142
5.6	Effect of reaction time on the gasification rates (dX/dt) of various char samples at gasification temperatures of (a) 850°C (b) 900°C, and (c) 950°C... 143
5.7	Testing gasification models of VRM, SCM, RPM, and MVRM for the carbon samples gasified at the temperatures of (a) 850°C, (b) 900°C, and (c) 950°C. 144
5.8	Comparison of various gasification kinetic models with the experimental kinetic data of char oxidized at 300°C and 24 h at the gasification temperatures of 900°C..... 146
5.9	Effects of oxidation time and temperature on the char reactivity index (k_m) for char gasification at 900°C 146
5.10	The effect of acidic groups on the char reactivity index (k_m)..... 147
5.11	The relationship between the activation energy and the pre-exponential factor from the present and previous studies (see references in Table 5.6). 149
5.12	Effect of reaction conversion on the activation energy of char gasification for various oxidized longan-seed chars 150
5.13	Schematic representation for the effect of char oxidation on the isothermal CO ₂ gasification kinetics of longan-seed chars 152
6.1	The residual weight (TG) and the weight loss rate (DTG) curves for non-isothermal pyrolysis in N ₂ of the organic xerogels using a thermogravimetric analyzer (TGA) 164

LIST OF FIGURES (Continued)

Figure		Page
6.2	N ₂ adsorption isotherms at -196°C of mesoporous activated carbons prepared by (A) the conventional activation method (AC series) and (B) the OTA method (OTA series) at the same activation temperatures of 1000°C	166
6.3	Effect of carbon burn-off on the BET surface area of carbon products by the OTA and the conventional preparation methods	169
6.4	Pore size distributions of activated carbon gels determined by the DH method for (A) the AC series and (B) the OTA series	170
6.5	N ₂ adsorption isotherms (-196°C) of mesoporous activated carbons prepared under the same activation conditions by the OTA method from carbon precursors having different initial porous properties.....	171
6.6	Effect of the surface area of initial precursors on the surface area of activated carbon produced by the OTA method	172
6.7	Pore size distributions of carbon samples obtained by using the NLDFT method	175
6.8	(A) CO (B) CO ₂ and (C) H ₂ desorption spectra of the OTA samples.....	178
6.9	(A) the carbon conversion profiles for CO ₂ gasification at 1000°C of the activated carbons prepared by the conventional activation (AC) and by the OTA method (AC-OT) and (B) the effect of carbon conversion on the carbon reactivity towards CO ₂ gasification.....	180
6.10	Cyclic voltammetry curves of AC2 (blue) and AC1-OTA (red) at a scan rate of 2 mV/s	183
6.11	Charge-discharge curves of (A) AC2 and (B) AC1-OTA at various current densities	183
6.12	The effect of current density on specific capacitances of (A) AC2 and (B) AC1-OTA.....	184
6.13	FE-SEM micrographs of AC2 (left) and AC1-OTA (right)	184

SYMBOLS AND ABBREVIATIONS

a	Constant of the power law
AC	Activated Carbon
b	Exponent of the power law
BET	Brunauer-Emmett-Teller theory
C	Capacitance ($F\ g^{-1}$)
C	Concentration at time t ($mg\ L^{-1}$)
C_e	Equilibrium concentration ($mg\ L^{-1}$)
C_0	Initial concentration ($mg\ L^{-1}$)
CG	Carbon Gel
D_{av}	Average pore diameter (nm)
D_e	Effective pore diffusivity ($cm^2\ s^{-1}$)
DH	Dollimore-Heal method
DR	Dubinin-Radushkevich equation
DTG	Derivative Thermogravimetric
E	Activation energy ($kJ\ mol^{-1}$)
EoS	Equation of State
F	Fractional uptake of the adsorbate
FF	Fluid-Fluid (a.k.a. Adsorbate-Adsorbate)
FTIR	Fourier Transform Infrared Spectroscopy
GCMC	Grand Canonical Monte Carlo
HPVA	High-Pressure Volumetric Analyzer
i	Current density ($A\ g^{-1}$)
IUPAC	International Union of Pure and Applied Chemistry
k	Apparent gasification rate constant
k_B	Boltzmann constant ($1.380649 \times 10^{-23}\ J\ K^{-1}$)
k_m	Average gasification rate constant
k_R	Rate constant in RPM model (min^{-1})
k_S	Rate constant in SCM model (min^{-1})
k_V	Rate constant in VRM model (min^{-1})

SYMBOLS AND ABBREVIATIONS (Continued)

k_0	Pre-exponential factor
k_1	Pseudo first rate constant (min^{-1})
k_2	Pseudo second rate constant ($\text{g mg}^{-1} \text{min}^{-1}$)
K_d	Distribution coefficient for the adsorption
K_F	Binding capacity (L mg^{-1})
K_L	Affinity or Langmuir constant (L mg^{-1})
K_R	Modified Langmuir constant (L g^{-1})
LB	Lorentz-Berthelot mixing rule
LJ	Lennard-Jones
MB	Methylene Blue dye
MVRM	Modified Volume Reaction Model
n_F	Surface heterogeneity
N	Number of particles in the simulations box
N	Number of data points
OTA	Oxidation Thermal destruction and Activation
pH_{PZC}	pH at the point of zero charge
P	Gas equilibrium pressure
P_L	Gas equilibrium pressure at half of V_L
P_0	Saturation vapor pressure
P/P_0	Relative pressure
PBC	Periodic Boundary Condition
PSD	Pore Size Distribution
q	Charges in the potential models (e)
q_e	Adsorption capacity at equilibrium (mg g^{-1})
q_m	Monolayer capacity (mg g^{-1})
q_{st}	Isotheric heat of adsorption (kJ mol^{-1})
q_t	Adsorption capacity at time t (mg g^{-1})
R	Universal gas constant ($8.314 \text{ J mol}^{-1} \text{K}^{-1}$)
R_c	Carbon reactivity for CO_2 gasification (min^{-1})
R_c	Effective radius (nm)
R_e	Removal Efficiency (%)

SYMBOLS AND ABBREVIATIONS (Continued)

R_p	Radius of the adsorbent particle
R^2	Regression coefficient
RF	Resorcinol-Formaldehyde
RPM	Random Pore Model
S_{BET}	BET specific area ($m^2 g^{-1}$)
SCM	Shrinking Core Model
SEM	Scanning Electron Microscope
SF	Solid-Fluid (a.k.a. Adsorbent-Adsorbate)
SSE	Sum of squared estimate of errors
STP	Standard Temperature and Pressure
t	Time (minute or second)
T	Temperature ($^{\circ}C$ or K)
TG	Thermogravimetric
TGA	Thermogravimetric Analysis
TPD	Temperature Programmed Desorption
U_{FF}	The potential energy between adsorbate-adsorbate in the simulation (K)
U_{SF}	The potential energy between adsorbent-adsorbate in the simulation (K)
v	potential scan rate ($mV s^{-1}$)
V_{ab}	Absolute adsorption capacity
V_{acc}	Accessible volume of the simulation box (nm^3)
V_{ex}	Excess adsorption capacity
V_L	Maximum absolute adsorption capacity
V_{me}	Mesopore volume ($cm^3 g^{-1}$)
V_{mi}	Micropore volume ($cm^3 g^{-1}$)
V_T	Total pore volume ($cm^3 g^{-1}$)
VRM	Volume Reaction Model
X	Fractional conversion of carbon
Δ	Interspacing between two graphene layers (0.3354 nm)
Δq	Normalized standard deviation

SYMBOLS AND ABBREVIATIONS (Continued)

ΔH°	Enthalpy change (kJ mol^{-1})
ΔG°	Gibbs free energy change (kJ mol^{-1})
ΔS°	Entropy change ($\text{kJ mol}^{-1} \text{K}^{-1}$)
ΔV	Potential window (volt, V)
β	Exponent value in Redlich-Peterson equation (lies between 0 and 1)
ϵ_0	Vacuum permittivity of free space
ϵ_{ff}	Well depth of fluid (K)
ϵ_{ss}	Well depth of solid (K)
ϵ_{sf}	Cross-well depth of solid and fluid (K)
ψ	Structural parameter in the RPM equation
ρ_{ads}	Adsorbed phase density
ρ_{bulk}	Bulk gas density
ρ_{ex}	Excess pore density
ρ_g	Gas density of the box
ρ_s	Surface density of carbon (38.2 nm^{-2})
σ_{ff}	Collision diameter of fluid (nm)
σ_{ss}	Collision diameter of solid (nm)
σ_{sf}	Cross-collision diameter between solid and fluid (nm)
τ	Dimensionless time

CHAPTER I

INTRODUCTION

1.1 Introduction to the Research

Activated carbon, a type of amorphous carbon-based material, was widely recognized for its high degree of porosity, large surface area, microporous structure, strong adsorption capacity, and high degree of surface reactivity. The use of activated carbon dates back to prehistoric times when charcoal was used as a treatment for diarrhea and as a purifying agent for water (Bansal et al., 1988). Nowadays, activated carbon is considered a highly versatile porous material, extensively used in various separation and purification processes in both gas and liquid phases (Bansal & Goyal, 2005). Activated carbon is typically prepared from a diverse range of carbon-containing materials, including cellulosic sources, carbonaceous sources, and the entire coal family (Marsh & Rodríguez-Reinoso, 2006). The manufacturing process of activated carbon can involve either a two-step physical activation process using oxidizing agents such as CO_2 or steam, or a single-step preparation method through impregnation of the raw material with inorganic chemical agents such as ZnCl_2 , NaOH , or H_3PO_4 , followed by a carbonization process (Pallarés et al., 2018). To suit various applications that require different pore size ranges in carbon materials, the pore size distribution of activated carbon must be controlled during preparation by proper selection of a precursor and adjusting the preparation conditions (Kyotani, 2000). In general, micropores are primarily formed when activated carbon is prepared through physical activation, and this type of carbon is suitable for use in gas adsorption (Román et al., 2008). Conversely, activated carbon with a higher proportion of mesopores is necessary for effective adsorption in liquid systems. Typically, the control of mesoporosity in activated carbon is achieved through chemical activation and the combination of chemical and physical activation methods (Hu et al., 2003; Hu et al., 2001; Saygılı & Güzel, 2016; Tseng, 2006). However, an effective method for controlling the amount and size range of mesopores using only physical activation has not yet been reported. Therefore, it is the purpose of this thesis work to propose a new preparation method based purely

on physical activation to investigate the formation of mesopores in activated carbon and the underlying mechanism involved.

The innovative method proposed for preparing activated carbon in the present work, being named the Oxidation, Thermal treatment, and Activation (OTA) method, is a modified conventional activation process achieved by introducing air oxidation to create additional surface functional groups. Then, the existing functional groups are thermally destroyed in an inert gas at a high temperature, resulting in an increase in the number of surface defects involving many unpaired electrons, thus helping increase the reactivity of the pre-existing micropore surfaces. Further exposure to CO₂ activation, the pre-existing micropores with a high surface reactivity undergo gasification, resulting in the formation of a greater number of mesopores by pore enlargement. Essentially, the OTA method involves two consecutive steps of air oxidation and thermal destruction of the already formed surface functional groups prior to activation with CO₂, hence producing highly porous activated carbons with higher proportional amounts of mesopore volume as compared to the conventional activation method. The close control of the conditions used during various preparation steps of the OTA process permits the production of the desired amounts of micropores and mesopores. The OTA method is advantageous due to its ease of operation, cost-effectiveness, and environmental friendliness, as it merely requires air, N₂, and CO₂, without involving any acid solutions or oxidizing agents in the liquid phase. Overall, the OTA method shows great promise as a new approach for producing highly porous activated carbons with tailored pore structures and enhanced porous properties.

The starting raw material used in this work was longan seed biomass, which is the inner seed of the longan fruit. The longan fruit, a member of the Sapindaceae family, is widely consumed and produced in large quantities in Thailand, with approximately 1.57 million tons being produced in 2021 according to the Office of Agricultural Economics Ministry of Agriculture and Cooperatives. Longan seeds account for about 17% of the total fruit weight, and they are often discarded from processing plants and disposed of in landfills, thus causing an environmental issue. To convert this waste into useful value-added products, the longan seeds were utilized as the raw material for producing activated carbon using the OTA method in the present study. Additionally, the analysis of gas adsorption and pore size

distribution of the activated carbon produced from longan seed biomass were studied using Monte Carlo (MC) simulation in the grand canonical (GC) ensemble along with a surface defect model. Furthermore, a similar technique of air oxidation used in the OTA method was extended to study a simple pre-oxidation of longan-seed chars to increase its CO₂ gasification kinetics. The use of this technique prior to the gasification step for increasing the char gasification rate developed in this study would be of significant value for the production of both activated carbon and synthesis gas.

The removal of dyes from wastewater presented a significant challenge for industries. Dyes are complex organic compounds (Yagub et al., 2014) used across many industries and are resistant to the action of detergent treatments (Nayeri & Mousavi, 2020). Therefore, the search for inexpensive and efficient porous materials for the removal of dyes was a worthwhile endeavor. Activated carbon was a commonly used adsorbent to eliminate organic water pollutants, including dyes. Extensive research has been conducted on the adsorption of organic water pollutants by activated carbon (Chen et al., 2020; Nezhad et al., 2021; Radovic et al., 1997). However, despite the numerous studies on the kinetics and adsorption properties of activated carbon, further research was needed to better comprehend the underlying adsorption mechanism. Methylene blue dye (MB) was often used as a model dye to investigate the adsorption mechanisms of dyes. Therefore, this work was further aimed to study the kinetics and equilibrium of MB dye adsorption from aqueous solution by activated carbon produced using the conventional two-step activation method and the OTA method. Moreover, the effects of adsorbent dosage, temperature, and solution pH on the efficiency of MB dye uptake were also examined.

The advantages of utilizing the OTA method for enhancing the porous properties of carbon-based materials were investigated and demonstrated in this research project. It is tempting to apply this method to another well-known carbon gel adsorbent, which possesses a unique hierarchical porous structure. Due to their polymeric structure of interconnected nodules, the carbon gel essentially included both micropores and mesopores. The interparticle spaces of the carbon gel form its mesoporous structure, which remains relatively stable even after a subsequent activation process is applied (Canal-Rodríguez et al., 2017). On the other hand, the

activation process is directly responsible for generating micropores within the nanoparticles that form the carbon matrix. As a result, the OTA method was applied in this work to introduce small mesopores within the nanoparticles of carbon gel, thus enhancing the porous properties of this mesoporous carbon. This particular study aimed to investigate how the initial porous properties of the carbon gel affected the enhancement of porous properties in activated carbon produced using the OTA method. Additionally, the activated carbon gel derived from the OTA method was applied for use as an electrode material, for the potential use in energy storage applications. The reason for using the OTA method on carbon gels was to emphasize the importance of applying this technique to improve the porous properties of carbon materials. The overall results obtained from the present thesis work will be of great value in the fields of improving the porous properties of porous adsorbents and adsorption applications.

The overall objective of this dissertation was to study the development of a new and effective method, based entirely on a physical approach, for preparing activated carbon with large amounts of micropores and mesopores. This method was referred to as the OTA (Oxidation, Thermal treatment, and Activation). To achieve this goal, the underlying mechanism of pore development by the OTA method was proposed, and supporting experimental evidence as well as its applications were also presented. The specific objectives of this research are as follows:

- 1.1.1 To propose a new method for the preparation of microporous-mesoporous activated carbon with large surface area and pore volume from longan fruit seed using the OTA method.
- 1.1.2 To study and compare the equilibrium and kinetics of methylene blue adsorption from aqueous solution by activated carbon prepared from the conventional two-step activation and the OTA method.
- 1.1.3 To investigate the gas adsorption and pore development in activated carbon based on the GCMC simulation approach along with the surface defect model.
- 1.1.4 To investigate a simple pre-oxidation technique for increasing CO₂ gasification rates of longan-seed char.
- 1.1.5 To apply the OTA method for improving the porous properties of activated carbon gel and demonstrate its use as an electrode material.

1.2 Scope and Limitation of the Research

This research work aimed to provide insights into the preparation and characterization of microporous-mesoporous activated carbon using the OTA method and its potential applications in adsorption and gasification. The research was conducted using longan seed biomass obtained from Saha-Prachinburi Foods Industry Ltd., a local fruit processing plant in Chiangmai province, Thailand. The research was divided into five main parts, as follows.

1.2.1 Preparation of Microporous-Mesoporous Activated Carbon by the OTA Method

The OTA method involved three consecutive steps, including air oxidation, thermal destruction, and CO₂ activation. The preparation conditions, such as temperature and time, were varied and investigated. The resulting activated carbons were characterized using various methods, including N₂ adsorption, thermogravimetric analysis, Boehm's titration, Fourier Transform Infrared Spectroscopy, and Field Emission Scanning Electron Microscopy. The experimental results were analyzed to propose the underlying mechanism of pore development by the OTA method.

1.2.2 Use of Activated Carbon for Increasing Capacity and Kinetics of Methylene Blue Adsorption from Aqueous Solution

The kinetics of methylene blue adsorption was studied using the produced longan-seed activated carbon to determine the adsorption rate and equilibrium time as well as the study on dye adsorption equilibrium. The effects of adsorbent dosage, solution pH, and adsorption temperature on the equilibrium adsorption were also investigated.

1.2.3 Analysis of Adsorption and Pore Development in Activated Carbon Based on a Surface Defect Model

Monte Carlo (MC) simulation in the grand canonical (GC) ensemble was used to investigate the adsorption of N₂ gas on both perfective and defective carbon surfaces to explore the mechanism of pore development. The behavior of N₂ gas adsorption was described by the isosteric heat of adsorption on perfective and defective surfaces. Furthermore, the adsorption isotherms of CO₂ on a perfective surface and the pore size distributions were also investigated.

1.2.4 Increasing Gasification Reactivity of Longan-Seed Char by a Technique of Char Pre-Oxidation

The effect of air oxidation conditions (temperature and time) of longan-seed char on increasing gasification reactivity during CO₂ activation was studied. Four kinetic models (volume reaction model, shrinking core model, random pore model, and modified volume reaction model) were tested to describe the gasification reactivity and the kinetics behaviors of longan seed chars. The effect of char oxidation temperature on increasing the CO₂ gasification kinetics of longan-seed char was represented schematically for a better and clearer understanding of the mechanisms involved.

1.2.5 Application of the OTA Method for Improving the Porous Properties of Activated Carbon Gels

The OTA method was applied to prepare high surface area mesoporous carbons from organic gels and to investigate its effect on improving the porous properties of activated carbon gels. Furthermore, a comparison between the capacitance of mesoporous activated carbon gels produced via the conventional activation method and the OTA method when utilized as electrode materials were performed.

1.3 Output of Research

The primary goal of this research was to develop a new method for producing microporous-mesoporous activated carbon. The method, known as the OTA method, involves the combined consecutive processes of oxidation, thermal treatment, and physical activation. The findings from this investigation could provide valuable data for preparing activated carbon with superior porous properties using a modified physical activation approach. The results of the study on the kinetics and equilibrium of MB dye adsorption would provide knowledge that can be applied to practical systems. The analysis of the adsorption behavior of activated carbon samples produced from longan seed biomass could be useful in the design and optimization of activated carbon materials for various applications in the field of adsorption. Additionally, the Monte Carlo simulation-derived pore size distribution (PSD) using the defective surface model could serve further as an alternative approach for describing the pore development of activated carbon. In addition to the

development of the OTA method for producing microporous-mesoporous activated carbon, the study also discovered a simple pre-oxidation technique that significantly increases CO₂ gasification rates in longan-seed chars, thus contributing to the overall production of activated carbon and synthesis gas. This technique will be of significant value for the production of both activated carbon and synthesis gas. Furthermore, the OTA method is usefully applied to improve the porous properties of mesoporous carbon gels, providing an alternative method for producing activated carbon with superior porous properties using a modified activation technique. Overall, this research provides valuable findings for the production of activated carbon, with potential implications for practical applications and future research directions.

1.4 Research Development

This dissertation is divided into 7 chapters. The introduction in Chapter I describes the rationale, objectives, scope and limitations, output of this research, and research development. In Chapter II, a new method for the preparation of mesoporous activated carbon from longan seeds was proposed, using the combined consecutive processes of oxidation, thermal treatment, and activation (the OTA method). To compare the adsorption performance of activated carbon prepared from the two-step activation and the OTA method, the kinetics and equilibrium of methylene blue adsorption from aqueous solution by produced activated carbons are demonstrated in Chapter III. To provide insights into the OTA method for improving both the texture properties and gas adsorption, Chapter IV presents the analysis of gas adsorption and pore development in activated carbon by following the derived variation of the PSD based on surface defect models using the Monte Carlo (MC) simulation in the grand canonical (GC) ensemble. Chapter V provides additional results related to the gasification reactivity during CO₂ activation of longan-seed chars that are oxidized by air prior to the gasification reaction. Chapter VI presents the application of the OTA method to other well-defined carbons such as carbon gels and their performance evaluated as electrode materials, as well as provides insights into the pore development in carbon gels during the OTA processes. Finally, Chapter VII summarizes the important results found in this dissertation and proposes recommendations for future studies.

1.5 References

- Bansal, R., & Goyal, M. (2005). *Activated Carbon Adsorption*. CRC Press.
- Bansal, R. C., Donnet, J. B., & Stoeckli, F. (1988). *Active carbon*. Marcel Dekker.
- Canal-Rodríguez, M., Menéndez, J. A., & Arenillas, A. (2017). Carbon Xerogels: The Bespoke Nanoporous Carbons. In *Porosity-Process, Technologies and Applications* (pp. 69-89). IntechOpen London, UK.
- Chen, Y., Zi, F., Hu, X., Yang, P., Ma, Y., Cheng, H., Wang, Q., Qin, X., Liu, Y., Chen, S., & Wang, C. (2020, 2020/01/02/). The use of new modified activated carbon in thiosulfate solution: A green gold recovery technology. *Separation and Purification Technology*, 230, 115834.
- Hu, Z., Guo, H., Srinivasan, M. P., & Yaming, N. (2003, 2003/04/01/). A simple method for developing mesoporosity in activated carbon. *Separation and Purification Technology*, 31(1), 47-52.
- Hu, Z., Srinivasan, M. P., & Ni, Y. (2001, 2001/05/01/). Novel activation process for preparing highly microporous and mesoporous activated carbons. *Carbon*, 39(6), 877-886.
- Kyotani, T. (2000, 2000/01/01/). Control of pore structure in carbon. *Carbon*, 38(2), 269-286.
- Marsh, H., & Rodríguez-Reinoso, F. (2006). *Activated carbon*. Elsevier Science Ltd.
- Nayeri, D., & Mousavi, S. A. (2020, 2020/11/05). Dye removal from water and wastewater by nanosized metal oxides - modified activated carbon: a review on recent researches. *Journal of Environmental Health Science and Engineering*.
- Nezhad, M. M., Semnani, A., Tavakkoli, N., & Shirani, M. (2021, 2021/12/01/). Selective and highly efficient removal of uranium from radioactive effluents by activated carbon functionalized with 2-aminobenzoic acid as a new sorbent. *Journal of Environmental Management*, 299, 113587.

- Pallarés, J., González-Cencerrado, A., & Arauzo, I. (2018, 2018/08/01/). Production and characterization of activated carbon from barley straw by physical activation with carbon dioxide and steam. *Biomass and Bioenergy*, 115, 64-73.
- Radovic, L. R., Silva, I. F., Ume, J. I., Menéndez, J. A., Leon, C. A. L. Y., & Scaroni, A. W. (1997, 1997/01/01/). An experimental and theoretical study of the adsorption of aromatics possessing electron-withdrawing and electron-donating functional groups by chemically modified activated carbons. *Carbon*, 35(9), 1339-1348.
- Román, S., González, J. F., González-García, C. M., & Zamora, F. (2008, 2008/08/01/). Control of pore development during CO₂ and steam activation of olive stones. *Fuel Processing Technology*, 89(8), 715-720.
- Saygili, H., & Güzel, F. (2016, 2016/02/01/). High surface area mesoporous activated carbon from tomato processing solid waste by zinc chloride activation: process optimization, characterization and dyes adsorption. *Journal of Cleaner Production*, 113, 995-1004.
- Tseng, R.-L. (2006, 2006/11/15/). Mesopore control of high surface area NaOH-activated carbon. *Journal of Colloid and Interface Science*, 303(2), 494-502.
- Yagub, M. T., Sen, T. K., Afroze, S., & Ang, H. M. (2014, 2014/07/01/). Dye and its removal from aqueous solution by adsorption: A review. *Advances in Colloid and Interface Science*, 209, 172-184.

CHAPTER II

THE CONSECUTIVE PROCESS OF AIR OXIDATION, THERMAL DESTRUCTION OF SURFACE FUNCTIONAL GROUPS, AND CARBON ACTIVATION (THE OTA METHOD)

2.1 Abstract

A new and simple method, based entirely on a physical approach, was proposed to produce activated carbon from longan fruit seed with controlled mesoporosity. This method referred to as the OTA, consisted of three consecutive steps of (1) air oxidation of initial microporous activated carbon to introduce oxygen surface functional groups, (2) the thermal destruction of the functional groups by heating the oxidized carbon in an N₂ atmosphere at a high temperature to increase the surface reactivity due to increased surface defects by bond disruption, and (3) the final reactivation of the resulting carbon in CO₂. Mesopores formation is achieved by enlarging the original micropores after heat treatment through CO₂ gasification, generating new micropores at the same time, which increases the amount of mesopore volume and the total surface area compared to the conventional two-step activation method at the same activation time and temperature. For the activation temperatures of 850 and 900°C and the activation time of up to 240 min, it was found that the porous properties of activated carbon increased with the increase in activation time and temperature for both preparation methods. A maximum volume of mesopores of 0.474 cm³/g, which accounts for 44.1% of the total pore volume, and a maximum BET surface area of 1,773 m²/g was achieved using three cycles of the OTA method at the activation temperature of 850°C and 60 min activation time for each preparation cycle. The two-step activation method yielded activated carbon with a maximum mesopore volume of 0.270 cm³/g (33.0% of total pore volume) and surface area of 1,421 m²/g when the activation temperature of 900°C and a comparable activation time of 240 min was employed. Production of activated carbon by the OTA method is superior to the two-step activation method for better and more precise control of mesopore development.

2.2 Introduction

Activated carbon is one of the most versatile porous adsorbents, and is used in many separations and purification processes for both gas and liquid phase systems (Pallarés et al., 2018). Activated carbon is an amorphous carbon-based material, which exhibits a high degree of porosity, an extended surface area, a microporous structure, high adsorption capacity as well as a high degree of surface reactivity. Typically, activated carbon can be synthesized from a variety of low-cost cellulosic materials such as wood, rice straw, nutshell, corn hull, coconut shell, oil-palm shell, longan seed, bamboo, and peach stone, or carbonaceous materials such as bituminous coal, lignite, and peat (González-García, 2018; Mohamad Nor et al., 2013). It can be prepared through a two-step physical activation with oxidizing agents such as CO_2 , O_2 , and steam (Pallarés et al., 2018; Román et al., 2008), or a single-step preparation through wet impregnation of a precursor with inorganic chemical agents such as ZnCl_2 , KOH , NaOH , and H_3PO_4 , followed by a carbonization process (Carrott et al., 2006).

In general, the preparation of activated carbon by physical activation will predominantly produce micropores (Román et al., 2008). This type of carbon is suitable for use in gas adsorption applications. However, effective adsorption in liquids, both in terms of kinetics and adsorption capacity, requires activated carbon with a high proportion of mesopore volume. To be able to use activated carbon in the separation processes more widely and more efficiently, it is necessary to develop a process of activated carbon synthesis that can control proportionally the amounts of micropores and mesopores. The control of mesopores in activated carbon is mostly achieved through chemical activation, which consists of several methods such as a one-step chemical activation (Borhan et al., 2019; Hadoun et al., 2013; Jawad et al., 2017; Lee et al., 2021; Marrakchi et al., 2017; Nasrullah et al., 2019; Saygılı & Güzel, 2016), a two-step chemical activation (Khamkeaw et al., 2020; Muniandy et al., 2014; Tseng, 2006; Tseng & Tseng, 2005), a hydrothermal pretreatment followed by a simple chemical activation (Hossain et al., 2018; Xin et al., 2020), and chemical activation with dual activation agents (Le Van & Luong, 2019). Furthermore, the combined chemical and physical activation has also been used to control the amount of mesopores in activated carbon (Ariyadejwanich et al., 2003; Hu et al., 2003; Hu & Srinivasan, 2001; Hu et al., 2001; Juárez-Galán et al., 2009). On the other

hand, attempts to effectively control mesopore volume in activated carbon by using only a physical activation approach have not yet been reported to date. The use of chemical activating agents may cause a serious environmental problem and their corrosiveness is harmful to process equipment. Hence, this research work aims to study a new method based on the combined processes of oxidation, thermal treatment, and activation, which is purely based on a physical activation method.

Normally, the synthesis of activated carbon by the gasification reaction of a precursor with CO_2 mainly produces a large number of micropores (Molina-Sabio et al., 1996). The extent of the reaction, and hence the developed pore structure, is determined by the activation time and temperature. Now, if the course of the activation process is interrupted by air oxidation that creates new surface groups, followed by the destruction of those surface groups by heat treatment at a high temperature in an inert gas, the gasification reactivity of the original micropore surfaces should be enhanced due to the increasing number of unpaired electrons and free radicals resulting from the bond disruption. Therefore, when the activated carbon is reactivated with CO_2 , it is possible that the original micropores with a higher surface reactivity could be enlarged by the gasification reaction, resulting in a greater amount of mesopores. This method was proposed to produce a high ratio of mesopore volume to total pore volume and highly porous activated carbons when compared with the conventional two-step physical activation. This new method is capable of producing the desired amounts of micropores and mesopores by precise control of the conditions used during the various preparation steps. The advantages of this method are that it is easy to operate, has a low cost, and will not be the major cause of any pollution, since the process is conducted solely in the gas phase using only air, inert gas, and CO_2 and it is not associated with any acid solutions or oxidizing agents in the liquid phase.

The objective of this study is therefore to propose a new and simple method for the preparation of mesoporous activated carbon from longan fruit seed by the combined consecutive processes of oxidation, thermal treatment, and activation, abbreviated as the OTA preparation method. The parameters being studied included time and temperature during the activation step, the number of repeated OTA cycles, and the pore characteristics of the starting activated carbons. Furthermore, the Grand Canonical Monte Carlo (GCMC) simulation was employed to determine the

pore size distribution of the activated carbon produced from longan seed biomass. The underlying mechanism of pore development by the OTA method was also proposed and the supporting experimental evidence was presented.

2.3 Experimental Procedure

2.3.1 Materials

Longan seed was used as the raw material in this work for the preparation of activated carbon. It was supplied by Saha-Prachinburi Foods Industry Ltd., a local fruit processing plant in Chiangmai province, Thailand. Typically, longan is consumed as fresh and processed fruits while the seeds, which account for about 17% of the fresh weight of whole fruits, are discarded as waste or burned as fuel. Longan seed is a round black inner seed of longan fruit and has a diameter of around 1 cm. The as-received longan seed was rinsed and cleaned thoroughly with water and dried in an electric oven at 110°C for 48 h. The dried longan seed was crushed in a jaw crusher and sieved to obtain an average particle size of 1.70 mm (10 × 14 US mesh designation). The obtained sample was kept in a desiccator for further analysis.

2.3.2 Preparation of Char and Microporous Activated Carbons

The char was prepared by loading about 50 g of the longan seed sample in a ceramic boat and was heated in a horizontal electric tube furnace of 7 cm inside diameter and 100 cm length (CTF 12, Carbolite, UK) from room temperature to 500°C at the rate of 10°C/min under a constant flow of N₂ (99.99% of purity, Linde Thailand PCL) at 100 cm³/min and held at this temperature for 90 min. After that, the furnace was turned off and the char obtained was cooled down to room temperature inside the furnace under the flow of N₂. These carbonization conditions for char preparation were employed to ensure a complete devolatilization of the raw biomass. Next, about 15 g of the prepared char were gasified (activated) in a quartz tube reactor of 3.0 cm inside diameter and 120 cm length and inserted in a vertical tube furnace (CTF 12, Carbolite, Staffordshire, UK) under a constant flow of CO₂ (99.99% of purity, Linde Thailand PCL). The activation temperatures used were 850 and 900°C and the holding time varied between 60 and 240 min, giving carbon burn-off for the activation step of up to 90%.

2.3.3 Preparation of Mesoporous Activated Carbon by the OTA Method

The OTA method for preparing mesoporous activated carbon from longan seed was carried out in the same quartz tube reactor inserted in the vertical tube furnace (CTF 12, Carbolite, Staffordshire, UK). About 15 g of the activated carbon prepared in section 2.3.2 with a carbon burn-off of around 30% was oxidized in the reactor by heating the activated carbon from room temperature at a flow rate of 100 cm³/min in a stream of air (99.99% of purity, Linde Thailand PCL) to the oxidation temperature of 230°C and held at this temperature for 12 h. The purpose of this step was to create surface functional groups, particularly at the newly formed pores of the original activated carbon. Next, the carbon sample was heated at 950°C for 2 h under N₂ at a flow rate of 100 cm³/min to remove the surface functional groups, leading to the formation of more active sites for further gasification reactions at the originally formed micropores. After that, the sample was gasified with CO₂ again at the desired activation temperature of 850 or 900°C for 60 min to enlarge the original micropores, thus producing an increasing amount of mesopore volume. This process completed the first cycle (cycle 1) of the OTA preparation procedure and a total of three cycles (cycles 1, 2, and 3) were performed, using the same activation time (60 min) and temperature (850 or 900°C) for each cycle. The derived microporous carbon prepared in section 2.3.2 using the two-step activation was designated as AX-Y, where A stands for activated carbon and symbols X and Y represent the activation temperature (850 or 900°C) and activation time (60, 120, 180, or 240 min), respectively. The mesoporous activated carbon prepared by the OTA method was designated as AX-Y-Z, where A stands for activated carbon originally prepared by the two-step activation method at the activation temperature X (850 or 900°C), and time Y (60 min) and Z is the number of repeated cycles (1, 2 or 3) for the processes of oxidation, heat treatment and reactivation at the same temperature X and time Y. The final yield of activated carbon was calculated based on the weight of the original longan seed char.

2.3.4 Raw Material Characterization

The longan seed sample was characterized for proximate analysis (wt% fixed carbon, volatile content, and ash content) and ultimate analysis (wt.% C, H, N, S, and O). The proximate analysis was performed using a thermogravimetric analyzer (TGA/DSC 1 STAR^e System, METTLER TOLEDO, Greifensee, Switzerland) and the heating scheme proposed by Guo and Lua (Guo & Chong Lua, 1998). The ultimate analysis was determined by a CHNS analyzer (CHN 628S, LECO Corporation, USA). The thermal decomposition behavior of the longan seed precursor was also studied using the TGA by non-isothermal heating from room temperature to the final temperature of 900°C using a heating rate of 10°C/min under a constant flow of N₂.

2.3.5 Porous Properties of the Prepared Activated Carbons

Porous properties of the derived activated carbons were determined from the N₂ adsorption isotherms at -196°C measured by using a high-performance adsorption analyzer (ASAP2010, Micromeritics, Norcross, GA, USA). The specific surface area was calculated from the N₂ adsorption isotherm data for relative pressures (P/P_0) over a range from 0.05 to 0.20 by applying the Brunauer Emmett Teller (BET) equation (Brunauer et al., 1938). The total pore volume was estimated from the volume of N₂ adsorbed at the relative pressure of 0.98 and converted to the volume of N₂ in the liquid state at a given temperature. Micropore volume was determined by applying the Dubinin-Radushkevich (DR) equation (Dubinin, 1975). The mesopore volume was estimated by subtracting the micropore volume from the total pore volume. The pore size distributions of the derived activated carbons were determined from the N₂ adsorption isotherms data by applying the Grand Canonical Monte Carlo (GCMC) simulation (see Chapter IV for the methodology of GCMC simulation). The average pore size (D_{av}) was computed based on the equation $4V_T/S$, assuming cylindrical pores, where V_T is the total pore volume and S is the BET surface area. Activated carbons prepared by the two-step activation and the OTA method were also analyzed for the proximate and ultimate analyses.

2.3.6 Surface Reactivity of Activated Carbon Towards CO₂ Gasification Reaction

To assist the understanding of pore development in activated carbon prepared by the OTA method, the reactivity of activated carbon towards CO₂ gasification reaction was studied by following the weight loss of a sample in a thermogravimetric analyzer (TGA/DSC 1 STAR^e System, METTLER TOLEDO, Greifensee, Switzerland). About 15 mg of the initial activated carbon sample, prepared from activating char in CO₂ at 850 and 900°C, which went through the oxidation and heat treatment in the tube furnace was loaded into an alumina crucible (70 µL capacity) of the thermogravimetric analyzer and heated from room temperature to the desired gasification temperature at the heating rate of 20°C/min under a constant flow of N₂ at 100 cm³/min. When the final gasification temperature was reached, the gas flow was switched from N₂ to CO₂ flowing at the rate of 100 cm³/min, and held at this temperature for 60 min. The sample weight loss via gasification reaction was continuously recorded as a function of time. The gasification temperatures of 850 and 900°C were studied for the activated carbons after being oxidized and heat-treated in the tube furnace for cycles 1 and 2 of the OTA preparation method. For comparison, the TGA measurement was also carried out on longan seed char for CO₂ gasification at 850 and 900°C as a function of time to determine its carbon reactivity for the two-step activation method.

2.3.7 Surface Functional Groups of Activated Carbons

The presence of surface functional groups upon air oxidation of activated carbon was determined qualitatively by Fourier Transform Infrared Spectroscopy (FTIR) and quantitatively by applying the Boehm titration technique (Boehm, 1966, 1994; Goertzen et al., 2010; Seung Kim & Rae Park, 2016).

For the FTIR analysis, about 0.50 g of an activated carbon powder was placed in a micro-sample holder of an FTIR spectrophotometer (Vertex 70 FT-IR, Bruker, Billerica, MA, USA). The IR spectra were collected by the acquisition of 64 scans for each run, using the wavenumber in the mid-IR spectrum (400–4,000 cm⁻¹) with an incremental measurement resolution of 4 cm⁻¹.

For the Boehm titration analysis, 0.50 g of the carbon sample was loaded into two Erlenmeyer flasks, each of which was filled with 25 mL of 0.05 M solutions of sodium hydroxide and hydrochloric acid. Next, each flask was sealed and

shaken at room temperature for 36 h, and after that, the mixture was filtered using Whatman 44 filter paper. 5 mL of the filtrate from each flask were pipetted and the excess base and acid remaining in the filtrate were determined by titrating with hydrochloric and sodium hydroxide solutions, respectively. The amounts of total acid groups were determined under the assumption that NaOH neutralizes the carboxylic, lactonic, and phenolic acid groups. The number of basic groups was determined by the amount of hydrochloric acid that reacts with the basic surface groups on the carbon surfaces. Dried potassium hydrogen phthalate (KHP) was the primary standard used to standardize NaOH and HCl concentrations for the correct calculation of the amounts of surface oxygen functional groups. Titration of the sample solution was performed in triplicate and the average value was used for determining the amounts of surface functional groups.

2.4 Results and Discussion

2.4.1 Thermal Decomposition Behavior of Longan Seed Precursor

The thermal decomposition behavior of longan seed in an N_2 atmosphere was investigated through the utilization of thermogravimetric analysis, as depicted in Figure 2.1. The TG curve demonstrated the weight remaining versus the heating temperature, while the DTG curve illustrated the decomposition rate as the first derivative of the TG curve. A slow weight loss was observed from 150°C onwards, which was attributed to the initial decomposition of lignin at a relatively low temperature of around 150°C, which proceeded up to a temperature of 900°C (Yang et al., 2007). Subsequently, a peak on the DTG curve was observed within the temperature range of 250 to 400°C, indicating the devolatilization process resulting from the release of most volatile substances caused by the decomposition of cellulose and hemicellulose (Yang et al., 2007). The main pyrolysis decomposition of longan seed occurred over this temperature range, with the maximum weight loss rate occurring at 305°C. A gradual decrease in the remaining weight was observed above 400°C, with a constant yield of solid char of approximately 24 wt% eventually being approached.

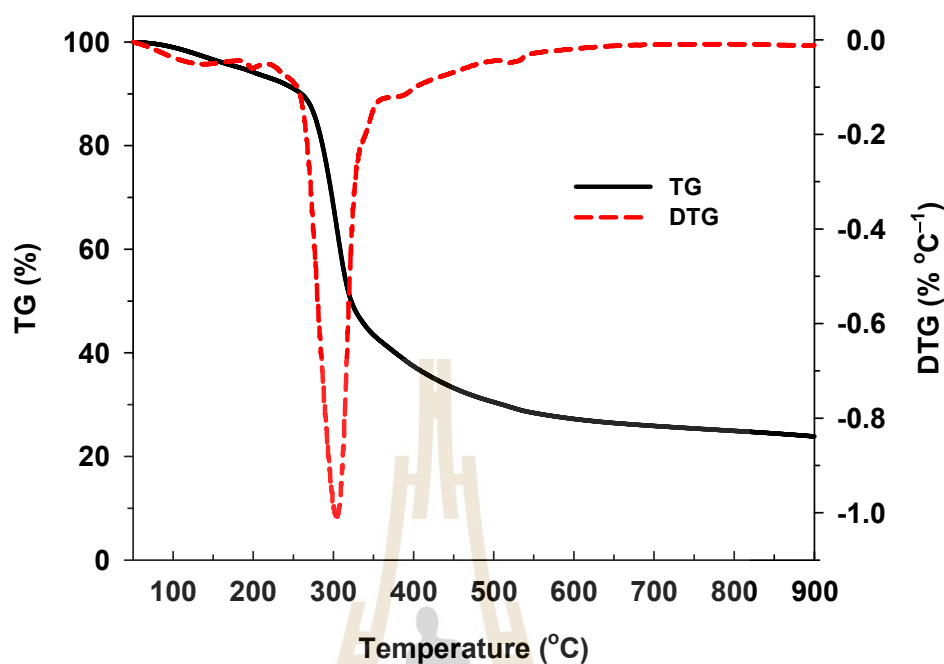


Figure 2.1 Typical residual weight (TG) and weight loss rate (DTG) for the non-isothermal pyrolysis in an N_2 atmosphere of longan seed biomass.

2.4.2 Proximate and Ultimate Analyses of Longan Seed Precursor and Activated Carbon

Table 2.1 shows the results of the proximate analysis of the longan seed used in this study, along with those of other biomass wastes. The fixed carbon content of longan seed from the present work is 22.34 wt% with a relatively low ash content of 1.15 wt%. Volatile content is high (76.51 wt%) which is typical for biomass materials. These values are comparable with those of the other biomasses reported in the literature. Therefore, with reasonably high carbon content and low ash composition, the longan seed precursor used in this study could be used as a promising precursor for activated carbon production.

Table 2.2 shows the proximate and ultimate analyses of activated carbons prepared by the two-step activation and the OTA method. For the two-step activation method, increasing the activation time from 60 to 240 min decreased the fixed carbon content by about 4.2% from 86.25 to 82.58 wt%. Obviously, the reduction in fixed carbon is the result of carbon removal by CO_2 gasification during

the activation step. The volatile content also decreased with the increase in activation time, and this is possibly caused by the additional devolatilization of char at the high activation temperature of 850°C. The ultimate analysis also showed a decrease in carbon content as the activation time was increased from 60 to 240 min, in line with the results of the proximate analysis. Hydrogen content increased by about 20%, while oxygen content increased much more, by about 300%.

Similar to the two-step activation, the fixed carbon content of activated carbon produced by the OTA method decreased with each treatment cycle (60 min activation time for each cycle). Volatile content also slightly decreased for activated carbons from cycle 1 to cycle 3. It is interesting to note that for the same activation time, the percentage of fixed carbon produced by the OTA method was lower than that of the two-step activation method when, for example, comparing A850-180 vs A850-60-2 and A850-240 vs A850-60-3. This proves that the gasification reaction of carbon from the OTA method is faster (more reactive) than that of carbon prepared by the two-step activation.

Table 2.1 Proximate analysis of longan seed and some industrial biomass wastes

Biomass	Proximate analysis (dry basis) [wt.%]		
	Fixed carbon	Volatile matters	Ash
Longan seed (this study)	22.34	76.51	1.15
Longan seed ⁽¹⁾	19.60	78.70	1.70
Oil palm shell ⁽²⁾	19.80	77.60	2.60
Coconut shell ⁽³⁾	19.40	79.20	0.60
Peanut shell ⁽³⁾	16.50	81.00	2.50
Eucalyptus sawdust ⁽³⁾	15.38	83.70	0.90
corn cob ⁽³⁾	14.60	83.00	2.40

Sources: ⁽¹⁾ (Junpirom et al., 2005); ⁽²⁾ (Guo & Lua, 2001); ⁽³⁾ (García et al., 2012)

Table 2.2 Proximate and ultimate analysis results of longan seed, longan seed char, and activated carbons

Sample name	Proximate analysis (dry basis) [wt.%]			Ultimate analysis (dry basis) [wt.%]				
	Fixed carbon	Volatile	Ash	C	H	N	S	O _{diff.}
Longan seed	22.34	76.51	1.15	47.56	6.55	1.09	0.03	44.76
C500-90	83.58	14.81	1.61	85.92	3.55	2.32	0.00	8.20
A850-60	86.25	11.57	2.18	91.91	0.77	2.38	0.00	4.93
A850-120	83.21	11.49	5.30	85.58	0.85	2.47	0.00	11.10
A850-180	83.02	11.45	5.53	81.16	0.98	2.48	0.00	15.38
A850-240	82.58	11.32	6.10	76.75	0.88	2.50	0.00	19.87
A850-60-1	83.40	10.93	5.67	84.00	0.63	2.16	0.00	13.21
A850-60-2	82.57	10.89	6.54	81.71	0.61	1.99	0.00	15.70
A850-60-3	80.08	10.38	9.54	76.60	0.44	1.90	0.00	21.06

2.4.3 N₂ Isotherms of Prepared Activated Carbons

The isotherms of N₂ adsorption by the prepared activated carbons are presented in Figure 2.2 for the activated carbon series A850 and A900. The variation of isotherms over a low-pressure range of relative pressure less than 0.1 is also demonstrated on a semi-log scale, as shown in Figures 2.2c,d. It appeared that the effect of pressure on the adsorption isotherms is the same for both the low and high relative pressures. The activated carbons A850-60 and A900-60, prepared by the two-step activation with CO₂, showed Type I isotherm according to the IUPAC classification (Sing et al., 1985), typified by a sharp increase in the amount of N₂ adsorbed at low pressures and followed by a long plateau region at higher pressures. This adsorption behavior is indicative of adsorption in micropores either in pores of molecular dimensions by the pore-filling mechanism at very low pressures or in larger micropores over a range of higher pressures (Rouquerol et al., 2013). It appeared that as the activation time was progressively increased from 60 to 240 min, the amounts of N₂ adsorbed tended to increase, due largely to the consequent increase in porous properties (pore volume and surface area) of the activated carbon samples. At the longest activation time of 240 min, the isotherms for both carbons

changed from Type I to Type II with small hysteresis loops, indicating the presence of some mesopores. It was also noted that for the same activation time, the amount of N_2 adsorbed with the A900 series was slightly higher than those of the A850 series because the former was prepared at a higher activation temperature, thus resulting in a larger extent of pore development due to the increase in char burn-off.

Activated carbon derived from the OTA method showed a distinct change in the isotherms from Type I for A850-60 and A900-60 to Type IV isotherm (Type II plus a hysteresis loop), with an increase in both the amount adsorbed and the size of the hysteresis loop as the number of preparation cycles was increased from cycle 1 to cycle 3. This indicates the progressive development of mesopores with the distribution of pore sizes. The hysteresis loop closed at the relative pressure of about 0.4 for all samples and its shape resembled Type H2 for the classification of hysteresis loops, according to the IUPAC classification (Sing et al., 1985), which indicated that the adsorbent consists of interconnected networks of pores of different sizes and shapes (Rouquerol et al., 2013).

It is further noted from N_2 isotherms in Figure 2.2 that sample A850-60-3 had greater amounts of N_2 adsorbed as compared to that sample A900-60-3, although the latter was activated at a higher temperature. This can be explained based on the porous properties of activated carbon presented in the next section, as shown in Table 2.3. It was discovered that the mesopore volume, the total pore volume, and the surface area of A900-60-3 were slightly lower than those of sample A850-60-3, thus allowing a lower amount of N_2 to be adsorbed on the carbon surface, as shown in Figure 2.2. It is likely that for such a very high carbon burn-off (93.7%) of sample A900-60-3, some adjacent mesopores collapsed and combined to form a larger mesopore, thus providing a reduction in mesopore volume and a smaller surface area.

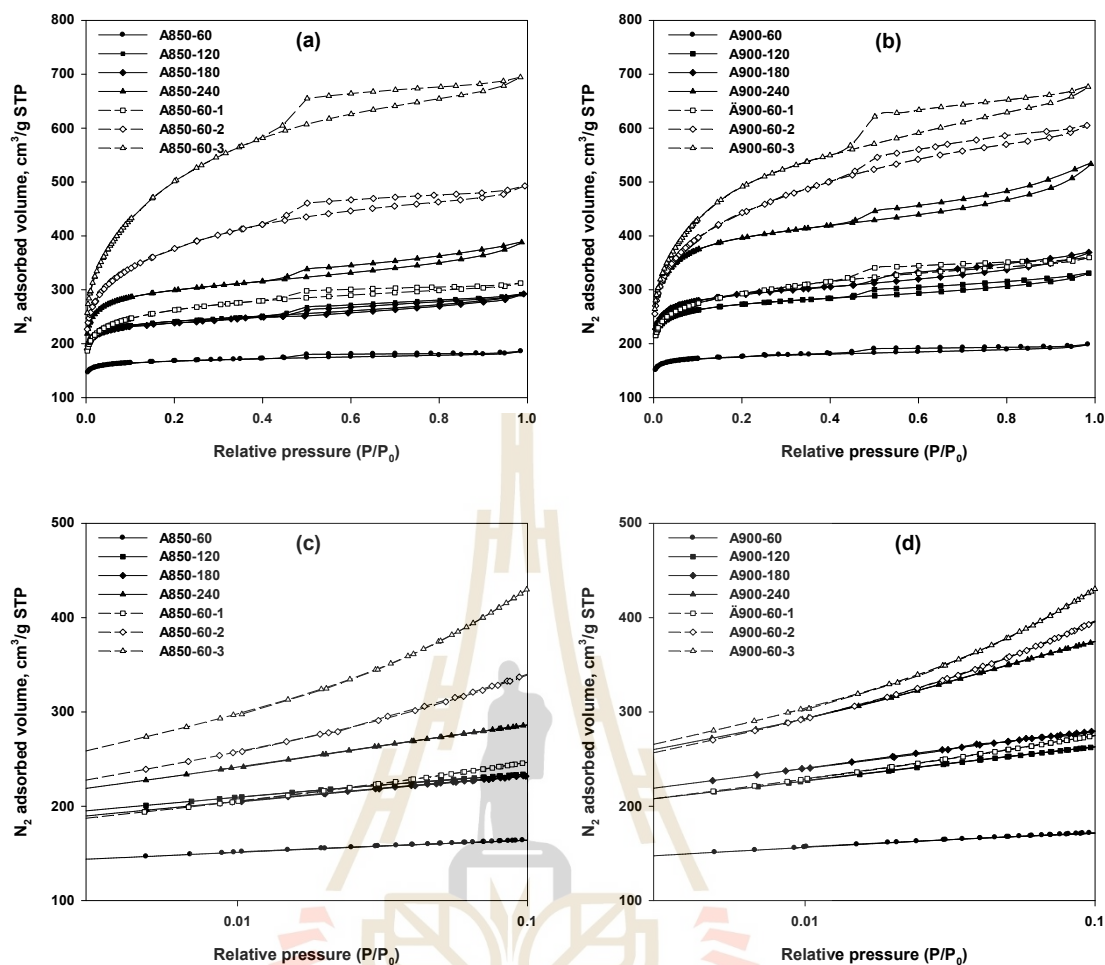


Figure 2.2 N_2 adsorption isotherms of microporous activated carbons prepared by the two-step activation method and mesoporous activated carbons prepared by the OTA method at two activation temperatures of (a) 850°C and (b) 900°C, while (c, d) show the corresponding isotherms at a low-pressure range ($P/P_0 < 0.1$) on a semi-log scale.

2.4.4 Porous Properties of Prepared Activated Carbons

Table 2.3 compares the porous properties of activated carbons prepared by the two-step activation method and by the OTA method for the activation temperatures of 850 and 900°C conditions. If we consider first the results of activated carbons produced by the two-step activation method for the A850 and A900 series (samples nos. 1–4 and 8–11). For each carbon series, all porous properties including the average pore size, the BET surface area, the micropore

volume, the mesopore volume, and the total pore volume increased with the increase in activation time from 60 to 240 min. This is ascribed to the increase in the carbon burn-off with increasing activation time that removes more carbon atoms via the CO₂ gasification reaction. The percentage of micropore volume relative to the total pore volume dropped from 91.1 to 69.7% and from 86.0 to 67.0% for A850 and A900 carbon series, respectively, as the activation time was increased from 60 to 240 min. Obviously, employing a higher activation temperature of 900°C promotes higher values of porous properties as compared to the lower temperature of 850°C. An increase in the average pore size as the activation time was increased should result from the enlargement of some small pores caused by the effect of CO₂ gasification, not by the pore coalescence which usually occurs at a relatively high carbon burn-off. The amount of mesopore volume increased from 0.024 to 0.178 cm³/g (8.9 to 30.3% of total pore volume) and from 0.041 to 0.270 cm³/g (14.0 to 33.0% of total pore volume) for A850 and A900 carbon series, respectively, as the activation time was increased from 60 to 240 min. From these results, it can be inferred that under the preparation conditions studied, the two-step activation with CO₂ produced logan- seed activated carbon which mostly contains the micropore size range.

Next, the porous properties of activated carbon produced by the OTA method are considered. Again, increasing the activation time gave rise to the increase in all porous properties for the A850 series (sample nos.1, 5–7) and A900 series (sample nos. 8, 12–14). It was noticed that activated carbons from the OTA preparation showed remarkably higher volumes of both micropores and mesopores for the same activation time as compared to those obtained from the two-step activation method (for example, comparing sample no.3 vs no. 6 and no. 11 vs no.14). The mesopore volume and the total surface area also increased with the increase in the number of repeated cycles of the OTA method (sample nos. 5–7 and sample nos.12–14). The maximum amount of mesopores of 0.474 cm³/g, corresponding to 44.1% of the total pore volume, and a maximum BET surface area of 1,773 m²/g was achieved for sample no. 7 (A850-60-3) for the three-cycle treatment of the OTA preparation method. It was noted that the activated carbon produced from the three-cycle preparation of the OTA method at the higher activation temperature of 900°C (sample no. 14, A900-60-3) showed a slight decrease in porous properties, as compared to sample no. 7 (A850-60-3) of lower activation

temperature. This is probably caused by the merging of some mesopores of sample A900-60-3, resulting in an increase in the average pore size from 2.42 nm for A850-60-3 to 2.54 nm for A900-60-3. For comparison, the activated carbon prepared by the two-step activation (sample no. 11, A900-240) provided the maximum amount of mesopores and surface area of 0.270 cm³/g and 1,421 m²/g, respectively, using the activation temperature and time of 900°C and 240 min. It is therefore obvious that the OTA method is an effective means for producing activated carbon from longan seed with increasing amounts of mesopores and a high surface area, as compared to the two-step activation method with a comparable carbon burn-off.

Table 2.3 Porous properties of activated carbons prepared by the two-step activation and the OTA method

Sample no.	Sample name	D _{av} (nm)	V _{mi} (cm ³ /g) (%)	V _{me} (cm ³ /g) (%)	V _T (cm ³ /g)	V _{me} /V _{mi} (%)	S _{BET} (m ² /g)	Burn-off (%)	Yield (%)
1	A850-60	1.67	0.248 (91.1)	0.024 (8.9)	0.272	9.50	652	27.7	72.3
2	A850-120	1.88	0.343 (78.5)	0.094 (21.5)	0.437	27.6	932	42.1	57.9
3	A850-180	1.91	0.340 (76.9)	0.102 (23.1)	0.442	30.0	926	52.2	47.8
4	A850-240	2.06	0.409 (69.7)	0.178 (30.3)	0.587	43.5	1,140	68.8	31.2
5	A850-60-1	1.96	0.375 (78.1)	0.105 (21.9)	0.480	27.8	980	46.1	53.9
6	A850-60-2	2.32	0.466 (63.3)	0.270 (36.7)	0.736	58.1	1,271	62.1	37.9
7	A850-60-3	2.42	0.600 (55.9)	0.474 (44.1)	1.074	78.9	1,773	78.4	21.6
8	A900-60	1.73	0.253 (86.0)	0.041 (14.0)	0.294	16.3	684	34.8	65.2
9	A900-120	1.96	0.376 (77.5)	0.109 (22.5)	0.485	29.1	990	58.8	41.2
10	A900-180	2.16	0.406 (70.6)	0.169 (29.4)	0.575	41.6	1,065	63.9	36.1
11	A900-240	2.30	0.547 (67.0)	0.270 (33.0)	0.817	49.3	1,421	92.7	7.30
12	A900-60-1	2.06	0.434 (77.0)	0.130 (23.0)	0.564	29.9	1,093	56.2	43.8
13	A900-60-2	2.49	0.583 (62.0)	0.357 (38.0)	0.940	61.3	1,510	76.5	23.5
14	A900-60-3	2.54	0.576 (55.0)	0.471 (45.0)	1.047	81.8	1,649	93.7	6.30

Table 2.4 shows the values of the BET surface area and mesopore volume of activated carbons produced by various activation techniques from previous investigations, with the purpose of increasing the amount of mesopores. These results show that chemical activation and chemical activation augmented with physical activation are quite effective in increasing the mesopore volume in the derived activated carbon, except for the activation with NaOH which gives relatively low values of surface area and the amount of mesopores. The OTA preparation method proposed in this study provided activated carbon with a reasonable amount of developed mesopores and a high specific surface area. More importantly, it causes less pollution and involves a lower preparation cost, as compared to traditional chemical activation methods.

Table 2.4 Preparation of activated carbon by various methods for mesoporous activated carbon production

Raw material	Activation method	V_{me}	S_{BET}
		(cm^3/g) (%)	(m^2/g)
Coconut shell ⁽¹⁾	ZnCl ₂ + CO ₂	1.364 (71%)	2,191
Waste tires ⁽²⁾	HCl + steam	1.620 (74%)	1,119
Date stems ⁽³⁾	H ₃ PO ₄	0.993 (95%)	1,455
Rice husk ⁽⁴⁾	KOH	0.691 (46%)	2,696
Chitosan flakes ⁽⁵⁾	NaOH	0.157 (62%)	318
Coconut leaves ⁽⁶⁾	H ₃ PO ₄	1.276 (93%)	982
Longan seed (this study)	OTA method	0.474 (44%)	1,773

Sources: ⁽¹⁾(Hu et al., 2001); ⁽²⁾(Ariyadejwanich et al., 2003); ⁽³⁾(Hadoun et al., 2013);
⁽⁴⁾(Muniandy et al., 2014); ⁽⁵⁾(Marrakchi et al., 2017); ⁽⁶⁾(Jawad et al., 2017)

Obviously, the extent of pore development is clearly dependent on the time and temperature of activation which in turn have a direct bearing on the carbon burn-off during char activation, where the percentage of carbon burn-off during the activation step is determined by the following equation,

$$\text{Burn-off (\%)} = \frac{(W_{\text{char}} - W_{\text{AC}})}{W_{\text{char}}} \times 100 \quad (2.1)$$

where W_{char} and W_{AC} are the initial weight of char and the weight of activated carbon, respectively.

Therefore, it is possible that the effect of time and temperature of activation could be consolidated into a single effect of char burn-off on the porous properties of the prepared activated carbons. Figure 2.3 typically compares the dependence of BET surface, total pore volume, micropore volume, and mesopore volume on the percentage of char burn-off of activated carbons prepared by the two-step activation and the OTA methods, respectively. It is clear that the porous properties of activated carbon correlated well with the percentage of char burn-off for each preparation method and the porous properties of activated carbons tended to increase with the increase in % char burn-off, as expected. It is interesting to observe further that the porous properties of activated carbons produced by the OTA method appeared to increase with increasing char burn-off at a much faster rate (steeper slope of the curve). These results suggest that for the same char burn-off level, the OTA method was able to significantly increase the char reactivity for CO₂ gasification over that of activated carbon produced by the conventional two-step activation method. To correlate the porous properties of prepared activated carbon (y) as a function of the percentage of char burn-off (x), empirical equations were proposed and presented in Table 2.5, along with the regression coefficient of the fitting (R^2). Overall, the proposed equations are capable of predicting the porous properties of the prepared activated carbon with reasonable accuracy.

The correlation between the percentage of carbon burn-off and porous properties of the prepared activated carbon by CO₂ activation present in Figure 2.3 was also found in a number of previous investigations using different types of precursors, for example, sewage sludge (Alvarez et al., 2016), waste tires (Lopez et al., 2012), and sugarcane bagasse (Gonçalves et al., 2016). It was summarized that the porous properties of activated carbon, including the micropore volume, the total pore volume, and BET surface area, tended to increase almost linearly with the increase in activated carbon burn-off to the value of about 70% and then decreased at higher burn-off. The reduction in porous properties at a high carbon burn-off was

explained to result from the coalescence of adjacent small pores to form larger-size pores with lower surface area and chemical reactivity. However, as shown in Figure 2.3, the porous properties of activated carbon prepared by the two-step activation in the present study showed a continuous increase in porous properties up to a very high degree of char burn-off of 92.7%, although a slight drop in porous properties was observed for activated carbon produced by the OTA method over the burn-off values from 78.4 to 93.7%. It is believed that all porous properties will finally decrease when almost all carbon atoms are consumed by the CO₂ gasification. The different results could depend to a larger extent on the difference in the chemical nature of the precursor used and to a lesser extent on the preparation conditions employed for activated carbon synthesis.

Table 2.5 Empirical equations correlating porous properties of activated carbon (y) prepared by the two-step activation and the OTA methods as a function of % carbon burn-off (x)

Porous properties	Activation method	Empirical equations	R ²
(a) BET surface area (m ² /g)	2-step	$y = 669\ln(x) - 1639$	0.931
	OTA	$y = 1158\ln(x) - 3462$	0.958
(b) Total pore volume (cm ³ /g)	2-step	$y = 0.429\ln(x) - 1.20$	0.920
	OTA	$y = 0.856\ln(x) - 2.78$	0.943
(c) Micropore volume (cm ³ /g)	2-step	$y = 0.234\ln(x) - 0.56$	0.911
	OTA	$y = 0.364\ln(x) - 1.03$	0.946
(d) Mesopore volume (cm ³ /g)	2-step	$y = 0.195\ln(x) - 0.65$	0.915
	OTA	$y = 0.491\ln(x) - 1.76$	0.894

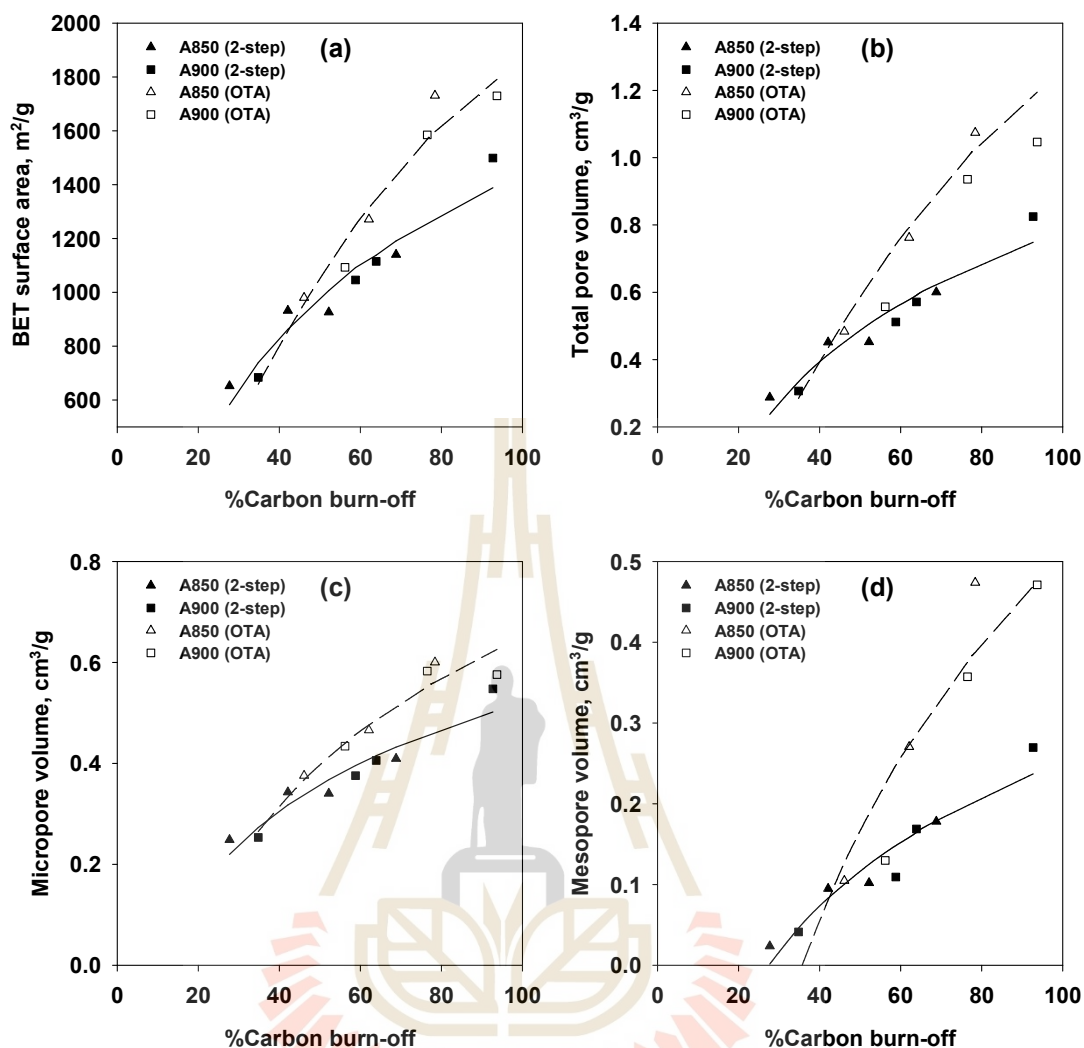


Figure 2.3 Effect of carbon burn-off during CO₂ activation step of longan seed biomass on the porous properties of activated carbons prepared by the two-step activation and the OTA methods, (a) BET surface area, (b) total pore volume, (c) micropore volume, and (d) mesopore volume.

2.4.5 On Mesopore Development by the OTA Method

The porous properties of activated carbon presented in the previous section indicated that the incorporation of oxidation and thermal treatment steps for initial activated carbon with a certain degree of carbon burn-off prior to the subsequent activation step, referred to as the OTA preparation method, was able to effectively promote the development of mesopores in longan seed-based activated carbon. In addition to producing a higher amount of mesopores as compared to the

two-step activation method, the OTA method was also capable of increasing the amount of micropores under the same activation conditions of time and temperature, which also produced a higher total BET surface area.

Based on the porous properties results of the prepared activated carbon in Table 2.3, the mechanism of mesopore development was proposed in this study, which is schematically presented in Figure 2.4, starting from Figure 2.4a, which represents an initial activated carbon prepared by the two-step activation method, for example, A850-60 carbon which contains a certain amount of micropores (pore nos. 1–9). Next, some micropores (labeled as pore nos. 1, 3, 5, and 6) containing hetero atoms which are reactive enough to be oxidized by oxygen in the air form a certain quantity of oxygen functional groups on the surfaces of pore nos. 1, 3, 5, and 6, as shown in Figure 2.4b. After heating the carbon in an inert atmosphere of N_2 at a high temperature, the bonds of the surface functional groups are destroyed, creating more surface defects with a high degree of surface reactivity due to the presence of a large number of unpaired electrons and free radicals, as illustrated in Figure 2.4c. The number of reactive pores subjected to functional group formation will depend on the distribution of the activation energy level for bond formation, which in turn is dictated by the oxidation temperature employed. Finally, the resulting carbon is further activated in CO_2 , as shown in Figure 2.4d. This produces the enlargement of the original reactive pores (nos. 1, 3, 5, and 6) by the gasification reaction, thus creating mesopores as well as some newly formed micropores (nos. 10, 11, and 12). Repeating the OTA cycle will increase the amount of mesopores and additional micropores, but mesopores are developed in a greater proportion due to the higher degree of surface reactivity towards CO_2 gasification.

To support the proposed mechanism of mesopore development by the OTA method, experimental evidence is presented in the following sections for the increased amount of surface functional groups after air oxidation, the increase in carbon reactivity towards CO_2 gasification after the heat treatment step, and the pore size distributions of the microporous-mesoporous activated carbon after the reactivation step.

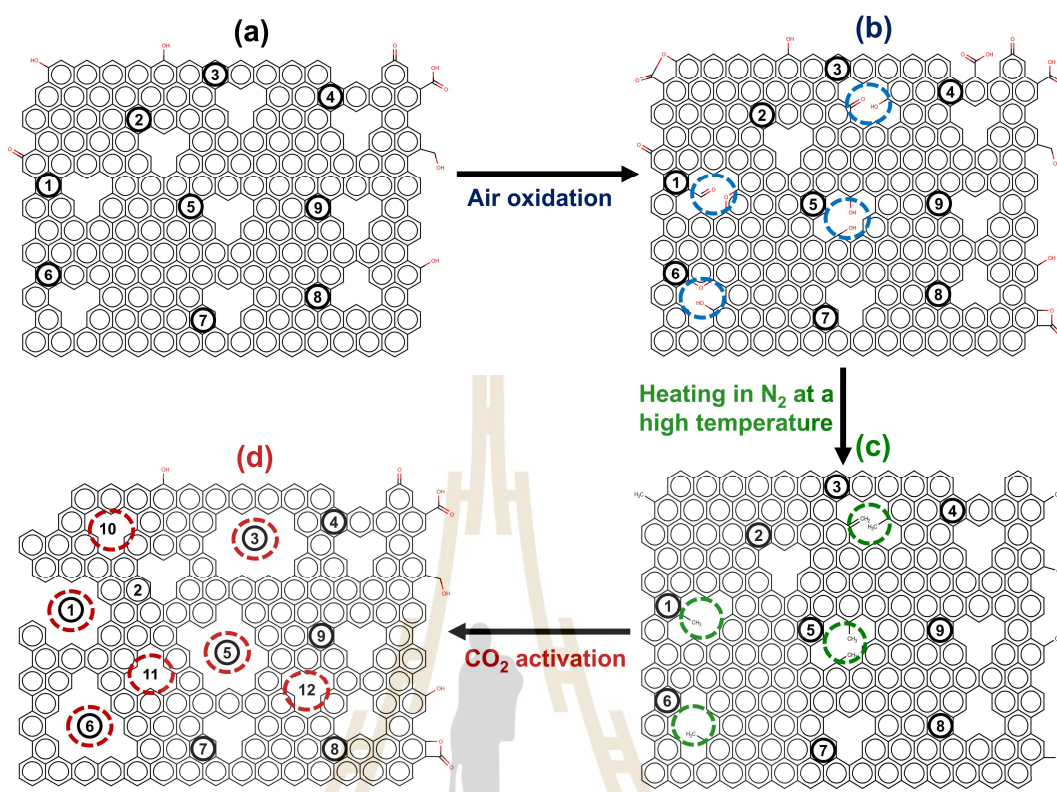


Figure 2.4 The model for mesopore development by the OTA method is represented schematically by the following steps, (a) the initial activated carbon contains a certain number of micropores (nos.1-9), (b) formation of oxygen functional groups on the surface of some original micropores (nos.1, 3, 5, 6) by air oxidation, (c) bond dissociation of the functional groups increases the surface reactivity of micropores (nos.1, 3, 5, 6) due to the increasing number of free radicals and unpaired electrons, and (d) formation of new mesopores (nos.1, 3, 5, 6) by enlargement as well as the formation of new micropores (nos.10-12) by CO₂ gasification reaction.

2.4.6 Surface Functional Groups of Prepared Activated Carbons

The FTIR results of activated carbon samples from the OTA method, namely the original carbon from the two-step activation (A850-60), the air oxidized sample (A850-60-OX), a sample with heat treatment (A850-60-HT), and the final reactivated carbons from cycles 1-3 (A850-60-1, A850-60-2, and A850-60-3) are shown in Figure 2.5a. For the initial activated carbon (sample no. 1, A850-60), a peak detected near the wavenumber of $2,100\text{ cm}^{-1}$ is assigned to terminal alkyne (Nandiyanto et al., 2019), while the peak near $2,320\text{ cm}^{-1}$ could be attributed to NH stretching vibration (Nandiyanto et al., 2020), or carbon-oxygen groups due to ketone (Pradhan & Sandle, 1999). A peak detected at $1,554\text{ cm}^{-1}$ is generally assigned to ring vibrations in large condensed aromatic carbon skeletons or likely responding to aromatic rings (Bouwman & Freriks, 1980; Burg et al., 2002). These aromatic rings are usually associated with the appearance of weak to medium absorption around $3,000$ to $3,150\text{ cm}^{-1}$. Two small peaks at $1,080$ and $1,016\text{ cm}^{-1}$ are due to the vibration of C-O stretching of primary alcohols, and O-H bending modes of phenolic, alcoholic, and carboxylic groups (Burg et al., 2002; Pradhan & Sandle, 1999). For air-oxidized carbon (sample 2, A850-60-OX), there exist two sharp peaks in the range of $3,600$ – $3,780\text{ cm}^{-1}$ which have been assigned to isolated hydroxyl groups (O-H) stretching (Socrates, 2004). There is also another large peak between $1,730$ and $1,880\text{ cm}^{-1}$, which indicates strong carbonyl double bonds (C=O) such as anhydrides, aldehydes, carboxyl, and lactones (El-Hendawy, 2006; Fanning & Vannice, 1993). It is obvious that the oxidation of activated carbon with air could introduce a number of surface functional groups on the graphene sheet of activated carbon.

After heating the oxidized carbon at a high temperature in N_2 , the heat-treated sample (A850-60-HT) showed several peaks at $2,329\text{ cm}^{-1}$, $2,107\text{ cm}^{-1}$, and $1,557\text{ cm}^{-1}$ which are the same as the initial activated carbon. However, no peaks were detected over the range $1,100$ – $1,000\text{ cm}^{-1}$ which indicates the removal of oxygen functional groups such as phenolic and carboxylic groups as a result of the heat treatment. The reactivated carbons by CO_2 (sample nos. 4–6 for A850-60-1, A850-60-2, and A850-60-3) showed similar spectra to the initial activated carbon but with significant bands between $1,100$ and $1,000\text{ cm}^{-1}$, which is indicative of functional group formation by CO_2 oxidation during the activation step. The similar FTIR spectra pattern of the three activated carbons indicated that the number of the repeated

cycle for producing microporous-mesoporous activated carbon by the OTA method had no influence on the types of the created surface functional groups.

The FTIR results of four activated carbon samples produced from the two-step activation method are shown in Figure 2.5b. It is observed that increasing the activation time from 60 to 240 min had virtually no bearing on the FTIR spectra pattern and the detected peaks were similar to those of activated carbons produced by the OTA method. It is further observed that a sharp peak was detected at $1,551\text{ cm}^{-1}$, and another large peak was detected between $1,730$ and $1,880\text{ cm}^{-1}$. In addition, the peak intensity of C-O stretching and O-H bending at $1,072$ and $1,016\text{ cm}^{-1}$ for A850-240 was higher than those of the other samples, implying that the amounts of oxygen-containing functional groups can be affected by varying the activation time. This is in agreement with studies from the previous investigation (He et al., 2010).

On Boehm's titration results, Table 2.6 typically shows the amounts of oxygen functional groups for activated carbon samples as basic and acid groups for the OTA preparation method. The surface chemistry of activated carbon is related to the presence of heteroatoms within the carbon matrix that can form various oxygen surface groups during the activation step by oxidizing gases such as O_2 , CO_2 , and steam or by direct oxidation in the liquid or gas phase (Kwiatkowski, 2011). The presence of oxygen functional groups renders activated carbon an acid-base character. Examples of acid functional groups are carboxylic, phenolic, and lactonic groups, whereas carbonyl and chromene groups are the typical basic groups. Boehm's titration results showed that after A850-60 was oxidized with air the amount of acidic groups increased substantially by about five times from 0.069 to 0.393 mmol/g for sample A850-60-OX, while the amount of basic groups decreased by about 18% from 1.090 to 0.894 mmol/g. After heating the oxidized carbon in the inert atmosphere of N_2 at a high temperature, almost all of the acidic groups were removed with a remaining amount of about 0.002 mmol/g, whereas heat treatment increased the amount of basic groups from 0.894 to 1.331 mmol/g (sample A850-60-HT). Interestingly, the thermal destruction of oxygen functional groups from the surface of activated carbon can be used as one of the methods to increase the concentration of the basic functional groups on the carbon surface. The increase in the basicity of carbon surface enhances the capture of acidic gases such as CO_2 and

H₂S (Bandosz & Ania, 2006; Shafeeyan et al., 2010; Tangsathitkulchai et al., 2021). The reoxidation of activated carbon in cycle 2 (sample A850-60-1-OX) led to an increase in acidic groups which was twice as high, from 0.152 to 0.467 mmol/g, as compared to activated carbon from cycle 1 (A850-60-1), while the basic groups dropped slightly from 1.295 to 1.144 mmol/g. It can be said that there is an agreement in the qualitative and quantitative variations of the surface functional groups of activated carbon that went through the OTA preparation method, as analyzed by both the FTIR and the Boehm titration technique.

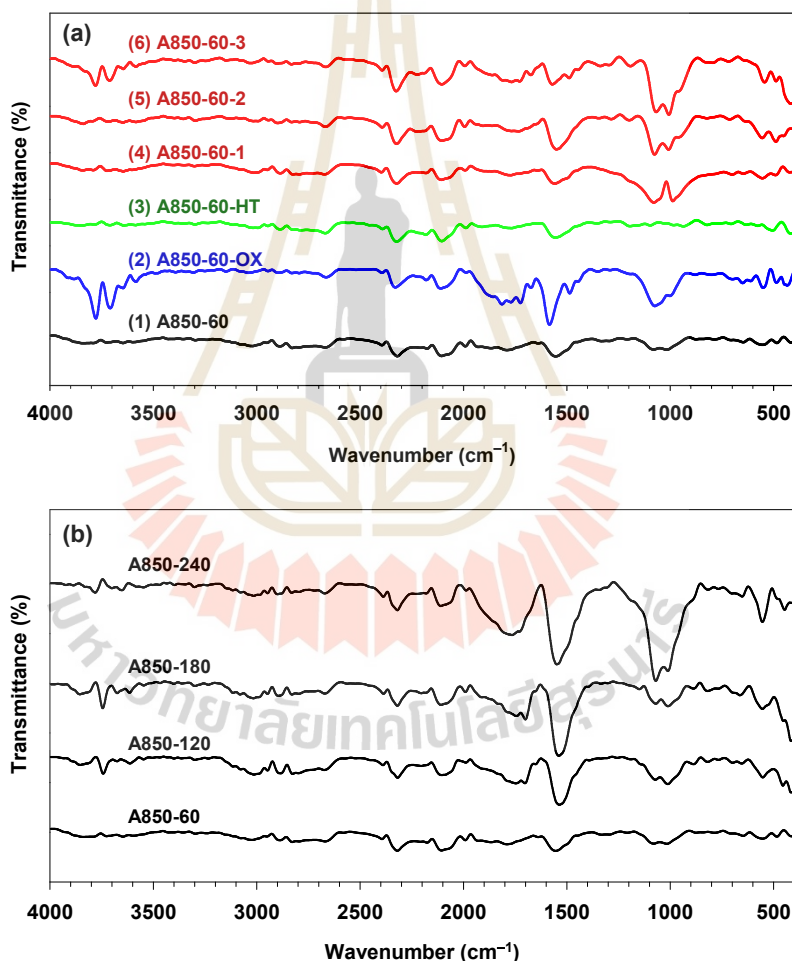


Figure 2.5 FTIR spectra of the derived activated carbon prepared by (a) the OTA method, including (1) the initial activated carbon (A850-60), (2) the air-oxidized carbon (A850-60-OX), (3) the heat treatment carbon (A850-60-HT), (4–6) the reactivated carbon (A850-60-1-3), and (b) by the two-step activation method for varying activation time (60–240 min).

Table 2.6 Amounts of oxygen functional groups on activated carbon surfaces determined by the Boehm titration technique

Sample code	Basic groups	Acidic groups	Total groups
	(mmol/g carbon)	(mmol/g carbon)	(mmol/g carbon)
A850-60	1.090	0.069	1.159
A850-60-OX	0.894	0.393	1.286
A850-60-HT	1.331	0.002	1.333
A850-60-1	1.295	0.152	1.447
A850-60-1-OX	1.144	0.467	1.611

2.4.7 Carbon Reactivity Towards CO₂ Gasification

The reactivity of activated carbon for CO₂ gasification was determined by following the weight loss of a carbon sample as a function of time in the thermogravimetric analyzer under a constant flow of CO₂. Figure 2.6a,b shows the TGA data of the time-residual weight of activated carbon samples prepared via the OTA method and the two-step activation method at two activation temperatures of 850 and 900°C, respectively. For a clearer explanation, the meanings of labels in the figures are typically shown in Table 2.7 for the gasification temperature of 850°C in the TGA.

Table 2.7 Sample description for the CO₂ gasification in TGA

Sample code	Description
850-60	The prepared char was gasified with CO ₂ at 850°C for 60 min in TGA
850-120 (two-step)	Activated carbon was prepared in a tube furnace (CO ₂ at 850°C for 60 min) and then gasified with CO ₂ for 60 min in TGA
850-180 (two-step)	Activated carbon was prepared in a tube furnace (CO ₂ at 850°C for 120 min) and then gasified with CO ₂ for 60 min in TGA

Table 2.7 Sample description for the CO₂ gasification in TGA (continued)

Sample code	Description
850-60-1 (OTA)	The heat-treated carbon from cycle 1 was prepared in a tube furnace and then gasified with CO ₂ for 60 min in TGA
850-60-2 (OTA)	The heat-treated carbon from cycle 2 was prepared in a tube furnace and then gasified with CO ₂ for 60 min in TGA
T900-2h	The heat-treated carbon was prepared in a tube furnace (N ₂ at 900°C for 2 h) and then gasified with CO ₂ for 60 min in TGA
T950-1h	The heat-treated carbon was prepared in a tube furnace (N ₂ at 950°C for 1 h) and then gasified with CO ₂ for 60 min in TGA

Based on the derived TGA data, the fractional char conversion (X) for gasification with CO₂ in a thermogravimetric analyzer was calculated based on the following defining equation.

$$X = \frac{(W_0 - W)}{(W_0 - W_{\text{ash}})} \quad (2.2)$$

where W_0 , W , and W_{ash} are the initial weight of char before gasification, the weight of char at time t , and the weight of ash in the char sample, respectively. The reactivity of activated carbon for CO₂ gasification (R_c) is defined as the rate of change of the fractional char conversion as follows.

$$R_c = \frac{dX}{dt} = -\frac{(dW / dt)}{(W_0 - W_{\text{ash}})} \quad (2.3)$$

The carbon reactivity (R_c) was calculated from the TGA data as a function of the fractional conversion (X) using the numerical discrete method, that is, $R_c = -(\Delta W / \Delta t) / (W_0 - W_{\text{ash}})$, and the calculated results are shown in Figure 2.7a,b. The reactivities of all samples show a characteristic continuous increase with the increase in fractional conversion which passed through a maximum at a certain fractional char

conversion, depending on the given type of activated carbon. The rising trend of reactivity curves could possibly be attributed to the increase of surface area with increasing carbon conversion that provided more active sites for the gasification, leading to a higher reaction rate. The falling of the reactivities at a high fractional carbon conversion of around 0.80 or the carbon burn-off of 80% is probably due to the consolidation of some adjacent pores that results in larger average pore sizes that produce a decrease in the surface area and hence a reduction in the gasification rate. It should be noted also that the carbon reactivity for the gasification at 900°C is about twofold higher than that at 850°C, thus indicating a strong effect of the gasification temperature on the carbon reactivity.

At the same carbon conversion (X), the reactivity of carbon appeared to increase for activated carbons prepared at a longer activation time for the two-step activation method, as observed from the comparison of the curves of symbols (1), (2) and (3) in Figure 2.7a,b. When the fractional carbon conversion was smaller than 0.80, the reactivity of carbon obtained from cycle 2 was higher than that of cycle 1 for the OTA preparation method. It was also noted that the reactivity of activated carbon from the OTA method was higher than that derived from the two-step activation method at the same activation time and temperature, for example, if we compare conditions (2) with (4) and (3) with (5). These results indicate that the increase in the surface area as the carbon conversion increases brings about an increase in the number of active sites for the gasification reaction by CO_2 .

The effects of heat treatment time and temperature of the OTA method on the TGA weight loss and carbon reactivity are also shown in Figures 2.6c,d, and Figures 2.7c,d, respectively, for activated carbon prepared at the activation temperature of 850°C. For the heat treatment temperature of 950°C, the carbon reactivity increased with an increase in the heat treatment time only up to the period of 4 h and the increase in heat treatment temperature from 900 to 950°C enhanced the carbon reactivity by about 50%. Therefore, it is expected that the development of mesopores and surface area by the OTA method can also be affected by the time and temperature used during the heat treatment step.

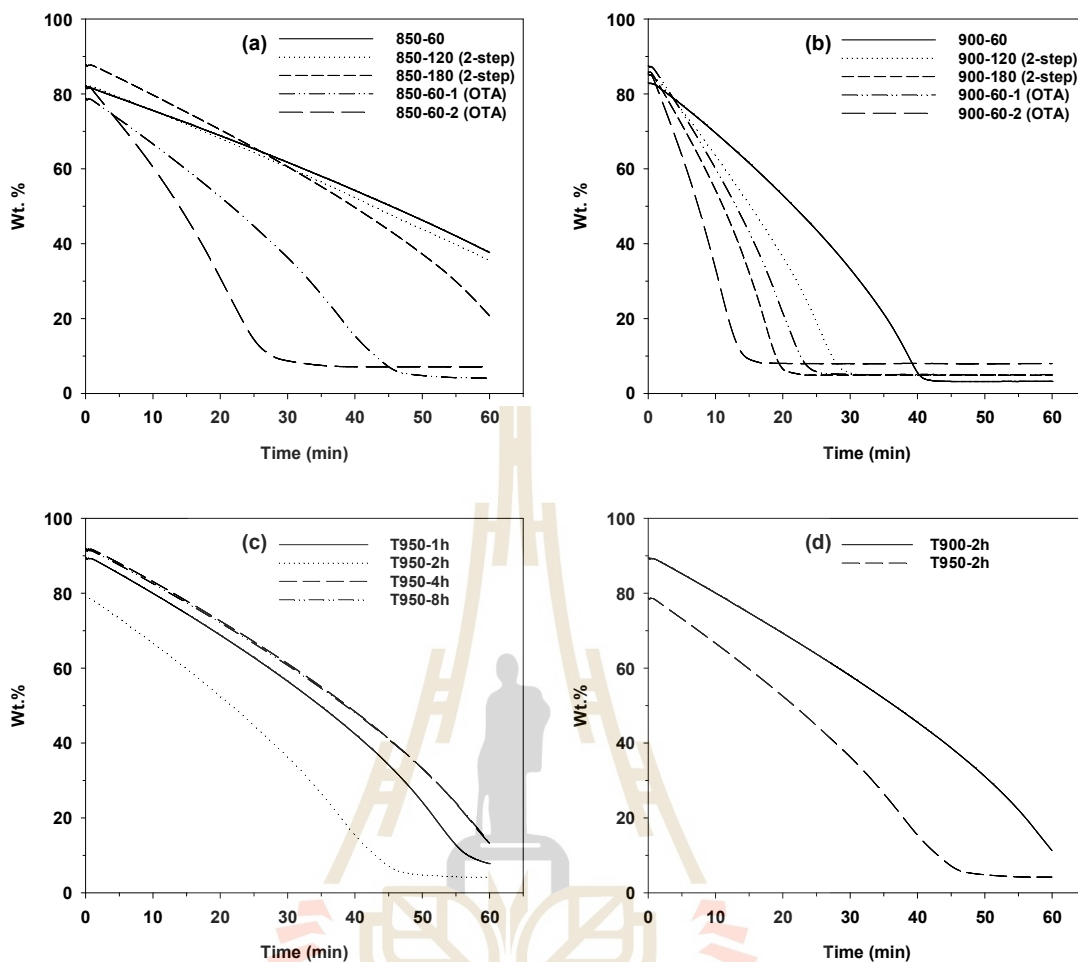


Figure 2.6 TG curves for CO₂ gasification of longan-seed activated carbons prepared by the two-step activation and the OTA methods for activation temperatures of (a) 850°C and (b) 900°C, and TG curves for A850-60 carbon showing, (c) the effect of heat treatment time at temperature of 950°C and (d) the effect of heat treatment temperature for the treatment time of 2 h.

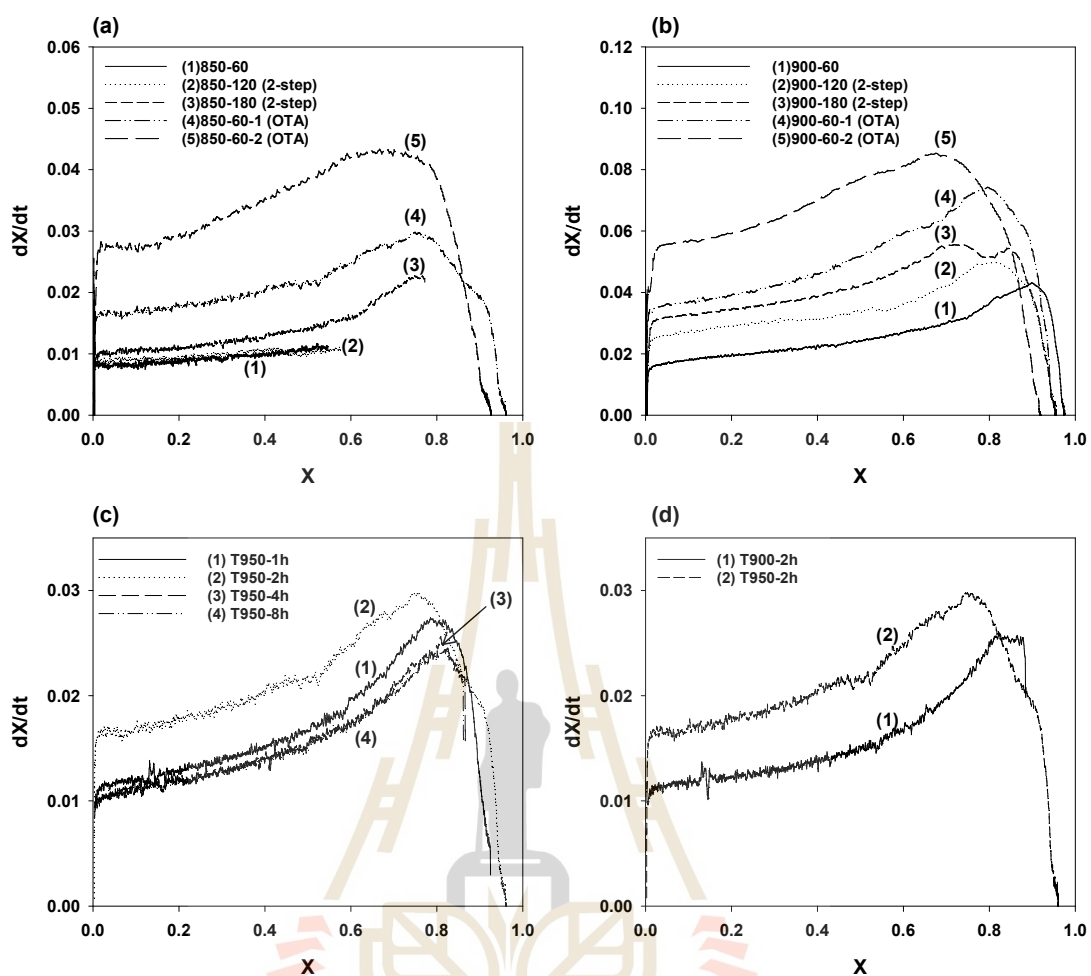


Figure 2.7 Effect of carbon conversion (a) on char reactivity (R_c) towards CO_2 gasification of temperature 850°C and (b) 900°C, and the effect of (c) heat treatment time and (d) heat treatment temperature on the char reactivity.

2.4.8 Pore Size Distributions and Surface Morphology of Prepared Activated Carbons

Figure 2.8 shows the typical variations of pore size distributions of activated carbon samples prepared by the two-step activation method (A850 carbon series) as a function of activation time and the OTA method as a function of a repeated preparation cycle. For the sake of discussion, the pore size distributions are divided into five ranges: <0.6 nm (ultra-micropores), 0.6–1.4 nm (micropores), 1.4–2 nm (super-micropores), and 2–3 nm and 3–4 nm for the mesopore size ranges.

Table 2.8 shows the calculated pore volume data for each pore size range. The initial activated carbon (A850-60) contains mainly micropores (0.6–1.4 nm) and a small amount of mesopores in the range of 3–4 nm. After further activation by the two-step activation method at various times, the derived activated carbons show a multi-modal pore size distribution. By activating the initial activated carbon in CO₂ for 60 min, the volume of micropores (0.6–1.4 nm) increased by 26.4 % from 0.242 to 0.306 cm³/g. However, a further increase in the activation time from 60 to 240 min had no significant effect on the micropore volumes. On the other hand, the volume of super-micropores (1.4–2 nm) tended to increase continuously from 0.006 to 0.102 cm³/g, as the activation time was increased from 60 to 240 min. The mesopores were created in the upper pore size range of 3–4 nm and increased substantially from 0.022 to 0.166 cm³/g, as the activation time was increased from 60 to 240 min.

For mesoporous activated carbon produced by the OTA method, it is seen that the total pore volume increased from 0.480 to 1.074 cm³/g, which is an increase of about 124% when using three preparation cycles from cycles 1 to 3. The pore size distribution of all three samples (A850-60-1, A850-60-2, and A850-60-3) covered every pore size range from 0.6 to 4 nm. In general, the shape of the distribution curve for each pore size is quite similar except that the size of the peak or magnitude of the area under the curve is different. The volume of micropores in the size range from 0.6–1.4 nm seemed to increase from 0.309 for cycle 1 to 0.339 cm³/g for cycle 2 and then dropped to the value of 0.207 cm³/g for the cycle 3 sample. This could have resulted from the transformation of some micropores to larger super-micropores (1.4–2 nm) as a result of the gasification reaction. The substantial increase in the volume of super-micropores from the values of 0.066 to 0.393 cm³/g at the expense of smaller micropores was obvious when the three OTA

preparation cycles were used. The progressive increases in the volume of the mesopores in the range of 2–3 and 3–4 nm are discernible in Figure 3.8, with a pore size range from 2 to 3 nm constituting about 43.8, 65, and 70% of the total mesopore volume for carbon samples produced from cycle 1, cycle 2 and cycle 3 of the OTA method, respectively. This indicates a significant increase in the chemical reactivity of activated carbon with an increasing number of repeated cycles of the OTA method.

Figure 2.9 shows the surface images obtained from a Field Emission Scanning Electron Microscope (FE-SEM, Carl Zeiss AURIGA[®], Oberkochen, Germany) of mesoporous activated carbon prepared by the OTA method for the original carbon (A850-60) and activated carbons from cycle 1 (A850-60-1), cycle 2 (A850-60-2) and cycle 3 (A850-60-3). Figures a1, b1, c1, and d1 and a2, b2, c2, and d2 present low and high magnifications, respectively. It can be seen that there was a tendency for an increase in the average pore size and the number of pores with increases in the number of treatment cycles of the OTA method, although the change is not very pronounced. These results are in agreement with those of the average pore size and pore volume results as presented in Table 2.3.

In summary, the OTA method is a modified method of the conventional two-step activation method for producing mesoporous activated carbon by incorporating two consecutive steps of air oxidation and thermal destruction of the developed surface functional groups prior to activation by CO₂ oxidizing gas. Mesopores are created not by the coalescence of micropores at a high degree of carbon burn-off, but as a result of micropore widening caused by the increased surface reactivity of micropores for CO₂ gasification. Therefore, with the OTA method, the creation of mesopores can occur at any level of char burn-off.

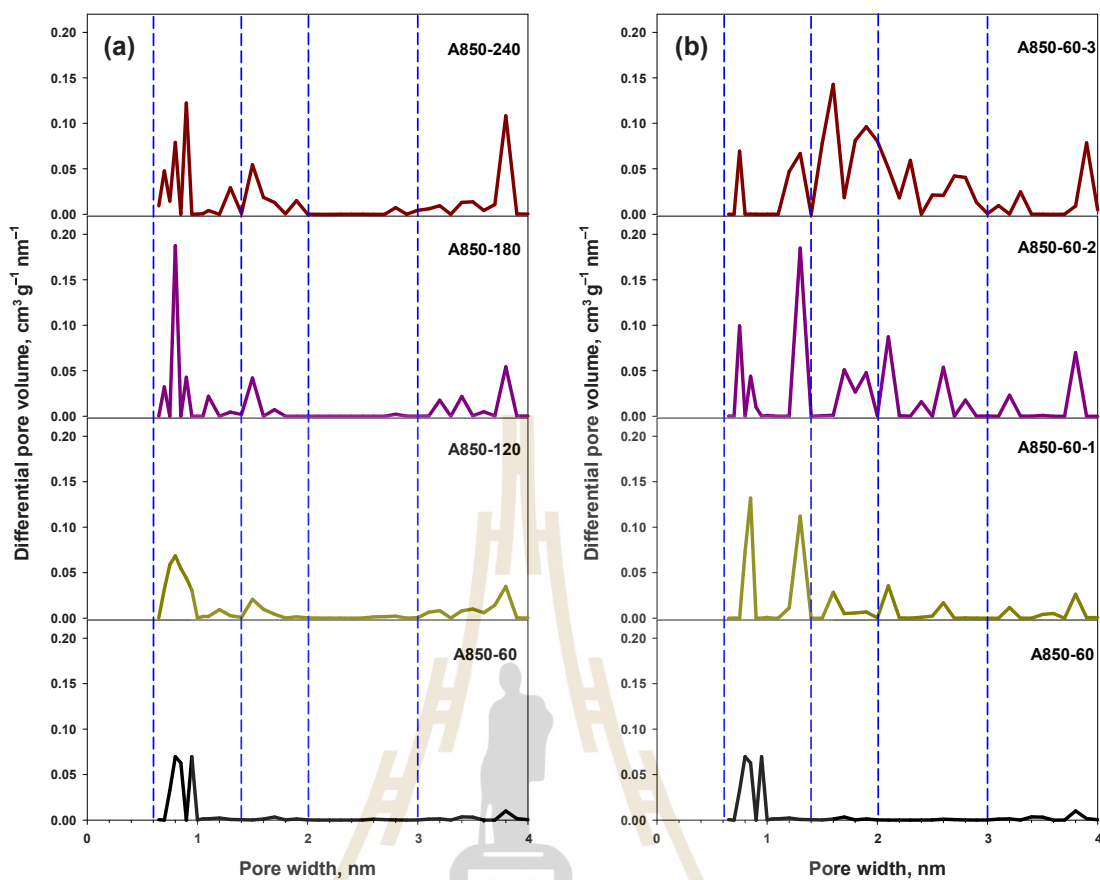


Figure 2.8 Pore size distributions of longan seed-derived activated carbon prepared by (a) the two-step activation method and (b) the OTA method, as determined by the GCMC simulation.

Table 2.8 The pore volume for the pore size distribution of longan seed-derived activated carbon

Sample no.	Sample name	V_T (cm^3/g)	Pore Volume for Pore width (cm^3/g)			
			0.6–1.4 nm	1.4–2 nm	2–3 nm	3–4 nm
1	A850-60	0.272	0.242	0.006	0.002	0.022
2	A850-120	0.437	0.306	0.037	0.006	0.088
3	A850-180	0.442	0.291	0.049	0.002	0.100
4	A850-240	0.587	0.307	0.102	0.012	0.166
5	A850-60-1	0.480	0.309	0.066	0.046	0.059
6	A850-60-2	0.736	0.339	0.127	0.176	0.094
7	A850-60-3	1.074	0.207	0.393	0.330	0.144

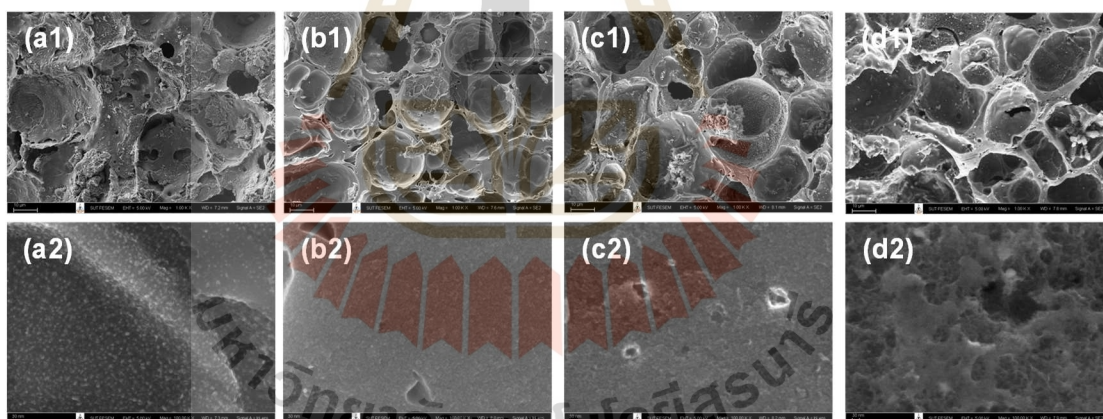


Figure 2.9 SEM micrographs of activated carbon prepared by the OTA method for (a) A850-60, (b) A850-60-1, (c) A850-60-2, and (d) A850-60-3, with a magnification of 1K for (a1)–(d1) and 100K. for (a2)–(d2).

2.5 Conclusions

The results obtained from this study indicate that the preparation of activated carbon from longan seed biomass via the OTA method is a simple and effective means for producing and controlling the proportional volume of mesopores. One cycle of the OTA method consists of three consecutive steps of air oxidation to form surface oxygen functional groups, the thermal destruction of the functional groups to enhance the surface reactivity caused by the increasing number of defects, and the reactivation of activated carbon by CO₂ that results in the widening of the original micropores as well as the creation of more new micropores.

The maximum amount of both mesopores (0.474 cm³/g) and BET surface area (1,773 m²/g) was achieved by using three cycles of the OTA preparation method at the activation temperature of 850°C and 60 min activation time for each treatment cycle. By comparison, the conventional two-step activation method yielded the maximum mesopore volume and surface area of 0.270 cm³/g and 1,421 m²/g, respectively, under the activation conditions of 900°C and 240 min.

In this study, three OTA cycles have been studied to affect mesopore development. To increase the flexibility of controlling the amounts of mesopores, further investigation may involve studying the effects of different types of biomass precursors, the time and temperature of the air oxidation step, the number of repeated thermal destruction steps, the time and temperature of carbon activation step, and the initial porous texture of activated carbon. Activated carbon produced by the OTA method is particularly suitable for use in a liquid adsorption system since its mesoporous structure could help increase the diffusion rate of relatively large-size adsorbate molecules to the adsorption sites. The utilization of such activated carbon would be advantageous because of rapid kinetics due to the ability to control the mesopore volume to suit the nature of a given adsorbate and a high adsorption capacity (equilibrium) due to the large specific surface area of the produced activated carbon.

2.6 References

- Alvarez, J., Lopez, G., Amutio, M., Bilbao, J., & Olazar, M. (2016, 2016/09/01/). Preparation of adsorbents from sewage sludge pyrolytic char by carbon dioxide activation. *Process Safety and Environmental Protection*, 103, 76-86.
- Ariyadejwanich, P., Tanthapanichakoon, W., Nakagawa, K., Mukai, S. R., & Tamon, H. (2003, 2003/01/01/). Preparation and characterization of mesoporous activated carbon from waste tires. *Carbon*, 41(1), 157-164.
- Bandosz, T. J., & Ania, C. O. (2006). Chapter 4 Surface chemistry of activated carbons and its characterization. In T. J. Bandosz (Ed.), *Interface Science and Technology* (Vol. 7, pp. 159-229). Elsevier.
- Boehm, H. P. (1966). Chemical Identification of Surface Groups. In D. D. Eley, H. Pines, & P. B. Weisz (Eds.), *Advances in Catalysis* (Vol. 16, pp. 179-274). Academic Press.
- Boehm, H. P. (1994, 1994/01/01/). Some aspects of the surface chemistry of carbon blacks and other carbons. *Carbon*, 32(5), 759-769.
- Borhan, A., Yusup, S., Lim, J. W., & Show, P. L. (2019). Characterization and Modelling Studies of Activated Carbon Produced from Rubber-Seed Shell Using KOH for CO₂ Adsorption. *Processes*, 7(11).
- Bouwman, R., & Freriks, I. L. C. (1980, 1980/05/01/). Low-temperature oxidation of a bituminous coal. Infrared spectroscopic study of samples from a coal pile. *Fuel*, 59(5), 315-322.
- Brunauer, S., Emmett, P. H., & Teller, E. (1938, 1938/02/01). Adsorption of Gases in Multimolecular Layers. *Journal of the American Chemical Society*, 60(2), 309-319.
- Burg, P., Fydrych, P., Cagniant, D., Nanse, G., Bimer, J., & Jankowska, A. (2002, 2002/08/01/). The characterization of nitrogen-enriched activated carbons by IR, XPS and LSER methods. *Carbon*, 40(9), 1521-1531.
- Carrott, P. J. M., Ribeiro Carrott, M. M. L., & Mourão, P. A. M. (2006, 2006/03/01/). Pore size control in activated carbons obtained by pyrolysis under different

- conditions of chemically impregnated cork. *Journal of Analytical and Applied Pyrolysis*, 75(2), 120-127.
- Dubinin, M. M. (1975). Physical Adsorption of Gases and Vapors in Micropores. In D. A. Cadenhead, J. F. Danielli, & M. D. Rosenberg (Eds.), *Progress in Surface and Membrane Science* (Vol. 9, pp. 1-70). Elsevier.
- El-Hendawy, A.-N. (2006, 03/01). Variation in the FTIR spectra of a biomass under impregnation, carbonization and oxidation conditions. *Journal of Analytical and Applied Pyrolysis*, 75, 159-166.
- Fanning, P. E., & Vannice, M. A. (1993, 1993/01/01/). A DRIFTS study of the formation of surface groups on carbon by oxidation. *Carbon*, 31(5), 721-730.
- García, R., Pizarro, C., Lavín, A. G., & Bueno, J. L. (2012, 2012/01//). Characterization of Spanish biomass wastes for energy use. *Bioresource Technology*, 103(1), 249-258.
- Goertzen, S. L., Thériault, K. D., Oickle, A. M., Tarasuk, A. C., & Andreas, H. A. (2010, 2010/04/01/). Standardization of the Boehm titration. Part I. CO₂ expulsion and endpoint determination. *Carbon*, 48(4), 1252-1261.
- Gonçalves, G. d. C., Pereira, N. C., & Veit, M. T. (2016, 2016/02/01/). Production of bio-oil and activated carbon from sugarcane bagasse and molasses. *Biomass and Bioenergy*, 85, 178-186.
- González-García, P. (2018, 2018/02/01/). Activated carbon from lignocellulosics precursors: A review of the synthesis methods, characterization techniques and applications. *Renewable and Sustainable Energy Reviews*, 82, 1393-1414.
- Guo, J., & Chong Lua, A. (1998, 1998/08/01/). Characterization of chars pyrolyzed from oil palm stones for the preparation of activated carbons. *Journal of Analytical and Applied Pyrolysis*, 46(2), 113-125.
- Guo, J., & Lua, A. C. (2001, 2001/03/01/). Kinetic study on pyrolytic process of oil-palm solid waste using two-step consecutive reaction model. *Biomass and Bioenergy*, 20(3), 223-233.

- Hadoun, H., Sadaoui, Z., Souami, N., Sahel, D., & Toumert, I. (2013, 2013/09/01/). Characterization of mesoporous carbon prepared from date stems by H₃PO₄ chemical activation. *Applied Surface Science*, 280, 1-7.
- He, X., Geng, Y., Qiu, J., Zheng, M., Long, S., & Zhang, X. (2010, 2010/04/01/). Effect of activation time on the properties of activated carbons prepared by microwave-assisted activation for electric double layer capacitors. *Carbon*, 48(5), 1662-1669.
- Hossain, M. Z., Wu, W., Xu, W. Z., Chowdhury, M. B. I., Jhavar, A. K., Machin, D., & Charpentier, P. A. (2018). High-Surface-Area Mesoporous Activated Carbon from Hemp Bast Fiber Using Hydrothermal Processing. *C*, 4(3).
- Hu, Z., Guo, H., Srinivasan, M. P., & Yaming, N. (2003, 2003/04/01/). A simple method for developing mesoporosity in activated carbon. *Separation and Purification Technology*, 31(1), 47-52.
- Hu, Z., & Srinivasan, M. P. (2001, 2001/05/01/). Mesoporous high-surface-area activated carbon. *Microporous and Mesoporous Materials*, 43(3), 267-275.
- Hu, Z., Srinivasan, M. P., & Ni, Y. (2001, 2001/05/01/). Novel activation process for preparing highly microporous and mesoporous activated carbons. *Carbon*, 39(6), 877-886.
- Jawad, A. H., Abd Rashid, R., Ismail, K., & Sabar, S. (2017, 02/11). High surface area mesoporous activated carbon developed from coconut leaf by chemical activation with H₃PO₄ for adsorption of methylene blue. *Desalination and water treatment*.
- Juárez-Galán, J. M., Silvestre-Albero, A., Silvestre-Albero, J., & Rodríguez-Reinoso, F. (2009, 2009/01/01/). Synthesis of activated carbon with highly developed "mesoporosity". *Microporous and Mesoporous Materials*, 117(1), 519-521.
- Junpirom, S., Do, D. D., Tangsathitkulchai, C., & Tangsathitkulchai, M. (2005, 2005/08/01/). A carbon activation model with application to longan seed char gasification. *Carbon*, 43(9), 1936-1943.
- Khamkeaw, A., Asavamongkolkul, T., Perngyai, T., Jongsomjit, B., & Phisalaphong, M. (2020). Interconnected Micro, Meso, and Macro Porous Activated Carbon from

Bacterial Nanocellulose for Superior Adsorption Properties and Effective Catalytic Performance. *Molecules*, 25(18).

Kwiatkowski, J. F. (2011). *Activated Carbon: Classifications, Properties and Applications*. Nova Science Publishers, Incorporated.

Le Van, K., & Luong, T. (2019, 01/15). Preparation of Pore-Size Controllable Activated Carbon from Rice Husk Using Dual Activating Agent and Its Application in Supercapacitor. *Journal of Chemistry*, 2019, 1-11.

Lee, B.-H., Lee, H.-M., Chung, D. C., & Kim, B.-J. (2021). Effect of Mesopore Development on Butane Working Capacity of Biomass-Derived Activated Carbon for Automobile Canister. *Nanomaterials*, 11(3).

Lopez, G., Artetxe, M., Amutio, M., Erkiaga, A., Alvarez, J., Barbarias, I., & Olazar, M. (2012). Preparation of adsorbents derived from waste tires. *Chemical Engineering Transactions*, 29, 811-816.

Marrakchi, F., Ahmed, M. J., Khanday, W. A., Asif, M., & Hameed, B. H. (2017, 2017/05/01/). Mesoporous-activated carbon prepared from chitosan flakes via single-step sodium hydroxide activation for the adsorption of methylene blue. *International Journal of Biological Macromolecules*, 98, 233-239.

Mohamad Nor, N., Lau, L. C., Lee, K. T., & Mohamed, A. R. (2013, 2013/12/01/). Synthesis of activated carbon from lignocellulosic biomass and its applications in air pollution control—a review. *Journal of Environmental Chemical Engineering*, 1(4), 658-666.

Molina-Sabio, M., Gonzalez, M. T., Rodriguez-Reinoso, F., & Sepúlveda-Escribano, A. (1996, 1996/01/01/). Effect of steam and carbon dioxide activation in the micropore size distribution of activated carbon. *Carbon*, 34(4), 505-509.

Muniandy, L., Adam, F., Mohamed, A. R., & Ng, E.-P. (2014, 2014/10/01/). The synthesis and characterization of high purity mixed microporous/mesoporous activated carbon from rice husk using chemical activation with NaOH and KOH. *Microporous and Mesoporous Materials*, 197, 316-323.

- Nandiyanto, A., Oktiani, R., & Ragadhita, R. (2019, 03/07). How to Read and Interpret FTIR Spectroscopy of Organic Material. *Indonesian Journal of Science and Technology*, 4, 97-118.
- Nandiyanto, A. B. D., Oktiani, R., Ragadhita, R., Sukmafitri, A., & Zaen, R. (2020, 2020/01/01/). Amorphous content on the photocatalytic performance of micrometer-sized tungsten trioxide particles. *Arabian Journal of Chemistry*, 13(1), 2912-2924.
- Nasrullah, A., Saad, B., Bhat, A. H., Khan, A. S., Danish, M., Isa, M. H., & Naeem, A. (2019, 2019/02/20/). Mangosteen peel waste as a sustainable precursor for high surface area mesoporous activated carbon: Characterization and application for methylene blue removal. *Journal of Cleaner Production*, 211, 1190-1200.
- Pallarés, J., González-Cencerrado, A., & Arauzo, I. (2018, 2018/08/01/). Production and characterization of activated carbon from barley straw by physical activation with carbon dioxide and steam. *Biomass and Bioenergy*, 115, 64-73.
- Pradhan, B. K., & Sandle, N. K. (1999, 1999/01/01/). Effect of different oxidizing agent treatments on the surface properties of activated carbons. *Carbon*, 37(8), 1323-1332.
- Román, S., González, J. F., González-García, C. M., & Zamora, F. (2008, 2008/08/01/). Control of pore development during CO₂ and steam activation of olive stones. *Fuel Processing Technology*, 89(8), 715-720.
- Rouquerol, J., Rouquerol, F., Llewellyn, P., Maurin, G., & Sing, K. S. (2013). *Adsorption by powders and porous solids: principles, methodology and applications*. Academic press.
- Saygılı, H., & Güzel, F. (2016, 2016/02/01/). High surface area mesoporous activated carbon from tomato processing solid waste by zinc chloride activation: process optimization, characterization and dyes adsorption. *Journal of Cleaner Production*, 113, 995-1004.
- Seung Kim, Y., & Rae Park, C. (2016). Chapter 13 - Titration Method for the Identification of Surface Functional Groups. In M. Inagaki & F. Kang (Eds.),

- Materials Science and Engineering of Carbon (pp. 273-286). Butterworth-Heinemann.
- Shafeeyan, M. S., Daud, W. M. A. W., Houshmand, A., & Shamiri, A. (2010, 2010/11/01/). A review on surface modification of activated carbon for carbon dioxide adsorption. *Journal of Analytical and Applied Pyrolysis*, 89(2), 143-151.
- Sing, K. S. W., EVERETT, D. H., HAUL, R. A. W., MOSCOU, L., PIEROTTI, R. A., ROUQUEROL, J., & SIEMIENIEWSKA, T. (1985, 01 Jan. 1985). Reporting physisorption data for gas/solid systems with special reference to the determination of surface area and porosity (Recommendations 1984). *Pure and Applied Chemistry*, 57(4), 603-619.
- Socrates, G. (2004). *Infrared and Raman characteristic group frequencies: tables and charts*. John Wiley & Sons.
- Tangathitkulchai, C., Naksusuk, S., Wongkoblaph, A., Phadungbut, P., & Borisut, P. (2021). Equilibrium and Kinetics of CO₂ Adsorption by Coconut Shell Activated Carbon Impregnated with Sodium Hydroxide. *Processes*, 9(2), 201.
- Tseng, R.-L. (2006, 2006/11/15/). Mesopore control of high surface area NaOH-activated carbon. *Journal of Colloid and Interface Science*, 303(2), 494-502.
- Tseng, R.-L., & Tseng, S.-K. (2005, 2005/07/15/). Pore structure and adsorption performance of the KOH-activated carbons prepared from corncob. *Journal of Colloid and Interface Science*, 287(2), 428-437.
- Xin, W., Li, X., & Song, Y. (2020, 2020/06/01). Sludge-based mesoporous activated carbon: the effect of hydrothermal pretreatment on material preparation and adsorption of bisphenol A. *Journal of Chemical Technology & Biotechnology*, 95(6), 1666-1674.
- Yang, H., Yan, R., Chen, H., Lee, D. H., & Zheng, C. (2007, 2007/08/01/). Characteristics of hemicellulose, cellulose and lignin pyrolysis. *Fuel*, 86(12), 1781-1788.

CHAPTER III

THE USE OF ACTIVATED CARBON FROM LONGAN SEED BIOMASS FOR INCREASING CAPACITY AND KINETICS OF METHYLENE BLUE ADSORPTION FROM AQUEOUS SOLUTION

3.1 Abstract

Microporous and mesoporous activated carbons were produced from longan seed biomass through physical activation with CO₂ under the same activation conditions of time and temperature. These activated carbons were utilized as porous adsorbents for the removal of methylene blue (MB) from an aqueous solution and their effectiveness was evaluated for both the adsorption kinetics and capacity. The adsorption kinetic data of MB were analyzed by the pseudo-first-order model, the pseudo-second-order model, and the pore-diffusion model equations. The effective pore diffusivity (D_e) derived from the pore diffusion model had the values of 4.657×10^{-7} – 6.014×10^{-7} cm²/s and 4.668×10^{-7} – 19.920×10^{-7} cm²/s for the microporous and mesoporous activated carbons, respectively. Three well-known adsorption models, namely the Langmuir, Freundlich, and Redlich-Peterson equations were tested with the experimental MB adsorption isotherms and the results showed that the Redlich-Peterson model provided the overall best fitting of the isotherm data. In addition, the maximum capacity for MB adsorption of 1000 mg/g was achieved with the mesoporous carbon having the largest surface area and pore volume. The initial pH of MB solution had virtually no effect on the adsorption capacity and removal efficiency of the methylene blue dye. Increasing temperature over the range from 35 to 55°C increased the adsorption of methylene blue, presumably caused by the increase in the diffusion rate of methylene blue to the adsorption sites that could promote the interaction frequency between the adsorbent surface and the adsorbate molecules. Overall, the high-surface-area-mesoporous carbon was superior to the microporous carbon in view of the adsorption kinetics and capacity, when both carbons were used for the removal of MB from an aqueous solution.

3.2 Introduction

Adsorption has gained increasing acceptance in the separation and purification processes for both gas and liquid systems, due to its process simplicity, less energy consumption, high separation efficiency at trace concentrations, low maintenance cost, and adsorbent reusability (Azari et al., 2020; Li et al., 2020). Among the various available commercial adsorbents, activated carbon has been recognized as the oldest and most widely used porous adsorbent for a variety of applications and is the most popularly used adsorbent in water and wastewater treatment processes (González-García, 2018). This arises from its large specific surface area and pore volume, the flexibility of pore manipulation by controlling the preparation conditions, and the capability of surface chemistry modification to improve the adsorbate selectivity. Concerning the adsorption in a liquid phase, it is generally recognized that dyes are one of the most detrimental pollutants present in industrial wastewater. Dyes are natural or synthetic, organic compounds that are utilized in various industries such as leather, paper, rubber, textile, plastic, cosmetic, pharmaceutical, and food industries (Yagub et al., 2014). Colored dye wastewater is generated during the production of the dye itself or as a result of its use in textile and related industries. Dyes can also affect aquatic plants and ones who use these effluents without an awareness of their detrimental health effects from washing, bathing, and drinking (Tkaczyk et al., 2020). Therefore, the search for inexpensive and effective porous solids for the removal of dyes would be a worthwhile endeavor.

Research on the adsorption of organic water pollutants by activated carbon has been carried out extensively and a voluminous literature is available, especially in the field of surface modification of activated carbon for effective water pollution control (Bhatnagar et al., 2013). In general, activated carbon is more efficient in removing organic compounds than metals and inorganic pollutants, and continued research efforts have been made to increase the adsorption efficiency of carbon sorbents (Chen et al., 2020; Monser & Adhoum, 2002; Nezhad et al., 2021; Radovic et al., 1997). Obviously, the adsorption capacity of activated carbon is strongly dependent on the porous properties and surface chemistry of the carbon adsorbents that can be controlled by the judicious use of activation conditions, types of precursors, and chemical additives (Faria et al., 2004). Although numerous results have been reported on the kinetics and sorption properties, much work remains to

be performed for a better understanding of the underlying sorption mechanisms (Santoso et al., 2020).

In studying the adsorption mechanisms of a cationic dye that can dissociate into positively charged ions in an aqueous solution, methylene blue dye (MB) has often been used as a model cationic dye. Methylene blue is an organic chloride salt with a dark green color, having a formula $C_{16}H_{18}ClN_3S$ and a molecular weight of 319.85 g/mol. Some important physical properties of MB are the density of 1 g/mL at 20°C, melting point of 100–110°C, and solubility in water of 40 g/L at 20°C. MB is mainly used in the production of coloring paper, cotton, silk, and wool and is also used as a chemical indicator, medicinal, and biological stain (Lu et al., 2018). MB is a toxic dye, which can result in harmful effects on humans and environmental problems. Common side effects include headache, vomiting, high blood pressure, and the eventual breakdown of red blood cells. The removal of MB from industrial wastes has been reported using various methods such as electrochemical removal, photodegradation reaction, chemical coagulation, membrane filtration, and physical adsorption methods (Katheresan et al., 2018; Mashkoo & Nasar, 2020; Rafatullah et al., 2010). Of these removal techniques, the application of adsorption utilizing low-cost adsorbents to remove this dye is an attractive process for the efficient removal of this dye and has been the focal point of a number of investigations (Rafatullah et al., 2010; Yagub et al., 2014).

With regard to activated carbon, an understanding of the correlation between its porous properties, including the surface area and pore size distribution, and the adsorption capacity is essential for the selection of the most appropriate adsorbent for the effective removal and control of the dyes. Graham (Graham, 1955) studied the effect of the pore size of activated carbon on MB adsorption capacity and found that the surface area of activated carbon available for MB adsorption was usually limited to the minimum permissible pore size of around 1.33 nm. Later, Reffas et al. (Reffas et al., 2010) studied the adsorption of MB on activated carbon with a high proportion of mesopores and found that the highest adsorption uptake was achieved in the supermicropore size range of 1.4 to 2.0 nm. This finding was in agreement with the work of Benadjemia et al. (Benadjemia et al., 2011), who confirmed that the adsorption of MB molecules mostly occurred in the wider supermicropore range when compared with the adsorption in meso-macroporous activated carbon.

Recently, it has been reported that activated carbon with a high surface area of about 1438 m²/g and containing a micropore volume of around 80% of the total pore volume demonstrated an extremely high adsorption capacity of up to 1930 mg MB/g carbon (Motejadded Emrooz et al., 2021).

However, to obtain both the low mass transfer resistance in pores (fast kinetics) and the high equilibrium adsorption capacity of relatively large dye molecules, activated carbon with a relatively high proportion of mesopore volume and a high surface area is obviously required (Lei et al., 2006; Saygılı & Güzel, 2016; Tseng et al., 2003; Zhang et al., 2021). In our previous work, we successfully prepared mesoporous activated carbon from longan fruit seed with a high surface area (1773 m²/g) through a process of modified physical activation with CO₂, which was referred to as the OTA method (Lawtae & Tangsathitkulchai, 2021). Therefore, the present work aimed to study and compare the equilibrium and kinetics of methylene blue adsorption from an aqueous solution by a microporous activated carbon and a high surface area mesoporous activated carbon prepared from longan fruit seed. In addition, the effects of the process conditions including adsorbent dosage, temperature, and solution pH on the efficiency of MB dye uptake were also investigated.

3.3 Experimental Procedure

3.3.1 Materials

Fresh longan fruit seed was obtained from Saha-Prachinburi Foods Industry Ltd., a local fruit processing plant in Chiangmai province, Thailand. The raw longan seed was thoroughly rinsed with water and dried at 110°C for 48 hours, then it was crushed and sieved to obtain an average particle size of 1.70 mm (10 × 14 US mesh). The chemicals used in this study including NaCl, NaOH, HCl, and Methylene Blue were acquired from Carlo Erba (Carlo Erba Reagent, Italy). All chemicals were of analytical grade and were used without further purification. The dye stock solution was prepared by dissolving accurately weighed MB dye powder in distilled water to obtain a solution with a methylene blue concentration of 1000 mg/L. Then, different initial dye solutions required for the adsorption tests were prepared by diluting the stock solution in appropriate proportions.

3.3.2 Preparation of Longan Seed Activated Carbons

Details for the preparation of longan seed-activated carbon follow those reported in Chapter II. In brief, the char was first prepared by carbonizing the longan seed under the flow of N_2 at $500^\circ C$ for 90 min. Then, the derived char was further activated under the flow of CO_2 at $850^\circ C$ for 120–240 min in a vertical tube furnace (CTF 12, Carbolite, Staffordshire, UK). This activation process, known as the two-step activation method, produced microporous activated carbon with around 70–80% of the micropore volume. For the preparation of activated carbon with larger amounts of mesopores, about 15 g of activated carbon produced from the two-step activation process at the activation temperature and time of $850^\circ C$ and 1h, respectively, were first oxidized in a quartz tube reactor by heating the activated carbon from room temperature in a stream of air ($100\text{ cm}^3/\text{min}$) to the required oxidation temperature of $230^\circ C$ and held at this temperature for 12 h. The purpose of this step was to create additional oxygen functional groups on the carbon surfaces. Then, the oxidized carbon was heated at $950^\circ C$ for 2 h under N_2 flowing at the rate of $100\text{ cm}^3/\text{min}$ to remove most of the surface functional groups, thus giving increasing surface reactivity caused by chemical bond disruption. After that, the sample was activated again with CO_2 at $850^\circ C$ for another 1 h. This process completed the first cycle of the preparation method for mesoporous carbon production which is referred to as the OTA method (Oxidation, Thermal destruction, and Activation). In this study, a total of three cycles for the OTA method were performed.

The derived microporous carbon prepared by the conventional two-step activation was designated as A850–X, where A850 represents the activated carbon derived under the activation temperature of $850^\circ C$ and symbol X represents the activation time (120–240 min). The mesoporous carbon was designated as A850–X–Y, where A850 stands for the mesoporous activated carbon originally prepared by activating the char at the temperature of $850^\circ C$ for time X (60 min) and Y is the number of repeated OTA cycles (1–3). The final yield of activated carbon was calculated based on the weight of the initial longan seed char.

3.3.3 Characterization of the Prepared Activated Carbons

The prepared microporous and mesoporous activated carbons were characterized for their porous properties using N₂ adsorption isotherms measured at -196°C by using a high-performance adsorption analyzer (ASAP2010, Micromeritics, Norcross, GA, USA). The isotherms of N₂ adsorption and discussion on the N₂ isotherm behavior of the prepared activated carbons were shown in Chapter II. The specific surface area was calculated from the N₂ adsorption isotherm data by applying the Brunauer-Emmett-Teller (BET) equation (Brunauer et al., 1938). The total pore volume was estimated from the volume of N₂ adsorbed at the relative pressure of 0.98 and converted to the volume of N₂ in the liquid state at a given temperature. Micropore volume was determined by applying the Dubinin-Radushkevich (DR) equation (Dubinin, 1975). The mesopore volume was estimated by subtracting the micropore volume from the total pore volume. The pore size distributions of the derived activated carbons were determined from the N₂ adsorption isotherms data by applying the Grand Canonical Monte Carlo (GCMC) simulation (Lawtae & Tangsathitkulchai, 2021; Phothong et al., 2021; Tangsathitkulchai et al., 2021). The average pore size (D_{av}) was computed based on the equation $4V_T/S$, where V_T is the total pore volume and S is the BET surface area, assuming the pores are cylinders.

The contents of the oxygen functional groups on the activated carbon surfaces were additionally measured by applying the Boehm titration technique (Boehm, 1994, 2002). Moreover, pH at the point of zero charges (pH_{pzc}) of the activated carbon was measured by the following procedure: 25 mL of 0.01 N NaCl solution was placed in an Erlenmeyer flask. The pH was adjusted to a value between 3 and 11 by using either HCl or NaOH. Then, 50 mg of the activated carbon sample was added to each of the sample solutions and shaken for 48 h at room temperature and the final pH of each solution was measured. A plot of the final solution pH against the initial pH was made and the pH at which the plotted curve intersected the straight line of $pH_{initial} = pH_{final}$ was taken as the point of zero charges (pH_{pzc}) of the resulting carbon (Ocampo-Pérez et al., 2013), as graphically shown in Figure 3.1.

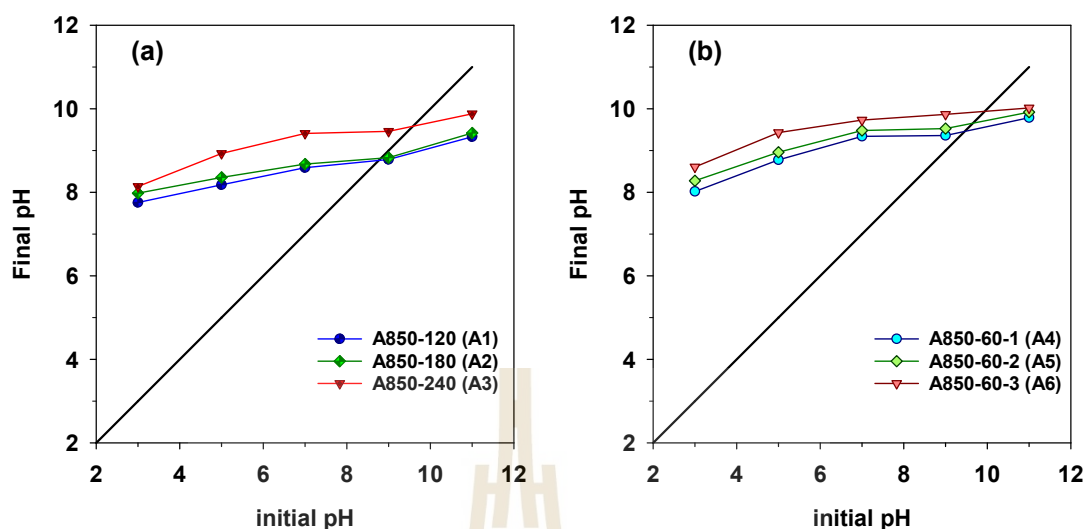


Figure 3.1 The determination of pH_{PZC} of (a) microporous activated carbon, and (b) mesoporous activated carbon from the intersection between the curve of $pH_{initial}$ vs pH_{final} and the straight line of $pH_{initial} = pH_{final}$.

3.3.4 Methylene Blue Adsorption

The kinetics of MB adsorption was first performed to study the dye adsorption rate and to determine the equilibrium time of adsorption (the time at which the amount of dye adsorbed becomes constant) for the subsequent adsorption equilibrium experiments. The concentration of dye in the solution after adsorption was determined from a calibration curve based on the absorbance of a series of standard dye solutions of known concentrations. The absorbance was measured with a double beam ultraviolet-visible (UV-Vis) spectrophotometer (T80+ UV-Vis, PG Instrument Ltd, Leicestershire, UK) using the wavelength (λ_{max}) of 665 nm. For the kinetics tests, 25 mL of the dye solution with an initial concentration of 200 mg/L was mixed with 0.02 g of activated carbon and shaken at a set temperature of 35°C in a temperature-controlled water bath at 150 rpm. The solution sample was then collected over a time interval of up to 48 h and the collected sample was analyzed for the MB concentration using the measured UV absorbance and the prepared calibration curve. For the study of equilibrium adsorption isotherms, 25 mL of each dye solution with a concentration in the range of 50–500 mg/L was mixed with a fixed amount of activated carbon and shaken at a constant temperature of

35°C for about 48 h (as determined by the kinetics study) to reach the equilibrium. Then, the final solution was collected for the analysis of the equilibrium dye concentration using the prepared calibration curve. The amount of activated carbon used for the adsorption experiments was carefully chosen to give the final equilibrium dye concentration of up to 300 mg/L. The equilibrium adsorption study was additionally carried out to study the effects of such process variables as adsorbent dosage, solution pH, and adsorption temperature. Table 3.1 summarizes the experimental conditions used for the study of MB adsorption by longan seed-activated carbons in the present study.

The adsorption capacity (q_t) and the removal efficiency (R_e) of MB by activated carbons are expressed as follows:

$$q_t = \frac{(C_0 - C)V}{W} \quad (3.1)$$

$$R_e (\%) = \frac{(C_0 - C)}{C_0} \times 100 \quad (3.2)$$

where q_t is the adsorption capacity of MB (mg/g) at time t , R_e (%) is the removal efficiency of MB dye, C_0 and C are the initial concentration and the concentration at time t of MB (mg/L), respectively, V is the volume of the solution (L), and W is the amount of longan seed activated carbon employed (g). For adsorption at equilibrium, $C = C_e$ and $q_t = q_e$.

Table 3.1 Experimental conditions for the study of batch MB adsorption by longan seed-based activated carbons

Studied variables	Time	Initial conc.	Carbon dosage	Temp.	pH
	(h)	(mg/L)	(g)	(°C)	
Time (kinetics)	0.5–48	200	0.020	35	4.5
Equilibrium conc.	48	50–500	0.010–0.020	35	4.5
Adsorbent dosage	48	300	0.005–0.050	35	4.5
Solution pH	48	400	0.020	35	3–11
Temperature	48	50–500	0.010–0.020	35–55	4.5

3.4 Adsorption Analysis

3.4.1 Adsorption Kinetic Models

The kinetics of dye adsorption was analyzed using the two well-known rate equations, namely the pseudo-first-order kinetic model and the pseudo-second-order kinetic model (Ho & Mckay, 1998, 1999), as shown in Equations (3.3) and (3.4), respectively:

$$\frac{dq_t}{dt} = k_1 (q_e - q_t) \quad (3.3)$$

$$\frac{dq_t}{dt} = k_2 (q_e - q_t)^2 \quad (3.4)$$

Integrating the above equations gives Equations (3.5) and (3.6), respectively.

$$q_t = q_e (1 - e^{-k_1 t}) \quad (3.5)$$

And

$$q_t = \frac{q_e^2 k_2 t}{1 + q_e k_2 t} \quad (3.6)$$

where q_e is the amount of dye adsorbed at equilibrium (mg/g carbon), q_t is the amount adsorbed at time t , k_1 (min^{-1}) and k_2 ($\text{g}/(\text{mg}\cdot\text{min})$) are the corresponding model rate constants.

Moreover, the prediction of adsorption kinetics can also be achieved by employing a pore-diffusion model (Do, 1998), in which the adsorption process is governed by the intraparticle diffusion of adsorbate molecules, neglecting the external or film mass transfer resistance. The advantage of the pore-diffusion model lies in its ability to provide a more relevant estimation of the effective pore diffusivity for the actual adsorption process. For a spherical adsorbent, the final solution for the fractional uptake of adsorbate (F) is shown in Equation (3.7):

$$F(t) = \frac{q_t}{q_e} = 1 - \left(\frac{6}{\pi^2} \right) \sum_{n=1}^{\infty} \frac{1}{n^2} e^{-n^2 \pi^2 \tau} \quad (3.7)$$

where $F(t)$ is the fractional uptake of the adsorbate at time t , τ is a non-dimensional time parameter defined as $\tau = D_e t / R_p^2$, where D_e is the average of effective pore diffusivity, and R_p is the radius of the adsorbent particle (0.85 mm for this work). At the adsorption time close to equilibrium ($F > 0.7$), only the first term of the series in Equation (3.7) needs to be considered since the higher terms may be neglected (Do, 1998). Finally, this gives:

$$F(t) = 1 - \left(\frac{6}{\pi^2} \right) e^{-\frac{\pi^2 D_e t}{R_p^2}} \quad (3.8)$$

The three kinetic model equations, Equations (3.5), (3.6), and (3.8), were used to fit the experimental kinetic data of MB adsorption to determine the kinetic model parameters that gave the best-fitting results.

3.4.2 Adsorption Isotherm Models

In designing an adsorption system, it is essential to use an accurate mathematical description of the adsorption isotherms. Several isotherm equations have been proposed for the adsorption of a wide variety of adsorbates from solutions by activated carbons (Foo & Hameed, 2010). The parameters of these isotherm equations indicate the nature of the surface heterogeneity and the affinity between the adsorbent and adsorbate at a fixed temperature and pH. In this study, the experimental isotherm data were fitted with the following isotherm models, namely the Langmuir isotherm (Langmuir, 1918), Freundlich isotherm (Freundlich, 1906), and Redlich-Peterson isotherm (Redlich & Peterson, 1959) equations to validate the prediction capability of the tested models, as shown in Equations (3.9)–(3.11), respectively.

$$\text{Langmuir:} \quad q_e = \frac{q_m K_L C_e}{(1 + K_L C_e)} \quad (3.9)$$

$$\text{Freundlich:} \quad q_e = K_F C_e^{1/n_F} \quad (3.10)$$

$$\text{Redlich-Peterson:} \quad q_e = \frac{K_R C_e}{1 + A_R C_e^\beta} \quad (3.11)$$

It should be noted that most adsorption models were originally developed for gas adsorption with certain assumptions. Therefore, when applying these models to liquid systems, they are used simply as empirical equations. The Langmuir equation was originally proposed for the monolayer adsorption of a gas on a homogeneous flat surface (constant adsorption energy) and contains two model parameters, namely the monolayer capacity (q_m , mg/g) and the Langmuir or affinity constant (K_L , L/mg), which is a measure of how strong an adsorbate molecule is attracted onto an adsorbent surface. The two-parameter Freundlich equation was developed based on the assumption of monolayer adsorption on a patch-wise heterogeneous surface (distribution of adsorption energy). The Freundlich isotherm equation was originally developed as an empirical equation, but it can also be derived based on thermodynamic consideration (Adamson et al., 1997). It also contains two model parameters, namely K_F which corresponds to the binding capacity and n_F which characterizes the surface heterogeneity. The larger the value of n_F , the higher the heterogeneity of the surface and the more non-linearity of the isotherms. The Redlich–Peterson equation is a three-parameter empirical model that incorporates features of both the Langmuir and Freundlich equations. At low adsorbate concentrations, it follows a linear isotherm, and at high concentrations, its behavior approaches the Freundlich isotherm, which does not have a saturation limit. It can describe the adsorption process over a wide range of concentrations. A_R , β , and K_R are the model constants, where β is an exponent that lies between 0 and 1, and K_R is the modified Langmuir constant (L/g). As a first approximation, it is generally assumed that K_R is equal to K_L .

The parameters of the isotherm and the kinetic models were determined by fitting the experimental data with the corresponding model equations using a non-linear regression analysis that minimizes the sum of a squared estimate of errors (SSE) between the experimental and the computed values. The goodness-of-fit between the model and the experimental results was tested by the value of the regression coefficient, R^2 , and the normalized standard deviation (Δq) which is defined by Equation (3.12) as follows,

$$\Delta q(\%) = 100 \times \sqrt{\frac{\sum [(q_{t,\text{exp}} - q_{t,\text{cal}}) / q_{t,\text{exp}}]^2}{N - 1}} \quad (3.12)$$

where the subscripts *exp* and *cal* denote the experimental and calculated values, respectively, and N is the number of data points. The higher the value of R^2 and the lower the value of Δq , the better goodness-of-fit.

3.5 Results and Discussion

3.5.1 Characterization of the Prepared Activated Carbons

Table 3.2 shows the porous properties of the prepared microporous carbon series (A1–A3) and mesoporous carbon series (A4–A6). It should be noted that the activation temperature and time for each pair of A1 and A4, A2 and A5, and A3 and A6 are the same, that is 850°C and 120 min, 850°C and 180 min, and 850°C and 240 min, respectively. Overall, the mesoporous activated carbons produced by the OTA method had larger porous properties than those of microporous activated carbons prepared by the two-step activation process under the same activation conditions (time and temperature). It is noticed that the porous properties and the average pore size of activated carbons increased with the increase in activation time, but the percentage increase was more pronounced for the mesoporous carbons. Furthermore, when the activation time increased, the percentage of micropore volume decreased whereas that of the mesopore volume tended to increase. This indicates that the mesopores were created at the expense of newly formed micropores. The highest porous properties (V_{mi} of 0.600 cm³/g, V_{me} of 0.474 cm³/g, V_T of 1.074 cm³/g, and S_{BET} of 1773 m²/g) were obtained with the activated carbon A6 produced by the three-cycle OTA method. Again, these results clearly show that the OTA method is more effective, as compared to the two-step activation, for the production of activated carbons with higher amounts of micropores and mesopores and a larger surface area.

Table 3.3 shows the distribution of pore sizes for the prepared activated carbons. The pore size distribution data showed the type of multimodal distribution, covering the pore sizes ranging from 0.65 to 4 nm. Most of the microporous carbons (A1–A3) were in the micropore size range (0.65–1.4 nm), followed by the upper mesopore size range of 3–4 nm. The volume of micropores (0.65–1.4 nm) decreased with the increase of activation time for carbons A1 to A3, while the opposite trend is observed for the supermicropores (1.4–2 nm). This observation indicates that supermicropores are responsible for the increase of

surface area with increasing activation time. The upper mesopore size of 3–4 nm constituted most of the mesopore volume for A1 to A3 carbons, and this pore size range played a significant role in facilitating the diffusion of dye molecules in the activated carbon. The mesoporous carbons (A4–A6) also contained large proportions of micropores (0.65–1.4 nm) and most of the mesopores were concentrated in the lower size range of 2 to 3 nm. Intuitively, a large surface area of activated carbon should promote MB adsorption capacity, whereas a large volume of mesopores should enhance the kinetics of MB diffusion through internal pores.

Table 3.4 shows the point of zero charges (pH_{PZC}) and the amounts of oxygen functional groups on the carbon surfaces of microporous and mesoporous activated carbons. The amounts of both acid and basic functional groups increased with increasing activation time for the microporous carbons (A1–A3) and with the increasing number of preparation cycles for the mesoporous carbons (A4–A6). The amounts of basic groups were higher than those of the acid groups for all carbon samples, possibly because CO_2 was used as the activating agent rather than water vapor (steam) (Marsh & Rodríguez-Reinoso, 2006). The increasing amounts of basic groups for samples A1 to A3 and samples A4 to A6 indicate the increasing degree of basicity of the carbon surface and this coincides with the increasing values of pH_{PZC} of the activated carbon, as expected. It is further noted that the mesoporous carbons had fewer acid groups and higher basic groups, as compared to microporous carbons. The lower number of surface acid groups of mesoporous carbons could result from the high-temperature treatment of the oxidized carbon as part of the OTA method that may have removed most of the acid functional groups prior to the following activation step.

Figure 3.2 shows the surface images obtained from a field emission scanning electron microscope (FE-SEM) of microporous activated carbon prepared by the two-step activation method (sample A2 or A850-180) and the mesoporous activated carbon prepared by the OTA method (sample A5 or A850-60-2). Figure 3.2a1, b1 and Figure 3.2a2, b2 present the images at low and high magnifications, respectively. It can be seen that there was a tendency for an increase in the average pore size and the number of pores for the mesoporous carbon (A5), as compared with the microporous carbon (A2). These results are in line with those of the average pore size and pore volume results, as presented in Table 3.2.

Table 3.2 Porous properties of prepared activated carbons

Sample code	Sample name	D_{av}	V_{mi}	V_{me}	V_T	S_{BET}
		(nm)	(cm^3/g) (%)	(cm^3/g) (%)	(cm^3/g)	(m^2/g)
A1	A850-120	1.88	0.343 (78.5)	0.094 (21.5)	0.437	932
A2	A850-180	1.91	0.340 (76.9)	0.102 (23.1)	0.442	926
A3	A850-240	2.06	0.409 (69.7)	0.178 (30.3)	0.587	1140
A4	A850-60-1	1.96	0.375 (78.1)	0.105 (21.9)	0.480	980
A5	A850-60-2	2.32	0.466 (63.3)	0.270 (36.7)	0.736	1271
A6	A850-60-3	2.42	0.600 (55.9)	0.474 (44.1)	1.074	1773

Table 3.3 Pore size distribution of prepared activated carbons

Sample code	V_T (cm^3/g)	Pore volume for pore width (cm^3/g)			
		0.65–1.4 nm	1.4–2 nm	2–3 nm	3–4 nm
A1	0.437	0.306 (70.0%)	0.037 (8.5%)	0.006 (1.4%)	0.088 (20.1%)
A2	0.442	0.291 (65.8%)	0.049 (11.1%)	0.002 (0.5%)	0.100 (22.6%)
A3	0.587	0.307 (52.3%)	0.102 (17.4%)	0.012 (2.0%)	0.166 (28.3%)
A4	0.480	0.309 (64.4%)	0.066 (13.7%)	0.046 (9.6%)	0.059 (12.3%)
A5	0.736	0.339 (46.1%)	0.127 (17.2%)	0.176 (23.9%)	0.094 (12.8%)
A6	1.074	0.207 (19.3%)	0.393 (36.6%)	0.330 (30.7%)	0.144 (13.4%)

Table 3.4 Point of zero charge and surface functional groups in activated carbons

Sample code	pH_{PZC}	Acidic groups	Basic groups	Total
		(mmol/g)	(mmol/g)	(mmol/g)
A1	8.77	0.243 (20.5%)	0.941 (79.5%)	1.184
A2	8.81	0.334 (22.4%)	1.160 (77.6%)	1.494
A3	9.48	0.400 (23.1%)	1.329 (76.9%)	1.729
A4	9.36	0.152 (10.5%)	1.295 (89.5%)	1.447
A5	9.54	0.218 (14.1%)	1.331 (85.9%)	1.549
A6	9.94	0.251 (14.4%)	1.491 (85.6%)	1.742

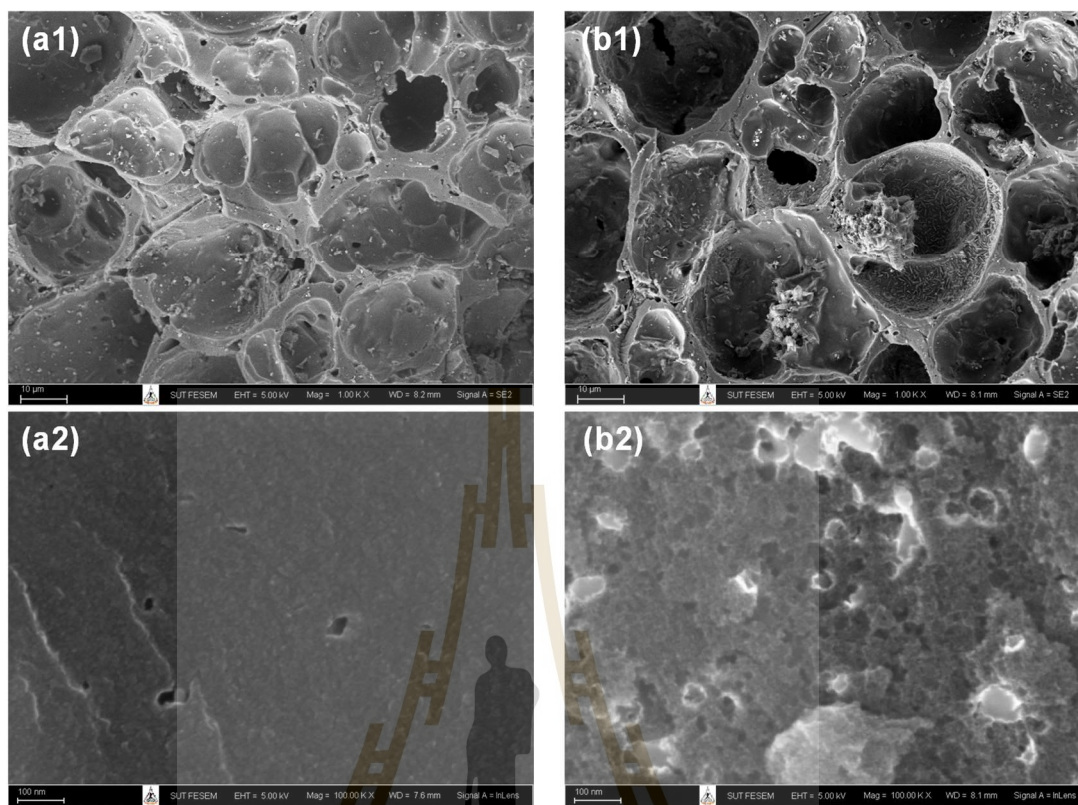


Figure 3.2 SEM micrographs of (a) the microporous activated carbon of A2 (A850-180), and (b) the mesoporous activated carbon of A5 (A850-60-2), with a magnification of 1K for (a1–b1) and 100K for (a2–b2).

3.5.2 Adsorption Kinetics and Model Testing

The kinetic results of MB adsorption by the microporous (A1–A3) and mesoporous carbons (A4–A6) are displayed in Figure 3.3. The kinetic curves showed a rapid increase in the amounts adsorbed over the first 500 min, followed by a slow increase before attaining an equilibrium at approximately 2,000 min. However, the amount of MB adsorbed by the sample A850-60-3 (A6) approached the equilibrium sooner at 1,500 min, obviously resulting from its largest average pore diameter (2.42 nm) that allows a faster diffusion rate of dye molecules to the adsorption sites. The amount of dye adsorbed appeared to be higher for the adsorbent with a higher surface area (see Table 3.2). This indicates that the adsorption sites are distributed

more or less uniformly on the carbon surfaces, irrespective of the carbon surface area. In other words, the density of adsorption sites (number per unit area) is approximately constant. The best-fitted model parameters are listed in Table 3.5. From the values of R^2 and Δq , it is clear that the experimental kinetic data of MB adsorption by longan seed-activated carbons are best described by the pseudo-second-order model, followed by the pore-diffusion model and the pseudo-first-order model, respectively. The success of the pseudo-second-order model in describing the kinetics of MB adsorption was also reported for activated carbons prepared from various precursors such as *Abelmoschus esculentus* seeds (Nayak & Pal, 2017), Black cumin seeds (Thabede et al., 2020), and Lychee seed (Sahu et al., 2020).

Results from Table 3.5 indicate that the rate constants k_1 and k_2 , as well as the effective pore diffusivity (D_e), all increased with an increase in the average pore diameter of samples A1 to A3 and A4 to A6. This was anticipated since the larger pore sizes would be able to accommodate the rapid diffusion of relatively large dye molecules. It should also be noted that the pore diffusivities of mesoporous activated carbons in the range of 4.67×10^{-7} – 19.92×10^{-7} cm^2/s were larger than those of the microporous carbons (4.66×10^{-7} – 6.01×10^{-7} cm^2/s) by almost an order of magnitude which should result from higher amounts of mesopores of the former that lower the mass transfer resistance for the transport of dye molecules through the pore network (see Table 3.2). The molecular diffusivity of methylene blue in water at 35°C, as estimated by the Wilke-Chang equation (Reid et al., 1977), is about 5.57×10^{-6} cm^2/s , which is about 10 times and 6 times larger than the average pore diffusivities of the microporous carbon and mesoporous carbon, respectively. This suggests that the process of MB adsorption is controlled by the intra-particle diffusion of MB molecules since the adsorption rate is generally much faster than the internal mass transport rate of the adsorbate molecules (Fogler, 2016).

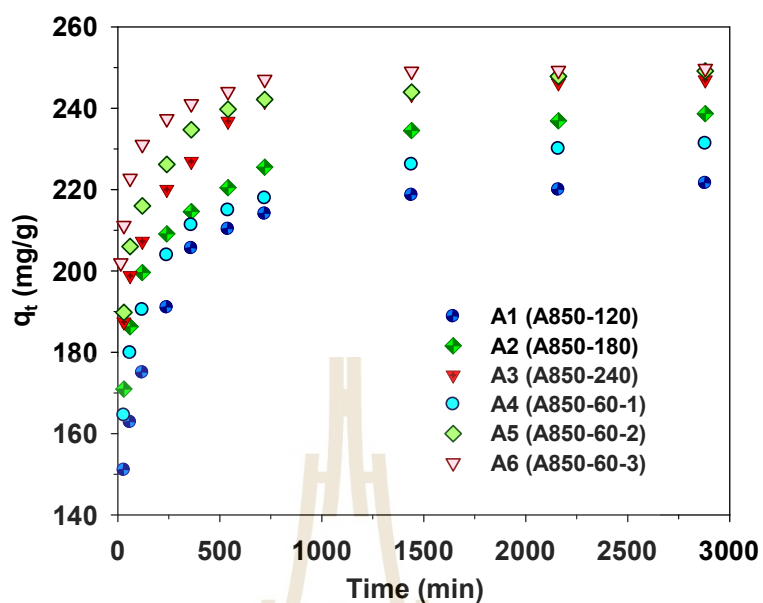


Figure 3.3 Kinetics of methylene blue adsorption on the prepared microporous and mesoporous activated carbons from the longan fruit seed.

Table 3.5 Kinetic parameters of various adsorption kinetic models for MB adsorption by longan seed-activated carbons

Code	Pseudo-first order				Pseudo-second order				Pore-diffusion			
	q_e mg/g	k_1 min^{-1}	R^2 %	Δq %	q_e mg/g	$k_2 (\times 10^4)$ g/(mg·min)	R^2 %	Δq %	q_e mg/g	$D_e (\times 10^7)$ cm^2/s	R^2 %	Δq %
A1	206.98	0.034	0.914	8.94	222.22	2.265	0.999	4.39	218.52	4.657	0.987	5.38
A2	221.63	0.042	0.912	6.81	238.10	2.669	0.999	4.40	235.98	4.667	0.957	5.14
A3	232.43	0.047	0.819	6.81	240.45	3.850	0.999	3.57	244.76	6.014	0.990	4.26
A4	215.08	0.041	0.947	7.00	232.56	2.548	0.999	4.06	226.94	4.668	0.984	4.02
A5	236.40	0.048	0.895	5.39	243.15	4.312	0.999	2.51	241.39	10.76	0.989	3.85
A6	239.91	0.110	0.805	5.09	246.60	8.962	0.999	1.82	248.30	19.92	0.974	3.74

A closer examination of pore size distribution data in Table 3.3 reveals that the largest pore diffusivity of $19.92 \times 10^{-7} \text{ cm}^2/\text{s}$ for sample A6 prepared by the three-cycle OTA method is associated with the large proportions of supermicropores (36.6% by volume) and mesopores of 2–3 nm (30.7%). Therefore, supermicropores (1.4–2 nm) and small mesopores (2–3 nm) would play an important part in controlling the adsorption kinetics of methylene blue adsorption by activated carbon with a high surface area and a high mesopore volume. The dominant transport mechanism of methylene blue molecules in the supermicropores is possibly the result of Knudsen diffusion, since the molecular size of methylene blue, 1.447 nm (Dotto et al., 2015), is comparable to the pore size. The diffusion of MB in the small mesopores (2–3 nm) which have a pore size twice that of the molecular size of methylene blue could involve both the Knudsen diffusion and molecular diffusion. It should be realized that the optimum pore size distribution of activated carbon that leads to rapid kinetic behavior does not necessarily provide the maximum adsorption capacity because the maximum adsorption will depend on the available surface area and the number of adsorption sites.

Table 3.6 lists the value of k_2 of the pseudo-second-order kinetic model derived from the present and previous studies of methylene blue adsorption by activated carbons prepared from different biomass precursors and the effect of the percentage of mesopore volume on k_2 is shown in Figure 3.4. Although there are differences in the porous properties of activated carbons prepared from various sources of raw materials, as well as the adsorption conditions used, there appears an optimum percentage of mesopore volume of around 50% that yields a maximum rate constant k_2 . From these limited data, it could be deduced that the kinetics of MB diffusion in the porous structure of activated carbon is determined primarily by the relative proportion of micropores and mesopores. A smaller amount of mesopores tends to lower the diffusion rate of methylene blue due to an increase in the mass transfer resistance offered by the larger amounts of micropores. Since the transport of an adsorbate through the pore network and the adsorption on the carbon surface occur in series, the lower adsorption rate caused by the decrease of the surface area of larger mesopore volume would therefore lower the diffusive flux of the dye molecules inside the pores, and hence giving a relatively low value for k_2 .

Table 3.6 Comparison of the kinetic parameter (k_2) of the pseudo-second-order model for various types of activated carbons

Biomass precursors	S_{BET}	V_{mi}	V_{me}	V_T	$k_2 \times 10^4$
	(m^2/g)	(cm^3/g) (%)	(cm^3/g) (%)	(cm^3/g)	($g/(mg \cdot min)$)
Mangosteen peel ⁽¹⁾	890	0.010 (1.4)	0.701 (98.6)	0.711	0.480
Coconut leaves ⁽²⁾	982	0.095 (6.9)	1.276 (93.1)	1.371	2.000
Jerusalem artichoke ⁽³⁾	1632	0.120 (9.8)	1.100 (90.2)	1.220	1.678
Vetiver roots (P1.5) ⁽⁴⁾	1004	0.220 (21.6)	0.800 (78.4)	1.020	0.110
Vetiver roots (P1.0) ⁽⁴⁾	1272	0.390 (32.8)	0.800 (67.2)	1.190	1.050
Rattan stalks ⁽⁵⁾	1135	0.170 (27.9)	0.440 (72.1)	0.610	5.000
Chitosan flakes ⁽⁶⁾	318	0.098 (38.4)	0.157 (61.6)	0.255	7.160
Orange peel ⁽⁷⁾	1104	0.247 (40.2)	0.368 (59.8)	0.615	7.333
<i>Posidonia oceanica</i> ⁽⁸⁾	1483	0.494 (48.3)	0.528 (51.7)	1.022	16.00
Dipterocarpus alatus ⁽⁹⁾	843	0.256 (54.1)	0.217 (45.9)	0.473	10.99
Waste tea ⁽¹⁰⁾	854	0.310 (60.1)	0.206 (39.9)	0.516	0.010
Coconut shell ⁽¹¹⁾	876	0.272 (61.7)	0.169 (38.3)	0.441	1.833
Eucalyptus sawdust ⁽¹²⁾	645	0.280 (63.6)	0.160 (36.4)	0.440	4.770
Thevetia peruviana ⁽¹³⁾	588	0.342 (70.7)	0.142 (29.3)	0.484	0.031
Durian shell ⁽¹⁴⁾	992	0.368 (78.1)	0.103 (21.9)	0.471	0.357
Longan seed (A6)	1773	0.600 (55.9)	0.474 (44.1)	1.074	8.962

Sources: ⁽¹⁾ (Nasrullah et al., 2018); ⁽²⁾ (Jawad et al., 2017); ⁽³⁾ (Yu & Luo, 2014); ⁽⁴⁾ (Altenor et al., 2009);

⁽⁵⁾ (Islam et al., 2017a); ⁽⁶⁾ (Marrakchi et al., 2017); ⁽⁷⁾ (Foo & Hameed, 2012); ⁽⁸⁾ (Dural et al., 2011);

⁽⁹⁾ (Patawat et al., 2020); ⁽¹⁰⁾ (Auta & Hameed, 2011); ⁽¹¹⁾ (Islam et al., 2017b);

⁽¹²⁾ (Chen et al., 2019); ⁽¹³⁾ (Williams & Aydinlik, 2021); ⁽¹⁴⁾ (Chandra et al., 2007).

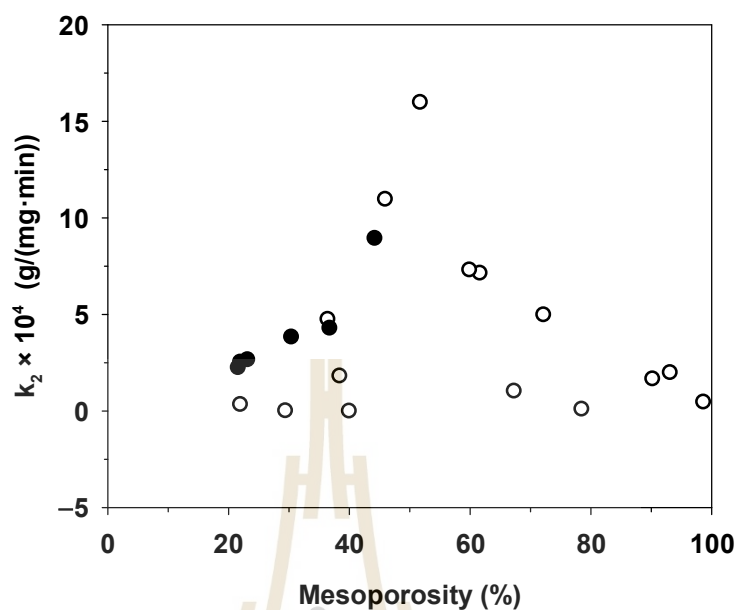


Figure 3.4 Effect of percent mesoporosity in activated carbons on the rate constant (k_2) of the pseudo-second-order kinetic model. The black circles represent the results from the present study and the white circles are those from other investigators (see references in Table 3.6).

3.5.3 Adsorption Isotherms and Model Testing

Adsorption isotherms provide essential information for the adsorption capacity and adsorption behavior of porous adsorbents. In the present study, the measured isotherm data for MB adsorption by the prepared activated carbons were tested with the Langmuir, Freundlich, and Redlich-Peterson equations and the best-fitted model parameters achieved by applying regression analysis are listed in Table 3.7.

Figure 3.5 compares the measured and the model-predicted isotherms for MB adsorption by the longan-seed activated carbons. Based on visual observation of Figure 3.5 and the values of R^2 and Δq , the Langmuir equation gave the least prediction capability of MB isotherms for all carbons. It is interesting to note that the Redlich-Peterson model can best describe the isotherms of microporous carbons prepared by the two-step activation (A1–A3), while the Freundlich equation is most appropriate for predicting the MB adsorption by the mesoporous carbons produced

by the OTA method (A4–A6). The better description of MB adsorption isotherms by the Redlich-Peterson equation for the microporous carbons is possibly due to their higher percentage of micropore volume (see Table 3.2), thus showing a sharper linear isotherm behavior at low concentrations by micropore-filling adsorption. The ability of the Freundlich equation that in better predict the isotherm behavior of the mesoporous carbons may arise from the higher degree of heterogeneity of the carbon surfaces.

Figure 3.6 shows the dependence of the binding capacity parameters, that is, the monolayer capacity (q_m) of the Langmuir model and K_F of the Freundlich model, on the surface area of activated carbons. Both parameters increased with an increase in the specific surface area. This is understandable since a greater surface area could provide a larger number of adsorption sites for the methylene blue dye. From Table 3.7, the surface heterogeneity parameter of the Freundlich equation (n_F) appeared to be almost insensitive to the change in surface area, which suggests that the distribution of adsorption energy as a function of adsorption sites is to a certain degree almost independent of the developed surface area of activated carbons.

Figure 3.7 shows the effect of the surface area of activated carbons on the affinity coefficients, K_L and K_R . Both parameters increased with the increase of surface area in the same fashion as that observed with the binding capacity parameters. The development of surface area due to the removal of carbon atoms from the graphene layer by gasification may create surface defects with stronger interaction forces, thus providing stronger adsorbent-adsorbate affinity. Furthermore, it can be seen from Table 3.7 that under the same activation time and temperature, the monolayer capacity (q_m) of the Langmuir equation for the mesoporous carbons is higher than that of the microporous activated carbons. For comparison, the percentage increase of q_m from A1 to A4, A2 to A5, and A3 to A6 are 6.3%, 43%, and 54%, respectively. The highest value of the monolayer capacity of 1000 mg/g for MB adsorption was observed with the mesoporous activated carbon prepared by the three-cycle OTA method (sample A6).

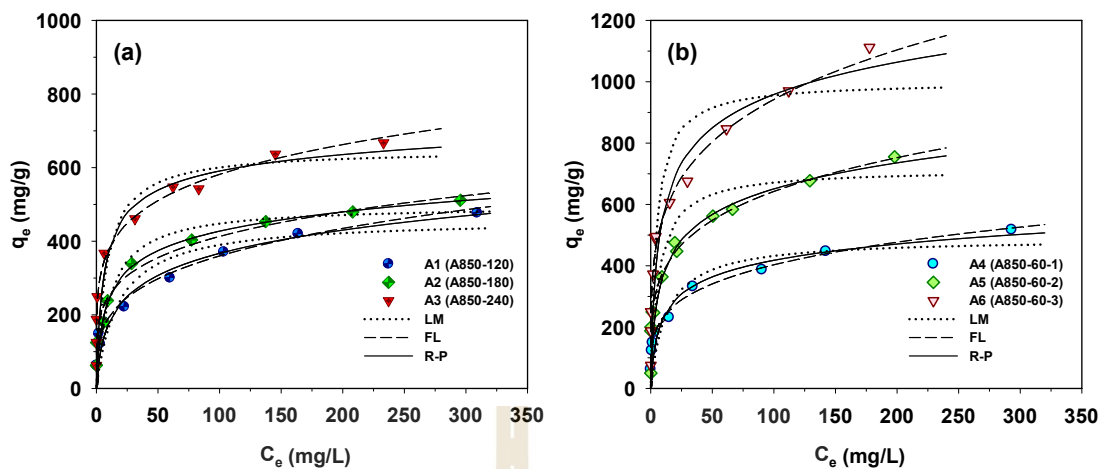


Figure 3.5 Adsorption isotherms at 35°C of MB dye on longan seed-activated carbons prepared by (a) the two-step activation method, and (b) the OTA method.

Table 3.7 Parameters of adsorption isotherm equations for MB adsorption at 35°C by the prepared activated carbons

Code	Langmuir				Freundlich				Redlich-Peterson				
	q_m (mg/g)	K_L (L/mg)	R^2	Δq (%)	n_F	K_F	R^2	Δq (%)	K_R (L/g)	β	A_R	R^2	Δq (%)
A1	459.35	0.056	0.984	24.4	3.67	102.6	0.992	8.04	56.0	0.81	0.34	0.999	5.87
A2	497.12	0.090	0.995	5.45	4.61	152.2	0.957	12.5	90.2	0.86	0.38	0.998	4.29
A3	648.12	0.125	0.989	12.6	5.31	244.2	0.980	11.7	125	0.93	0.28	0.992	5.74
A4	488.29	0.076	0.987	22.8	4.13	132.1	0.996	4.69	76.3	0.86	0.32	0.970	7.54
A5	714.29	0.154	0.986	15.4	4.38	224.2	0.996	4.88	153.8	0.85	0.45	0.989	9.40
A6	1000.0	0.214	0.986	18.5	4.38	328.9	0.991	6.82	214	0.88	0.37	0.981	12.4

Table 3.8 compares the maximum adsorption capacity of MB adsorption by activated carbons from the present and previous investigations, together with the porous properties of the relevant adsorbents. It was observed that the percentage of micropore volume and mesopore volume varied from 13.2–90.0% and 10.0–86.8%, respectively, depending on the raw materials and the preparation conditions employed. As shown in Figure 3.8, the BET surface area increased almost linearly with an increase in micropore volume, emphasizing that the surface area of activated carbons is determined primarily by the amount of micropores.

Figure 3.9 shows a plot of the maximum capacity of MB adsorption as a function of the surface area of activated carbons from the present and previous studies. The adsorption capacity increased with the increase of surface area as expected, since an adsorption process is a surface phenomenon of adsorbent-adsorbate interactions. It is seen that all data points from the present study were above those of the previous results, notably with the A6 carbon that gave the largest value of the adsorption capacity of 1000 mg/g. The relatively larger adsorption capacity of mesoporous carbons prepared by the OTA method (A4–A6) clearly indicates that activated carbons produced by the OTA method contain a larger number of adsorption sites. Also, the ratio of q_m/S_{BET} in Table 3.8 for mesoporous carbon A6 from this study remarkably showed that its ratio of 0.564 was about twofold higher than the average value of 0.296 for activated carbons reported by previous studies.

Table 3.8 The maximum adsorption capacity of methylene blue from solutions (q_m) by activated carbons prepared from various materials and activation methods

Raw materials	Activating agent	S_{BET}	V_{mi}	V_{me}	V_T	D_{av}	q_m	q_m/S_{BET}
		(m^2/g)	(cm^3/g) (%)	(cm^3/g) (%)	(cm^3/g)	(nm)	(mg/g)	(mg/m^2)
Flamboyant pods ⁽¹⁾	NaOH	2854	1.440 (90.0)	0.160 (10.0)	1.600	2.24	874.7	0.306
Coconut shell ⁽²⁾	NaOH	2825	1.143 (76.3)	0.355 (23.7)	1.498	2.12	916.3	0.324
Date press cake ⁽³⁾	KOH	2633	0.952 (76.8)	0.287 (23.2)	1.239	1.88	546.8	0.208
Oily sludge+rice husk ⁽⁴⁾	KOH	2575	1.080 (67.1)	0.530 (32.9)	1.610	2.50	757.6	0.294
Globe artichoke ⁽⁵⁾	H ₃ PO ₄	2038	0.608 (24.7)	1.800 (75.3)	2.466	4.84	780.0	0.383
Rice husk ⁽⁶⁾	H ₃ PO ₄	2028	0.787 (58.7)	0.554 (41.3)	1.341	2.64	578.1	0.285
Rawdon coal ⁽⁷⁾	KOH	1951	0.776 (74.0)	0.273 (26.0)	1.049	2.15	841.9	0.432
Refuse-derived fuel ⁽⁸⁾	KOH	1734	0.623 (53.2)	0.547 (46.8)	1.170	2.70	571.0	0.329
<i>Posidonia oceanica</i> ⁽⁹⁾	ZnCl ₂	1483	0.494 (48.3)	0.528 (51.7)	1.022	2.76	285.7	0.193
Commercial AC ⁽¹⁰⁾	-	1440	0.368 (51.6)	0.345 (48.4)	0.713	1.98	370.4	0.257
Pomelo skin ⁽¹¹⁾	NaOH	1335	0.290 (37.7)	0.480 (62.3)	0.770	2.31	501.1	0.375
Vetiver roots ⁽¹²⁾	H ₃ PO ₄	1272	0.390 (32.8)	0.800 (67.2)	1.190	3.74	394.0	0.310
Orange peel ⁽¹³⁾	K ₂ CO ₃	1104	0.247 (40.2)	0.368 (59.8)	0.615	2.23	382.8	0.347
Waste apricot ⁽¹⁴⁾	ZnCl ₂	1060	0.150 (19.0)	0.640 (81.0)	0.790	2.98	102.0	0.096
Coffee grounds ⁽¹⁵⁾	H ₃ PO ₄	925	0.211 (29.4)	0.507 (70.6)	0.718	3.10	181.8	0.197
Cotton stalk ⁽¹⁶⁾	ZnCl ₂	795	0.083 (13.2)	0.547 (86.8)	0.630	3.17	315.5	0.397
Longan seed (A6)	CO ₂	1773	0.600 (55.9)	0.474 (44.1)	1.074	2.42	1000	0.564

Sources: ⁽¹⁾ (Vargas et al., 2011); ⁽²⁾ (Cazetta et al., 2011); ⁽³⁾ (Heidarinejad et al., 2018); ⁽⁴⁾ (Wang et al., 2018);

⁽⁵⁾ (Benadjemia et al., 2011); ⁽⁶⁾ (Chen et al., 2013); ⁽⁷⁾ (Gokce et al., 2021); ⁽⁸⁾ (Wu et al., 2013);

⁽⁹⁾ (Dural et al., 2011); ⁽¹⁰⁾ (Reffas et al., 2010); ⁽¹¹⁾ (Foo & Hameed, 2011); ⁽¹²⁾ (Altenor et al., 2009);

⁽¹³⁾ (Foo & Hameed, 2012); ⁽¹⁴⁾ (Başar, 2006); ⁽¹⁵⁾ (Reffas et al., 2010); ⁽¹⁶⁾ (Deng et al., 2009)

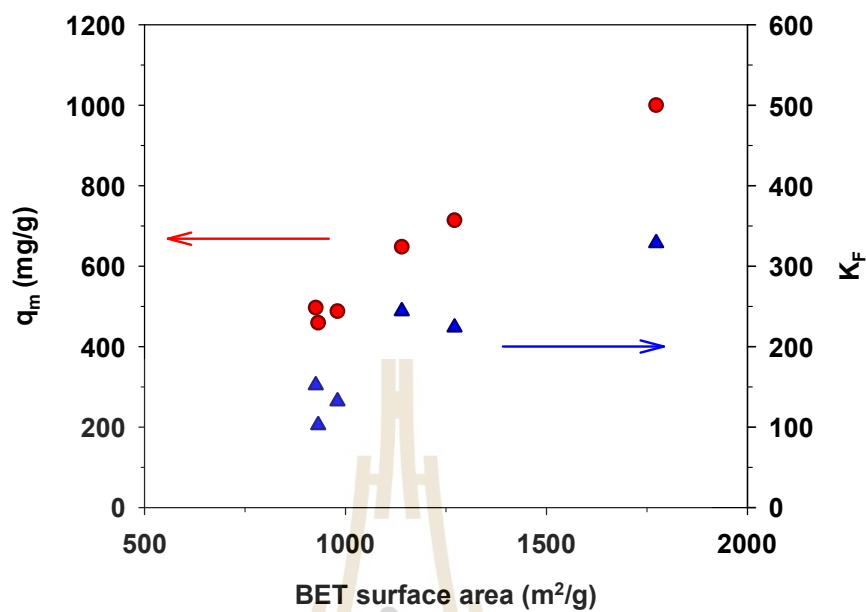


Figure 3.6 Effect of BET surface area on monolayer capacity (q_m) of the Langmuir isotherm equation and K_F of the Freundlich equation.

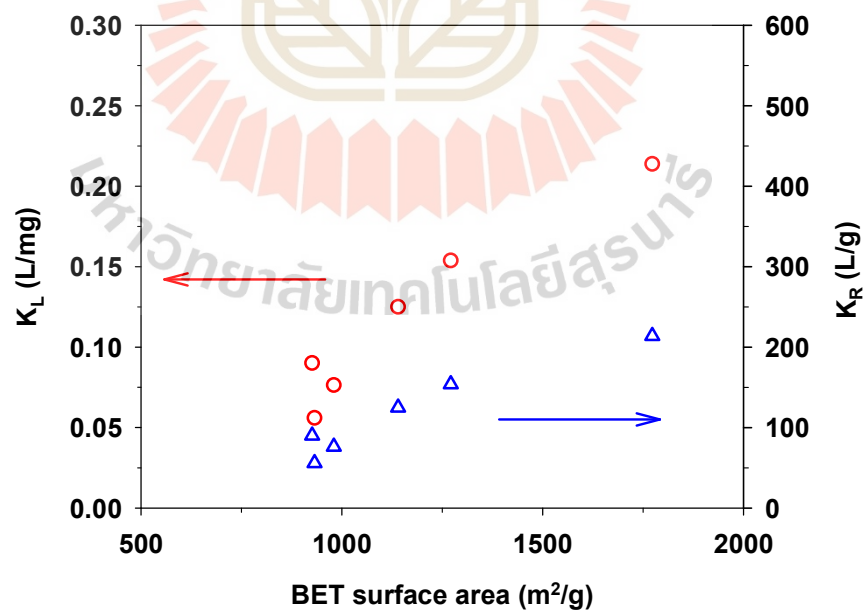


Figure 3.7 Effect of BET surface area on K_L of the Langmuir equation and K_R of the Redlich-Peterson equation.

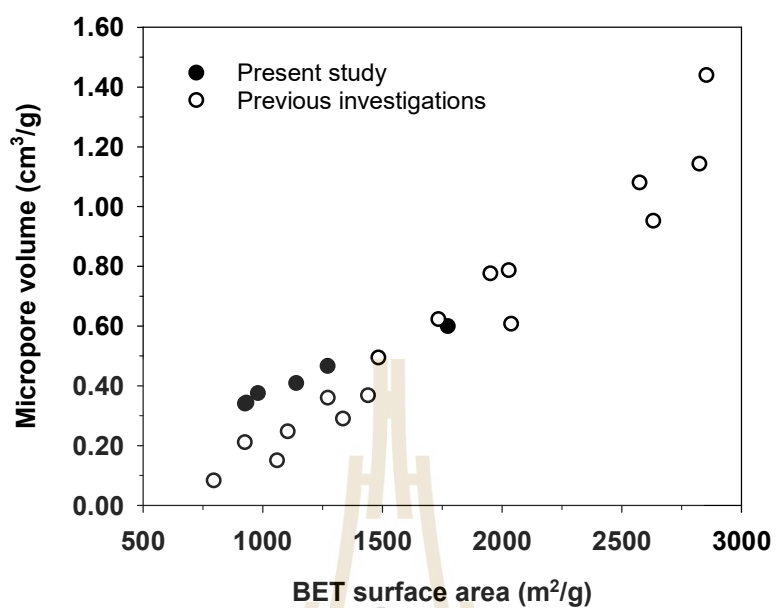


Figure 3.8 Correlation between BET surface area and the maximum MB adsorption capacity from the data in Table 3.8.

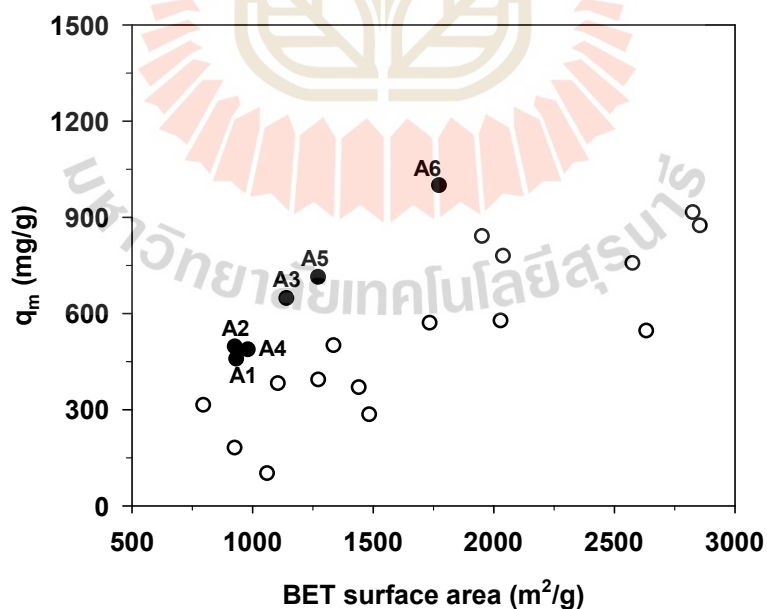


Figure 3.9 Effect of BET surface area on the maximum MB adsorption capacity. The black circles represent results from the present study (A1–A6) and the white circles belong to previous investigations.

3.5.4 Effect of Adsorbent Dosage

Figure 3.10 shows the effects of carbon dosage on the adsorption capacity and removal efficiency of methylene blue when the performances of microporous carbon A3 and mesoporous carbon A6 are compared with both carbons being produced at the same activation time and temperature at 240 min and 850°C, respectively. The adsorption conditions used were an initial MB concentration (C_0) of 300 mg/L, solution volume (V) of 25 mL, and adsorption temperature (T) of 35°C.

Figure 3.10a shows that the amount of MB adsorbed in mg increased with an increase in carbon dosage and became constant when the dosage reached a certain maximum value. Clearly, the increase in the amount adsorbed is the result of an increase in the number of adsorption sites provided by the increase in the amount of the adsorbent. Therefore, when the number of adsorption sites is in excess of those required for adsorption, the amount of MB adsorbed will reach a maximum and further addition of the adsorbent will exert no effect on the amount of adsorption. It can be seen from Figure 3.10a that the maximum carbon dosage for the mesoporous carbon and microporous carbon were 0.02 and 0.03 g, respectively. When multiplying the dosage with the corresponding BET surface area, the maximum area required for the maximum amount adsorbed was 34.2 m² (0.03 g × 1140 m²/g) and 35.5 m² (0.02 g × 1773 m²/g) for the microporous and mesoporous carbons, respectively, which are approximately the same. This clearly indicates that the porous property of surface area is important for determining the adsorption capacity of methylene blue dye, since the larger the surface area of the adsorbent, the higher the amount of the dye being adsorbed. It should be noted that before reaching the maximum adsorption, the amount of MB adsorbed was higher for the mesoporous carbon compared to that of the microporous carbon. Obviously, this is the result of the larger surface area of the mesoporous carbon that can provide a larger number of adsorption sites.

Figure 3.10b shows that the removal efficiency of methylene blue, calculated according to Equation (4.2), increased with the increase in the amount of adsorbent used. The trend of the curves was the same as that for the amount of MB adsorbed as shown in Figure 3.10a. The maximum removal efficiency of MB at the maximum carbon dosage was 99.71 and 99.90% for the microporous and

mesoporous activated carbons, respectively. This indicates that activated carbon is suitable for the effective removal of an organic dye like methylene blue.

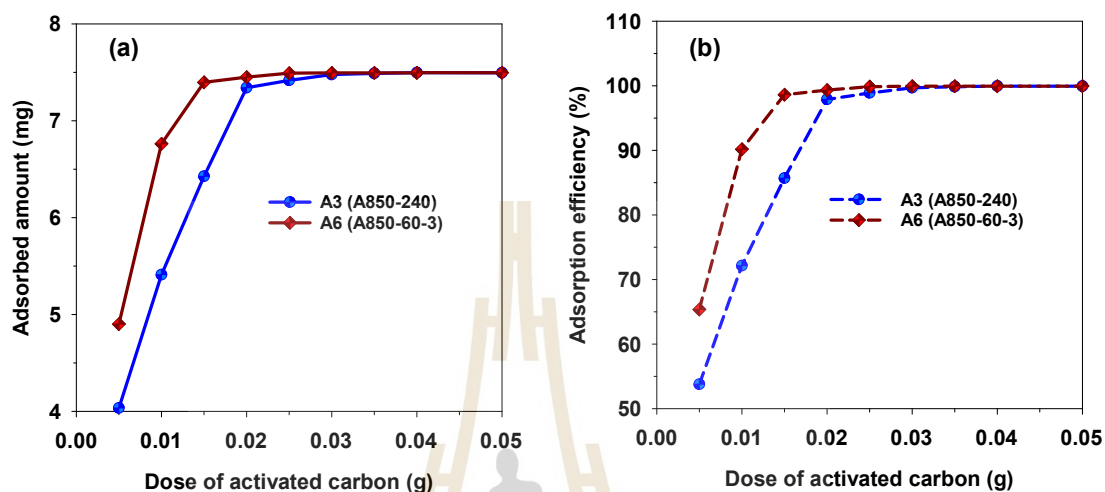


Figure 3.10 The effect of carbon dosage on (a) MB adsorption capacity and (b) MB removal efficiency for microporous (A3) and mesoporous (A6) activated carbons ($C_0 = 300$ mg/L, $V = 25$ mL and $T = 35^\circ\text{C}$).

3.5.5 Effect of Initial pH

The effect of the initial pH of the MB solution on the removal efficiency of methylene blue dye was investigated using activated carbon with a maximum surface area, mesoporous carbon A6, by varying the initial pH in the range of 3 to 11 under fixed conditions of adsorbent dosage of 0.8 g/L, initial dye concentration of 400 mg/L, adsorption time of 48 h and the temperature of 35°C . Figure 3.11 shows the results obtained. It can be observed that the adsorption capacity remained substantially constant over the pH range of 3–10. However, when the solution pH increased from the value of 10 to 11, the removal efficiency increased slightly from 98.98% to 99.15%, corresponding to the amount of MB adsorbed from 494.92 to 495.75 mg/g. This increase could arise as a result of the adsorbent surface becoming more negatively charged at a pH above 10, since the solution pH is higher than the experimentally determined pH_{PZC} of 9.94 for the activated carbon. This would enhance the strong electrostatic attraction between the

cationic MB dye and the negatively charged carbon surface. Therefore, the slight effect of the solution pH on the adsorption efficiency of methylene blue seems to suggest that the electrostatic attraction alone may not be the primary mechanism for the adsorption of methylene blue onto the activated carbon. The other types of underlying interactions between methylene blue and the carbon surface will be briefly outlined in the next section.

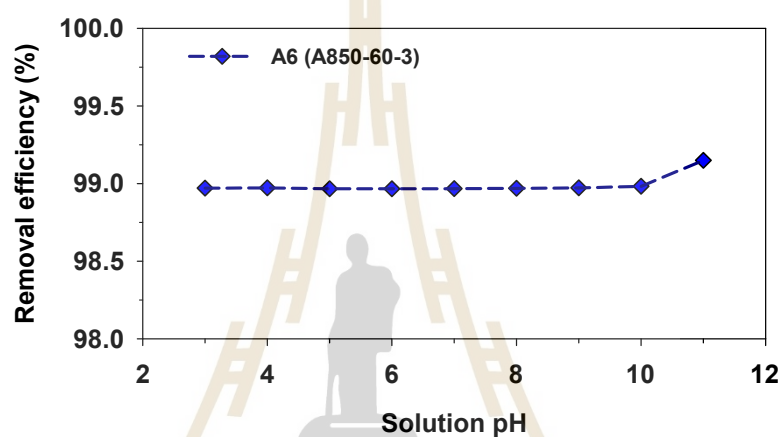


Figure 3.11 Effect of the initial solution pH on the removal efficiency of MB by the mesoporous activated carbon (A6), with $C_0 = 400$ mg/L, carbon dosage = 0.8 g/L and $T = 35^\circ\text{C}$.

3.5.6 Effect of Temperature and Adsorption Thermodynamics Study

The variation of MB adsorption isotherms of the mesoporous activated carbon, A6, as a function of temperature is displayed in Figure 3.12. Over the temperature range from 35 to 55°C, the amount of MB adsorbed increased with the increase in the adsorption temperature. The role of the temperature in adsorption is twofold, that is, it can affect the rate of adsorbate diffusion through the internal pores of an adsorbent and the adsorption ability of the adsorbate on the adsorbent surface via some kind of interaction forces (Ghaffar & Younis, 2015). Three dominant interactions between methylene blue molecules and the surface of activated carbon have been reported (Giraldo et al., 2021). They are (i) π - π interactions between the aromatic rings of MB and the graphene sheet of activated carbon, (ii) Hydrogen

bonding between the hydrogen in the hydroxyl group on the carbon surface and the nitrogen in the MB structure, and (iii) electrostatic interactions between electron-deficiency nitrogen (N^+) in the MB structure and electron-rich oxygen (O^-) of the surface functional groups on activated carbon. Since it is known that the magnitude of these interaction forces decreases with an increase in temperature (Ghasemi & Asadpour, 2007; Yao et al., 2010), thus the increasing amount of MB adsorbed with the increase in temperature must be related to its effect on the transport of the methylene molecules in the carbon pore structure. It is likely that the increase in temperature would increase the diffusion rate of methylene blue molecules to the adsorption sites which would increase the likelihood of an adsorbent-adsorbate interaction, hence the increasing amount of methylene blue adsorbed. A similar temperature effect on the amount of MB adsorbed was also observed by a number of investigators working on different adsorbents, for example, tannin (Sánchez-Martín et al., 2010), rejected tea (Nasuha & Hameed, 2011), magnetic graphene-CNTs (Wang et al., 2014), N and S co-doped porous carbon spheres (Ren et al., 2021).

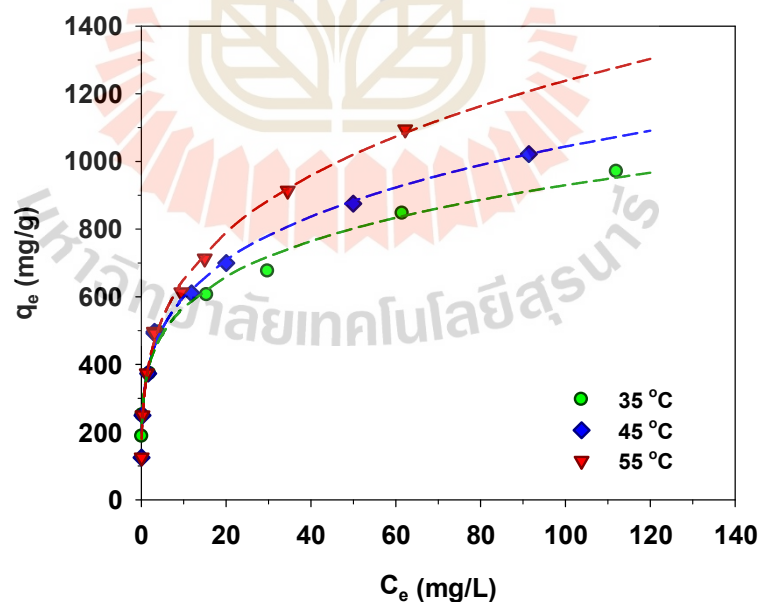


Figure 3.12 Effect of temperature on isotherms of MB adsorption by the mesoporous activated carbon (A6).

In order to gain a fuller understanding of the dye adsorption process, the various thermodynamic parameters including the values of enthalpy change (ΔH°), Gibbs free energy change (ΔG°), and entropy change (ΔS°) were estimated from the isotherm data at various temperatures by using the following equations (Theydan & Ahmed, 2012),

$$\ln K_d = \frac{\Delta S^\circ}{R} - \frac{\Delta H^\circ}{RT} \quad (3.13)$$

$$\Delta G^\circ = -RT \ln K_d \quad (3.14)$$

where R is the universal gas constant (8.314 J/(mol·K)), T (K) is the absolute solution temperature, and K_d is the distribution coefficient for the adsorption, which is the ratio of the amount of MB in the adsorbed phase and that in the aqueous phase and which can be computed from the relation, $K_d = (q_e/C_e) \cdot (W/V)$. Figure 3.13 shows plots of $\ln K_d$ versus $1/T$ for three different values of C_e (20, 40, and 80 mg/L). The values of ΔH° and ΔS° were then determined from the slope and intercept of the straight-line graph. Equation (3.14) was used for the calculation of the Gibbs free energy change (ΔG°) at various temperatures.

The estimated thermodynamic parameters for MB adsorption by the mesoporous carbon (A6) are summarized in Table 3.9. The values of the three thermodynamic parameters changed over a narrow range with respect to the change in the equilibrium concentration of the MB solution. The positive values of ΔH° indicate that the adsorption of methylene blue and activated carbon in this work is an endothermic process, in accordance with the increase of MB adsorbed with increasing temperature. In addition, the relatively low enthalpy change (ΔH°) in the range of 8.03–10.98 kJ/mol indicates that the adsorption of MB on the carbon surface occurs by the physisorption process through intermolecular forces (Liu, 2009). Furthermore, the positive adsorption entropy (ΔS°) indicates the affinity of the adsorbate towards the adsorbent which reflects an increase in randomness at the solid/solution interface during the adsorption process. The negative free energy change ($\Delta G^\circ < 0$) indicates a favorable process of adsorption and the spontaneous nature of methylene blue uptake over the temperature range studied.

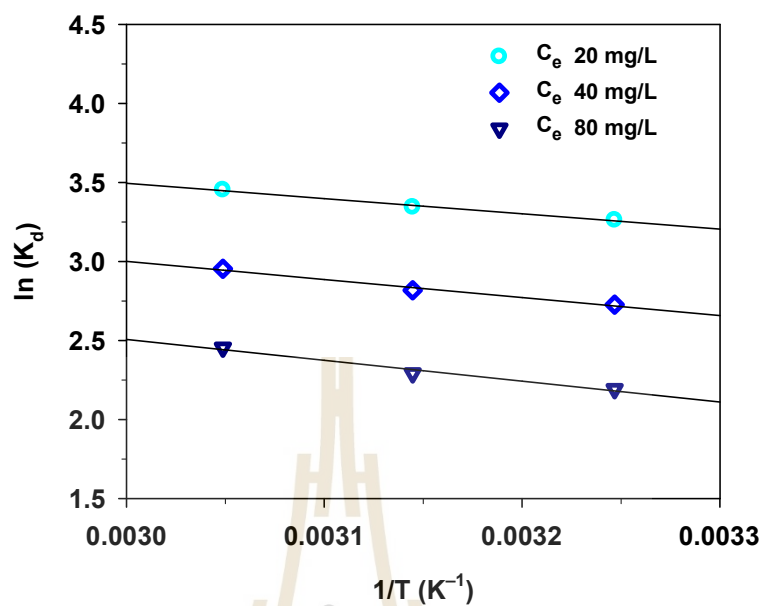


Figure 3.13 The plot of $\ln(K_d)$ versus $1/T$ for MB adsorption onto mesoporous activated carbon (A6).

Table 3.9 Thermodynamic parameters of the MB adsorption on longan seed activated carbon

C_e (mg/L)	ΔH°	ΔS°	ΔG° (kJ/mol)		
	(kJ/mol)	(kJ/(mol·K))	308 K	318 K	328 K
20	8.03	0.0531	-8.35	-6.98	-5.61
40	9.50	0.0535	-8.84	-7.45	-6.06
80	10.98	0.0538	-9.42	-8.05	-6.69

3.6 Conclusions

Microporous and mesoporous activated carbons were produced from longan fruit seeds by the two-step activation and the OTA method, respectively, using carbon dioxide as the activating agent. Micropores of size range 0.65–1.4 nm and the upper mesopore size of 3–4 nm constituted most of the pores in the microporous activated carbons, whereas the mesoporous carbons contained most of the pores in the micropore size of 0.65–1.4 nm and the smaller mesopore size of 2–3 nm. The maximum porous properties of activated carbon, including surface area (1773 m²/g), micropore volume (0.600 cm³/g), mesopore volume (0.474 cm³/g), and the average pore size (2.42 nm) were derived from the mesoporous carbon produced by the three-cycle OTA method. During the transient adsorption of MB from the solution, the amount of MB adsorbed increased proportionally with the increase in time and the carbon surface area. The pseudo-second-order kinetic model was found to provide the best description for the kinetics of MB adsorption, followed by the pore-diffusion model and the pseudo-first-order model, respectively. The rate constants k_1 of the pseudo-first-order model, k_2 of the pseudo-second-order model, and the effective pore diffusivity (D_e) of the pore-diffusion model all increased with the increase in the average pore size, which can be explained by the reduction of mass transfer resistance with increasing pore size. The average pore diffusivity of the mesoporous carbon was found to have a value of 11.8×10^{-7} cm²/s which was about an order of magnitude larger than that of the microporous carbon.

The adsorption isotherms of methylene blue by the microporous and mesoporous carbons are best described by the Redlich-Peterson and Freundlich equations, respectively. The maximum MB adsorption capacity of 1000 mg/g was achieved with the highest surface area of the mesoporous carbon. The initial pH of the MB solution had virtually no effect on the adsorption capacity or the removal efficiency of methylene blue by the activated carbons tested. An increase in the adsorption temperature over the range from 35 to 55°C gave rise to an increase in the amount of MB adsorbed, which was presumably caused by the increase in the diffusion rate of methylene blue molecules to the adsorption sites that provided an increase in the frequency of adsorbent-adsorbate interactions, hence leading to successful adsorption. A thermodynamic analysis of the adsorption revealed that the MB adsorption by longan-seed-based activated carbon is an endothermic, favorable,

and physically adsorbed process. In summary, the high surface area of mesoporous activated carbon prepared from longan seed biomass in this study has been proven to be highly effective for the adsorption of methylene blue from an aqueous solution from the perspective of rapid kinetics and high adsorption equilibrium capacity.

3.7 References

- Adamson, T. A., Adamson, A. W., & Gast, A. P. (1997). *Physical Chemistry of Surfaces, sixth ed.* Wiley-Interscience.
- Altenor, S., Carene, B., Emmanuel, E., Lambert, J., Ehrhardt, J.-J., & Gaspard, S. (2009). Adsorption studies of methylene blue and phenol onto vetiver roots activated carbon prepared by chemical activation. *Journal of Hazardous materials*, 165(1-3), 1029-1039.
- Auta, M., & Hameed, B. H. (2011, 2011/11/15/). Optimized waste tea activated carbon for adsorption of Methylene Blue and Acid Blue 29 dyes using response surface methodology. *Chemical Engineering Journal*, 175, 233-243.
- Azari, A., Nabizadeh, R., Nasser, S., Mahvi, A. H., & Mesdaghinia, A. R. (2020, 2020/07/01/). Comprehensive systematic review and meta-analysis of dyes adsorption by carbon-based adsorbent materials: Classification and analysis of last decade studies. *Chemosphere*, 250, 126238.
- Başar, C. A. (2006, 2006/07/31/). Applicability of the various adsorption models of three dyes adsorption onto activated carbon prepared waste apricot. *Journal of Hazardous materials*, 135(1), 232-241.
- Benadjemia, M., Millière, L., Reinert, L., Benderdouche, N., & Duclaux, L. (2011, 2011/06/01/). Preparation, characterization and Methylene Blue adsorption of phosphoric acid activated carbons from globe artichoke leaves. *Fuel Processing Technology*, 92(6), 1203-1212.

- Bhatnagar, A., Hogland, W., Marques, M., & Sillanpää, M. (2013, 2013/03/01/). An overview of the modification methods of activated carbon for its water treatment applications. *Chemical Engineering Journal*, 219, 499-511.
- Boehm, H. P. (1994, 1994/01/01/). Some aspects of the surface chemistry of carbon blacks and other carbons. *Carbon*, 32(5), 759-769.
- Boehm, H. P. (2002, 2002/02/01/). Surface oxides on carbon and their analysis: a critical assessment. *Carbon*, 40(2), 145-149.
- Brunauer, S., Emmett, P. H., & Teller, E. (1938, 1938/02/01). Adsorption of Gases in Multimolecular Layers. *Journal of the American Chemical Society*, 60(2), 309-319.
- Cazetta, A. L., Vargas, A. M. M., Nogami, E. M., Kunita, M. H., Guilherme, M. R., Martins, A. C., Silva, T. L., Moraes, J. C. G., & Almeida, V. C. (2011, 2011/10/15/). NaOH-activated carbon of high surface area produced from coconut shell: Kinetics and equilibrium studies from the methylene blue adsorption. *Chemical Engineering Journal*, 174(1), 117-125.
- Chandra, T. C., Mirna, M. M., Sudaryanto, Y., & Ismadji, S. (2007, 2007/03/01/). Adsorption of basic dye onto activated carbon prepared from durian shell: Studies of adsorption equilibrium and kinetics. *Chemical Engineering Journal*, 127(1), 121-129.
- Chen, C., Mi, S., Lao, D., Shi, P., Tong, Z., Li, Z., & Hu, H. (2019). Single-step synthesis of eucalyptus sawdust magnetic activated carbon and its adsorption behavior for methylene blue. *RSC Advances*, 9(39), 22248-22262.
- Chen, Y., Zhai, S.-R., Liu, N., Song, Y., An, Q.-D., & Song, X.-W. (2013, 2013/09/01/). Dye removal of activated carbons prepared from NaOH-pretreated rice husks by low-temperature solution-processed carbonization and H₃PO₄ activation. *Bioresource Technology*, 144, 401-409.
- Chen, Y., Zi, F., Hu, X., Yang, P., Ma, Y., Cheng, H., Wang, Q., Qin, X., Liu, Y., Chen, S., & Wang, C. (2020, 2020/01/02/). The use of new modified activated carbon in thiosulfate solution: A green gold recovery technology. *Separation and Purification Technology*, 230, 115834.

- Deng, H., Yang, L., Tao, G., & Dai, J. (2009, 2009/07/30/). Preparation and characterization of activated carbon from cotton stalk by microwave assisted chemical activation—Application in methylene blue adsorption from aqueous solution. *Journal of Hazardous materials*, 166(2), 1514-1521.
- Do, D. D. (1998). Analysis of Adsorption Kinetics in a Single Homogeneous Particle. In *Adsorption Analysis: Equilibria and Kinetics* (Vol. Volume 2, pp. 519-602). Imperial College Press.
- Dotto, G. L., Santos, J. M. N., Rodrigues, I. L., Rosa, R., Pavan, F. A., & Lima, E. C. (2015, 2015/05/15/). Adsorption of Methylene Blue by ultrasonic surface modified chitin. *Journal of Colloid and Interface Science*, 446, 133-140.
- Dubinin, M. M. (1975). Physical Adsorption of Gases and Vapors in Micropores. In D. A. Cadenhead, J. F. Danielli, & M. D. Rosenberg (Eds.), *Progress in Surface and Membrane Science* (Vol. 9, pp. 1-70). Elsevier.
- Dural, M. U., Cavas, L., Papageorgiou, S. K., & Katsaros, F. K. (2011, 2011/03/15/). Methylene blue adsorption on activated carbon prepared from *Posidonia oceanica* (L.) dead leaves: Kinetics and equilibrium studies. *Chemical Engineering Journal*, 168(1), 77-85.
- Faria, P. C. C., Órfão, J. J. M., & Pereira, M. F. R. (2004, 2004/04/01/). Adsorption of anionic and cationic dyes on activated carbons with different surface chemistries. *Water Research*, 38(8), 2043-2052.
- Fogler, H. S. (2016). *Elements of Chemical Reaction Engineering (5th Edition)*. Prentice Hall.
- Foo, K. Y., & Hameed, B. H. (2010, 2010/01/01/). Insights into the modeling of adsorption isotherm systems. *Chemical Engineering Journal*, 156(1), 2-10.
- Foo, K. Y., & Hameed, B. H. (2011, 2011/09/15/). Microwave assisted preparation of activated carbon from pomelo skin for the removal of anionic and cationic dyes. *Chemical Engineering Journal*, 173(2), 385-390.
- Foo, K. Y., & Hameed, B. H. (2012, 2012/01/01/). Preparation, characterization and evaluation of adsorptive properties of orange peel based activated carbon via microwave induced K₂CO₃ activation. *Bioresource Technology*, 104, 679-686.

- Frenudlich, H. M. F. (1906, 1906//). Over the adsorption in solution. *Journal of Physical Chemistry*, 57, 385-471.
- Ghaffar, A., & Younis, M. N. (2015). Interaction and thermodynamics of methylene blue adsorption on oxidized multi-walled carbon nanotubes. *Green Processing and Synthesis*, 4(3), 209-217.
- Ghasemi, J., & Asadpour, S. (2007, 2007/06/01/). Thermodynamics' study of the adsorption process of methylene blue on activated carbon at different ionic strengths. *The Journal of Chemical Thermodynamics*, 39(6), 967-971.
- Giraldo, S., Robles, I., Godínez, L. A., Acelas, N., & Flórez, E. (2021). Experimental and Theoretical Insights on Methylene Blue Removal from Wastewater Using an Adsorbent Obtained from the Residues of the Orange Industry. *Molecules*, 26(15), 4555.
- Gokce, Y., Yaglikci, S., Yagmur, E., Banford, A., & Aktas, Z. (2021, 2021/04/01/). Adsorption behaviour of high performance activated carbon from demineralised low rank coal (Rawdon) for methylene blue and phenol. *Journal of Environmental Chemical Engineering*, 9(2), 104819.
- González-García, P. (2018, 2018/02/01/). Activated carbon from lignocellulosics precursors: A review of the synthesis methods, characterization techniques and applications. *Renewable and Sustainable Energy Reviews*, 82, 1393-1414.
- Graham, D. (1955, 1955/09/01). Characterization of Physical Adsorption Systems. III. The Separate Effects of Pore Size and Surface Acidity upon the Adsorbent Capacities of Activated Carbons. *The Journal of Physical Chemistry*, 59(9), 896-900.
- Heidarinejad, Z., Rahmanian, O., Fazlzadeh, M., & Heidari, M. (2018, 2018/08/15/). Enhancement of methylene blue adsorption onto activated carbon prepared from Date Press Cake by low frequency ultrasound. *Journal of Molecular Liquids*, 264, 591-599.
- Ho, Y. S., & McKay, G. (1998, 1998/06/01/). Sorption of dye from aqueous solution by peat. *Chemical Engineering Journal*, 70(2), 115-124.

- Ho, Y. S., & McKay, G. (1999, 1999/07/01/). Pseudo-second order model for sorption processes. *Process Biochemistry*, 34(5), 451-465.
- Islam, M. A., Ahmed, M. J., Khanday, W. A., Asif, M., & Hameed, B. H. (2017a, 2017/04/01/). Mesoporous activated carbon prepared from NaOH activation of rattan (*Lacosperma secundiflorum*) hydrochar for methylene blue removal. *Ecotoxicology and Environmental Safety*, 138, 279-285.
- Islam, M. A., Ahmed, M. J., Khanday, W. A., Asif, M., & Hameed, B. H. (2017b, 2017/12/01/). Mesoporous activated coconut shell-derived hydrochar prepared via hydrothermal carbonization-NaOH activation for methylene blue adsorption. *Journal of Environmental Management*, 203, 237-244.
- Jawad, A. H., Ramlah Abd, R., Khudzir, I., & Sabar, S. (2017). High surface area mesoporous activated carbon developed from coconut leaf by chemical activation with H₃PO₄ for adsorption of methylene blue. *Desalination and Water Treatment*, 74, 326-335.
- Katheresan, V., Kansedo, J., & Lau, S. Y. (2018, 2018/08/01/). Efficiency of various recent wastewater dye removal methods: A review. *Journal of Environmental Chemical Engineering*, 6(4), 4676-4697.
- Langmuir, I. (1918). The adsorption of gases on plane surfaces of glass, mica and platinum. *Journal of the American Chemical society*, 40(9), 1361-1403.
- Lawtae, P., & Tangsathitkulchai, C. (2021). A New Approach for Controlling Mesoporosity in Activated Carbon by the Consecutive Process of Air Oxidation, Thermal Destruction of Surface Functional Groups, and Carbon Activation (the OTA Method). *Molecules*, 26(9), 2758.
- Lei, S., Miyamoto, J.-i., Kanoh, H., Nakahigashi, Y., & Kaneko, K. (2006, 2006/08/01/). Enhancement of the methylene blue adsorption rate for ultramicroporous carbon fiber by addition of mesopores. *Carbon*, 44(10), 1884-1890.
- Li, X., Zhang, L., Yang, Z., Wang, P., Yan, Y., & Ran, J. (2020, 2020/03/18/). Adsorption materials for volatile organic compounds (VOCs) and the key factors for VOCs adsorption process: A review. *Separation and Purification Technology*, 235, 116213.

- Liu, Y. (2009, 2009/07/09). Is the Free Energy Change of Adsorption Correctly Calculated? *Journal of Chemical & Engineering Data*, 54(7), 1981-1985.
- Lu, G., Nagbanshi, M., Goldau, N., Mendes Jorge, M., Meissner, P., Jahn, A., Mockenhaupt, F. P., & Müller, O. (2018, 2018/04/25). Efficacy and safety of methylene blue in the treatment of malaria: a systematic review. *BMC Medicine*, 16(1), 59.
- Marrakchi, F., Ahmed, M. J., Khanday, W. A., Asif, M., & Hameed, B. H. (2017, 2017/05/01/). Mesoporous-activated carbon prepared from chitosan flakes via single-step sodium hydroxide activation for the adsorption of methylene blue. *International Journal of Biological Macromolecules*, 98, 233-239.
- Marsh, H., & Rodríguez-Reinoso, F. (2006). *Activated carbon*. Elsevier Science Ltd.
- Mashkoo, F., & Nasar, A. (2020, 2020/04/15/). Magsorbents: Potential candidates in wastewater treatment technology – A review on the removal of methylene blue dye. *Journal of Magnetism and Magnetic Materials*, 500, 166408.
- Monser, L., & Adhoum, N. (2002, 2002/03/01/). Modified activated carbon for the removal of copper, zinc, chromium and cyanide from wastewater. *Separation and Purification Technology*, 26(2), 137-146.
- Motejadded Emrooz, H. B., Maleki, M., Rashidi, A., & Shokouhimehr, M. (2021, 2021/06/01). Adsorption mechanism of a cationic dye on a biomass-derived micro- and mesoporous carbon: structural, kinetic, and equilibrium insight. *Biomass Conversion and Biorefinery*, 11(3), 943-954.
- Nasrullah, A., Bhat, A. H., Naeem, A., Isa, M. H., & Danish, M. (2018, 2018/02/01/). High surface area mesoporous activated carbon-alginate beads for efficient removal of methylene blue. *International Journal of Biological Macromolecules*, 107, 1792-1799.
- Nasuha, N., & Hameed, B. H. (2011, 2011/01/15/). Adsorption of methylene blue from aqueous solution onto NaOH-modified rejected tea. *Chemical Engineering Journal*, 166(2), 783-786.

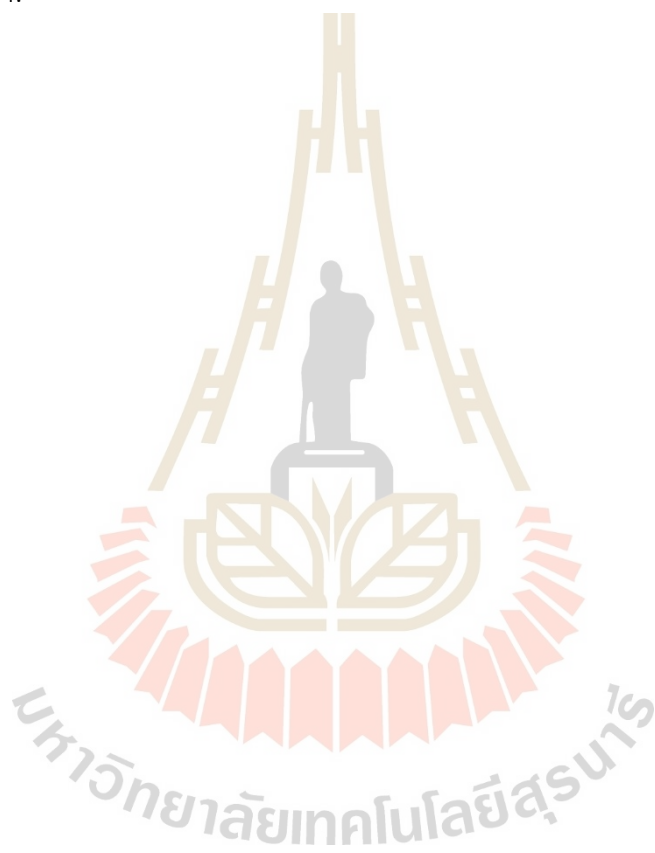
- Nayak, A. K., & Pal, A. (2017, 2017/09/15/). Green and efficient biosorptive removal of methylene blue by *Abelmoschus esculentus* seed: Process optimization and multi-variate modeling. *Journal of Environmental Management*, 200, 145-159.
- Nezhad, M. M., Semnani, A., Tavakkoli, N., & Shirani, M. (2021, 2021/12/01/). Selective and highly efficient removal of uranium from radioactive effluents by activated carbon functionalized with 2-aminobenzoic acid as a new sorbent. *Journal of Environmental Management*, 299, 113587.
- Ocampo-Pérez, R., Leyva-Ramos, R., Sanchez-Polo, M., & Rivera-Utrilla, J. (2013). Role of pore volume and surface diffusion in the adsorption of aromatic compounds on activated carbon. *Adsorption*, 19(5), 945-957.
- Patawat, C., Silakate, K., Chuan-Udom, S., Supanchaiyamat, N., Hunt, A. J., & Ngernyen, Y. (2020). Preparation of activated carbon from *Dipterocarpus alatus* fruit and its application for methylene blue adsorption. *RSC Advances*, 10(36), 21082-21091.
- Phothong, K., Tangsatitkulchai, C., & Lawtae, P. (2021). The Analysis of Pore Development and Formation of Surface Functional Groups in Bamboo-Based Activated Carbon during CO₂ Activation. *Molecules*, 26(18), 5641.
- Radovic, L. R., Silva, I. F., Ume, J. I., Menéndez, J. A., Leon, C. A. L. Y., & Scaroni, A. W. (1997, 1997/01/01/). An experimental and theoretical study of the adsorption of aromatics possessing electron-withdrawing and electron-donating functional groups by chemically modified activated carbons. *Carbon*, 35(9), 1339-1348.
- Rafatullah, M., Sulaiman, O., Hashim, R., & Ahmad, A. (2010, 2010/05/15/). Adsorption of methylene blue on low-cost adsorbents: A review. *Journal of Hazardous materials*, 177(1), 70-80.
- Redlich, O., & Peterson, D. L. (1959, 1959/06/01). A Useful Adsorption Isotherm. *The Journal of Physical Chemistry*, 63(6), 1024-1024.
- Reffas, A., Bernardet, V., David, B., Reinert, L., Lehocine, M. B., Dubois, M., Batisse, N., & Duclaux, L. (2010, 2010/03/15/). Carbons prepared from coffee grounds by H₃PO₄ activation: Characterization and adsorption of methylene blue and Nylosan Red N-2RBL. *Journal of Hazardous materials*, 175(1), 779-788.

- Reid, R. C., Prausnitz, J., & Sherwood, T. K. (1977). *The properties of gases and liquids*. McGraw-Hill.
- Ren, Y., Chen, F., Pan, K., Zhao, Y., Ma, L., & Wei, S. (2021). Studies on Kinetics, Isotherms, Thermodynamics and Adsorption Mechanism of Methylene Blue by N and S Co-Doped Porous Carbon Spheres. *Nanomaterials*, 11(7), 1819.
- Sahu, S., Pahi, S., Tripathy, S., Singh, S. K., Behera, A., Sahu, U. K., & Patel, R. K. (2020, 2020/10/01/). Adsorption of methylene blue on chemically modified lychee seed biochar: Dynamic, equilibrium, and thermodynamic study. *Journal of Molecular Liquids*, 315, 113743.
- Sánchez-Martín, J., González-Velasco, M., Beltrán-Heredia, J., Gragera-Carvajal, J., & Salguero-Fernández, J. (2010, 2010/02/15/). Novel tannin-based adsorbent in removing cationic dye (Methylene Blue) from aqueous solution. Kinetics and equilibrium studies. *Journal of Hazardous materials*, 174(1), 9-16.
- Santoso, E., Ediaty, R., Kusumawati, Y., Bahruji, H., Sulistiono, D. O., & Prasetyoko, D. (2020, 2020/06/01/). Review on recent advances of carbon based adsorbent for methylene blue removal from waste water. *Materials Today Chemistry*, 16, 100233.
- Saygılı, H., & Güzel, F. (2016, 2016/02/01/). High surface area mesoporous activated carbon from tomato processing solid waste by zinc chloride activation: process optimization, characterization and dyes adsorption. *Journal of Cleaner Production*, 113, 995-1004.
- Tangsathitkulchai, C., Naksusuk, S., Wongkoblap, A., Phadungbut, P., & Borisut, P. (2021). Equilibrium and Kinetics of CO₂ Adsorption by Coconut Shell Activated Carbon Impregnated with Sodium Hydroxide. *Processes*, 9(2), 201.
- Thabede, P. M., Shooto, N. D., & Naidoo, E. B. (2020). Removal of methylene blue dye and lead ions from aqueous solution using activated carbon from black cumin seeds. *South African Journal of Chemical Engineering*, 33(1), 39-50.
- Theydan, S. K., & Ahmed, M. J. (2012, 2012/09/01/). Adsorption of methylene blue onto biomass-based activated carbon by FeCl₃ activation: Equilibrium, kinetics, and thermodynamic studies. *Journal of Analytical and Applied Pyrolysis*, 97, 116-122.

- Tkaczyk, A., Mitrowska, K., & Posyniak, A. (2020, 2020/05/15/). Synthetic organic dyes as contaminants of the aquatic environment and their implications for ecosystems: A review. *Science of the Total Environment*, 717, 137222.
- Tseng, R.-L., Wu, F.-C., & Juang, R.-S. (2003, 2003/01/01/). Liquid-phase adsorption of dyes and phenols using pinewood-based activated carbons. *Carbon*, 41(3), 487-495.
- Vargas, A. M. M., Cazetta, A. L., Kunita, M. H., Silva, T. L., & Almeida, V. C. (2011, 2011/04/01/). Adsorption of methylene blue on activated carbon produced from flamboyant pods (*Delonix regia*): Study of adsorption isotherms and kinetic models. *Chemical Engineering Journal*, 168(2), 722-730.
- Wang, J., Sun, C., Lin, B.-C., Huang, Q.-X., Ma, Z.-Y., Chi, Y., & Yan, J.-H. (2018, 2018/03/01/). Micro- and mesoporous-enriched carbon materials prepared from a mixture of petroleum-derived oily sludge and biomass. *Fuel Processing Technology*, 171, 140-147.
- Wang, P., Cao, M., Wang, C., Ao, Y., Hou, J., & Qian, J. (2014, 2014/01/30/). Kinetics and thermodynamics of adsorption of methylene blue by a magnetic graphene-carbon nanotube composite. *Applied Surface Science*, 290, 116-124.
- Williams, N. E., & Aydinlik, N. P. (2021, 2021/08/03). KOH ratio effect, characterization, and kinetic modeling of methylene blue from aqueous medium using activated carbon from *Thevetia peruviana* shell. *Chemical Engineering Communications*, 208(8), 1189-1208.
- Wu, K.-T., Wu, P.-H., Wu, F.-C., Jheng, R.-L., & Juang, R.-S. (2013, 2013/04/01/). A novel approach to characterizing liquid-phase adsorption on highly porous activated carbons using the Toth equation. *Chemical Engineering Journal*, 221, 373-381.
- Yagub, M. T., Sen, T. K., Afroze, S., & Ang, H. M. (2014, 2014/07/01/). Dye and its removal from aqueous solution by adsorption: A review. *Advances in Colloid and Interface Science*, 209, 172-184.
- Yao, Y., Xu, F., Chen, M., Xu, Z., & Zhu, Z. (2010, 2010/05/01/). Adsorption behavior of methylene blue on carbon nanotubes. *Bioresource Technology*, 101(9), 3040-3046.

Yu, L., & Luo, Y.-m. (2014, 2014/03/01/). The adsorption mechanism of anionic and cationic dyes by Jerusalem artichoke stalk-based mesoporous activated carbon. *Journal of Environmental Chemical Engineering*, 2(1), 220-229.

Zhang, Z., Xu, L., Liu, Y., Feng, R., Zou, T., Zhang, Y., Kang, Y., & Zhou, P. (2021, 2021/02/01/). Efficient removal of methylene blue using the mesoporous activated carbon obtained from mangosteen peel wastes: Kinetic, equilibrium, and thermodynamic studies. *Microporous and Mesoporous Materials*, 315, 110904.



CHAPTER IV

ANALYSIS OF GAS ADSORPTION AND PORE DEVELOPMENT IN ACTIVATED CARBON BASED ON SURFACE DEFECT MODEL

4.1 Abstract

This study aimed to investigate the adsorption of N_2 and CO_2 and pore development in microporous-mesoporous activated carbon from longan seed prepared by the OTA method, using the GCMC simulation approach plus a surface defect model. The analysis of N_2 adsorption isotherms at 77 K and CO_2 adsorption isotherms at 273 K on the perfective (defect-free) surfaces revealed that the adsorption took place by a pore-filling mechanism with a single layer for a pore width of less than 0.85 nm. Capillary condensation was observed for N_2 adsorption in pore widths larger than 1.7 nm, while this phenomenon was not observed for CO_2 adsorption. As compared to the adsorption on the perfective surfaces, the adsorption on defective surfaces showed a decrease in the adsorbed density for defect sizes smaller than 0.246 nm but with an increase for larger defect sizes. The pore size distribution (PSD) obtained from N_2 and CO_2 adsorption isotherms indicated that the activated carbon samples consisted mainly of micropores and small mesopores with a multimodal size distribution covering the pore size range from 0.65 to 4 nm. With increasing carbon porous properties, the computed PSD showed a decrease in the volume of micropores (0.65–1.4 nm) and an increase in the volume of supermicropores (1.4–2 nm) and small mesopores (2–3 nm). It was also found that the development of mesopores in microporous-mesoporous activated carbon from longan seed biomass during the course of CO_2 gasification was the result of the coalescence of adjacent micropores and the widening of micropores due to the gasification reaction.

4.2 Introduction

Activated carbon is a highly versatile adsorbent used extensively in industrial separation and purification processes (Bansal & Goyal, 2005), owing to its remarkably large surface area, and large amounts of micropores and mesopores (Marsh & Rodríguez-Reinoso, 2006). In order to increase its use in various applications, there is a need to develop an activated carbon synthesis process that can tailor the desired proportional amounts of micropores and mesopores (Bakar et al., 2021; Wang et al., 2022). Recently, a modified physical activation method with CO₂, being named the Oxidation, Thermal treatment, and Activation method (the OTA method), has been proposed for the synthesis of microporous-mesoporous activated carbon (Lawtae & Tangsathitkulchai, 2021a). This innovative preparation method involves two consecutive steps of air oxidation and thermal destruction of the already formed surface functional groups prior to activation with CO₂, hence producing highly porous activated carbons with higher proportional amounts of mesopore volume as compared to the conventional two-step activation method. The microporous-mesoporous activated carbon produced from longan seed biomass has demonstrated excellent performance in removing methylene blue dye from an aqueous solution, both in terms of adsorption capacity and removal efficiency (Lawtae & Tangsathitkulchai, 2021b). By its ability in tailoring the pore size distribution of activated carbon, the OTA method has shown great promise for the development of advanced materials with enhanced adsorption properties for diverse applications.

To assist the understanding of pore development in this special activated carbon for its wider applications, it is necessary to be able to characterize and predict the pore size distributions of the carbon adsorbent. In general, gas adsorption is the most widely used method for the characterization of porous adsorbents (Liu & Chen, 2014; Sing, 1989). N₂ gas (Kruk & Jaroniec, 2002) and Ar gas (Dombrowski et al., 2000) are generally used as probe molecules at their boiling points because under this condition the condensation pressure is an explicit function of the pore size (Thommes et al., 2015). In addition, CO₂ adsorption is also used specifically for probing the narrowest micropores at experimentally measurable pressures (Ravikovitch et al., 2000). Moreover, CO₂ has the potential to be an effective probe molecule as it has a faster diffusion rate and better infiltration in micropores at a near ambient temperature (Garrido et al., 1987). Thus, CO₂ is also used as a probe

molecule to monitor the pore development of microporous materials, especially activated carbon.

The Monte Carlo (MC) simulation in the grand canonical (GC) ensemble is currently regarded as an effective tool for studying adsorption behavior and calculating pore size distributions in microporous and mesoporous materials (Ohba & Kaneko, 2001; Pantatosaki et al., 2004; Sitprasert et al., 2013). There have been several studies comparing the pore size distributions (PSD) achieved by the MC simulation and the density functional theory (DFT) (D.D. Do & H.D. Do, 2003) as well as the non-local density functional theory (NLDFT) (Ravikovitch et al., 2000; Vishnyakov et al., 1999). In addition, the MC simulation was applied to obtain PSD of activated carbons based on the slit and mixed geometries for the solid model and Lennard-Jones models for N₂ and CO₂ (Toso et al., 2011), and more recently N₂, CO₂, and Ar have been applied for the characterization of micro-mesoporous carbons (Dantas et al., 2021). Overall, the estimation of PSD for activated carbon by the Monte Carlo simulation is well accepted and widely used by a number of investigators (Alexandre De Oliveira et al., 2013; Azevedo et al., 2010; Kohmuean et al., 2021; Phothong et al., 2021; Samios et al., 1997; Tangsatitkulchai et al., 2021). Normally, activated carbon structure is modeled as graphene sheets with a finite length (Wongkoblak et al., 2005) which contain functional groups and morphological defects on the basal graphene layers (Do, 1998). Therefore, a carbon pore of finite length and carbon surfaces as graphene layers which consists of carbon atoms arranged in a hexagonal pattern (Wongkoblak & Do, 2006; Wongkoblak et al., 2005), as well as the presence of surface defects were adopted in this study for simulating the adsorption behavior of the microporous-mesoporous activated carbon prepared by the OTA method. In general, high-pressure isotherm experiments can provide the adsorption capacity for most pores, whereas the structural properties such as specific surface area, pore size distribution, micropore volume, and mesopore volume are usually evaluated via the adsorption tests at low-pressures (< 10 bars) (Klewiah et al., 2020). However, to determine the micropore-mesopore size distributions in activated carbons, CO₂ adsorption at 273 K (0°C) and at pressures up to the saturation pressure was adopted in the present study.

Therefore, this study aims to investigate, through GCMC simulation, the gas adsorption behavior of activated carbon on both defect-free and defective surfaces

and to examine the pore development of micro-mesoporous activated carbon by analyzing the derived pore size distributions. We also evaluate specifically the effect of the OTA preparation method on mesopore development and the corresponding strength of adsorption sites, as indicated by the isosteric heat of adsorption. The findings of this study will certainly contribute to a better understanding of the adsorption properties of activated carbon with real heterogeneous carbon surfaces, which should have important implications for various applications in the field of adsorption.

4.3 Experimental Procedure

The microporous-mesoporous activated carbons were specially prepared by the so-called OTA method. Details of this preparation method follow those reported in Chapter II. In brief, 15 g of activated carbon produced by a two-step CO₂ activation at 850°C for 1 h in a vertical tube furnace (CTF 12, Carbolite, Staffordshire, UK) were oxidized in a quartz tube reactor by heating the activated carbon from room temperature in a stream of air (100 cm³/min) to the required oxidation temperature of 230°C and held at this temperature for 12 h. The purpose of this step was to create additional oxygen functional groups on the carbon surfaces. Then, the oxidized carbon was heated at 950°C for 2 h under N₂ gas flowing at the rate of 100 cm³/min to remove most of the surface functional groups, thus giving increasing surface reactivity caused by chemical bond disruption of the functional groups. After that, the sample was activated again with CO₂ at 850°C for another 1 h. This process completed the first cycle of the OTA preparation method. In this study, a total of three cycles for the OTA method were performed, giving carbon samples designated as AC1, AC2, and AC3. The experimental isotherms of CO₂ for the tested activated carbons were measured at 273 K (0°C) with a pressure ranging from 0.01 to 35 bars by using a High-Pressure Volumetric Analyzer (HPVA II, Micromeritics, Norcross, GA, USA). Before starting the measurement, the sample was degassed at 300°C for 16 h under a high vacuum (< 0.1 mbar) to eliminate any physisorbed substances on the carbon adsorbent. The high and low-pressure transducers of the equipment provide a reading accuracy of ±0.04% and ±0.15%, respectively. The static volumetric method was used to calculate the CO₂ adsorption capacity. The dual free-space measurements and correction for nonideality of the analysis gas were used to

enhance the accuracy of the isotherm data. Porous properties of the derived activated carbons were determined from the adsorption isotherms of N₂ at 77 K (−196°C) measured by using a high-performance adsorption analyzer (ASAP 2010, Micromeritics, Norcross, GA, USA). The BET-specific surface area (S_{BET}) was calculated from the N₂ adsorption isotherm data by applying the Brunauer-Emmett-Teller (BET) equation (Brunauer et al., 1938). The total pore volume (V_{T}) was estimated from the volume of N₂ adsorbed at the relative pressure (P/P_0) of 0.98 and converted to the volume of N₂ in the liquid state at 77 K (−196°C). Micropore volume (V_{mi}) was determined by applying the Dubinin-Radushkevich (DR) equation (Dubinin, 1975). The mesopore volume (V_{me}) was estimated by subtracting the micropore volume from the total pore volume. The Monte Carlo (MC) simulation in the grand canonical (GC) ensemble was applied to compute the pore size distribution of the derived activated carbon using the N₂ and CO₂ adsorption isotherm data.

4.4 Simulation Model

4.4.1 Fluid-Fluid Models and the Interaction Energy (U_{FF})

In this study, N₂ gas is modeled as a single Lennard-Jones (LJ) site (Ravikovitch et al., 2000) while CO₂ is modeled as a 3-center LJ molecule with fixed partial charges (Harris & Yung, 1995). The molecular parameters are listed in Table 5.1. The dispersive potential energy of interaction between a site “ a ” on molecule “ i ” with a site “ b ” on molecule “ j ” was calculated using Equation (4.1), which follows the Lennard-Jones 12-6 equation (Lennard-Jones, 1931, 1932):

$$U_{i,j}^{a,b} = \sum_{a=1}^A \sum_{b=1}^B 4\epsilon_{i,j}^{a,b} \left[\left(\frac{\sigma_{i,j}^{a,b}}{r_{i,j}^{a,b}} \right)^{12} - \left(\frac{\sigma_{i,j}^{a,b}}{r_{i,j}^{a,b}} \right)^6 \right] \quad (4.1)$$

where $r_{i,j}^{a,b}$ is the separation distance between a site “ a ” on molecule “ i ” and a site “ b ” on molecule “ j ”, while $\sigma_{i,j}^{a,b}$ and $\epsilon_{i,j}^{a,b}$ are the cross collision diameter and cross well-depth of the interaction energy, which can be calculated with the Lorentz (Lorentz, 1881) and Berthelot (Berthelot, 1898) (LB) mixing rules.

For a molecule with a number of dispersive sites and fixed partial charges, the interaction energy is the summation of LJ interactions and the

electrostatic energy which was calculated with Coulomb's law (Tipler, 1999) as shown in Equations (4.2) and (4.3), respectively.

$$U_{FF} = U_{LJ} + U_q \quad (4.2)$$

$$U_{q,i,j}^{\alpha,\beta} = \sum_{\alpha=1}^{M_q} \sum_{\beta=1}^{M_q} \frac{1}{4\pi\epsilon_0} \frac{q_i^\alpha q_j^\beta}{r_{i,j}^{\alpha,\beta}} \quad (4.3)$$

where ϵ_0 is the permittivity of free space, $r_{i,j}^{\alpha,\beta}$ is the separation distance between two charges, α and β on molecules "i" and "j", respectively. q_i^α and q_j^β are the number of charges α on molecule "i" and the number of charges β on molecule "j", respectively. M_q is the number of charges on the molecule.

Table 4.1 Molecular parameters used in the GCMC simulation computation

Type	Interacting site	Energy	Collision	Atomic
		well depth (ϵ/k_B), K	diameter (σ), nm	charge (q), e^-
Carbon atom	C	28.0	0.34	0
N ₂ (Spherical model)	N ₂	101.5	0.3615	0
CO ₂ (Multi-site model)	C	28.129	0.2757	+0.6512
	O	80.507	0.3033	-0.3256

4.4.2 Solid-Fluid (U_{SF}) Potential Model

The potential energy between an LJ site of the molecules "i" and the homogeneous flat solid substrate with a separation distance of z_i of an infinite extent was determined by using Equation (4.4), which is the Steele 10-4-3 equation (Steele, 1978):

$$U_{i,s} = 2\pi\rho_s \epsilon_{sf} \left[\frac{2}{5} \left(\frac{\sigma_{sf}}{z_i} \right)^{10} - \left(\frac{\sigma_{sf}}{z_i} \right)^4 - \frac{\sigma_{sf}^4}{3\Delta(0.61\Delta + z_i)^3} \right] \quad (4.4)$$

where ρ_s is the surface carbon atom density of a graphene layer (38.2 nm^{-2}) and the interspacing distance between two graphene layers, (Δ) is 0.3354 nm. The reduced well-depth of a carbon atom, $\mathcal{E}_{ss}/k_B = 28\text{K}$, and the collision diameter of a carbon atom, $\sigma_{ss} = 0.34 \text{ nm}$. While the cross parameters, \mathcal{E}_{sf} and σ_{sf} were calculated via LB mixing rules using Equations (4.5) and (4.6), respectively.

$$\mathcal{E}_{sf} = \left(\mathcal{E}_{ss} \mathcal{E}_{ff} \right)^{1/2} \quad (4.5)$$

$$\sigma_{sf} = \left(\sigma_{ss} + \sigma_{ff} \right) / 2 \quad (4.6)$$

The dimensions of the simulation box were 6.0 nm in the x- and y-directions. We assumed that the top and the bottom of the simulation box form the two walls of the slit pore, and each wall consists of three graphene layers. These layers are stacked on top of each other with an interlayer spacing of 0.3354 nm. The pore width (H) of this slit pore model is defined as the distance between a plane passing through all carbon atom centers of the outermost layer of one wall and the corresponding plane of the opposite wall.

In this study, a model of surface defect is used to investigate the effects of the defect (surface heterogeneity) on the adsorption isotherms. The defects are constructed by first removing carbon atoms randomly from both pore walls to form a small pit, and next removing carbon atoms in the region covered by a circle of an effective radius (R_c) as shown in Figure 4.1. It should be noted that the defect pits could overlap with neighboring pits because the carbon atoms were randomly selected. The two important parameters for modeling an activated carbon surface are the percentage of the defect area and the size of the defect which is measured by the effective radius (Do & Do, 2006). In studying the effect of defect size, the effective radius (R_c) was varied from 0.246 to 0.615 nm holding a constant defect area of 30% of the total surface area. Moreover, to investigate the degree of surface defect, the defect area was varied from 15 to 45%. The R_c value of 0.246 nm was chosen based on the distance from a carbon atom to the adjacent carbon atom, as determined by the structure of hexagonal graphite with trigonal planar bonding within the graphene layers.

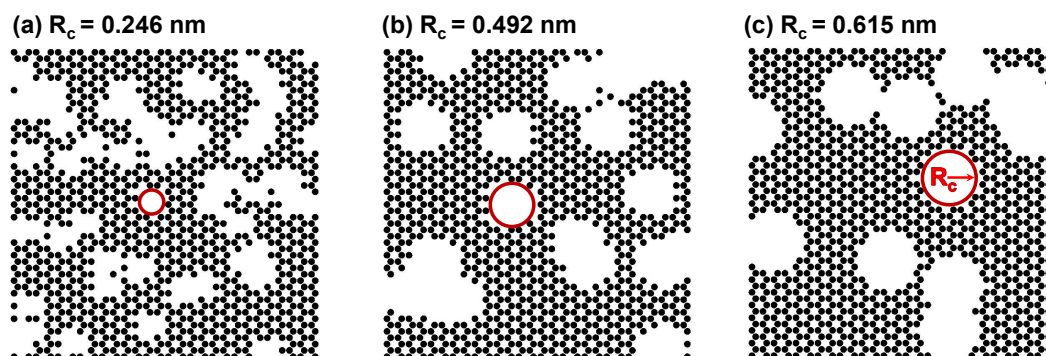


Figure 4.1 Solid configuration of one graphene layer with percentage defects of 30 % and the effective radius (R_c) of (a) 0.246 nm, (b) 0.492 nm, and (c) 0.615 nm. The black spheres represent carbon atoms of the graphene layer and the spaces represent the defect area.

4.4.3 The Computer Simulation for Determining Pore Size Distribution

The N_2 and CO_2 adsorption isotherms in the slit pores at 77 K (-196°C) and 273 K (0°C), respectively, were simulated over the same pressure range as the experimental adsorption isotherms. The pore widths (H) were varied from 0.65 to 4.0 nm which covered the micropore and mesopore size range in activated carbons, and a total of 39 local isotherms were then calculated. The calculation procedure of the Monte Carlo (MC) simulation (Metropolis et al., 1953; Metropolis & Ulam, 1949) in the grand canonical (GC) ensemble (Frenkel & Smit, 2001) is as follows. The volume of the simulation box, the chemical potential, and the temperature of the system were first specified to compute the adsorption equilibrium. For a simulation cycle used in this work, we provided an equal probability for displacement move, insertion, and deletion of the fluid molecules, which consists of 1000 steps. For an adsorption branch of the isotherm, 30000 cycles were executed for the system to reach equilibrium, resulting in 30 million configurations in the equilibration stage, and the same number of cycles were used to average the results in the sampling stage. In the equilibration stage, the maximum displacement length was initially set as half of the largest dimension of the simulation box and was adjusted at the end of each cycle to give an acceptance ratio of 20% (Mountain & Thirumalai, 1994) and kept constant in the sampling stage. For each point on the adsorption branch, we used an

empty box as the initial configuration, and the simulation was carried out until the number of particles in the box no longer changed. The pressure of the bulk gas at a given temperature corresponding to a given chemical potential was calculated from the equation of state (EoS) proposed by Johnson et al. (Johnson et al., 1993). Periodic boundary conditions (PBC) were applied in the x- and y-directions. The cut-off radius was chosen to be five times that of the first collision diameter of the concerning fluid.

In the simulation, the amount of pore density is related to the accessible volume of the simulation box and the number of particles in the box. The method to determine the accessible volume was proposed by Do and Do (Do & Do, 2007). The excess pore density is calculated by Equation (4.7).

$$\rho_{\text{ex}} = \frac{\langle N \rangle - \rho_g V_{\text{acc}}}{V_{\text{acc}}} \quad (4.7)$$

where $\langle N \rangle$ is the ensemble average of the molecules in the simulation box, ρ_g is the gas density of the box, calculated via EoS and V_{acc} is the accessible volume of the box.

Another important thermodynamics output from the simulation is the isosteric heat of adsorption. The definition of isosteric heat is the amount of heat released per unit mass of adsorbed molecules at a constant temperature and adsorption loading. The heat of adsorption consists of the interaction energy between fluid-fluid (FF) and solid-fluid (SF) interactions. This information is very useful since the heat of adsorption is related to the heterogeneity of the solid substrate, which can be used to characterize the solid adsorbent and to understand the adsorption mechanisms. Experimentally, the heat of adsorption can be obtained using a thermopile by direct measurement of the heat flux through the adsorption cell wall (Sircar et al., 1999). While in the simulation, the isosteric heat of adsorption can be estimated via the fluctuation theory (Nicholson & Parsonage, 1982), employing Equation (4.8) as follows:

$$q_{\text{st}} = \frac{\langle U \rangle \langle N \rangle - \langle UN \rangle}{\langle N^2 \rangle - \langle N \rangle \langle N \rangle} + k_B T \quad (4.8)$$

where $\langle \rangle$ is the ensemble average, U is the sum of potential energy in the system and N is the number of molecules in the system. k_B is the Boltzmann constant and, T is the temperature of the system.

To determine the pore size distribution of activated carbon, the experimental adsorption isotherms were fitted with the local isotherms generated by the models using the Solver program in Microsoft Excel by minimizing the sum of squared errors between the experimental and simulated isotherms. The goodness of fit was assessed based on two criteria: the regression coefficient (R^2) and the normalized standard deviation (ΔV) which is defined by Equation (4.9). A higher value of R^2 and a lower value of ΔV indicate a better fit between the experimental and simulated isotherms. The derived pore size distributions (PSD) of activated carbon were presented as the relationship between the differential pore volume per unit pore width and the average pore width.

$$\Delta V (\%) = 100 \times \sqrt{\frac{\sum [(V_{\text{exp}} - V_{\text{cal}}) / V_{\text{exp}}]^2}{N - 1}} \quad (4.9)$$

where the V_{exp} and V_{cal} are the experimental and calculated values, respectively, and N is the number of data points.

4.5 Results and Discussion

4.5.1 N₂ Adsorption Isotherms

Figure 4.2 shows the N₂ adsorption isotherms at 77 K for the three activated carbons (AC1, AC2, and AC3) that were prepared via the OTA method, and Table 4.2 presents their corresponding porous properties. The N₂ adsorption isotherms of the three activated carbons exhibited Type IV isotherm according to the IUPAC classification (Thommes et al., 2015), which is typical of monolayer-multilayer adsorption. As the number of OTA cycles increased from cycle 1 to cycle 3, both the amount of adsorbed gas and the size of the hysteresis loop increased, which implies the progressive development of mesopores with a distribution of pore sizes. Table 4.2 shows that the preparation of activated carbon from longan seed biomass by the OTA method provided a relatively large BET surface area and total pore volume. As the number of the OTA cycle increased (samples AC1 to AC3), the surface area,

micropore volume, mesopore volume, and average pore size increased progressively. This increase in the carbon porous properties was the result of the increase in the number of reaction sites caused by the increasing bond disruption at a high gasification temperature of functional groups formed during the oxidation step of the OTA preparation method. The increase in the amounts of mesopores is possibly attributed to the mechanism of micropore enlargement by gasification and coalescence of micropores. As seen also from Table 4.2 that there was a tendency for the volume percent of micropores to decrease and that of mesopores to increase from samples AC1 to AC3.

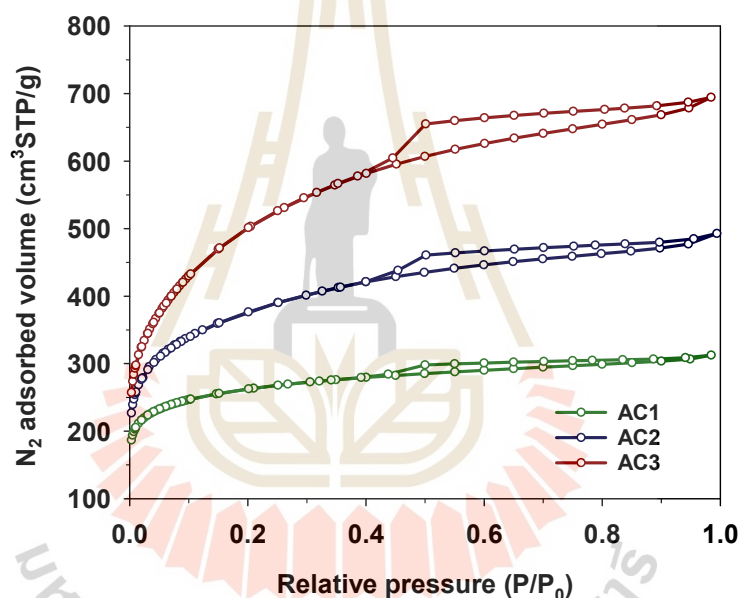


Figure 4.2 N_2 adsorption isotherms at 77 K of the three samples of microporous-mesoporous activated carbon (AC1, AC2, and AC3).

Table 4.2 Porous properties and percent char burn-off of the tested activated carbon

Sample	V_{mi}	V_{me}	V_T	S_{BET}	D_{av}	Burn-off
name	(cm^3/g) (%)	(cm^3/g) (%)	(cm^3/g)	(m^2/g)	(nm)	(%)
AC1	0.375 (78.1)	0.105 (21.9)	0.480	980	1.96	46.10
AC2	0.466 (63.3)	0.270 (36.7)	0.736	1,271	2.32	62.10
AC3	0.600 (55.9)	0.474 (44.1)	1.074	1,773	2.42	78.40

4.5.2 CO₂ Adsorption Isotherms

The CO₂ adsorption isotherms at 273 K of AC1, AC2, and AC3 are presented in Figure 4.3. The measured excess adsorbed amounts of CO₂ at high pressures up to the saturation pressure (34.85 bars) are shown in Figure 4.3a. As the pressure increased, the excess adsorbed amount increased continuously and reached the maximum at a relative pressure (P/P_0) around 0.40 and then declined continuously at higher pressures. Similar results were also observed in previous works for CO₂ adsorption at high pressures for activated carbon and other porous materials (Wang & Long, 2020; Zhang et al., 2018; Zhou et al., 2003; Zhou & Zhou, 2009). These trends can be attributed to the relationship between the excess adsorption capacity (V_{ex}) and the absolute adsorption capacity (V_{ab}) as presented later in Equation (4.11). At low pressures, bulk gas density (ρ_{bulk}) is much smaller than the adsorbed phase density (ρ_{ads}), thus V_{ex} is nearly the same as V_{ab} . In other words, the difference between the excess and the absolute adsorption quantities can be neglected. As the pressure increases, the bulk phase density increases rapidly as compared with the adsorbed phase density. The difference between these two quantities then becomes obvious ($V_{ex} < V_{ab}$) and CO₂ enters the supercritical or liquid state, thus making V_{ex} to exhibit a downward trend (Zhang et al., 2018).

However, the measured excess adsorbed amounts are usually converted to absolute amounts (Wang & Long, 2020), which are needed for practical applications. As for gas adsorption data measured by the high-pressure adsorption unit (HPVA II), the Langmuir equation has been popularly used to fit the experimental isotherm data due to its simplicity and accuracy (Ekundayo & Rezaee, 2019a, 2019b; Zhang et al., 2015; Zou et al., 2017). Therefore, the Langmuir model (Langmuir, 1918) was adopted and used in the present study. The derivation of this model is based on the molecular dynamic equilibrium of the adsorption rate and desorption rate of an adsorbate gas, where the adsorbate is represented as a monolayer-adsorbed phase on the surface of the adsorbent. The classic form of the Langmuir model can be expressed by Equation (4.10):

$$V_{ab} = \frac{V_L P}{P_L + P} \quad (4.10)$$

where V_{ab} is the absolute adsorption capacity, P is the gas equilibrium pressure, V_L and P_L are known as Langmuir constants where V_L is the maximum absolute adsorption capacity and P_L is the gas equilibrium pressure at half of V_L . The absolute adsorption capacity (V_{ab}) is related to the excess adsorption capacity (V_{ex}) by the following equation (D. D. Do & H. D. Do, 2003).

$$V_{ex} = V_{ab} \left(1 - \frac{\rho_{bulk}}{\rho_{ads}} \right) \quad (4.11)$$

Substituting Equation (4.11) into Equation (4.10) gives Equation (4.12) which is the final form for determining the excess adsorption capacity (V_{ex}).

$$V_{ex} = \frac{V_L P}{P_L + P} \left(1 - \frac{\rho_{bulk}}{\rho_{ads}} \right) \quad (4.12)$$

where ρ_{bulk} is the bulk density of the free gas phase, ρ_{ads} is the adsorbed gas phase density. Equation (4.12) was used in this work to model adsorption isotherms of CO_2 on tested three carbons. The 3-parameters Langmuir model (V_L , P_L , and ρ_{ads}) was used for non-linear curve fitting with each parameter bounded to $(0, +\infty)$. The adsorbed gas-phase density was assumed to be pressure-independent (Ekundayo & Rezaee, 2019a, 2019b).

Figure 4.3b shows the absolute adsorbed amounts of CO_2 at 273 K on AC1, AC2, and AC3. The fitting of the excess adsorption isotherms, which yielded the absolute adsorption isotherms, is shown in Figure 4.3a using Equation (4.12). Based on visual observation of Figure 4.3a, this model appeared to agree well with the measured excess adsorbed amounts. The statistical analysis indicated that the sum of the squared estimate of errors (SSE) between the experimental and the computed values is less than 0.001, and the value of R^2 was greater than 0.999 for all carbon samples. Therefore, it can be inferred that the absolute adsorbed amounts of CO_2 at 273 K can be employed to characterize the porous properties of the tested activated carbons. As illustrated, the CO_2 adsorption of each sample at relative pressures lower than 0.05 is almost indistinguishable for both the excess and the absolute adsorbed amount. This suggests that CO_2 adsorption at low pressures is insensitive to the different porous properties of the three activated carbons. Only a quarter of the total

pore volume is filled by CO₂ at low pressure, which can be attributed to the narrow micropore filling (Ravikovitch et al., 2000). However, as the pressure increased, the amount of CO₂ adsorbed increased dramatically, corresponding to the filling of micropores and narrow mesopores. This indicates that the surface area and proportion of micropores and mesopores play a crucial role in the adsorption of CO₂ at high pressures.

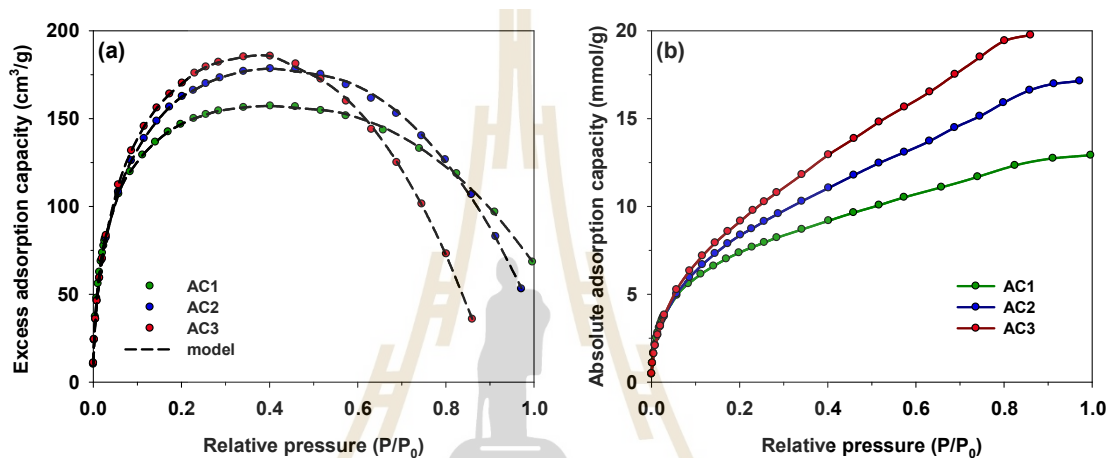


Figure 4.3 CO₂ adsorption isotherms at 273 K for (a) excess adsorption capacity and (b) absolute adsorbed amount in a microporous-mesoporous activated carbon.

4.5.3 Adsorption Isotherms of the Perfective Surface

Figures 4.4a and 4.4b show, respectively, the simulated isotherms for N₂ adsorption at 77 K and CO₂ adsorption at 273 K in carbon slit pores of various pore widths from 0.65 to 4 nm. A total of 39 simulation points for each isotherm at relative pressures (P/P_0) varying from 10^{-4} to 1 were computed. From the shape of the isotherm curves, both N₂ and CO₂ isotherms showed the continuous pore filling of a single layer in a pore width of less than 0.85 nm, for which the packing effect led to the difference in the maximum density for each pore size. The highest pore density for the pore size of 0.65 nm is due to the ability of the adsorbate to tightly fit inside the pore as a single layer. Furthermore, the capillary condensation was observed for N₂ adsorbed for a pore width larger than 1.7 nm as shown in Figure

4.4a, while this behavior is absent for CO₂ adsorption isotherms. This effect is due to the reason that the 3-center LJ model for CO₂ could form a less dense packing, while the spherical molecule of N₂ could form a denser structure (Ravikovitch et al., 2000).

However, the actual surface of activated carbon is not perfect but contains many defects due to the removal of carbon atoms during gasification by CO₂ as well as the defects caused by bond disruption of a number of surface functional groups at a high gasification temperature. In other words, the activated carbon surface is highly heterogeneous containing a number of active reaction sites with a distribution of chemical reactivity for the gasification reaction. In the following sections, the role of defective surfaces in the adsorption of N₂ by simulation is presented and discussed.

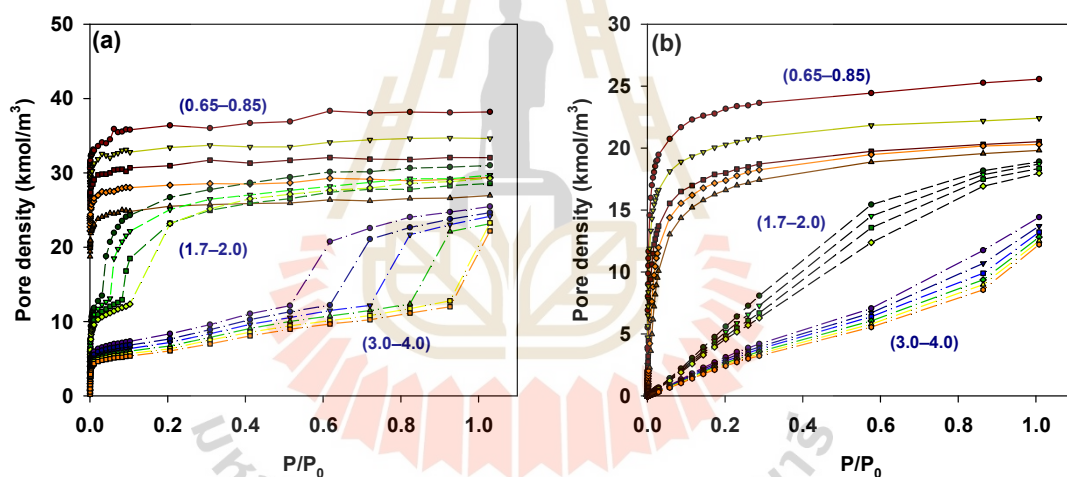


Figure 4.4 Simulated adsorption isotherms of (a) N₂ at 77 K and (b) CO₂ at 273 K in carbon slit pores.

4.5.4 Effect of Defect Size

To study the effect of surface heterogeneity on gas adsorption, a defective surface model was utilized. The study was made by varying the effective radius (R_c) from 0.246 to 0.615 nm maintaining a fixed defect area of 30%. This choice of defect area percentage was adopted from a similar study reported in the previous work (Wongkoblap & Do, 2007). The 30% defect area also coincided with the burn-off value of the initial activated carbon prior to the application of the OTA method. In

fact, any reasonable value of defect area, as long as it is not extremely high, can be used to investigate the effect of defect size on adsorption isotherms. First, we compared the simulated N_2 adsorption isotherms at 77 K for the effective radius of 0.246 nm and 0.492 nm with pore widths varying from 0.65 to 4 nm and presented the results in Figure 4.5. The isotherms showed a similar shape to those of the perfective surface (Figure 4.4a), with the same pattern of continuous pore filling for pore widths of less than 0.85 nm, resulting in a maximum adsorbed density for each pore size. The highest adsorbed density was observed for a pore size of 0.65 nm as well. However, for single-layer adsorption, we observed that the simulated isotherms with a 30% defect area and effective radius of 0.246 nm exhibited a lower adsorbed density than that of the perfective surface, whereas the isotherms with 30% defects and effective radius of 0.492 nm showed a higher adsorbed density. This indicates that the size and distribution of defects significantly affect the adsorbed density. The differences in the adsorbed density could be attributed to the effect of the defect size on the available surface area for adsorption. Surfaces containing small defect sizes can lead to a decrease in the number of available adsorption sites because the defect size is too small to accommodate the adsorbate molecules.

Next, Figure 4.6 shows the snapshots of N_2 molecules in the space of finite pores of 2.0 nm in width at 77 K with R_c varying from 0.246 to 0.615 nm. The choice of a pore width of 2.0 nm is noteworthy as it falls within the average pore size range observed in the activated carbon samples. For better visualization, only one graphene layer on each wall is presented. Typically, adsorptive molecules will first adsorb onto the strongest adsorption sites, followed by adsorption on the other respective weaker sites. Results from Figure 4.6 indicate that adsorption took place initially at the defect pits and then on the carbon surface. This suggests that the stronger solid-fluid (SF) interaction of the defect pits initiates the adsorption, and then the two contact layers adjacent to the two walls form due to the strong SF interaction near the pore wall (Wongkoblap & Do, 2007). The data of isosteric heat of adsorption on the defective surface are also employed to indicate the strong solid-fluid interaction, which is discussed in section 4.5.6.

Furthermore, when the pressure increased to the maximum of 100000 Pa, the inner pores are completely filled by the contact layers. Figure 4.6a shows that the R_c of 0.246 nm is too small to accommodate an adsorptive molecule,

leading to the weak interaction between the pits and the adsorbate molecules, thus resulting in a decrease in the adsorbed amount. In contrast, Figures 4.6b and 4.6c reveal that either R_c of 0.492 or 0.615 nm, respectively, is large enough to accommodate the molecules, resulting in an adequate attraction between the gas molecules and the carbon surface. Previous research has shown that the attraction between water molecules and the carbon surface is similarly affected by the size of defects (Xu, Do, et al., 2021). Thus, the suitable size of the defect on the activated carbon surface may be measured by the effective radius value, which leads to a good agreement between the simulated isotherms and the experimental isotherms. The simulated isotherms were compared with the experimental isotherms of N_2 adsorption, as illustrated in Figure 4.7. Excellent agreement of the experimental and simulated N_2 isotherms is achieved for R_c of 0.492 and 0.615 nm. In the next section, an effective radius of 0.492 nm was chosen to investigate the influence of defect area by varying the percent defect from 0 to 45% for N_2 adsorption. The use of R_c larger than 0.492 nm may not be feasible for the simulation, since the carbon surface may not retain its crystalline structure.

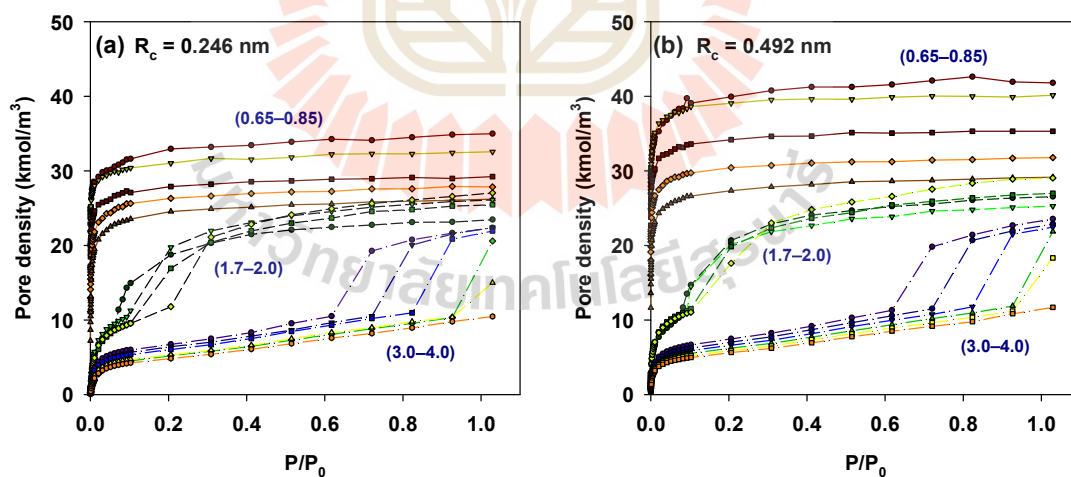


Figure 4.5 Simulated adsorption isotherms of N_2 at 77 K in carbon silt pores with 30% defects of the effective radius at (a) 0.246 nm and (b) 0.492 nm.

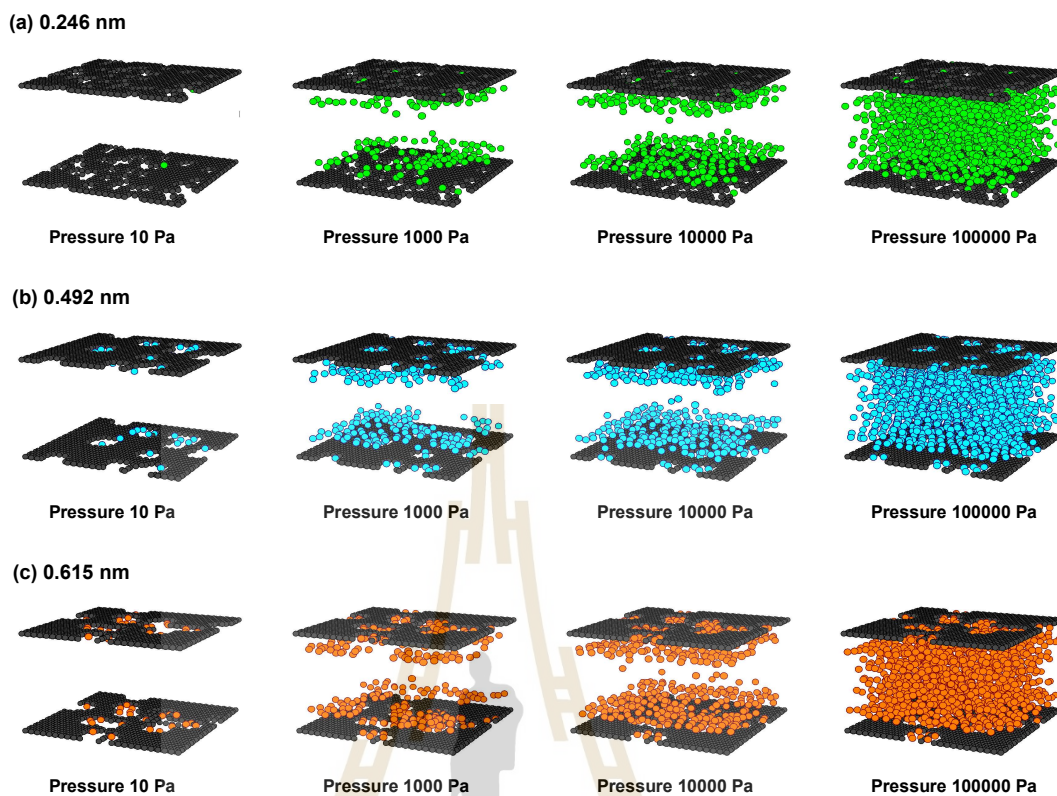


Figure 4.6 Snapshots of N_2 adsorption at 77 K in pore width of 2 nm at various adsorption pressure on the defective surface with R_c of (a) 0.246 nm, (b) 0.492 nm, and (c) 0.615 nm.

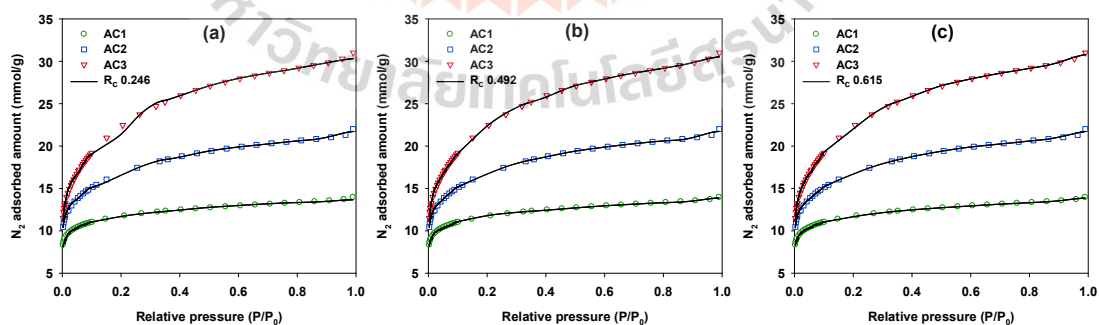


Figure 4.7 Comparison of experimental and simulated adsorption isotherms for 30% defective area with various R_c of (a) 0.246 nm, (b) 0.492 nm, and (c) 0.615 nm.

4.5.5 Effect of Defect Area

Figure 4.8 displays the snapshots of N_2 adsorption at 77 K in a pore width of 0.70 nm for one adsorbed layer at an initial pressure of 1 Pa on the carbon surface with R_c of 0.492 nm and with the percentage of defect area varying from 0 to 45%. It can be observed that the pores consisting of larger % defects exhibited lower adsorbed molecules at low loadings. This indicates a lower interaction between the adsorbate molecules and the carbon atoms on the surface with a higher defective area. Figure 4.9 shows the adsorption of N_2 in a 1.0 nm pore width. This pore width can accommodate two exact layers for different defect levels (0–45%), holding a fixed effective radius. The results show similar adsorption behavior to that observed for a pore width of 0.70 nm with one adsorbed layer. That is, pores with higher % defects exhibited lower adsorbed amounts at low pressures. However, as the pressure approaches the saturation vapor pressure, molecules will enter the pore and completely fill the pore interior and the defect sites. Even though pores with defects have weak adsorbent-adsorbate interaction forces, the maximum capacity is approximately the same as that of the perfective pores. This could be due to the fact that while the presence of defects can increase the available surface area and provide additional sites for adsorption, the weaker adsorbent-adsorbate interaction in these sites may limit the amount of adsorbate that can be adsorbed. As a result, the maximum capacity of the defective pore is similar to that of the perfective pore despite the presence of surface defects.

The results of the goodness-of-fit analysis are summarized in Table 4.3, which showed that the best models were found to be a defect-free surface for AC1, a defective surface with an effective radius of 0.492 nm and 15% defects for AC2, and a defective surface with an effective radius of 0.492 nm and 45% defects for AC3. The increase in mesopore volume was significantly associated with the effective radius which increased from 0 to 0.492 nm, while the percentage of defect area is related to the carbon burn-off. Both AC2 and AC3 were best described by an effective radius of 0.492 nm, with the difference between them being the percentage of the defect area. This finding suggests that an increase in the percentage of defect corresponds to an increase in the carbon burn-off, while an increase in the mesopore volume may be due to the overlapping of neighboring pits. This mechanism is consistent with the micropore enlargement process observed in the activated carbon

produced by the OTA method through the gasification and coalescence of micropores. Furthermore, the defect size of 0.492 nm has the same magnitude as the previous report on characterizing N₂ adsorption on non-graphitized carbon black (NGCB) with a defective surface (Wongkoblap & Do, 2007). This evidence tends to indicate that an effective radius of 0.492 nm could be the optimum value for N₂ adsorption on a defective surface.

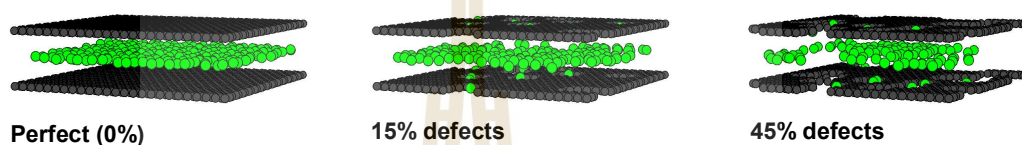


Figure 4.8 Snapshots of N₂ at 77 K in pore width of 0.70 nm at 1 Pa on the carbon surface with the effective radius of 0.492 nm at percentage defects varying from 0 to 45%.

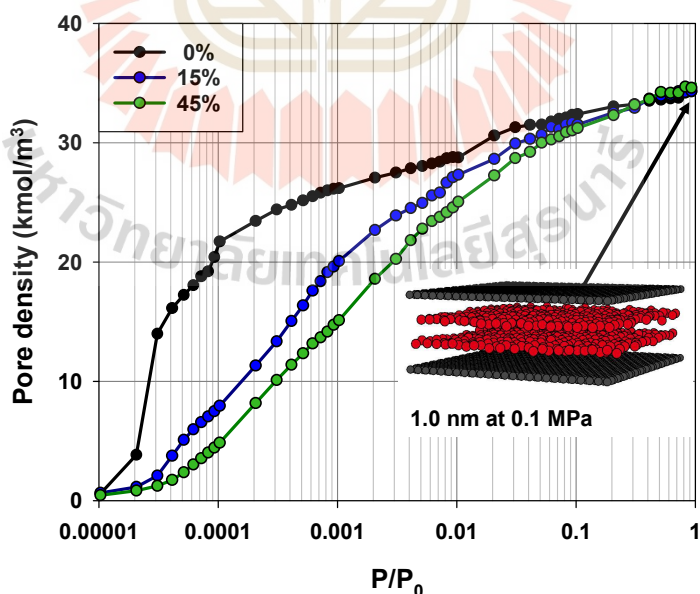


Figure 4.9 Adsorption isotherms of N₂ in 1.0 nm pores on the different percentages of defects (0–45%) with the effective radius of 0.492 nm.

Table 4.3 Values of R^2 and $\% \Delta V$ for the best fitting of N_2 and CO_2 adsorption isotherms

Sample name	Perfective surface		Defective surface				
	$(R_c = 0)$		$(\text{Extent of defect} = 30\%)$			$(R_c = 0.492 \text{ nm})$	
	CO_2	N_2	0.246 nm	0.492 nm	0.615 nm	15%	45%
AC1	0.9997 (3.05%)	0.9998 (0.17%)	0.9996 (0.27%)	0.9989 (0.50%)	0.9996 (0.30%)	0.9996 (0.28%)	0.9987 (0.60%)
AC2	0.9998 (3.43%)	0.9994 (0.64%)	0.9989 (0.75%)	0.9993 (0.60%)	0.9994 (0.58%)	0.9998 (0.45%)	0.9982 (1.05%)
AC3	0.9993 (4.70%)	0.9997 (0.72%)	0.9982 (1.31%)	0.9996 (0.69%)	0.9995 (0.79%)	0.9997 (0.72%)	0.9999 (0.30%)

4.5.6 Analysis of N_2 Adsorption Based on Isothermic Heat

The relationship between isothermic heat of adsorption of N_2 at 77 K in a 1.10 nm pore and the corresponding adsorbed density for the perfective surface is compared with that of the defective surface, as shown in Figure 4.10. The heat of adsorption can be separated into two contributions, namely fluid-fluid (FF) and solid-fluid (SF) interactions.

In the case of a perfective surface, as shown in Figure 4.10a, the isothermic heat progressively increased as the first layer was covered, reaching a maximum at the completion of the first layer at the density of about 18 kmol/m^3 . The total heat then decreased due to the formation of the second layer at higher densities, for which the contribution from SF decreased since the N_2 molecules are adsorbed further away from the carbon surfaces. This finding is consistent with the adsorption of simple and linear molecules on the homogeneous surface (Prasetyo et al., 2018; Xu, Phothong, et al., 2021).

Next, the heat of adsorption for the defective surface is considered, as shown in Figure 4.10b. The SF interaction is a dominant factor at a very low density, as it contributes about 13 kJ/mol for defective surfaces while the perfective surface provides only 10.5 kJ/mol . This implies that the adsorption occurs at the strong adsorbing sites at a low loading, which is the interaction between the defective sites and the adsorbate molecules, and then the adsorption proceeds progressively on

typical carbon sites. The high value of isosteric heat at a very low density was also observed in the adsorption of the simple and linear molecules at a strong adsorption site (Loi et al., 2020; Loi et al., 2021).

To further understand the mechanism of adsorption at a high-energy site, the configurations of snapshots are presented, as shown in Figure 4.6. The adsorbate molecules interacting with the defective pits at the low pressure (~ 10 Pa) can be observed. Moreover, the OTA method depends strongly on adsorbing sites to create mesopores from the gasification reactivity of the pre-existing micropores. These sites are strong defect pits resulting from an increasing number of unpaired electrons due to bond disruption of functional groups, as part of the OTA preparation method. They are enlarged via gasification reaction at the original micropores with strong adsorbing sites, resulting in a greater amount of produced mesopores.

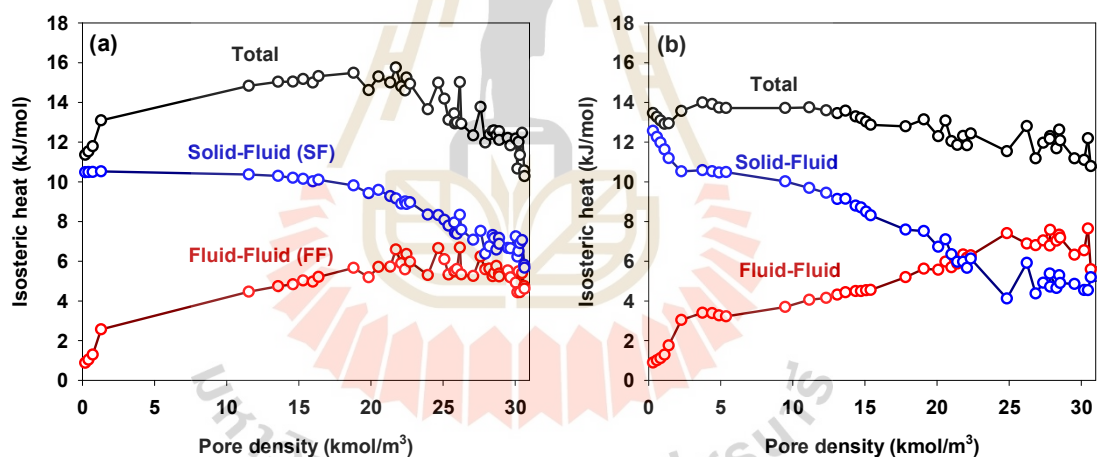


Figure 4.10 Isosteric heat as a function of loading for N_2 adsorption in 1.10 nm pore at 77 K on (a) perfective surface, (b) defective surface.

4.5.7 The PSD Derived from N_2 Adsorption Isotherms

The pore size distributions of activated carbon samples based on the perfective and defective models were obtained by comparing the simulated adsorption isotherms with the experimental data. The parameters used in the simulation for determining the PSD of the activated carbon from N_2 adsorption isotherms are presented in Table 4.4. The extent of carbon defects was found to be

in the order of $AC3 > AC2 > AC1$, which indicates that the magnitude of the defect area on the carbon surface increased with the increasing number of treatment cycles of the OTA method from 1 to 3.

Next, the development of pores in the activated carbon is considered. Table 4.5 presents the calculated pore volume data for each pore size range. For the computed PSD, it is noted that the volume of micropores in the range of 0.65 to 1.4 nm decreased continuously from 0.309 to 0.275 cm^3/g for the AC1 to AC3 samples. On the other hand, the volume of supermicropores (1.4–2 nm) increased from 0.066 to 0.325 cm^3/g , indicating the transformation of some micropores into larger supermicropores caused by the gasification reaction. Similar results were obtained for the micropore development derived from the perfective surface model.

Figure 4.11 shows a progressive increase in the mesopore volume in the range of 2–4 nm, with pore sizes between 2 and 3 nm accounting for about 43.8%, 65.9%, and 52.7% of the total mesopore volume for AC1, AC2, and AC3, respectively. It was observed that AC3 exhibited a significant increase in the pore volume in the range of 3–4 nm, accounting for up to 47.3% of the total mesopore volume. This could have resulted from the transformation of some small mesopores (2–3 nm) into larger mesopores (3–4 nm) as a result of the merging of adjacent mesopores. Although mesopore development in AC3 derived from the defective surface model had a higher pore volume in the range of 3–4 nm (47.3%) compared to that of AC3 derived from the perfective surface model (30.4%), it is important to note that the formation of mesopores is not solely determined by the surface model used. Mesopores are formed due to the changes in the pore structure caused by the gasification reaction, which involves the widening of micropores due to increasing surface reactivity for CO_2 gasification. This pore widening leads to the formation of larger pores with diameters between 2 and 50 nm, which is different from the creation of micropores through the gasification reaction that results in the formation of small pores with diameters of less than 2 nm. Therefore, while the choice of surface model can have an effect on mesopore distribution, it is not the only factor influencing the formation of mesopores.

However, these findings regarding the PSD reveal the development of pores in the activated carbon as the number of OTA cycles increases, notably the development of micropores and mesopores. In brief, this study has demonstrated

that mesopores in microporous-mesoporous activated carbon from longan seed biomass are not created only by the coalescence of micropores at a high degree of burn-off, but rather through micropore widening caused by the increase in the surface reactivity of micropores for CO₂ gasification.

Table 4.4 Parameters used in the simulation for determining the PSD of the activated carbon derived from N₂ adsorption isotherms

Parameter	AC1	AC2	AC3
Effective radius (nm)	0	0.492	0.492
Extent of defect (%)	0	15	45

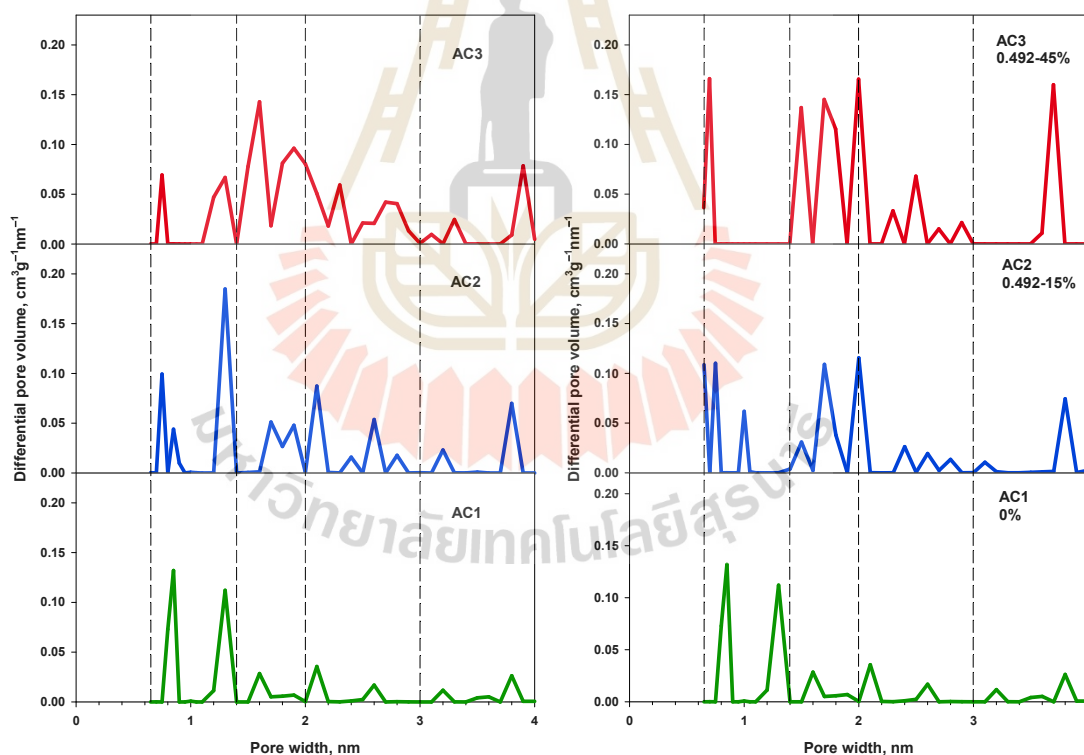


Figure 4.11 PSD of AC1, AC2, and AC3 derived from the perfective surface (left) and the defective surface models (right) as determined by the adsorption isotherms of N₂ at 77 K.

Table 4.5 Pore volume distributions in the activated carbons based on perfective and defective models derived from N₂ adsorption isotherms

Sample name	V _T (cm ³ /g)	Pore volume for pore width, cm ³ /g (%)			
		0.65–1.4 nm	1.4–2 nm	2–3 nm	3–4 nm
Perfective surface model					
AC1	0.480	0.309 (64.4)	0.066 (13.7)	0.046 (9.6)	0.059 (12.3)
AC2	0.736	0.339 (46.1)	0.127 (17.2)	0.176 (23.9)	0.094 (12.8)
AC3	1.074	0.207 (19.3)	0.393 (36.6)	0.330 (30.7)	0.144 (13.4)
Defective surface model					
AC1	0.480	0.309 (64.4)	0.066 (13.7)	0.046 (9.6)	0.059 (12.3)
AC2	0.736	0.284 (38.6)	0.182 (24.7)	0.178 (24.2)	0.092 (12.5)
AC3	1.074	0.275 (25.5)	0.325 (30.3)	0.250 (23.3)	0.224 (20.9)

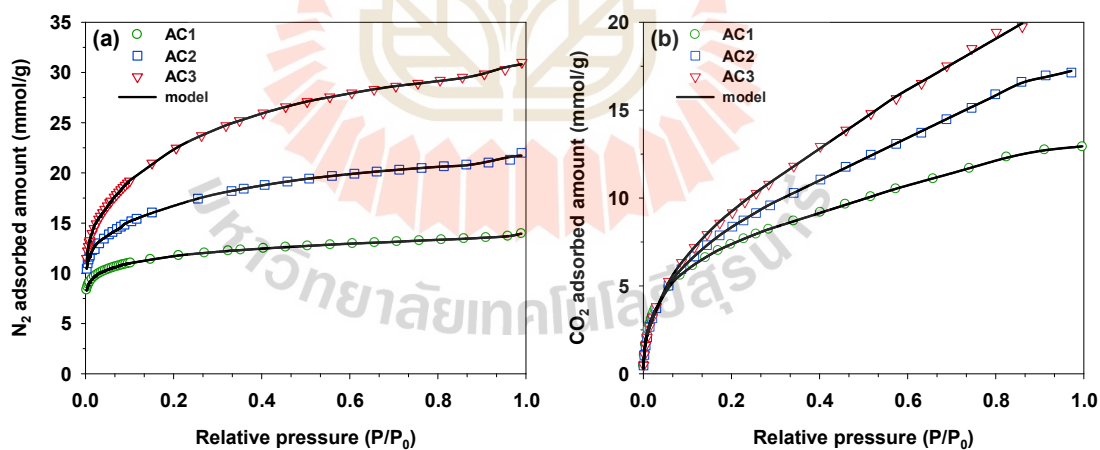


Figure 4.12 Comparison of simulated and experimental adsorption isotherms of (a) N₂ at 77 K and (b) CO₂ at 273 K.

4.5.8 The PSD Derived from CO₂ Adsorption Isotherms

Figure 4.12 displays a comparison between the simulated and experimental isotherms for CO₂ adsorption. The matching between the isotherms is excellent, with the regression coefficient (R^2) greater than 0.999 and a normalized standard deviation of less than 5%. The pore size distribution data of activated carbon samples generated from the optimal fitting of experimental and computed CO₂ isotherms are presented in Figure 13. The results show the type of multimodal distribution covering the pore size range from 0.65 to 4 nm. Table 4.6 presents the calculated pore volume data for each pore size range. Based on the resulting PSD, the activated carbon primarily consists of micropores (0.65–1.4 nm) and small mesopores (2–3 nm). With an increase in the number of OTA preparation cycles, the volume of micropores decreased, while an opposite trend was observed for supermicropores (1.4–2 nm). This observation suggests that supermicropores are responsible for the increase in the surface area of activated carbon.

Furthermore, Figure 4.13 shows a progressive increase in mesopore volume in the range of 2–3 and 3–4 nm. The mesopores were predominantly distributed within the 2–3 nm range, accounting for about 98.6%, 97.7%, and 99.9% of the total mesopore volume for carbon samples produced from cycle 1, cycle 2, and cycle 3 of the OTA method, respectively. The total pore volumes determined from the CO₂ adsorption data of AC1, AC2, and AC3 were slightly higher than those obtained from the N₂ isotherms. The difference among these results is attributed to the use of different molecular probes (N₂ vs CO₂). Since CO₂ has a smaller collision diameter than that of N₂ and the adsorption temperature of CO₂ (273 K) is much higher than that of N₂ (77 K), this would allow a faster diffusion rate of CO₂ through carbon pores enabling CO₂ to get access to much smaller pores.

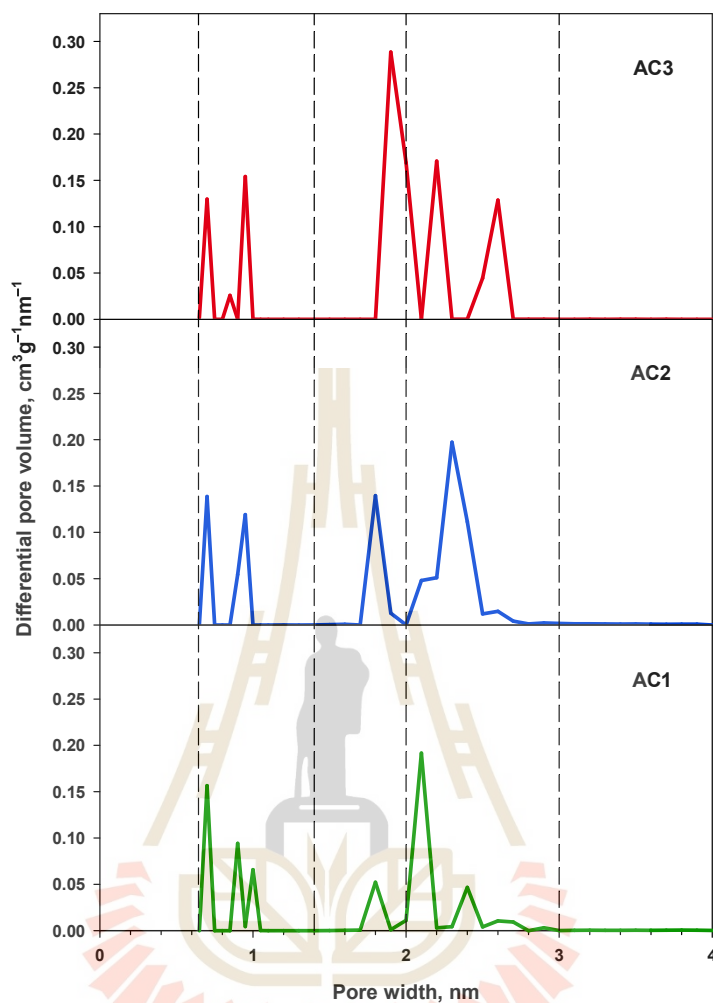


Figure 4.13 PSD for AC1, AC2, and AC3 calculated based on the adsorption isotherms of CO₂ at 273 K.

Table 4.6 The pore volume of the PSD in the activated carbon derived from CO₂ adsorption isotherms

Sample name	V_T (cm ³ /g)	V_{mi} (cm ³ /g)	V_{me} (cm ³ /g)	Pore volume for pore width (cm ³ /g)			
				0.65–1.4 nm	1.4–2 nm	2–3 nm	3–4 nm
AC1	0.663	0.375	0.288	0.3209	0.0541	0.2836	0.0041
AC2	0.918	0.466	0.452	0.3125	0.1535	0.4419	0.0106
AC3	1.113	0.600	0.513	0.3115	0.2885	0.5129	0.0003

4.6 Conclusions

This study provided valuable insights into the adsorption behavior and pore development in microporous-mesoporous activated carbon produced from longan-seed biomass, based on GCMC simulation and a surface defect model. The analysis of N₂ adsorption isotherms at 77 K and CO₂ adsorption isotherms at 273 K on the perfective surfaces revealed a continuous pore-filling mechanism for a single layer of pore width less than 0.85 nm. Capillary condensation was observed for N₂ adsorption at pore widths larger than 1.7 nm, while this was not observed for CO₂ adsorption. The isotherms for N₂ adsorption on the defective surfaces showed a similar pattern to that of the perfective surface, with continuous pore filling occurring for a pore width of less than 0.85 nm that resulted in a maximum adsorbed density for each pore size. However, smaller defects exhibited lower adsorbed density for single-layer adsorption, while larger defects showed higher adsorbed density, indicating that the size and the distribution of defects significantly affect the adsorbed density. Furthermore, adsorption was found to take place initially at the defect pits and then on the carbon surfaces suggesting that the stronger solid-fluid (SF) interaction of the defect pits initiates the adsorption, and then the two contact layers adjacent to the two walls are formed due to the strong SF interaction near the pore wall.

The pore size distribution (PSD) data obtained from N₂ and CO₂ adsorption isotherms indicated that the activated carbon samples primarily consisted of micropores and small mesopores, with a multimodal distribution covering the pore size range from 0.65 to 4 nm. The simulation adsorption isotherms of both perfective and defective surfaces were compared with the experimental data to obtain the PSD of activated carbon samples using N₂ adsorption isotherms. The results indicated that the percentage of carbon defect area increased with the number of the OTA-treatment cycles. The computed PSD revealed a decrease in the volume of micropores and an increase in the volume of supermicropores for AC1 to AC3 samples. The mesopore volume also increased progressively, with a significant increase in the pore volume in the range of 2–3 nm. Our findings demonstrate that mesopores in microporous-mesoporous activated carbon from longan seed biomass are formed not only by the coalescence of micropores but also by micropore widening caused by the increased surface reactivity of micropores for CO₂ gasification.

Analysis of the PSD of activated carbon samples using CO₂ adsorption isotherms showed a multimodal distribution showing peaks in the micropores size range of 0.65–1.4 nm and small mesopores size range of 2–3 nm. The supermicropores (1.4–2 nm) were responsible for increasing the surface area of activated carbon, and their volume increased with an increase in the number of OTA preparation cycles. The mesopore size was predominantly distributed within the 2–3 nm range, and its volume increased with the number of OTA cycles. The total pore volumes determined from CO₂ adsorption were slightly higher than those obtained from N₂ adsorption due to the faster diffusion rate of CO₂ being able to penetrate into smaller size pores.

4.7 References

- Alexandre de Oliveira, J. C., Soares Maia, D. A., Toso, J. P., Lopez, R. H., Azevedo, D. C. S., & Zgrablich, G. (2013, 2013/11/20/). Characterization of the PSD of activated carbons by a heterogeneous surface mixed model. *Colloids and Surfaces A: Physicochemical and Engineering Aspects*, 437, 69-75.
- Azevedo, D. C. S., Rios, R. B., López, R. H., Torres, A. E. B., Cavalcante, C. L., Toso, J. P., & Zgrablich, G. (2010, 2010/06/15/). Characterization of PSD of activated carbons by using slit and triangular pore geometries. *Applied Surface Science*, 256(17), 5191-5197.
- Bakar, N. A., Othman, N., Yunus, Z. M., Altowayti, W. A. H., Tahir, M., Fitriani, N., & Mohd-Salleh, S. N. A. (2021, 2021/05/01/). An insight review of lignocellulosic materials as activated carbon precursor for textile wastewater treatment. *Environmental Technology & Innovation*, 22, 101445.
- Bansal, R., & Goyal, M. (2005). *Activated Carbon Adsorption*. CRC Press.
- Berthelot, D. (1898). Sur le mélange des gaz. *Comptes rendus de l'Académie des sciences*, 126, 1703-1885.
- Brunauer, S., Emmett, P. H., & Teller, E. (1938, 1938/02/01). Adsorption of Gases in Multimolecular Layers. *Journal of the American Chemical Society*, 60(2), 309-319.

- Dantas, S., Struckhoff, K. C., Thommes, M., & Neimark, A. V. (2021, 2021/03/01/). Pore size characterization of micro-mesoporous carbons using CO₂ adsorption. *Carbon*, 173, 842-848.
- Do, D. D. (1998). *Adsorption Analysis: Equilibria and Kinetics* [doi:10.1142/p111]. Imperial College Press.
- Do, D. D., & Do, H. D. (2003, 2003/01/01/). Adsorption of supercritical fluids in non-porous and porous carbons: analysis of adsorbed phase volume and density. *Carbon*, 41(9), 1777-1791.
- Do, D. D., & Do, H. D. (2003). Pore Characterization of Carbonaceous Materials by DFT and GCMC Simulations: A Review. *Adsorption Science & Technology*, 21(5), 389-423.
- Do, D. D., & Do, H. D. (2006, 2006/09/01). Modeling of Adsorption on Nongraphitized Carbon Surface: GCMC Simulation Studies and Comparison with Experimental Data. *The Journal of Physical Chemistry B*, 110(35), 17531-17538.
- Do, D. D., & Do, H. D. (2007, 2007/08/01). Isotherm and heat of adsorption in porous solids with defective pores—adsorption of argon and nitrogen at 77 K in Saran activated carbon. *Molecular Simulation*, 33(9-10), 821-837.
- Dombrowski, R. J., Hyduke, D. R., & Lastoskie, C. M. (2000, 2000/05/01). Pore Size Analysis of Activated Carbons from Argon and Nitrogen Porosimetry Using Density Functional Theory. *Langmuir*, 16(11), 5041-5050.
- Dubinin, M. M. (1975). Physical Adsorption of Gases and Vapors in Micropores. In D. A. Cadenhead, J. F. Danielli, & M. D. Rosenberg (Eds.), *Progress in Surface and Membrane Science* (Vol. 9, pp. 1-70). Elsevier.
- Ekundayo, J. M., & Rezaee, R. (2019a, 2019/02/21). Effect of Equation of States on High-Pressure Volumetric Measurements of Methane–Coal Sorption Isotherms—Part 1: Volumes of Free Space and Methane Adsorption Isotherms. *Energy & Fuels*, 33(2), 1029-1036.
- Ekundayo, J. M., & Rezaee, R. (2019b). Volumetric Measurements of Methane–Coal Adsorption and Desorption Isotherms—Effects of Equations of State and Implication for Initial Gas Reserves. *Energies*, 12(10), 2022.

- Frenkel, D., & Smit, B. (2001). *Understanding molecular simulation: from algorithms to applications* (Vol. 1). Elsevier.
- Garrido, J., Linares-Solano, A., Martin-Martinez, J. M., Molina-Sabio, M., Rodriguez-Reinoso, F., & Torregrosa, R. (1987, 1987/01/01). Use of nitrogen vs. carbon dioxide in the characterization of activated carbons. *Langmuir*, 3(1), 76-81.
- Harris, J. G., & Yung, K. H. (1995, 1995/08/01). Carbon Dioxide's Liquid-Vapor Coexistence Curve And Critical Properties as Predicted by a Simple Molecular Model. *The Journal of Physical Chemistry*, 99(31), 12021-12024.
- Johnson, J. K., Zollweg, J. A., & Gubbins, K. E. (1993, 1993/02/20). The Lennard-Jones equation of state revisited. *Molecular Physics*, 78(3), 591-618.
- Klewiah, I., Berawala, D. S., Alexander Walker, H. C., Andersen, P. Ø., & Nadeau, P. H. (2020, 2020/01/01/). Review of experimental sorption studies of CO₂ and CH₄ in shales. *Journal of Natural Gas Science and Engineering*, 73, 103045.
- Kohmuean, P., Inthomya, W., Wongkoblap, A., & Tangsathitkulchai, C. (2021). Monte Carlo Simulation and Experimental Studies of CO₂, CH₄ and Their Mixture Capture in Porous Carbons. *Molecules*, 26(9).
- Kruk, M., & Jaroniec, M. (2002, 2002/05/01). Determination of Mesopore Size Distributions from Argon Adsorption Data at 77 K. *The Journal of Physical Chemistry B*, 106(18), 4732-4739.
- Langmuir, I. (1918). The adsorption of gases on plane surfaces of glass, mica and platinum. *Journal of the American Chemical society*, 40(9), 1361-1403.
- Lawtae, P., & Tangsathitkulchai, C. (2021a). A New Approach for Controlling Mesoporosity in Activated Carbon by the Consecutive Process of Air Oxidation, Thermal Destruction of Surface Functional Groups, and Carbon Activation (the OTA Method). *Molecules*, 26(9), 2758.
- Lawtae, P., & Tangsathitkulchai, C. (2021b). The Use of High Surface Area Mesoporous-Activated Carbon from Longan Seed Biomass for Increasing Capacity and Kinetics of Methylene Blue Adsorption from Aqueous Solution. *Molecules*, 26(21), 6521.

- Lennard-Jones, J. E. (1931, 1931/09/01). Cohesion. *Proceedings of the Physical Society*, 43(5), 461-482.
- Lennard-Jones, J. E. (1932). Processes of adsorption and diffusion on solid surfaces. *Transactions of the Faraday Society*, 28(0), 333-359.
- Liu, P. S., & Chen, G. F. (2014). Chapter Nine - Characterization Methods: Basic Factors. In P. S. Liu & G. F. Chen (Eds.), *Porous Materials* (pp. 411-492). Butterworth-Heinemann.
- Loi, Q. K., Horikawa, T., Tan, S., Prasetyo, L., Do, D. D., & Nicholson, D. (2020, 2020/02/01/). Characterization of Cabot BP280 with argon and nitrogen adsorption at temperatures above and below the triple point – Energetic vs Structural heterogeneities. *Microporous and Mesoporous Materials*, 293, 109762.
- Loi, Q. K., Phothong, K., Do, D. D., & Nicholson, D. (2021, 2021/08/01/). Effects of crystallite stacking on adsorption of ethylene on graphitized thermal carbon black. *Microporous and Mesoporous Materials*, 323, 111202.
- Lorentz, H. A. (1881, 1881/01/01). Ueber die Anwendung des Satzes vom Virial in der kinetischen Theorie der Gase. *Annalen der Physik*, 248(1), 127-136.
- Marsh, H., & Rodríguez-Reinoso, F. (2006). *Activated carbon*. Elsevier Science Ltd.
- Metropolis, N., Rosenbluth, A. W., Rosenbluth, M. N., Teller, A. H., & Teller, E. (1953). Equation of State Calculations by Fast Computing Machines. *The Journal of Chemical Physics*, 21(6), 1087-1092.
- Metropolis, N., & Ulam, S. (1949, 1949/09/01). The Monte Carlo Method. *Journal of the American Statistical Association*, 44(247), 335-341.
- Mountain, R. D., & Thirumalai, D. (1994, 1994/10/01/). Quantative measure of efficiency of Monte Carlo simulations. *Physica A: Statistical Mechanics and its Applications*, 210(3), 453-460.
- Nicholson, D., & Parsonage, N. G. (1982). *Computer Simulation and the Statistical Mechanics of Adsorption*. Academic Press Inc.

- Ohba, T., & Kaneko, K. (2001, 2001/06/01). GCMC Study on Relationship between DR Plot and Micropore Width Distribution of Carbon. *Langmuir*, 17(12), 3666-3670.
- Pantatosaki, E., Psomadopoulos, D., Steriotis, T., Stubos, A. K., Papaioannou, A., & Papadopoulos, G. K. (2004, 2004/07/14/). Micropore size distributions from CO₂ using grand canonical Monte Carlo at ambient temperatures: cylindrical versus slit pore geometries. *Colloids and Surfaces A: Physicochemical and Engineering Aspects*, 241(1), 127-135.
- Phothong, K., Tangsathitkulchai, C., & Lawtae, P. (2021). The Analysis of Pore Development and Formation of Surface Functional Groups in Bamboo-Based Activated Carbon during CO₂ Activation. *Molecules*, 26(18), 5641.
- Prasetyo, L., Tan, S., Akram, A., Do, D. D., & Nicholson, D. (2018, 2018/10/05/). Cluster growth and coalescence of argon on weakly adsorbing substrates: The origin of the thin-to-thick film transition. *Colloids and Surfaces A: Physicochemical and Engineering Aspects*, 554, 169-179.
- Ravikovitch, P. I., Vishnyakov, A., Russo, R., & Neimark, A. V. (2000, 2000/03/01). Unified Approach to Pore Size Characterization of Microporous Carbonaceous Materials from N₂, Ar, and CO₂ Adsorption Isotherms. *Langmuir*, 16(5), 2311-2320.
- Samios, S., Stubos, A. K., Kanellopoulos, N. K., Cracknell, R. F., Papadopoulos, G. K., & Nicholson, D. (1997, 1997/05/01). Determination of Micropore Size Distribution from Grand Canonical Monte Carlo Simulations and Experimental CO₂ Isotherm Data. *Langmuir*, 13(10), 2795-2802.
- Sing, K. S. W. (1989, 1989/01/01/). The use of gas adsorption for the characterization of porous solids. *Colloids and Surfaces*, 38(1), 113-124.
- Sircar, S., Mohr, R., Ristic, C., & Rao, M. B. (1999, 1999/08/01). Isosteric Heat of Adsorption: Theory and Experiment. *The Journal of Physical Chemistry B*, 103(31), 6539-6546.
- Sitprasert, C., Zhu, Z. H., Wang, F. Y., & Rudolph, V. (2013, 2013/05/24/). Multi-component adsorption in heterogeneous carbonaceous porous media through the integration of small-scale, homogenous models. *Chemical Engineering Science*, 95, 267-282.

- Steele, W. A. (1978, 1978/04/01). The interaction of rare gas atoms with graphitized carbon black. *The Journal of Physical Chemistry*, 82(7), 817-821.
- Tangsathitkulchai, C., Naksusuk, S., Wongkoblup, A., Phadungbut, P., & Borisut, P. (2021). Equilibrium and Kinetics of CO₂ Adsorption by Coconut Shell Activated Carbon Impregnated with Sodium Hydroxide. *Processes*, 9(2), 201.
- Thommes, M., Kaneko, K., Neimark, A. V., Olivier, J. P., Rodriguez-Reinoso, F., Rouquerol, J., & Sing, K. S. (2015). Physisorption of gases, with special reference to the evaluation of surface area and pore size distribution (IUPAC Technical Report). *Pure and Applied Chemistry*, 87(9-10), 1051-1069.
- Tipler, P. A. (1999). *Physics for Scientists and Engineers* (4th ed.). W.H. Freeman & Company.
- Toso, J. P., López, R. H., de Azevedo, D. C. S., Cavalcante, C. L., Prauchner, M. J., Rodríguez-Reinoso, F., & Zgrablich, G. (2011, 2011/06/01). Evaluation of a mixed geometry model for the characterization of activated carbons. *Adsorption*, 17(3), 551-560.
- Vishnyakov, A., Ravikovitch, P. I., & Neimark, A. V. (1999, 1999/12/01). Molecular Level Models for CO₂ Sorption in Nanopores. *Langmuir*, 15(25), 8736-8742.
- Wang, L., & Long, Z. (2020). Evolutions of CO₂ Adsorption and Nanopore Development Characteristics during Coal Structure Deformation. *Applied Sciences*, 10(14).
- Wang, X., Cheng, H., Ye, G., Fan, J., Yao, F., Wang, Y., Jiao, Y., Zhu, W., Huang, H., & Ye, D. (2022, 2022/01/01/). Key factors and primary modification methods of activated carbon and their application in adsorption of carbon-based gases: A review. *Chemosphere*, 287, 131995.
- Wongkoblup, A., & Do, D. D. (2006, 2006/05/01/). The effects of energy sites on adsorption of Lennard–Jones fluids and phase transition in carbon slit pore of finite length a computer simulation study. *Journal of Colloid and Interface Science*, 297(1), 1-9.

- Wongkoblap, A., & Do, D. D. (2007, 2007/06/01/). Characterization of Cabot non-graphitized carbon blacks with a defective surface model: Adsorption of argon and nitrogen. *Carbon*, 45(7), 1527-1534.
- Wongkoblap, A., Junpirom, S., & Do, D. (2005, 02/01). Adsorption of Lennard-Jones Fluids in Carbon Slit Pores of a Finite Length. A Computer Simulation Study. *Adsorption Science and Technology*, 23.
- Xu, H., Do, D. D., & Nicholson, D. (2021, 2021/04/01/). On the role of the quadrupole moment of carbon atom on water adsorption on graphite and in graphitic pores. *Chemical Engineering Journal*, 409, 128236.
- Xu, H., Phothong, K., Do, D. D., & Nicholson, D. (2021, 2021/09/01/). Wetting/non-wetting behaviour of quadrupolar molecules (N₂, C₂H₄, CO₂) on planar substrates. *Chemical Engineering Journal*, 419, 129502.
- Zhang, Y., Chi, Y., Zhao, C., Liu, Y., Zhao, Y., Jiang, L., & Song, Y. (2018, 2018/01/11). CO₂ Adsorption Behavior of Graphite Oxide Modified with Tetraethylenepentamine. *Journal of Chemical & Engineering Data*, 63(1), 202-207.
- Zhang, Y., Xing, W., Liu, S., Liu, Y., Yang, M., Zhao, J., & Song, Y. (2015). Pure methane, carbon dioxide, and nitrogen adsorption on anthracite from China over a wide range of pressures and temperatures: experiments and modeling. *RSC Advances*, 5(65), 52612-52623.
- Zhou, L., Bai, S., Su, W., Yang, J., & Zhou, Y. (2003, 2003/04/01). Comparative Study of the Excess versus Absolute Adsorption of CO₂ on Superactivated Carbon for the Near-Critical Region. *Langmuir*, 19(7), 2683-2690.
- Zhou, Y., & Zhou, L. (2009, 2009/12/01). Fundamentals of High Pressure Adsorption. *Langmuir*, 25(23), 13461-13466.
- Zou, J., Rezaee, R., & Liu, K. (2017, 2017/11/16). Effect of Temperature on Methane Adsorption in Shale Gas Reservoirs. *Energy & Fuels*, 31(11), 12081-12092.

CHAPTER V

A SIMPLE PRE-OXIDATION TECHNIQUE FOR INCREASING CO₂ GASIFICATION RATES IN LONGAN-SEED CHAR

5.1 Abstract

A simple and effective technique was presented to increase the longan-seed char gasification rate during CO₂ activation by pre-oxidizing the char with air. The kinetics of char gasification was studied in a thermogravimetric analyzer (TGA) for the temperatures of 850–950°C for char samples being oxidized in a tube furnace at the temperatures of 250, 280, and 300°C. It was found that the gasification rate of the oxidized char was about twice higher than that of the non-oxidized char. The increase in the char reactivity for CO₂ gasification is due to the increasing number of reaction sites caused by the disruption of functional group bonding created during the oxidation step. Additionally, the increase in the oxidation temperature gave rise to the increase in the char reactivity but the maximum temperature was limited by the ignition temperature of the longan-seed char. Four gasification kinetic models were tested against the experimental rate data and it was discovered that the modified volume reaction model (MVRM) provided the best description of the gasification conversion. The pre-exponential factor and the activation energy of the gasification reaction were determined from the Arrhenius equation. The estimated activation energy was found to be in the range of 156.87–218.98 kJ/mol and decreased with the increase of char oxidation temperature.

5.2 Introduction

Activated carbon is a porous material that is widely used in many separation and purification processes for both gas and liquid systems. It is typically produced by a physical activation process that involves converting a carbonaceous precursor into solid char in an inert atmosphere, thus providing the char rich in carbon content, and then activating the resultant char with an oxidizing agent such as carbon dioxide or

steam (Marsh & Rodríguez-Reinoso, 2006). In general, the reaction of char with an activating agent is crucial in any gasification process either for the production of active carbon or synthesis gas. The rate of gasification is dependent on both the developed pore structure and the chemical reactivity of carbon particles (Scott et al., 2005). The pore structure affects the mass transport of an oxidizing gas, while carbon reactivity determines the chemical reaction kinetics. The overall carbon reactivity is determined by the distribution and number of reaction sites for gasification to proceed. There are generally two methods that can be used to control the reaction rate; the temperature which is a measure of energy level and the reactivity of reaction sites. Recently, a novel method, called the OTA method, has been proposed to enhance carbon reactivity during CO₂ activation of longan seed char, rendering the derived activated carbon with a remarkable increase of surface area and pore volume in comparison with the traditional physical activation method (Lawtae & Tangsatthikulchai, 2021).

The OTA preparation method is based on three consecutive steps of (i) Oxidizing (O) an initial low percent burn-off activated carbon to create more surface oxygen functional groups, (ii) Thermal (T) heating the oxidized carbon at a high temperature in an inert atmosphere to disrupt the chemical bonds of the functional groups, leading to a large number of reaction sites due to the presence of a larger number of unpaired electrons, and (iii) Activating (A) the heat-treated carbon with CO₂ for a required period of time. In this work, this same technique for increasing the number of active sites, and hence the increase in the char gasification rate, was investigated by first oxidizing the prepared longan-seed char with air at a temperature lower than the ignition temperature to increase the amounts of surface groups and then activating the oxidized char at a high temperature in CO₂. For the activation step, the destruction of functional groups and CO₂ activation of the char occur simultaneously. In view of activated carbon synthesis, the rate of carbon gasification during the activation step will have a direct influence on the pore development and the porous characteristics of the final carbon product. The significance of being able to increase the gasification rate during activated carbon synthesis is that a smaller size reactor could be used, hence providing a decrease in the fabrication cost of the reactor.

The raw material used in the present study is longan seed biomass which is the inner seed of longan fruit. The longan fruit is widely consumed and produced in large

quantities in Thailand. Longan seeds account for about 17% of the fruit weight, and they are often discarded from processing plants and disposed of in landfills, thus causing an environmental issue. The conversion of longan fruit seeds into useful value-added products such as activated carbon by physical activation with an oxidizing gas should help alleviate the disposal problem.

Concerning the char gasification rates, there have been a number of reports studying the gasification reactivity of various biomass chars by activating with CO₂. Seo *et al.* (Seo *et al.*, 2010) investigated the gasification reactivity of biomass char with CO₂ using the TGA and various kinetic models, including the volume reaction model (VRM), shrinking core model (SCM), and random pore model (RPM) were tested. They found that the predicted kinetics by the RPM agreed well with the experimental data as compared to the other models. To improve the correlation between the conversion rate and the extent of conversion, the modified kinetic models such as the modified volume reaction model (MVRM), and the modified random pore model (MRPM) were employed to describe the gasification reactivity and kinetic behavior of oil palm biomass (Chew *et al.*, 2020). Tangsathitkulchai *et al.* (Tangsathitkulchai *et al.*, 2013) studied the low carbonization temperature effect on char reactivity in the range of 250–700°C by testing various kinetic models for CO₂ gasification of coconut-shell chars and found that the MVRM was most accurate in predicting the gasification kinetics. Moreover, the char reactivity index was found to decrease with the increase in the carbonization temperature, with the char produced at the lowest temperature of 250°C giving the highest reactivity. Wang *et al.* (Wang *et al.*, 2016) have studied the CO₂ gasification kinetics of various chars and found that the gasification reactivities of chars are mainly determined by their carbonaceous structure. An investigation into the effect of carbonization temperature on pore development in activated carbon from palm shell biomass has been made by Daud and co-workers (Daud *et al.*, 2000). It was found that activated carbon prepared from high-temperature carbonization had higher BET surface area, total pore volume, micropore volume, and yield as compared to those using low-temperature carbonization, which was consistent with the results from coconut shell (Li *et al.*, 2008). This is because a high carbonization temperature could provide more ordering carbon structure that produces more developed micropores with higher porous properties. However, the effect of the oxidation of chars on its gasification reactivity during CO₂ activation has not yet been reported to date.

Therefore, it was the purpose of this work to investigate CO₂ gasification kinetics of chars that was oxidized with air prior to the gasification reaction in a thermogravimetric analyzer (TGA). The kinetic data of these gasified chars were collected by following the char residual weight in a TGA under a CO₂ atmosphere as a function of heating time and for various gasification temperatures. The gasification rate and char reactivity of oxidized chars prepared at various oxidation temperatures were then assessed.

5.3 Experimental Procedure

5.3.1 Materials

Longan seed was used as a raw material in this work and was obtained from a local fruit processing plant in Chiangmai province, Thailand. It was rinsed and cleaned with distilled water and dried in an electric oven at 110°C overnight. The pre-dried longan seed was crushed in a jaw crusher and sieved to obtain a size fraction in the range of 1–1.4 mm (14 × 18 US mesh) with an average particle size of 1.2 mm. The longan seed sample was kept for char preparation.

5.3.2 Char Oxidation Preparation

The char was prepared by loading 40 g of longan seed sample in a ceramic boat and heated in a horizontal ceramic tube furnace (CTF 12/75/700, Carbolite, Staffordshire, UK) of 7 cm inside diameter and 100 cm long from room temperature to 500°C at the rate of 10°C/min under a constant flow of N₂ (100 cm³/min) and held at this temperature for 90 min. The char obtained was cooled down to room temperature inside the furnace under the flow of N₂. Next, about 5 g of the prepared char was oxidized by heating the char in the tube furnace from room temperature to the required oxidation temperature in a stream of air (100 cm³/min) and held at this temperature for the desired period of time. The oxidation temperature in the range of 250 to 300°C and oxidation time from 6–24 h were investigated. The weight of the oxidized char product was recorded, and the char yield and the char burn-off were determined. The preparation conditions for preparing oxidized chars and carbon weight losses are shown in Table 5.1.

Table 5.1 Experimental conditions of oxidized char preparation

Sample name	Oxidation conditions		Carbon burn-off
	Temperature (°C)	Time (h)	(%)
O250-6h	250	6	2.98
O250-12h	250	12	5.92
O250-24h	250	24	8.02
O280-6h	280	6	10.53
O280-12h	280	12	18.26
O280-24h	280	24	26.57
O300-6h	300	6	22.49
O300-12h	300	12	33.65
O300-24h	300	24	48.17

5.3.3 Analysis of Surface Functional Groups

The oxidized was analyzed for the presence and variation of the surface functional groups after the char oxidation process, using the Boehm titration and FTIR analysis. Boehm titration (Boehm, 1994) is one of the most widely used methods for the quantification of surface acid and basic groups on carbon surfaces. The amount and acidic strength are determined by titration with basic solutions of varying basic strengths. It is assumed that the following acid groups are neutralized with respective basic solutions: carboxylic group in a solution of NaHCO_3 , carboxylic and lactonic groups in a solution of Na_2CO_3 , and carboxylic, lactonic, and phenolic groups in a solution of NaOH . For determining the basic groups on the carbon surface, HCl is used to neutralize the basic groups. Boehm titration was carried out by mixing about 0.50 g of the carbon sample with each of the 25 cm^3 of 0.05 M solutions of HCl , NaOH , NaHCO_3 , and 0.025 M of Na_2CO_3 . Each vial was shaken at 150 rpm for 24 h at the ambient temperature and then the suspension was filtered (Seung Kim & Rae Park, 2016). 5 cm^3 of the filtrate solutions of NaOH , Na_2CO_3 , and NaHCO_3 were pipetted and titrated with 0.05 M HCl solution, while the filtrate solution of HCl was titrated with 0.05 M NaOH solution. The titrant volumes of the various bases and acids were used to determine the amounts of surface acid and basic functional groups on the carbon

surfaces. Fourier Transform Infrared (FTIR) spectroscopy (Vertex 70 FT-IR, Bruker, Billerica, MA, USA) was employed to identify the functional groups on the surfaces of carbon samples. The infrared spectra were generated by scanning using wave numbers varying in the range from 400 to 4000 cm^{-1} . About 64 scans were employed with increasing incremental steps 4 cm^{-1} .

5.3.4 Gasification Kinetics

The CO_2 gasification kinetics of the oxidized chars from longan seed was studied in a thermogravimetric analyzer (TGA/DSC 1 STAR^e System, METTLER TOLEDO, Greifensee, Switzerland). About 15 mg of the char sample was loaded into an alumina crucible of 70 μL and heated from the ambient condition to the desired gasification temperature at the heating rate of 20 $^{\circ}\text{C}/\text{min}$ in a stream of N_2 (100 cm^3/min). When the final gasification temperature was reached, the gas flow was switched from N_2 to CO_2 (100 cm^3/min) and the sample was held at the desired gasification temperature. The sample weight was continuously recorded as a function of time until the final weight of the sample became constant. The gasification temperatures studied were 850, 900, and 950 $^{\circ}\text{C}$. Table 5.2 summarizes the gasification conditions used in the TGA for the study of CO_2 gasification kinetics of the original char and oxidized chars in the present study.

Table 5.2 Gasification conditions of the carbon samples in TGA

Sample name	Gasification temperature ($^{\circ}\text{C}$)	Gasification time (min)
Char	850	60
Char	900	60
Char	950	60
O250-6h	900	30
O250-12h	900	30
O250-24h	900	30
O250-24h	850	60
O250-24h	950	30

Table 5.2 Gasification conditions of the carbon samples in TGA (continued)

Sample name	Gasification temperature (°C)	Gasification time (min)
O280-6h	900	30
O280-12h	900	30
O280-24h	900	30
O280-24h	850	60
O280-24h	950	30
O300-6h	900	30
O300-12h	900	30
O300-24h	900	30
O300-24h	850	60
O300-24h	950	30

5.4 Gasification Kinetic Modelling

The CO₂ gasification of the oxidized chars from longan seed is a gas-solid non-catalytic heterogeneous reaction and the reaction rate can be expressed as Equation (5.1):

$$\frac{dX}{dt} = k(T)f(X) \quad (5.1)$$

where X is the fractional conversion, $f(X)$ is a function representing the structural change of char during the course of the gasification reaction, and k is the apparent or overall gasification rate constant that is temperature dependence and can be typically described by the Arrhenius equation as shown in Equation (5.2):

$$k = k_0 e^{-E/RT} \quad (5.2)$$

where k_0 is the pre-exponential factor, E is the activation energy, T is the gasification temperature (K), and R is the universal gas constant.

Some gasification models that are commonly employed for describing the kinetics of a gas-solid reaction are the volume-reaction model (VRM), the shrinking-

core model (SCM), the random pore model (RPM), and the modified volume-reaction model (MVRM). These models provide the different terms of function $f(X)$ in the rate equation. The volume-reaction model (VRM) (Dutta et al., 1977) assumes a homogeneous reaction throughout a reactant solid, resulting in a linear decrease in the solid surface area as the reaction proceeds, and the model equation is represented by Equation (5.3):

$$\frac{dX}{dt} = k_v(1 - X) \quad (5.3)$$

The shrinking-core model (SCM) (Wen, 1968) assumes the shrinking core of a non-reacted solid as the reaction conversion increases, that is, the reaction initially occurs at the external surface and gradually moves inward. The overall reaction rate is described by Equation (5.4):

$$\frac{dX}{dt} = k_s(1 - X)^{2/3} \quad (5.4)$$

The random pore model (RPM) (Bhatia & Perlmutter, 1980) considers the creating and overlapping of pore surfaces as the reaction progresses, and the rate equation is expressed as Equation (5.5):

$$\frac{dX}{dt} = k_R(1 - X)\sqrt{1 - \psi \ln(1 - X)} \quad (5.5)$$

This model is able to predict the maximum value of the reaction rate at a certain reaction conversion. This model contains the structural parameter, ψ , which represents the pore structure of the non-reacted carbon sample.

The modified volume-reaction model (MVRM) (Kasaoka et al., 1985) was an extension of the volume reaction model (VRM), being proposed to improve the prediction of gas-solid reaction rate by assuming the dependence of model rate constant (k) on the reaction conversion (X). The equations involved in the MVRM are shown as Equations (5.6) to (5.9).

$$\frac{dX}{dt} = k(X)(1 - X) \quad (5.6)$$

$$X = at^b \quad (5.7)$$

$$\frac{dX}{dt} = abt^{b-1} \quad (5.8)$$

$$k(X) = \frac{a^{1/b} bX^{(b-1)/b}}{(1-X)}, \quad X \neq 1 \quad (5.9)$$

Since the rate constant (k) varies with the reaction conversion (X), its average value over the course of the reaction (k_m) can be obtained by integrating Equation (10) from $X=0$ to $X=0.99$, giving the following equation.

$$k_m = \int_0^X k(X) dX = \int_0^X \frac{a^{1/b} bX^{(b-1)/b}}{(1-X)} dX, \quad X \neq 1 \quad (5.10)$$

The kinetic parameters in the various proposed models mentioned earlier were obtained through data fitting by minimizing the sum-square errors (SSE) between the experimental and model-computed values of the reaction rate (dX/dt).

5.5 Results and Discussion

5.5.1 Surface Functional Groups of Prepared Carbons

The effects of oxidation time and temperature on the weight loss of longan-seed char are shown in Table 5.1 and Figure 5.1. As seen in Figure 5.1, the carbon weight loss increased with the oxidation conditions (time and temperature). It appears that the oxidation temperature showed a more pronounced effect with the maximum weight loss of 48% occurring at 300°C and 24 h. The weight loss of char due to air oxidation indicates that carbon atoms were consumed by a slow combustion process even at a temperature lower than the carbon ignition temperature. Therefore, char oxidation would lead to the formation of surface functional groups as well as the loss of carbon mass, which in turn could alter the porous structure of the resulting char.

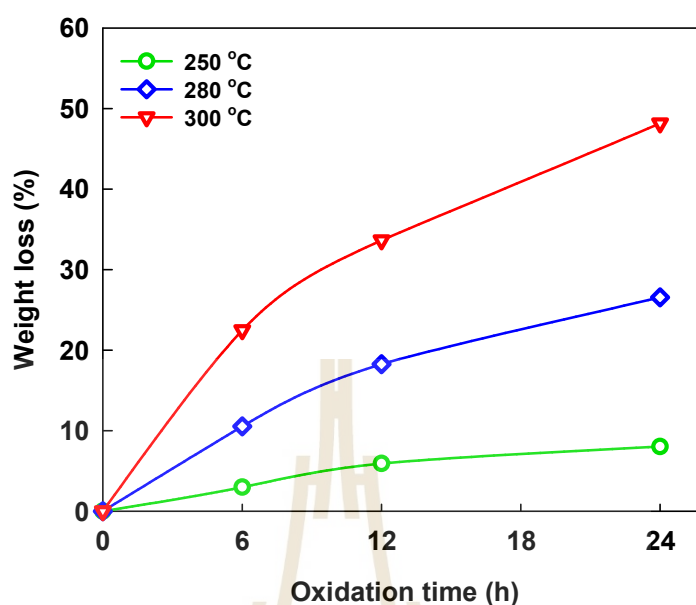


Figure 5.1 Effects of oxidation time and temperature on the char weight loss.

Figure 5.2 shows that after char oxidation the amounts of acidic groups increased substantially by almost 14 times. In contrast, the basic groups of oxidized chars barely increased as compared to those of the non-oxidized chars, except that an average increase of about 26% was noticed for chars being oxidized at 300°C. A slight increase in the amounts of acidic and basic groups was observed as the oxidation time and temperature increased. The maximum amounts of created functional groups are limited by the char ignition temperature which is around 300°C for the longan seed char in this study. Table 5.3 shows that phenolic groups are the major components of the total acidic groups, followed by carboxylic and lactonic, respectively. The amounts of carboxylic and phenolic groups increased significantly after char oxidation. However, the amount of phenolic group did not change significantly with the variation of oxidation conditions, while the amount of carboxylic group increased consistently with the increase of oxidation temperature. It can be said that phenolic groups could be easily created in the oxidized char, whereas the variation in the amounts of carboxylic groups was more affected by the char oxidation conditions. The increase of surface functional groups of the oxidized chars would increase the possibility of generating an additional number of reaction sites for CO₂ gasification due to the disruption of

functional group bonding at such a high gasification temperature and this would allow the increase in the rate of char gasification. The change in the amounts of surface functional groups also had an effect on the porous properties of the oxidized char, which were determined from CO₂ adsorption isotherms at 273K with a maximum applied pressure of 1 atm measured by a high-performance adsorption analyzer (ASAP 2020, Micromeritics, Norcross, GA, USA). The results are shown in Table 5.4 which indicate that the specific surface area and total pore volume decreased with the increase of oxidation time and temperature. This is indicative of the increasing amounts of functional groups on the char surface that occupy the free area for CO₂ adsorption, and this is reflected by a decrease in the adsorbed amounts of CO₂ isotherms, as shown in Figure 5.3.

Table 5.3 The amounts of surface functional groups in the char samples determined by Boehm titration

Sample	Concentration (mmol/g)				
	Carboxylic groups	Lactonic groups	Phenolic groups	Total acidic groups	Total basic groups
char	0.000	0.000	0.158	0.158	0.496
O250-6h	0.119	0.069	1.819	2.007	0.430
O250-12h	0.212	0.018	1.958	2.188	0.437
O250-24h	0.370	0.000	1.906	2.275	0.483
O280-6h	0.212	0.004	1.944	2.160	0.490
O280-12h	0.305	0.000	1.968	2.274	0.500
O280-24h	0.397	0.000	1.915	2.312	0.564
O300-6h	0.204	0.038	1.953	2.195	0.556
O300-12h	0.258	0.000	2.021	2.279	0.563
O300-24h	0.273	0.000	2.048	2.321	0.770

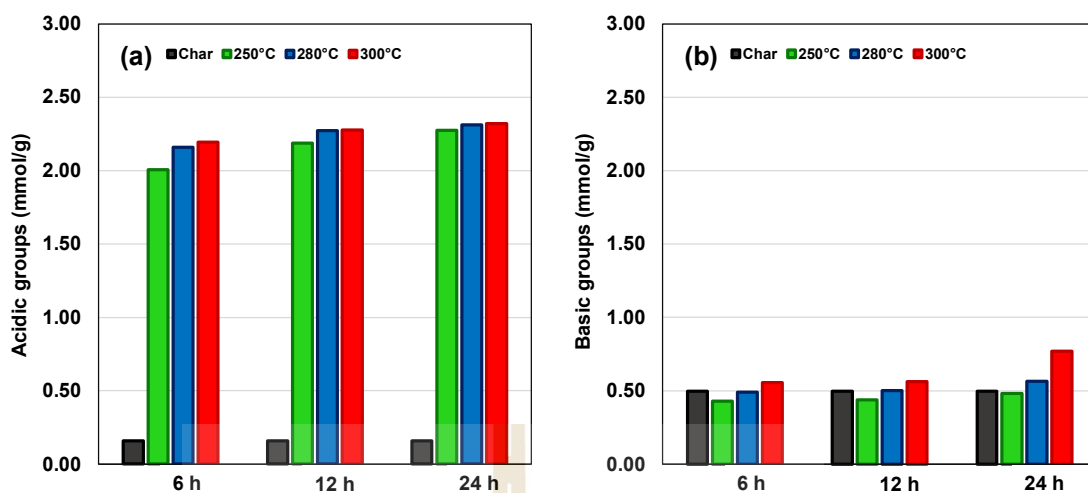


Figure 5.2 The effects of oxidation temperature and time on the amounts of (a) acidic groups and (b) basic groups.

Table 5.4 Effect of oxidation conditions on the porous properties of raw char and oxidized chars

Sample name	Specific surface area	Total pore volume
	(m ² /g)	(cm ³ /g)
Char	171.16	0.065
O250-24h	162.74	0.064
O280-24h	138.83	0.055
O300-24h	128.77	0.050
O300-12h	138.54	0.054
O300-6h	156.13	0.061

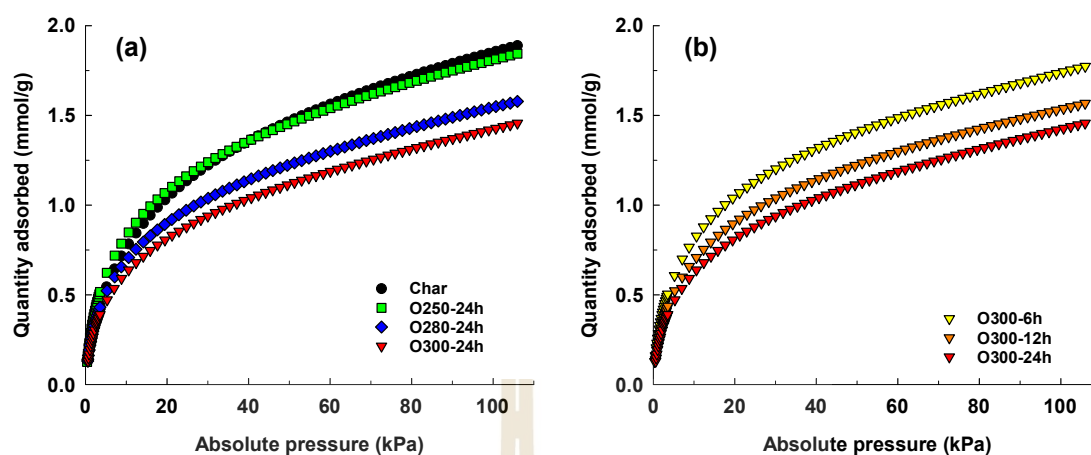


Figure 5.3 Isotherms of CO₂ adsorption at 0°C by the raw char and oxidized chars, (a) effect of oxidation temperature and (b) effect of oxidation time for chars oxidized at 300°C.

Next, FTIR results of char and oxidized char samples produced at different oxidation temperatures are shown in Figure 5.4. Except for the peak intensity, similar FTIR spectra patterns for chars oxidized at different temperatures (250–300°C) were observed. It is also noted that the oxidized chars showed more detected peaks than those of the non-oxidized char. For air-oxidized chars, there exists a sharp peak located at 1710 cm⁻¹, which has been assigned to the stretching vibration of carboxyl groups on the edges of graphitic layer planes or conjugated carbonyl groups (Nandiyanto et al., 2019). There is also another sharp peak at 1595 cm⁻¹ which indicates double bonds or aromatic rings and this is generally found in the carbonaceous materials that are derived from biomass (El-Hendawy, 2006). The huge band at about 1225 cm⁻¹ is attributed to phenolic, carboxyl, and carboxylate groups (Zielke et al., 1996). It is further observed that a small peak was detected at 740 cm⁻¹, which is generally assigned to aromatic compounds. It should be noted that the non-oxidized char hardly showed any significant peaks as compared to the case of oxidized chars. This is consistent with Boehm's titration results shown in Table 5.3 in that the amount of total acidic groups of oxidized chars was greater than that of the non-oxidized char by about 14 times. Therefore, there is a similar agreement in the qualitative and

quantitative variation of the surface functional groups of carbons, as analyzed by the FTIR and the Boehm titration technique.

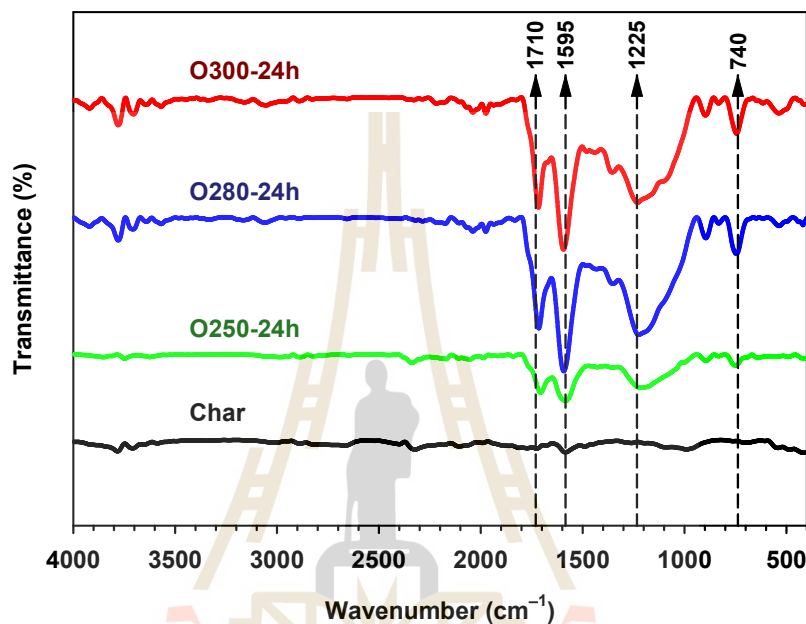


Figure 5.4 The FTIR spectra of the raw char and the oxidized chars at different oxidation temperatures.

5.5.2 Gasification Kinetics and Model Testing

Figure 5.5 shows CO_2 gasification kinetic data derived from the thermogravimetric analyzer of original char and oxidized chars at various gasification temperatures and these data were used to calculate the gasification rates of chars (dX/dt). Figure 5.6 presents the effect of reaction time on the gasification rates of the char samples at various gasification temperatures. It is observed that all the rate curves displayed a distinct pattern of the gasification rate, consisting of an initial rapid increase of the rate, followed by a continuous rising of the rate over most of the reaction time and the final abrupt decrease of the rate till the reaction was completed. The increase

in reaction rate is attributed to the increase in the number of reaction sites caused by the increase of char surface area as the gasification removes more carbon atoms. The final drop in the reaction rate was possibly due to the coalescence of adjacent micropores at a very high reaction conversion (close to unity) that results in the decrease of solid surface area and hence the decrease in the number of reactive sites for the gasification reaction. It is also obvious that the gasification rates of the oxidized chars were higher than that of the non-oxidized char on average by approximately twofold when comparing the maximum gasification rates. Furthermore, the increase in the oxidation temperature gave rise to the increase in the gasification rate. This increase can be explained by the increase in the amount of surface functional groups (see Table 5.3) that could produce more surface active sites by bond disruption when the char was subjected to a high gasification temperature. It can be concluded from this study that a large increase in the CO₂ gasification rate of longan-seed char can be easily and effectively achieved by simply oxidizing the char prior to the gasification step. The maximum oxidation temperature that can be applied for maximizing the gasification rate is primarily determined by the ignition temperature of the solid char.

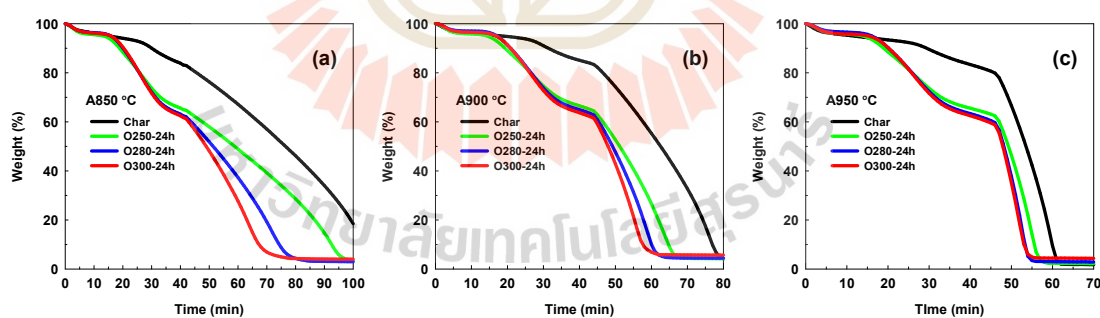


Figure 5.5 Typical TGA curves showing the weight loss vs time for CO₂ gasification at (a) 850°C (b) 900°C and (c) 950°C of the raw char and the oxidized chars (oxidation temperatures of 250–300°C for 24 h).

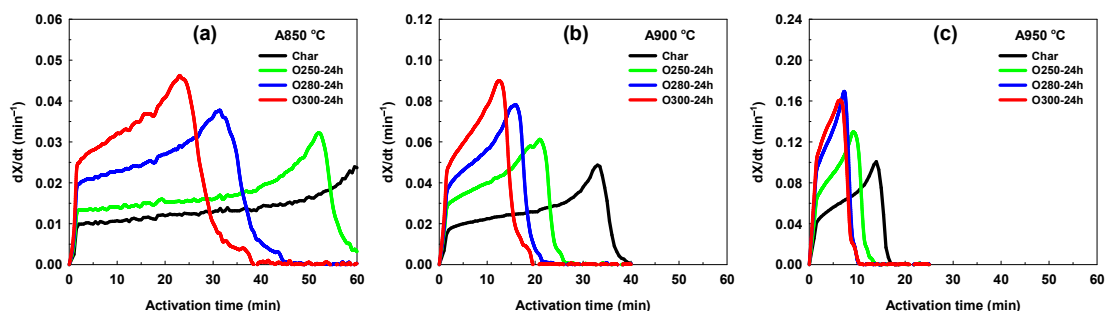


Figure 5.6 Effect of reaction time on the gasification rates (dX/dt) of various char samples at gasification temperatures of (a) 850°C, (b) 900°C, and (c) 950°C.

Next, the gasification rate data of the oxidized chars were tested against the various kinetic models and the results in terms of linear plots are shown in Figure 5.7 for comparison. The fitted parameters of the model along with the regression coefficients are shown in Table 5.5. Based on the values of regression coefficients (R^2), it was found that the experimental gasification kinetic data for all char samples are best described by the MVRM and the order of increasing predictive capability of the models is as follows, VRM < SCM < RPM < MVRM. The superiority of the MVRM as compared to the other models is typically shown in Figure 5.8 for longan seed char being oxidized at 300°C for 24h and gasified at 900°C. It is noted that the RPM could predict the gasification rates reasonably well up to the conversion of about 0.40, beyond which the model underpredicted the experimental results. This indicates that pore coalescence or pore enlargement did not occur in the longan-seed char even up to the relatively high conversion of 0.80, indicating a good dispersion of small pores throughout the carbon mass.

It should be noted that the apparent rate constant (k) of the MVRM varied with the progression of the gasification reaction. The average rate constant (k_m) can thus be obtained by integrating the rate constant from the fractional conversion of 0 to 0.99 according to Equation (5.10). This k_m can be alternatively considered as a char reactivity index for the process of char gasification at a given gasification temperature. The effects of oxidation time and temperature on the reactivity index are summarized in Table 5.5 and presented in Figure 5.9 for char gasification at 900°C. In line with the results of gasification rates previously discussed, the reactivity index

increased with the increase of time and temperature of char oxidation. It is evident from Figure 5.10 that the increase in the amount of acid functional groups by char oxidation would help increase the char reactivity for CO₂ gasification. These results further support the premise that the increase in the gasification rates of chars can be greatly increased by increasing the amount of surface functional groups of char prior to the start of the gasification process. The values of k_m derived at three different gasification temperatures for the oxidized and non-oxidized chars were fitted with the Arrhenius equation, $k_m = k_0 \exp(-E/RT)$.

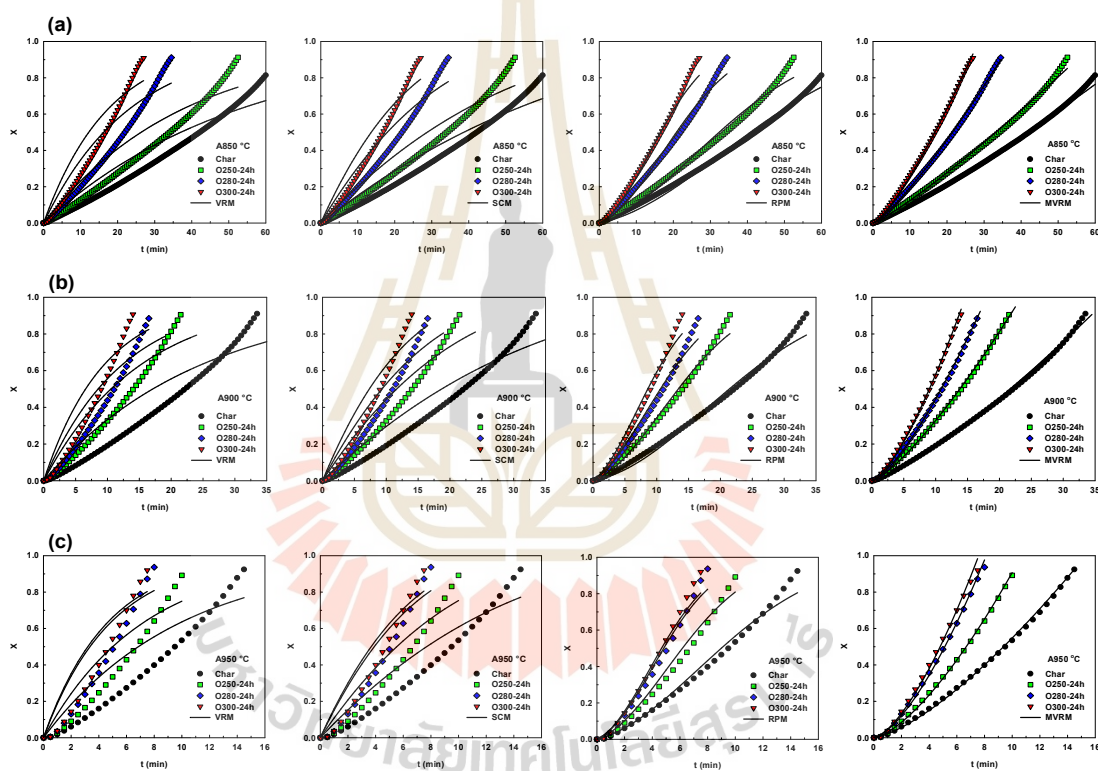


Figure 5.7 Testing gasification models of VRM, SCM, RPM, and MVRM for the carbon samples gasified at the temperatures of (a) 850°C, (b) 900°C, and (c) 950°C.

Table 5.5 The fitted parameters of gasification kinetic models for the carbon samples

Sample name	VRM		SCM		RPM			MVRM			
	k_v	R^2	k_s	R^2	ψ	k_R	R^2	a	b	k_m	R^2
	(min ⁻¹)		(min ⁻¹)		(min ⁻¹)			(min ⁻¹)			
850°C											
Char	0.019	0.947	0.016	0.971	71.04	0.004	0.997	0.005	1.109	0.044	0.999
O250-24	0.026	0.912	0.022	0.956	47.87	0.006	0.993	0.009	1.160	0.085	0.998
O280-24	0.043	0.907	0.034	0.952	82.77	0.008	0.994	0.011	1.239	0.116	0.997
O300-24	0.057	0.907	0.045	0.952	90.87	0.010	0.995	0.013	1.297	0.156	0.996
900°C											
Char	0.041	0.901	0.033	0.948	122.2	0.007	0.994	0.010	1.281	0.118	0.998
O250-6	0.055	0.919	0.045	0.962	137.6	0.008	0.994	0.026	1.071	0.132	0.999
O250-12	0.058	0.905	0.047	0.949	73.21	0.012	0.994	0.015	1.281	0.171	0.998
O250-24	0.066	0.901	0.053	0.947	69.77	0.013	0.993	0.016	1.309	0.190	0.998
O280-6	0.065	0.895	0.053	0.944	51.17	0.015	0.992	0.016	1.310	0.188	0.998
O280-12	0.073	0.905	0.059	0.948	38.05	0.020	0.992	0.017	1.344	0.221	0.997
O280-24	0.081	0.904	0.066	0.946	34.32	0.023	0.992	0.019	1.375	0.252	0.997
O300-6	0.074	0.897	0.060	0.944	47.25	0.019	0.993	0.017	1.349	0.223	0.997
O300-12	0.077	0.904	0.064	0.943	43.63	0.021	0.991	0.019	1.379	0.257	0.997
O300-24	0.106	0.893	0.084	0.941	40.96	0.026	0.990	0.022	1.422	0.312	0.996
950°C											
Char	0.101	0.875	0.081	0.933	71.40	0.020	0.989	0.021	1.413	0.298	0.997
O250-24	0.139	0.889	0.112	0.936	83.80	0.026	0.992	0.030	1.476	0.434	0.996
O280-24	0.207	0.858	0.159	0.924	94.57	0.033	0.986	0.042	1.509	0.573	0.995
O300-24	0.217	0.884	0.168	0.937	79.04	0.038	0.990	0.046	1.515	0.616	0.992

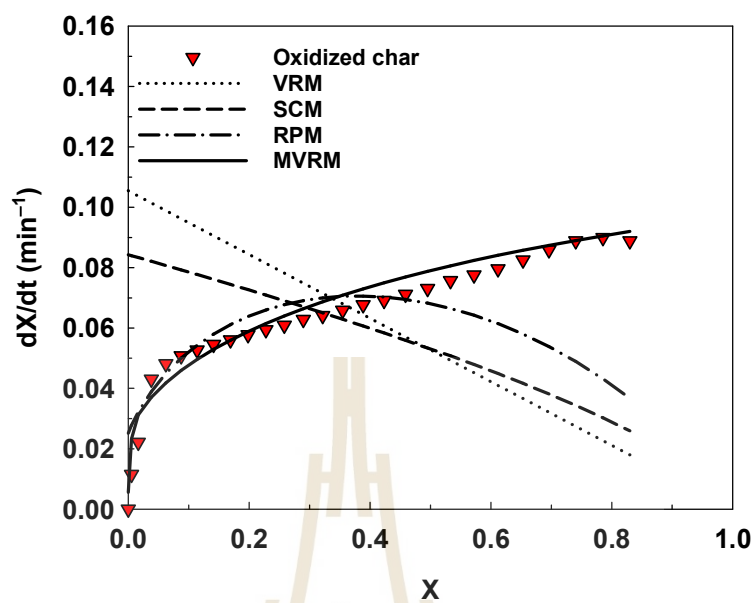


Figure 5.8 Comparison of various gasification kinetic models with experimental kinetic data of char oxidized at 300°C and 24 h at the gasification temperature of 900°C.

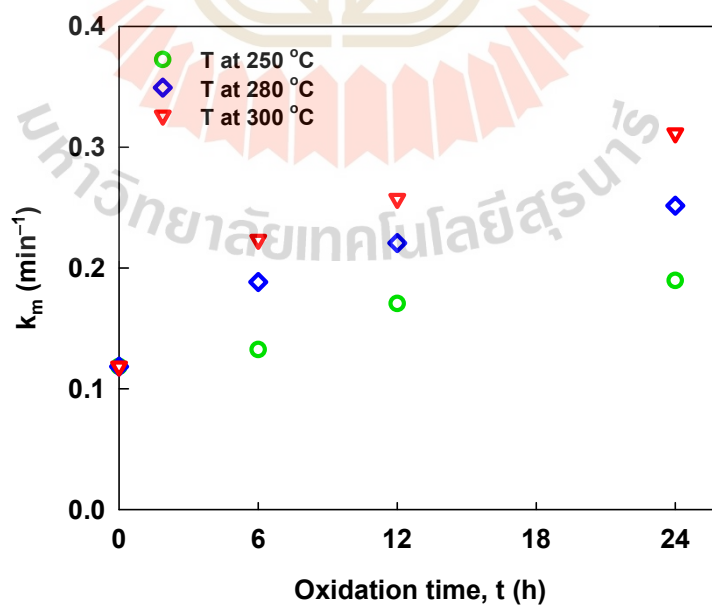


Figure 5.9 Effects of oxidation time and temperature on the char reactivity index (k_m) for char gasification at 900°C.

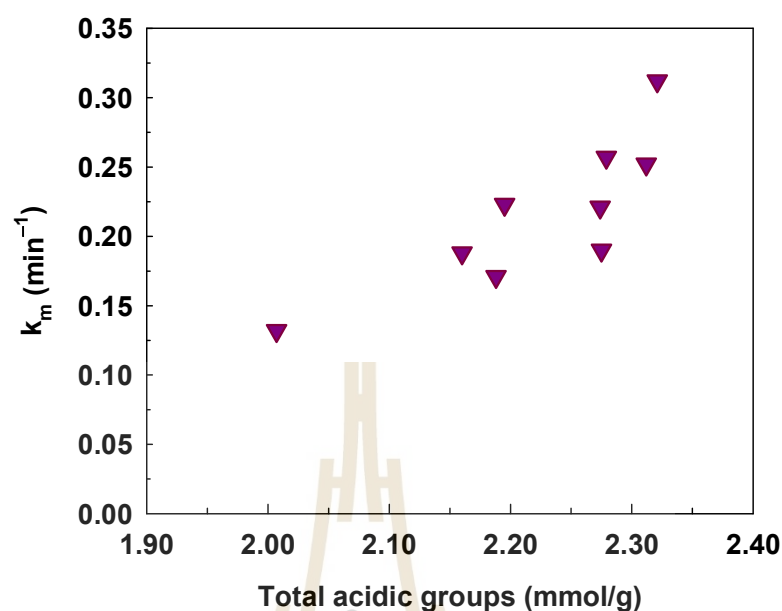


Figure 5.10 The effect of acidic groups on the char reactivity index (k_m).

Table 5.6 lists the values of the derived pre-exponential factor (k_0) and the activation energy (E) from the present study along with those from previous investigations. It can be observed that the activation energy derived from this work varied in the range of 156.87–218.98 kJ/mol. In addition, there was a tendency for both the pre-exponential factor and the activation energy of oxidized chars to decrease as the oxidation temperature increased. Low activation energy will ease the initiation of the gasification reaction, thus allowing the overall reaction to proceed at a faster rate. The increase of char oxidation temperature could increase the amounts of surface functional groups which in turn could produce a large number of surface defects at a high gasification temperature, resulting in the increase of reaction rate and hence the lowering of activation energy. The values of activation energy for gasification derived from various sources of coal and biomass among different investigators are found to vary widely from 35.25–293.25 kJ/mol. This could result from the differences in the precursors used, activation conditions, and the type of kinetic models employed. However, as shown in Figure 5.11, the relationship between the activation energy and the pre-exponential factor of the present and the previous studies is almost linear, thus demonstrating that the activation energies determined in this work are consistent with those of other studies.

Table 5.6 Comparison of the activation energy from various types of precursors

Materials	Gasification Temp.	E	ln k ₀	Model
	(°C)	(kJ/mol)	(min ⁻¹)	
<i>Pinus elliottii</i> (slash pine) ⁽¹⁾	750-900	184.30	18.33	RPM
birch charcoal ⁽²⁾	823-873	262.00	24.80	f(X)
<i>Pinus densiflora</i> ⁽³⁾	850-1050	134.00	9.63	RPM
rice straw ⁽⁴⁾	850-1050	238.30	21.58	RPM
Coconut shell ⁽⁵⁾	800-900	84.80	6.70	MVRM
sub-bituminous coals ⁽⁶⁾	800-1000	174.67	17.00	SCM
peanut shell ⁽⁷⁾	850-1000	163.70	14.08	MRPM
maize cob ⁽⁷⁾	850-1000	132.80	10.63	MRPM
wheat straw ⁽⁷⁾	850-1000	153.20	12.64	MRPM
rice lemma ⁽⁷⁾	850-1000	149.50	12.41	MRPM
pine sawdust ⁽⁷⁾	850-1000	144.70	10.77	MRPM
Zhundong coal ⁽⁸⁾	800-950	146.33	12.92	VRM
Corn cob ⁽⁹⁾	1000	224.90	21.22	RPM
rice straw ⁽¹⁰⁾	700-1000	155.70	16.15	f(X)
Rapeseed oil press cake ⁽¹¹⁾	800-900	222.10	19.56	RPM
Shenfu bituminous coal ⁽¹²⁾	1300	185.02	16.22	VRM
oil palm (PKS) ⁽¹³⁾	800-900	68.67	4.29	MRPM
oil palm (MF) ⁽¹³⁾	800-900	83.71	6.06	MRPM
oil palm (PKS) ⁽¹³⁾	800-900	35.25	0.39	MRPM
peanut straw ⁽¹⁴⁾	729-911	216.85	21.39	SCM
sesame straw ⁽¹⁴⁾	750-921	279.02	28.33	SCM
rice straw ⁽¹⁴⁾	798-947	228.52	21.02	SCM
soybean straw ⁽¹⁴⁾	760-885	293.25	29.73	SCM
cotton straw ⁽¹⁴⁾	773-909	292.10	29.12	SCM
corn straw ⁽¹⁴⁾	766-925	267.78	26.74	SCM
wheat straw ⁽¹⁴⁾	814-941	280.96	26.52	SCM
Longan seed	850-950	218.98	20.32	MVRM
Oxidized char (O250-24h)	850-950	186.32	17.47	MVRM
Oxidized char (O280-24h)	850-950	182.37	17.36	MVRM
Oxidized char (O300-24h)	850-950	156.87	14.93	MVRM

Sources: ⁽¹⁾ (Fermoso et al., 2009); ⁽²⁾ (Khalil et al., 2009); ⁽³⁾ (Seo et al., 2010); ⁽⁴⁾ (Yuan et al., 2011); ⁽⁵⁾ (Tangsathitkulchai et al., 2013); ⁽⁶⁾ (Veca & Adrover, 2014); ⁽⁷⁾ (Wang et al., 2016); ⁽⁸⁾ (Liu et al., 2018); ⁽⁹⁾ (Wang et al., 2018); ⁽¹⁰⁾ (Hu et al., 2019); ⁽¹¹⁾ (Nowicki et al., 2020); ⁽¹²⁾ (Wei et al., 2020); ⁽¹³⁾ (Chew et al., 2020); ⁽¹⁴⁾ (Li et al., 2021)

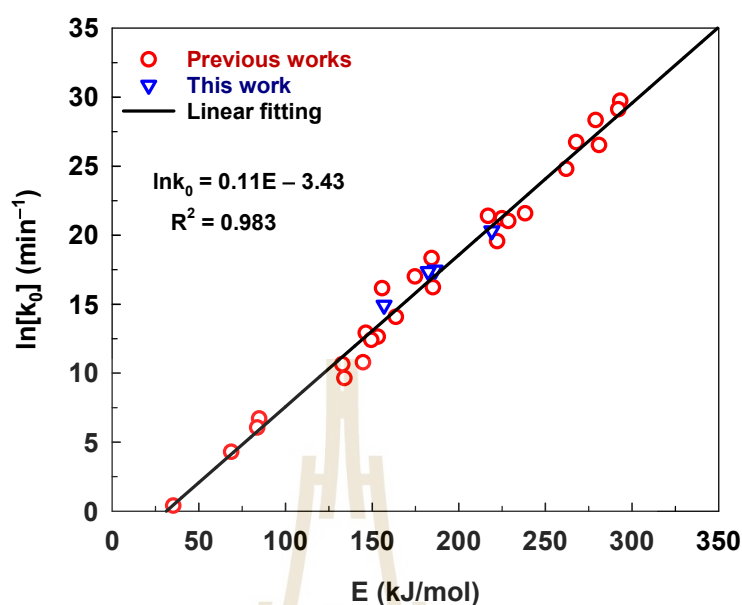


Figure 5.11 The relationship between the activation energy and the pre-exponential factor from the present and previous studies (see references in Table 5.6).

The effect of char oxidation on the gasification kinetics was further analyzed by fitting the rate constant (k) from the MVRM with the Arrhenius equation to obtain the values of activation energy (E) and the pre-exponential factor (k_0). Figure 5.12 shows the variation of both parameters with the reaction conversion. Clearly, the activation energy increased with the increase of fractional conversion. Generally, there exists a spectrum of activation energy of reaction associated with the reaction sites on the carbon surfaces. The increase in the activation energy with increasing conversion intuitively implies that the reaction initially occurs at low activation-energy sites and progresses at other new reaction sites with larger activation energies. It is also obvious that the increase in the oxidation temperature could lower the activation energy of the gasification reaction, hence the increase in the gasification rate of char. Similar results of increasing activation energy with the increase of conversion were also reported by He *et al.* (He *et al.*, 2019) who studied the CO_2 gasification of torrefied poplar-wood char. The increase of activation energy which indicates the increasing

reaction resistance was attributed to the evolutionary change of the cellulosic structure of the bio-char over the course of the gasification reaction.

Figure 5.12 also shows that the pre-exponential factor increased with the increase of conversion and the decrease of oxidation temperature in the same fashion as the activation energy. According to the Arrhenius equation, the pre-exponential factor is the maximum rate constant obtained at zero activation energy or at the gasification temperature approaching infinity.

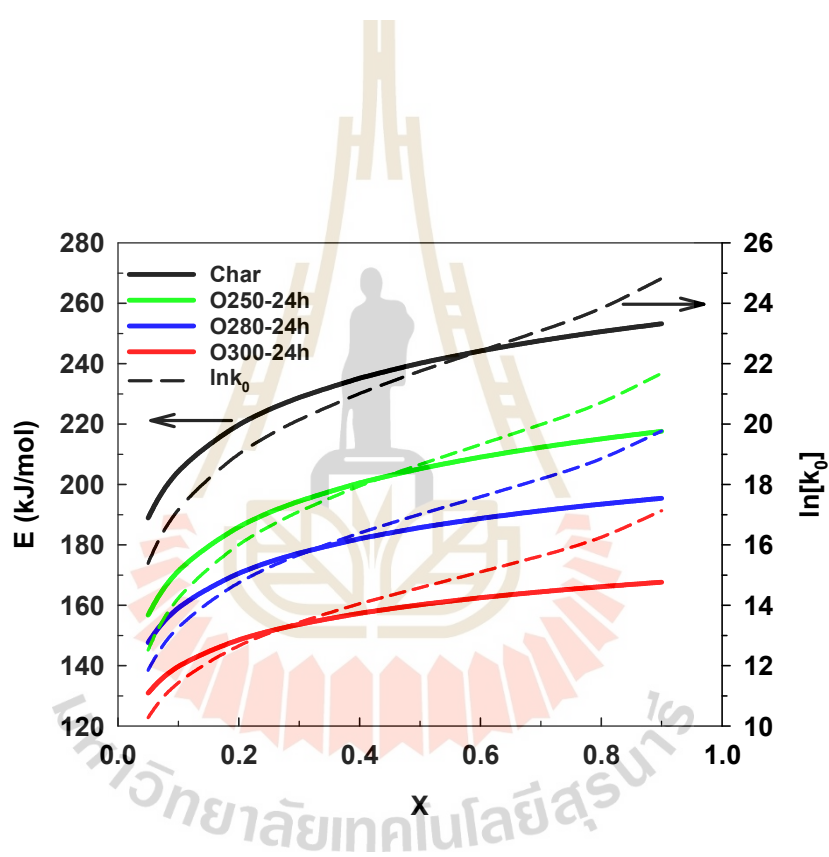


Figure 5.12 Effect of reaction conversion on the activation energy of char gasification for various oxidized longan-seed chars.

From the overall results obtained, the effect of char pre-oxidation on the increase of CO₂ gasification rate of longan-seed char can be schematically represented by the diagram shown in Figure 5.13. The figure shows reaction sites (yellow circles) and developed pores (white circles) presenting in a carbon matrix during the isothermal CO₂ gasification of oxidized longan-seed chars, along with the corresponding normal distribution of activation energy of the reaction. At any level of char conversion, there are two existing types of reaction sites. They are the reaction sites that originate from the removal of carbon atoms via CO₂ gasification and the reaction sites that results from the bond breakage of functional groups formed by air oxidation of char. For a series of low-conversion level chars (Figures 5.13(g) to 5.13(d) to 5.13(a)), increasing oxidation temperature will produce char with a larger number of reaction sites since the char being oxidized at a higher temperature will contain a larger amount of surface functional groups. This will promote a faster gasification rate which results in a decrease in the activation energy of the reaction as shown in the figures. Similarly, the same arguments can be applied to the cases of intermediate and high conversion levels. As the gasification reaction proceeds from a lower to a higher conversion level, illustrated by the transition from Figures 5.13(d) to 5.13(f), a larger number of carbon atoms are consumed through the gasification process. Consequently, this will lead to an increase in both the char surface area and the number of active sites. However, the activation energy appears to increase with the increase of reaction conversion and this stems from the reasoning that the low activation energy sites will react first with the oxidizing gas. It is of particular interest to note, especially for the longan-seed char, that the pores are always created at new separate reaction sites so that the collapse of adjacent pores to form larger-size pores is not observed even at a high char conversion, thus the gasification rate increases continuously with the increase of conversion.

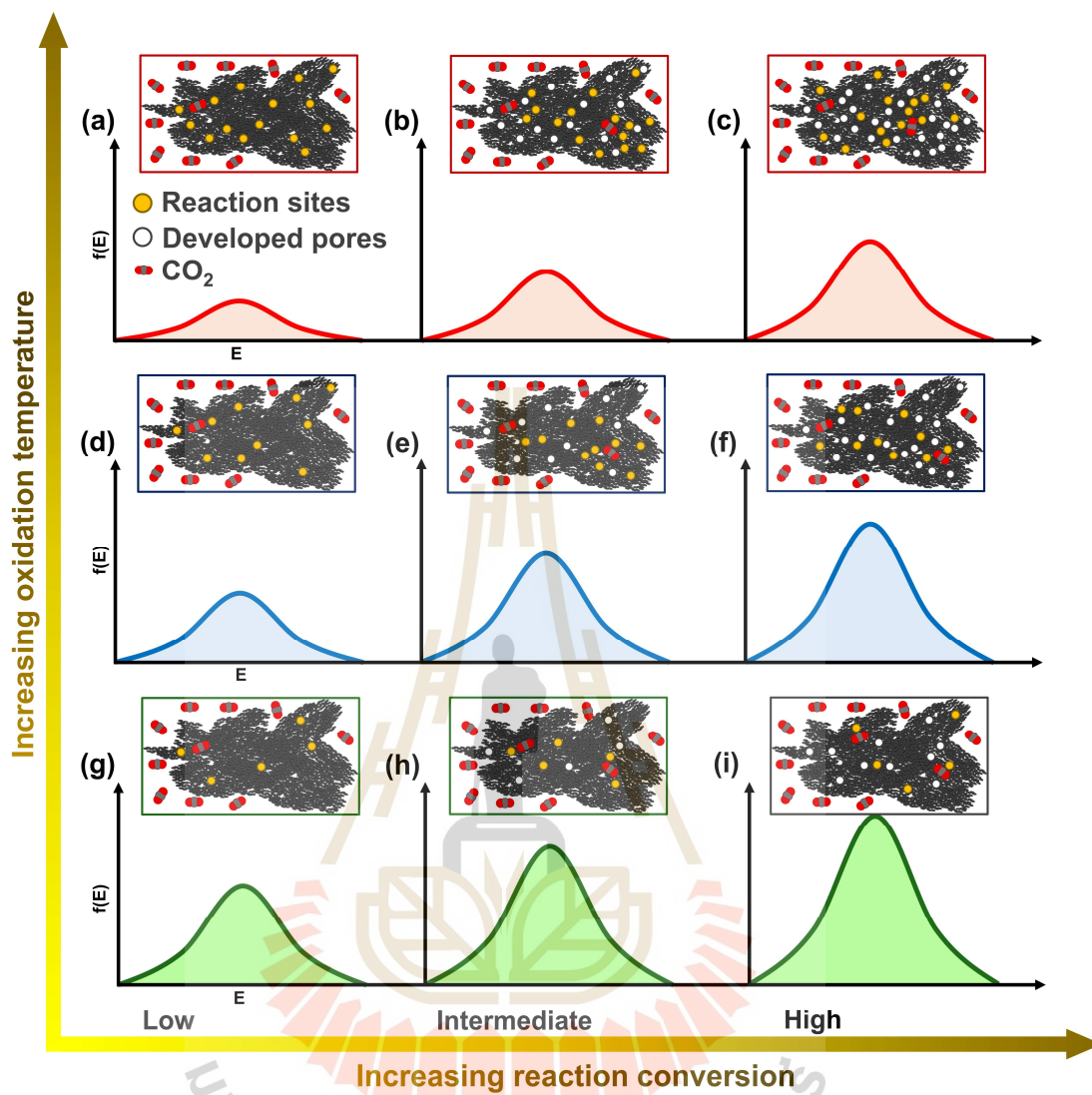


Figure 5.13 Schematic representation for the effect of char oxidation on the isothermal CO_2 gasification kinetics of longan-seed chars.

5.6 Conclusions

Oxidation of longan-seed chars with air prior to the CO₂ activation step helped increase the gasification rate of char substantially. Char reactivity increased with the increase of oxidation temperature in the range of 250 to 300°C. The increase in the char reactivity is the result of an increasing number of reaction sites resulting from the bond disruption of functional groups formed during air oxidation at high gasification temperatures in the range of 850–950°C. The gasification kinetic data derived from TGA were tested with four commonly used kinetic models and the modified volume reaction model (MVRM) provided the best prediction capability. The average rate constant of the MVRM over the course of the reaction (k_m) was used as a measure of char reactivity and was found to increase with the increase of oxidation temperature in the same way as the gasification rate. By fitting the k_m data with the Arrhenius equation, the activation energy of the gasification reaction was found to be in the range of 156.87–218.98 kJ/mol. The incorporation of the char pre-oxidation step prior to the CO₂ activation step is a simple and effective means for increasing the char gasification rates. As well, this technique can be extended to studying the production rate and compositions of synthesis gas produced by the thermal conversion process of gasification.



5.7 References

- Bhatia, S. K., & Perlmutter, D. D. (1980, 1980/05/01). A random pore model for fluid-solid reactions: I. Isothermal, kinetic control. *AIChE Journal*, 26(3), 379-386.
- Boehm, H. P. (1994, 1994/01/01/). Some aspects of the surface chemistry of carbon blacks and other carbons. *Carbon*, 32(5), 759-769.
- Chew, J. J., Soh, M., Sunarso, J., Yong, S.-T., Doshi, V., & Bhattacharya, S. (2020, 2020/03/01/). Isothermal kinetic study of CO₂ gasification of torrefied oil palm biomass. *Biomass and Bioenergy*, 134, 105487.
- Daud, W. M. A. W., Ali, W. S. W., & Sulaiman, M. Z. (2000, 2000/01/01/). The effects of carbonization temperature on pore development in palm-shell-based activated carbon. *Carbon*, 38(14), 1925-1932.
- Dutta, S., Wen, C. Y., & Belt, R. J. (1977, 1977/01/01). Reactivity of Coal and Char. 1. In *Carbon Dioxide Atmosphere. Industrial & Engineering Chemistry Process Design and Development*, 16(1), 20-30.
- El-Hendawy, A.-N. (2006, 03/01). Variation in the FTIR spectra of a biomass under impregnation, carbonization and oxidation conditions. *Journal of Analytical and Applied Pyrolysis*, 75, 159-166.
- Fermoso, J., Stevanov, C., Moghtaderi, B., Arias, B., Pevida, C., Plaza, M. G., Rubiera, F., & Pis, J. J. (2009, 2009/05/01/). High-pressure gasification reactivity of biomass chars produced at different temperatures. *Journal of Analytical and Applied Pyrolysis*, 85(1), 287-293.
- He, Q., Guo, Q., Ding, L., Wei, J., & Yu, G. (2019, 2019/12/01/). CO₂ gasification of char from raw and torrefied biomass: Reactivity, kinetics and mechanism analysis. *Bioresource Technology*, 293, 122087.
- Hu, Y., Yu, H., Zhou, F., & Chen, D. (2019). A comparison between CO₂ gasification of various biomass chars and coal char. *The Canadian Journal of Chemical Engineering*, 97, 1326-1331.
- Kasaoka, S., Sakata, Y., & Tong, C. (1985, 01/01). Kinetic Evaluation of the Reactivity of Various Coal Chars for Gasification with Carbon Dioxide in Comparison with Steam. *Int. Chem. Eng.; (United States)*, 25:1.

- Khalil, R., Várhegyi, G., Jäschke, S., Grønli, M. G., & Hustad, J. (2009, 2009/01/22). CO₂ Gasification of Biomass Chars: A Kinetic Study. *Energy & Fuels*, 23(1), 94-100.
- Lawtae, P., & Tangsathitkulchai, C. (2021). A New Approach for Controlling Mesoporosity in Activated Carbon by the Consecutive Process of Air Oxidation, Thermal Destruction of Surface Functional Groups, and Carbon Activation (the OTA Method). *Molecules*, 26(9), 2758.
- Li, S., Song, H., Hu, J., Yang, H., Zou, J., Zhu, Y., Tang, Z., & Chen, H. (2021, 2021/08/01/). CO₂ gasification of straw biomass and its correlation with the feedstock characteristics. *Fuel*, 297, 120780.
- Li, W., Yang, K., Peng, J., Zhang, L., Guo, S., & Xia, H. (2008, 09/01). Effects of Carbonization Temperatures on Characteristics of Porosity in Coconut Shell Chars and Activated Carbons Derived from Carbonized Coconut Shell Chars. *Industrial Crops and Products*, 28, 190-198.
- Liu, Y., Guan, Y., & Zhang, K. (2018, 2018/04/01). CO₂ gasification performance and alkali/alkaline earth metals catalytic mechanism of Zhundong coal char. *Korean Journal of Chemical Engineering*, 35(4), 859-866.
- Marsh, H., & Rodríguez-Reinoso, F. (2006). *Activated carbon*. Elsevier Science Ltd.
- Nandiyanto, A., Oktiani, R., & Ragadhita, R. (2019, 03/07). How to Read and Interpret FTIR Spectroscopy of Organic Material. *Indonesian Journal of Science and Technology*, 4, 97-118.
- Nowicki, L., Siuta, D., & Markowski, M. (2020). Carbon Dioxide Gasification Kinetics of Char from Rapeseed Oil Press Cake. *Energies*, 13(9), 2318.
- Scott, S. A., Davidson, J. F., Dennis, J. S., Fennell, P. S., & Hayhurst, A. N. (2005, 2005/01/01/). The rate of gasification by CO₂ of chars from waste. *Proceedings of the Combustion Institute*, 30(2), 2151-2159.
- Seo, D. K., Lee, S. K., Kang, M. W., Hwang, J., & Yu, T.-U. (2010, 2010/12/01/). Gasification reactivity of biomass chars with CO₂. *Biomass and Bioenergy*, 34(12), 1946-1953.

- Seung Kim, Y., & Rae Park, C. (2016). Chapter 13 - Titration Method for the Identification of Surface Functional Groups. In M. Inagaki & F. Kang (Eds.), *Materials Science and Engineering of Carbon* (pp. 273-286). Butterworth-Heinemann.
- Tangsathitkulchai, C., Junpirom, S., & Katesa, J. (2013, 01/01). Comparison of Kinetic Models for CO₂ Gasification of Coconut-Shell Chars: Carbonization Temperature Effects on Char Reactivity and Porous Properties of Produced Activated Carbons. *Engineering Journal*, 17, 13-28.
- Veca, E., & Adrover, A. (2014, 2014/05/01/). Isothermal kinetics of char-coal gasification with pure CO₂. *Fuel*, 123, 151-157.
- Wang, G., Zhang, J., Chang, W., Li, R., Li, Y., & Wang, C. (2018, 2018/03/15/). Structural features and gasification reactivity of biomass chars pyrolyzed in different atmospheres at high temperature. *Energy*, 147, 25-35.
- Wang, G., Zhang, J., Shao, J., Liu, Z., Wang, H., Li, X., Zhang, P., Geng, W., & Zhang, G. (2016, 2016/11/01/). Experimental and modeling studies on CO₂ gasification of biomass chars. *Energy*, 114, 143-154.
- Wei, J., Song, X., Guo, Q., Ding, L., Yoshikawa, K., & Yu, G. (2020, 2020/01/16). Reactivity, Synergy, and Kinetics Analysis of CO₂ Co-pyrolysis/Co-gasification of Biomass after Hydrothermal Treatment and Coal Blends. *Energy & Fuels*, 34(1), 294-303.
- Wen, C. Y. (1968, 1968/09/01). NONCATALYTIC HETEROGENEOUS SOLID-FLUID REACTION MODELS. *Industrial & Engineering Chemistry*, 60(9), 34-54.
- Yuan, S., Chen, X.-l., Li, J., & Wang, F.-c. (2011, 2011/05/19). CO₂ Gasification Kinetics of Biomass Char Derived from High-Temperature Rapid Pyrolysis. *Energy & Fuels*, 25(5), 2314-2321.
- Zielke, U., Hüttinger, K. J., & Hoffman, W. P. (1996, 1996/01/01/). Surface-oxidized carbon fibers: I. Surface structure and chemistry. *Carbon*, 34(8), 983-998.

CHAPTER VI

IMPROVING POROUS PROPERTIES OF ACTIVATED CARBON GEL BY THE OTA METHOD

6.1 Abstract

High-surface-area microporous-mesoporous carbons were produced from carbon gel by applying the three consecutive steps of air oxidation, thermal treatment, and activation (the OTA method) to the gel. The formation of mesopores occurs both inside and outside the nanoparticles which form the carbon gel, while micropores are predominantly created within the nanoparticles. The OTA method offered a greater increase in pore volume and BET surface area of the resulting activated carbon in comparison with conventional CO₂ activation either under the same activation conditions or at the same degree of carbon burn-off. Under the best preparation conditions, the maximum values of micropore volume, mesopore volume, and BET surface area achievable using the OTA method were found to be 1.19 cm³/g, 1.81 cm³/g, and 2,920 m²/g, respectively at a 72% carbon burn-off. The larger increase in porous properties of activated carbon gel prepared by the OTA method over those based on conventional activation stems from the effects of the oxidation and heat treatment steps of the OTA method that could produce a large number of reaction sites which lead to efficient pore formation during the following CO₂ activation process. The study also compared the electrochemical performances of activated carbons prepared using conventional activation and OTA methods at the same activation conditions. The results showed that using the OTA method increased the capacitance, suggesting that the incorporation of supermicropores and lower-size mesopores could enhance the rate performance. Therefore, designing porous carbon materials with an appropriate balance of supermicropores and lower-size mesopores could improve the specific surface area and mesopores, leading to high capacitance and enhanced rate performance.

6.2 Introduction

Continuous technological advancements have evoked efforts to apply various techniques for improving material properties as well as exploring new materials with superior properties. Because of the particular characteristics of the carbon element and the diversity of carbon-carbon bonds, carbon materials offer special benefits and are possibly one of the most versatile materials in terms of properties (Kang et al., 2021). From the view of controlling material properties, synthetic carbon materials with high purity and controllable chemistry have attracted much attention because of the flexibility in modifying their final properties. Carbon gels are porous carbon materials, which have a hierarchical and easily accessible porous structure. Carbon gels possess predominant properties as a controllable pore structure with a high porosity, low electrical resistivity as well as a high machinability (Celzard et al., 2012). These outstanding properties provide a remarkable potential for the designing and tailoring of this material for specific applications such as electric double-layer capacitors (Mori et al., 2019; Tsuchiya et al., 2014; Yoo et al., 2021), lithium-ion batteries (Kakunuri & Sharma, 2018; Velez et al., 2019; Wang et al., 2017), electrodes for fuel cells (Alegre et al., 2016; Figueiredo & Pereira, 2013; Kiciński et al., 2021), catalyst supports (Gómez-Cápiro et al., 2018; Guo et al., 2022; Mishra et al., 2017), gas adsorption (Czakkel et al., 2019; Majedi Far et al., 2019; Soni et al., 2022), and water treatment (Ganesamoorthy et al., 2021; Pillai & Kandasubramanian, 2020; Wei et al., 2013).

Pekala and co-workers (Pekala & Kong, 1989; Richard W Pekala, 1989; R. W. Pekala, 1989) were the first to prepare organic gels which can be used as the precursor for carbon gels by applying the sol-gel method in 1989. The most common way to synthesize such organic gels is through the polymerization reaction between resorcinol (R) and formaldehyde (F) with the use of a basic catalyst as the reaction promoter and water as the solvent. Since then, numerous publications on various synthesis and processing conditions for specific applications have appeared in the literature (Al-Muhtaseb & Ritter, 2003; Elkhatat & Al-Muhtaseb, 2011; Rey-Raap et al., 2014; Rey-Raap et al., 2016). However, the RF polymerization reaction is typically a prolonged process that must be carried out over several days. Thus, to reduce the processing time, fast synthesis has been the focal point of several investigations (Calvo et al., 2011; Isaacs Páez et al., 2015; Job et al., 2006). Normally, organic gels

obtained after the drying step are usually rich in oxygen surface chemistry and have a BET surface area (S_{BET}) of less than 500 m²/g (Job et al., 2004; Taylor et al., 2014). Once the organic gels have been obtained, the carbonization step must be performed to increase the carbon content so that thermally stable gels called carbon gels can be obtained. Carbonization temperatures between 800–1000°C are generally applied with a slow heating rate to prevent the excessive shrinkage of the structure (Arenillas et al., 2019). Indeed, the obtained carbon gels have a similar mesoporosity to their parent organic gels, but with more developed microporosity in the polymeric nodules which form it, hence the BET surface area is slightly increased to 500–700 m²/g. Obviously, the utilization of carbon gels in many applications often requires a relatively large surface area with controlled proportions of micropore and mesopore volumes (Pillai & Kandasubramanian, 2020). The physical activation process is one of the most widely used methods to increase surface area due to its simplicity and low cost. Activation processes can increase surface area to values higher than 2000 m²/g (Tsuchiya et al., 2014), which results mainly from the development of microporosity in the carbon gels. Narrow mesopores can also be introduced during the activation process, but introduction usually occurs at a relatively high carbon burn-off through the coalescence of some small pores developed during gasification (Marsh & Rodríguez-Reinoso, 2006).

Recently, a new physical activation method for activated carbon synthesis has been proposed that is capable of producing a relatively large amount of micropores and mesopores in carbons through a process of modified physical activation with CO₂, being referred to as the OTA method (Lawtae & Tangsathikulchai, 2021a). This method consists of three consecutive steps: (1) air oxidation of an initial microporous carbon to a relatively low burn-off level for the introduction of additional surface oxygen functional groups, (2) thermal destruction of the existing functional groups in an inert atmosphere at a high temperature to enhance the surface reactivity through bond disruption, and (3) CO₂ activation of the treated carbon to widen its original micropores as well as to form new micropores. Overall, the advantages of this innovative method are that it is easy to operate, eco-friendly, low cost, and is not associated with any liquid oxidizing agent, since the process is conducted using only air, inert gas, and CO₂. The maximum values of the porous properties of activated carbon obtained from longan seed biomass through three treatment cycles were

found to be $0.600 \text{ cm}^3/\text{g}$ of micropore volume, $0.474 \text{ cm}^3/\text{g}$ of mesopore volume, and $1,770 \text{ cm}^2/\text{g}$ of BET surface area. This activated carbon was proven to be applicable to the removal of methylene blue from an aqueous solution, both in view of adsorption efficiency and capacity (Lawtae & Tangsathitkulchai, 2021b). In this work, the OTA method was applied to improve the porous properties of activated carbon produced from carbon gel.

Therefore, the present work aims to prepare high-surface-area mesoporous carbons from organic gels by applying the OTA method. This work focused on investigating the effect of the surface reactivity of carbon prior to CO_2 activation on improving the porous properties of the activated carbon produced via the OTA method. Surface reactivity was controlled by adjusting conditions of the air oxidation/thermal treatment steps, as well as varying the porous properties of the initial carbon. The underlying mechanism of pore development by the OTA method for the carbon gel and experimental evidence which supports the mechanism were presented.

6.3 Experimental Procedure

6.3.1 Materials

Resorcinol (R, 99.0+%), aqueous formaldehyde solution (F, 37.0 wt.%, containing 5–10% of methanol as a stabilizer), and sodium carbonate (C, 99.8%) were purchased from Wako Pure Chemical Industries, Ltd. N_2 gas of high purity grade (UHP, 99.99%), CO_2 gas of high purity grade (99.99%), and air (99.99%) were supplied in gas cylinders by Air Water Inc. (Japan).

6.3.2 Carbon Gel Preparation

An organic xerogel was prepared through the sol-gel polymerization of resorcinol (R) and formaldehyde (F) in water (W), using sodium carbonate (C) as the catalyst. The preparation procedure described by Pekala and co-workers was adopted (Richard W Pekala, 1989; R. W. Pekala, 1989). Briefly, the molar ratios of R/C, R/F, and the concentration of R were 1000 mol/mol, 0.5 mol/mol, and 0.5 g/mL, respectively. All precursors were mixed by magnetic stirring and first kept under a constant temperature of 30°C for 26 h, and then kept at 85°C for 48 h in an electric oven to complete the gelation and curing stages. The resulting cross-linked gel was

then dried at 150°C for 24 h to obtain the xerogel product. After drying, the xerogel was carbonized in a quartz tube reactor (inner diameter: 50mm, length: 1000 mm) that was inserted in a vertical electric tube furnace (Asahi Rika Co., Ltd., ARF-30K, Japan). The xerogel was heated in a stream of N₂ (100 cm³/min) from room temperature to 250°C at a heating rate of 3.75°C/min, followed by heat treatment at 250°C for 2 h, then was subsequently heated up to 800°C at a heating rate of 4.17°C/min, and held at 800°C for 2 h. Finally, the produced carbon gel was kept in a constant-temperature vacuum dryer (Tokyo Rikakikai Co., Ltd., VOS-210C) for subsequent experiments.

6.3.3 Activated Carbon Production

High surface area mesoporous carbons were prepared by applying the OTA method (Lawtae & Tangsathitkulchai, 2021a) to the carbon gel. Briefly, the derived carbon gels were oxidized in a quartz tube reactor by heating them in an air stream (50 cm³/min) from room temperature to the required oxidation temperature of 350°C and held at this temperature for 6 h. The purpose of this step was to create additional oxygen functional groups within the carbons. Then, the oxidized carbon was heated at 1000°C for 1 h under a flow of N₂ (50 cm³/min) to remove oxygen functional groups. By this high-temperature thermal treatment, the surface reactivity of the treated carbons was expected to increase due to the production of a large number of unpaired electrons caused by the thermal destruction of the bonding of the functional groups. After that, the sample was activated at 1000°C for 1 h under a flow of CO₂ (50 cm³/min) which resulted in the production of large amounts of mesopores and micropores in the gel matrix. The activated carbon prepared from the carbon gel by the OTA method was denoted as CG-OTAx, where CG stands for carbon gel, and the symbol x represents the activation time varying from 1–3 h. The activated carbon prepared by the conventional activation method using CO₂ was denoted as ACx, where AC stands for activated carbon derived under the activation temperature of 1000°C, and the symbol x also represents the activation time (1–4 h). The carbon burn-off for the activation step was calculated by Equation (6.1), where W_i and W_f denote the weight of carbon gels before and after the activation process, respectively.

$$\text{Burn-off (\%)} = \frac{W_i - W_f}{W_i} \times 100 \quad (6.1)$$

6.3.4 Characterization

The porous properties of the derived carbon gels and activated carbons were determined from their N₂ adsorption isotherms measured at -196°C using an adsorption analyzer (BEL Japan, BELSORP-mini). The BET surface area (S_{BET}) was calculated from the N₂ adsorption isotherm data by applying the Brunauer-Emmett-Teller (BET) equation (Brunauer et al., 1938). The micropore volume (V_{mi}) was determined from the Dubinin-Radushkevich equation (Dubinin, 1975). Using V_{mi} and total pore volume calculated at the relative pressure (P/P_0) of 0.96 ($V_{0.96}$), the mesopore volume ($V_{\text{me}} = V_{0.96} - V_{\text{mi}}$) was then obtained. The total pore volume (V_{T}) was estimated from the amount of N₂ gas adsorbed at P/P_0 of 0.99 by converting it to the corresponding volume of N₂ in the liquid state at -196°C. The mesopore size distributions were determined by applying the Dollimore-Heal (DH) method (Dollimore & Heal, 1964).

The surface functional groups of the carbon samples were analyzed by the TPD method. The sample was weighed and loaded into a test-tube-shaped quartz reactor and then heated up under vacuum at a heating rate of 10°C/min. The gases emitted from the samples were then continuously analyzed by a quadrupole mass spectrometer (Qutee MGM-102, Ulvac). The desorption rates of the emitted gases were calculated from the area under the curves of each gas in the TPD spectra. The amount of each type of oxygen-containing functional group was determined through peak separation of the TPD spectra of CO₂ and CO, as described in the supplementary information.

A thermogravimetric analyzer (NETZSCH STA 2500, Japan) was applied to determine the reactivity of the mesoporous carbons toward the CO₂ gasification reaction. The carbon sample was loaded into a platinum crucible (70 μL capacity) of the thermogravimetric analyzer and heated from room temperature to 1000°C at a heating rate of 20°C/min under a constant flow of N₂ (10 cm³/min). When the final gasification temperature was reached, the gas flow was switched from N₂ to CO₂ (10 cm³/min), and the sample was held at this temperature for 1 h. The sample weight loss via the gasification reaction was continuously recorded as a function of time and the data collected were used for the computation of carbon reactivity. The thermal decomposition behavior of the xerogel precursor was also studied using the thermogravimetric analyzer (NETZSCH STA 2500, Japan) by non-isothermal heating

from room temperature to the final temperature of 1000°C, using a heating rate of 5°C/min under a constant flow of N₂ (10 cm³/min).

In addition, to evaluate the electrochemical performance of the prepared samples, they were mixed with polytetrafluoroethylene (PTFE 6J, Du Pont-Mitsui Fluorochemicals Co., Ltd.) as a binding agent and carbon black (CB) (Denka Black, Denki Kagaku Kogyo Co., Ltd.) as a conductive agent. The ratio of the mass of the carbon, PTFE, and CB was maintained at 8:1:1. The mixture was subsequently homogenized by kneading with a mortar and pestle and stretched into a sheet using a heat roll press machine until a thickness of approximately 0.1 mm was achieved. The electrodes were then dried at 120°C under vacuum for 24 h. A quantity of 1 ± 0.5 mg of the prepared sample was taken and pressed onto a nickel mesh (100 mesh, Nilaco Corp.) to serve as the working electrode. Electrochemical measurements were performed in beaker-type three-electrode cells containing a platinum mesh counter electrode, Ag/Ag⁺ reference electrode (RE-1C, BAS Inc.), and 1 M H₂SO₄ electrolyte solution (Wako Pure Chemical Industries Ltd.). Cyclic voltammetry measurements were conducted using a potentiostat (HSV-100, Hokuto Denko Corp.) by charging and discharging the cells within a potential range of 0–0.6 V and current densities ranging from 0.5–10 A/g. The capacitance of the sample, C (F/g), was calculated using Equation (6.2), where $\Delta V/\Delta t$ represents the slope of the discharging curves (V/s) and i represents the current density (A/g).

$$C = \frac{i}{-\Delta V / \Delta t} \quad (6.2)$$

6.4 Results and Discussion

6.4.1 Thermal Decomposition Behavior of the Organic Xerogels

Figure 6.1 shows the TG curve recorded during the non-isothermal heating of the xerogel precursor under an N₂ flow (10 cm³/min) in the TGA from room temperature to the final temperature of 1000°C, using the heating rate of 5°C/min. Weight loss of about 0.5 wt% was observed when the sample was heated from room temperature to about 100°C, and this was attributed mainly to the release of residual moisture remaining in the precursor. Then, significant weight loss

started to occur, which continued with the increase in pyrolysis temperature to about 750°C. Two peaks, one at around 380°C and the other at around 540°C, occurred in the DTG curve derived from the TG curve, showing the main pyrolysis decomposition of the xerogels progressing over the range between these two temperatures. The first peak probably corresponds to the elimination of H₂O formed from the condensation of OH groups, while the second peak could correspond to the release of CO₂ and CH₄ or other organic molecules as well as the desorption of adsorbed organic compounds (Job et al., 2004). The second region of the TG curve for the temperature above 750°C showed a slow decrease in the remaining weight and finally approached a constant solid carbon yield of about 55 wt%. These results are consistent with the findings of other investigators (Lin & Ritter, 2000; Mohaddespour et al., 2017; Moreno et al., 2013).

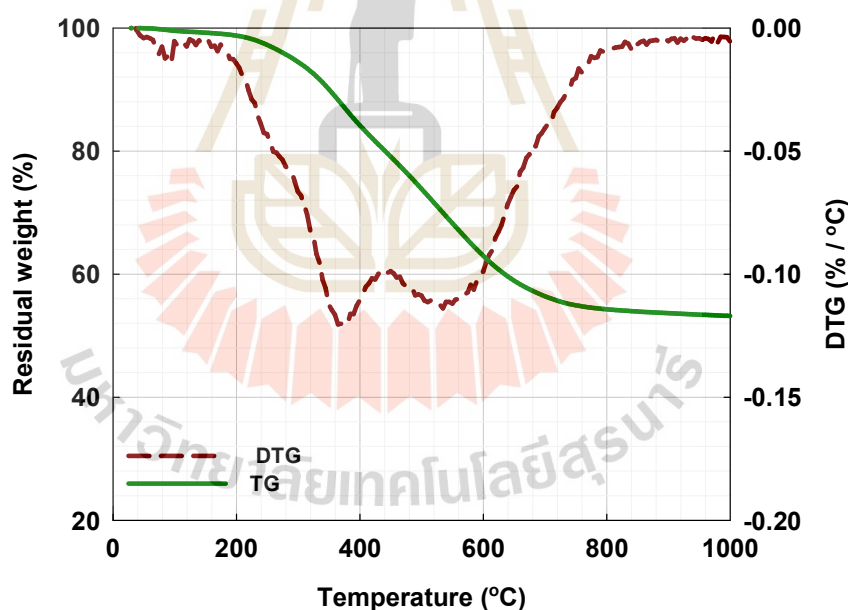


Figure 6.1 The residual weight (TG) and the weight loss rate (DTG) curves for non-isothermal pyrolysis in N₂ of the organic xerogels using a thermogravimetric analyzer (TGA).

6.4.2 N₂ Adsorption Isotherms of Prepared Activated Carbons

A mesoporous carbon gel was synthesized at a high R/C ratio of 1000 mol/mol. Typically, the use of a low concentration of the catalyst would lead to the formation of large resorcinol-formaldehyde (RF) particles leading eventually to the formation of a network akin to a string-of-pearls (Pekala & Schaefer, 1993), which has interparticle spaces corresponding to mesopores, while micropores are formed within the precursor RF nanoparticles. Therefore, the isotherms of all samples should represent the mesoporous structure. The adsorption isotherms of N₂ at -196°C are presented in Figure 6.2 for the activated carbons prepared by the conventional activation method and by the OTA method. All samples exhibited Type I adsorption isotherms with a sharp rise at extra-low relative pressures, indicating the presence of abundant micropores (Song et al., 2022). The high relative pressure region was characterized by a combination of Type I and Type IV isotherms, indicating a typical microporous/mesoporous structure (Yan et al., 2022; Zheng et al., 2022). Additionally, the hysteresis loop shape resembled Type H2(b) of the IUPAC classification of hysteresis loops (Thommes et al., 2015), which indicates the presence of interconnected networks of pores with similar shapes in the adsorbent.

The N₂ isotherms in Figure 6.2B indicate that the OTA samples adsorbed larger amounts of N₂ when compared with the AC samples (Figure 6.2A) prepared under the same activation conditions of time and temperature or activated to a comparable carbon burn-off. These results imply that the OTA method offers an increase in the number of active sites for the CO₂ gasification reaction resulting in improved porous properties under comparable activation conditions. The formation and destruction of oxygen functional groups prior to CO₂ gasification lead to a significant increase in carbon reactivity due to the increasing number of unpaired electrons generated by bond disruption (Lawtae & Tangsatitkulchai, 2021a). The carbon reactivity for CO₂ gasification will be discussed in section 6.4.5.

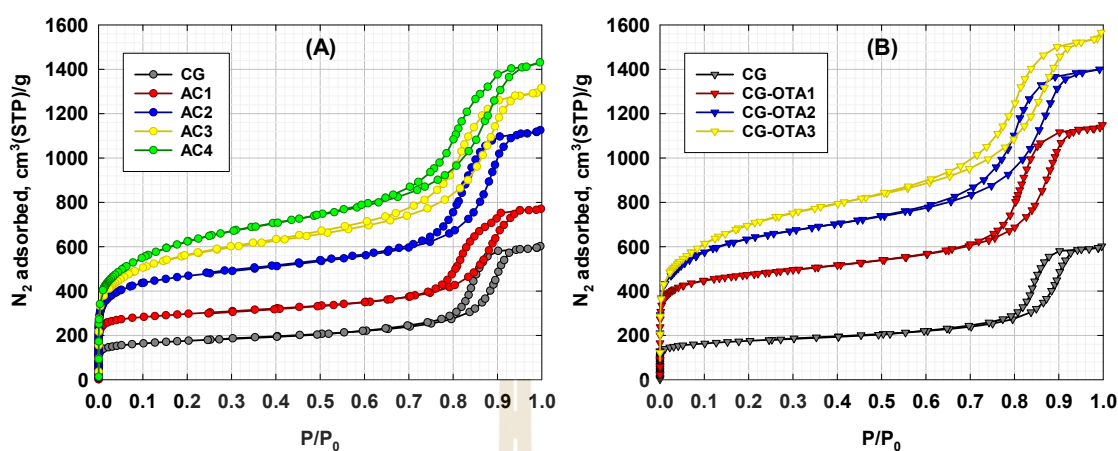


Figure 6.2 N₂ adsorption isotherms at -196°C of mesoporous activated carbons prepared by (A) the conventional activation method and (B) the OTA method at the same activation temperatures of 1000°C .

6.4.3 Porous Properties of Prepared Activated Carbons

Carbon xerogels have a hierarchical porous structure, which is a unique porous structure that is completely distinct from most porous carbons. Due to their polymeric structure of interconnected nodules, the carbon xerogel essentially includes both micropores and mesopores. Basically, the interparticle spaces of the carbon gel form its mesoporous structure which is relatively stable even when a subsequent activation process is applied (Canal-Rodríguez et al., 2017). On the other hand, the activation process is directly responsible for the generation of micropores within the nanoparticles which form the carbon. Table 6.1 compares the porous properties of activated carbons prepared from the carbon gel by the conventional method and by the OTA method. If we consider first the results of activated carbons produced by the conventional activation method (AC1–AC4), the BET surface area, the micropore volume, the mesopore volume, and the total pore volume increased with the increase in activation time from 1 to 4 h.

Concerning the effect of gasification time on the development of activated gel surface area, it was found from Table 6.1 that the rate of increase of surface area for both the AC series and the OTA series tended to decrease with time. This means that the surface area will finally reach a constant value at a limiting gasification time. We fitted the data in Table 6.1 with a second-order polynomial

function and found that the limiting times were approximately 4.96 and 3 hours, respectively, for the AC and OTA sample series. Therefore, the carbon gel burn-off will be less than 100% even if a very long gasification time is used. This could occur because only part of the total surface area was available for gasification since the carbon gel was gasified in the packed mode in a tube reactor, thus resulting in the presence of a dead spot (inaccessible surface area) at the point of particle contact. If, in another case, all the particle surface area is available for gasification, the increase in the gasification time may not be able to gasify the carbon to the condition of complete conversion. This could occur if a certain number of reaction sites on the carbon surface has a lower energy level than the activation energy of the reaction. Furthermore, the mesopore volume was higher than the micropore volume for all activation times which emphasizes the unique particle-network structure of the carbon gel. By increasing the activation time, the carbon burn-off increased from 24.5 to 89.0% which results from the removal of more carbon atoms through the CO₂ gasification reaction leading to the improvement of porous properties. AC4 prepared by conventional activation had the maximum BET surface area of 2,160 m²/g with a mesopore volume of 1.292 cm³/g corresponding to about 58.7% of the total pore volume.

Next, the porous properties of activated carbons produced by the OTA method (CG-OTA1-3) are presented. It was noticed that the activated carbons from the OTA method showed remarkably higher porous properties, that is, micropore volume, mesopore volume, and BET surface area for the same activation time as compared to those obtained through conventional activation, for example, by comparing sample AC1 with CG-OTA1, AC2 with CG-OTA2 or even for the same % carbon burn-off (see Figure 6.3). The OTA method using 3 h of activation time produced activated carbon (sample CG-OTA3) with the highest porous properties of 2,540 m²/g BET surface area, 0.987 cm³/g of micropore volume (41.2%), and 1.38 cm³/g of mesopore volume (57.4%). These results clearly illustrate that under the same activation conditions (time and temperature), the OTA method was able to remove more carbon atoms via the CO₂ gasification reaction than the conventional method. Therefore, this finding strongly indicates that the introduction of the oxidation and thermal treatment steps prior to the activation step could produce a larger number of reactive sites that favor pore development in the subsequent

gasification reaction. The OTA method is an effective means for increasing both the micropore volume and mesopore volume of activated carbons derived from carbon gels.

Now, consider only the development of mesopore size in the size distributions of activated carbons determined by the DH method. The results are shown in Figure 6.4. For the sake of discussion, the developed mesopores are divided into four size ranges, that is, 2–5, 5–10, 10–20, and 20–50 nm. In terms of pore volume, the presence of macropores (pores with sizes larger than 50 nm) is considered insignificant. First, for activated carbons of both the AC series (see Figure 6.4A) and the OTA series (Figure 6.4B), each sample (for each activation time) showed approximately a normal pore size distribution with a peak occurring at a pore size in the range of 10–20 nm. Thus, it may be inferred that the gasification reaction of carbon atoms with CO_2 , leading to pore development in activated carbon, should occur in a random manner. In other words, the active sites (reaction sites) for gasification should be distributed randomly on the carbon surface with a distribution of reaction activation energy. The extent of the gasification reaction, therefore, is dependent on both the number and reactivity of the active sites. Second, the highest production of mesopores in the pore size range of 10–20 nm indicates that the active sites probably concentrate mostly in this pore size range. Finally, for pore sizes in the range of 2–10 nm, there is a clear tendency for the mesopore volume to increase with the increase in activation time for both the AC series and the OTA series. It is probable that the distribution of activation energy of the active sites in this pore size range is relatively wide, thus the increase in activation time would help increase the probability of carbon- CO_2 reaction to occur, leading to mesopore development. There is no general definite trend for the variation of pore volume as a function of activation time for pore sizes in the range of 10–50 nm for both carbon series, except that the pore volume of mesopores remained relatively unchanged for the pore size range of 20–50 nm in both carbon series. This has to do with the nature of the distribution of both the number and activation energy of the active sites which are governed by the preparation conditions of the precursor carbon for activated carbon production. Overall, for the same activation time, the OTA method could produce activated carbons with a higher mesopore volume for all pore size ranges as compared to the conventional activation method.

Table 6.1. Textural properties of mesoporous carbons prepared by the conventional method and the OTA method

Sample name	S_{BET} (m^2/g)	V_{mi} (cm^3/g) (%)	V_{me} (cm^3/g) (%)	V_{T} (cm^3/g)	Burn-off (%)	Yield (%)
CG	631.66	0.254 (27.5)	0.657 (71.3)	0.922	–	–
AC1	1117.75	0.447 (37.5)	0.735 (61.7)	1.191	24.46	75.54
AC2	1702.64	0.677 (39.1)	1.038 (59.9)	1.732	51.91	48.09
AC3	1989.47	0.818 (40.8)	1.169 (58.2)	2.007	70.14	29.86
AC4	2160.32	0.879 (40.0)	1.292 (58.7)	2.200	89.04	10.96
CG-OTA1	1748.31	0.719 (40.9)	1.030 (58.5)	1.760	48.33	51.67
CG-OTA2	2313.99	0.925 (42.7)	1.223 (56.5)	2.166	67.09	32.91
CG-OTA3	2537.25	0.987 (41.2)	1.376 (57.4)	2.398	86.91	13.09

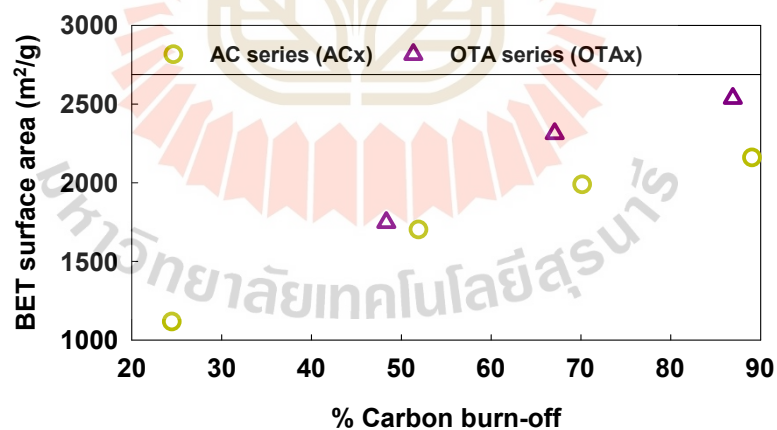


Figure 6.3 Effect of carbon burn-off on the BET surface area of carbon products by the OTA and the conventional preparation methods.

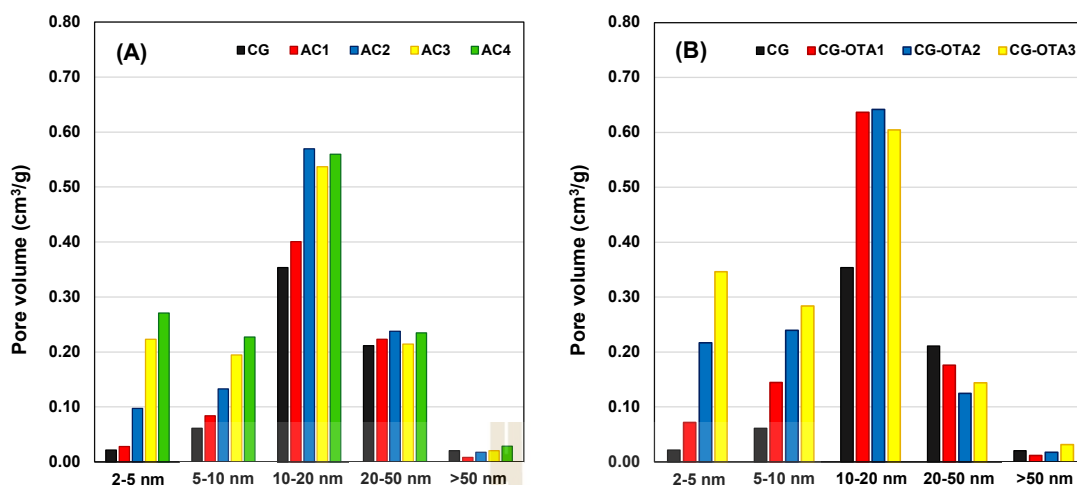


Figure 6.4 Pore size distributions of activated carbon gels determined by the DH method for (A) the AC series and (B) the OTA series.

6.4.4 The Effect of Porous Properties of the Initial Carbon Precursor

Obviously, the porous properties of activated carbons produced by the OTA method from a given precursor will depend on the preparation and treatment conditions including oxidation and heat treatment conditions, activation conditions, porous properties of the initial carbon precursor, etc. This section reports the effect of porous properties of the initial carbon precursor on mesopore development by the OTA method.

Activated carbons were prepared using the OTA method from three different carbon precursors with increasing porosity, namely CG, AC1, and AC2, giving the corresponding activated carbon products designated as CG-OTA, AC1-OTA, and AC2-OTA, respectively. Figure 6.5 shows the N_2 adsorption isotherms of the three activated carbon samples measured at -196°C . The derived isotherms display type IV isotherms of the IUPAC classification, typical of mesoporous adsorbents with a distribution of pore sizes. The sizes of the hysteresis loops are approximately the same but the relative pressure at which the desorption branch closes the loops tended to decrease in the order $\text{AC2-OTA} < \text{AC1-OTA} < \text{CG-OTA}$. The amount of N_2 adsorbed increased in the following order, $\text{AC2-OTA} > \text{AC1-OTA} > \text{CG-OTA}$, which is indicative of increases in the surface area and pore volume of the respective carbon

samples. The porous properties of activated carbon products, calculated from the adsorption isotherms, are listed in Table 6.2. All porous properties of activated carbons produced from each precursor by the OTA method were significantly higher than those of the original precursors. For example, increases in BET surface area of about 177, 120, and 72% were observed in activated carbons produced from CG, AC1, and AC2, respectively. Figure 6.6 shows the correlation between the porous properties of the initial precursors and those of the corresponding activated carbons, from which a linear relationship can be observed. This signifies that the number of reaction sites for CO₂ gasification increased proportionally with the increase in the surface area of the precursors. Again, the OTA method has proved to be an excellent process for increasing the porous properties of activated carbon produced from carbon gel.

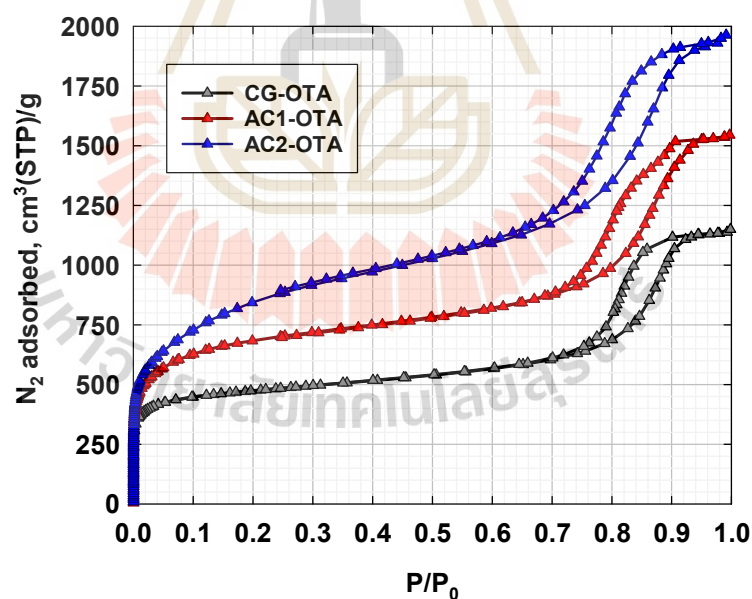


Figure 6.5 N₂ adsorption isotherms (−196°C) of mesoporous activated carbons prepared under the same activation conditions by the OTA method from carbon precursors having different initial porous properties.

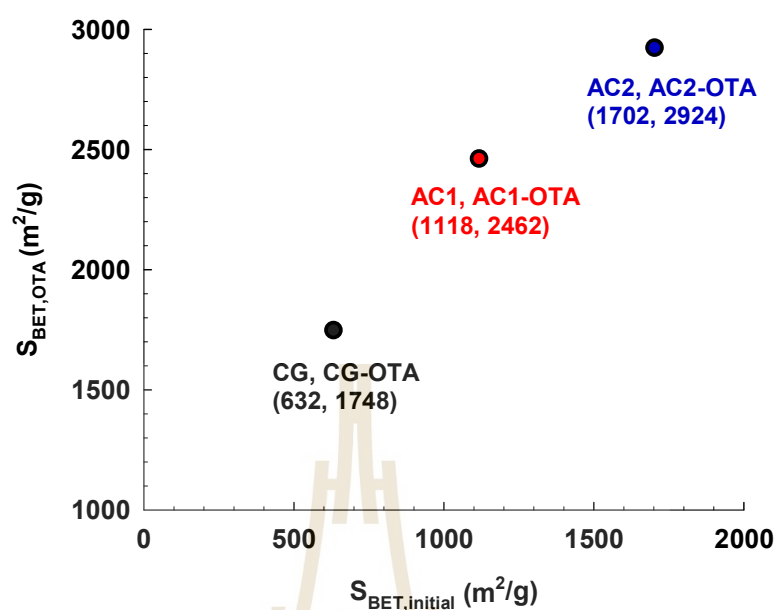


Figure 6.6 Effect of the surface area of initial precursors on the surface area of activated carbon produced by the OTA method.

Table 6.2 Textural properties of mesoporous carbons prepared by the OTA method from precursors having different initial porous properties

Sample name	S_{BET}	V_{mi}	V_{me}	V_T	Burn-off	Yield
	(m ² /g)	(cm ³ /g) (%)	(cm ³ /g) (%)	(cm ³ /g)		
CG	631.66	0.254 (27.5)	0.657 (71.3)	0.922	–	–
CG-OTA	1748.31	0.719 (40.9)	1.030 (58.5)	1.760	48.33	51.67
AC1	1117.75	0.447 (37.5)	0.735 (61.7)	1.191	24.46	75.54
AC1-OTA	2462.51	0.994 (41.7)	1.352 (57.4)	2.384	62.09	37.91
AC2	1702.64	0.677 (39.1)	1.038 (59.9)	1.732	51.91	48.09
AC2-OTA	2923.84	1.188 (39.2)	1.809 (59.6)	3.034	76.31	23.69

Next, the development of micropores and mesopores in activated carbons produced by the OTA method from carbon precursors with different porous properties (CG, AC1, and AC2) is further explored in more detail. We studied the pore development in terms of the pore size distribution for the following carbon samples, CG, AC1, AC2, CG-OTA, AC1-OTA, and AC2-OTA. The N₂ adsorption isotherms of the carbon samples were measured from a low relative pressure (P/P_0) of 1×10^{-6} to 1 by using a high-performance adsorption analyzer (BELMax, Belsorp, Japan), and the derived information was analyzed by the NLDFT method to obtain micropore and mesopore size distribution data. The obtained results are presented graphically and numerically in Figure 6.7 and Table 6.3, respectively, for the following pore size ranges: <0.7 nm (ultra-micropores), 0.7–2 nm (super-micropores), and 2–10 nm (lower-size mesopores) and 10–50 nm (upper-size mesopores).

Starting from the CG precursor, Table 6.3 indicates that most pores are concentrated in the mesopore size range of 2–50 nm (77.4 volume %) which in part reflects the mesoporous structure of the carbon gel. For the activated carbon AC1, derived by activating the CG sample with CO₂ for 1 h at 1000°C, the proportion of its upper-size mesopores notably decreased from 61.2 to 50.1% while those of smaller pores (0.7–10 nm) tended to increase. For the pore volume, the percentage increase of pore volume was 6.2, 108, 44, and 5.7% for the ultra-micropores, the super-micropores, the lower-size mesopores, and the upper-size mesopores, respectively. The large percentage increase of the super-micropores indicated that the micropores were created inside the particles at a much faster rate as compared to the development of mesopores. This could be attributed to the large internal surface area of the nanoparticles which favors the creation of micropores by gasification. It is further noted that the percentage increase of the upper-size mesopore volume was much lower than that of the lower-size mesopore volume (5.7% vs 44%). This appears to confirm that the upper-size mesopores are possibly created outside the carbon gel particles (inter-particle pore formation), while the lower-size mesopores are developed inside the particles (intra-particle pore formation), while the lower-size mesopores are developed inside the particles (intra-particle pore formation) by the enlargement of smaller micropores via the gasification reaction. It should be noted that the average size of interparticle spaces of carbon gels in the range of 17–80 nm has been reported (Job et al., 2006; Nagaishi et al., 2023) that approximately covers

the range of the upper-size mesopores in this work. The AC2 sample, which was derived by activating the AC1 sample for 1 h or by activating the CG sample for 2 h, showed a decrease in the proportional percentage of the upper-size mesopores from 50.1% to 43.9% but an increase from 18.1% to 21.6% was observed for the lower-size mesopores.

The CG-OTA sample, which was prepared from the CG precursor by the OTA method, showed significant increases in pore volume for all pore sizes, by about twofold. Furthermore, the order of increase in the proportional percentage of pore volumes of CG-OTA was the same as that of the CG sample, that is, upper-size mesopores > super-micropores > lower-size mesopores > ultra-micropores. However, a drop in the percentage of upper-size mesopore volume from 61.2 to 42.9% was observed which further substantiates that pore development mostly occurs inside the nanoparticles which form the carbon gel. Similar results were obtained when comparing AC1 with AC1-OTA and AC2 with AC2-OTA. In view of carbon preparation methods, both micropore and mesopore volumes of CG-OTA prepared by the OTA method were higher than those of the sample prepared by the conventional method (AC1) on the average by 50%, while similar results were obtained when comparing AC1-OTA with AC2. When the surface area of the precursor series increased (CG < AC1 < AC2), the volume percent of the upper-size mesopores in the activated carbons produced by the OTA method decreased from 42.9 to 29.6% but an increase in the volume percent of the lower-size mesopores from 22 to 40.5% was attained, possibly at the expense of the micropore volume by the pore enlargement mechanism.

It is interesting to examine further, from Table 6.3, the formation of mesopores from the enlargement of original micropores by the OTA method. As an example, comparing the porous properties of the CG and CG-OTA samples. The super-micropores volume of the CG-OTA carbon is $0.493 \text{ cm}^3/\text{g}$, while that of the original CG sample is $0.162 \text{ cm}^3/\text{g}$. Therefore, the increase in the volume of newly formed micropores = $(0.493 - 0.162)(100)/(0.162) = 204\%$. The lower-size mesopores volume (2–10 nm) of the CG and the CG-OTA are 0.150 and $0.388 \text{ cm}^3/\text{g}$, respectively. From these numerical values, the percentage of micropores of the original CG that is enlarged by CO_2 gasification to form the lower-size mesopores = $(0.388 - 0.150)(100)/(0.162) = 147\%$ which is greater than 100%. This indicates that

the widening of micropores to form mesopores could occur with the newly-formed micropores as well. Overall, the obtained results confirm that the preparation of activated carbon from carbon gel by the OTA method is superior to the conventional activation method for improving the porous properties of the resulting carbon. This is due principally to the higher gasification rate of the OTA-treated carbon, resulting from a larger number of reaction sites in the gel particles.

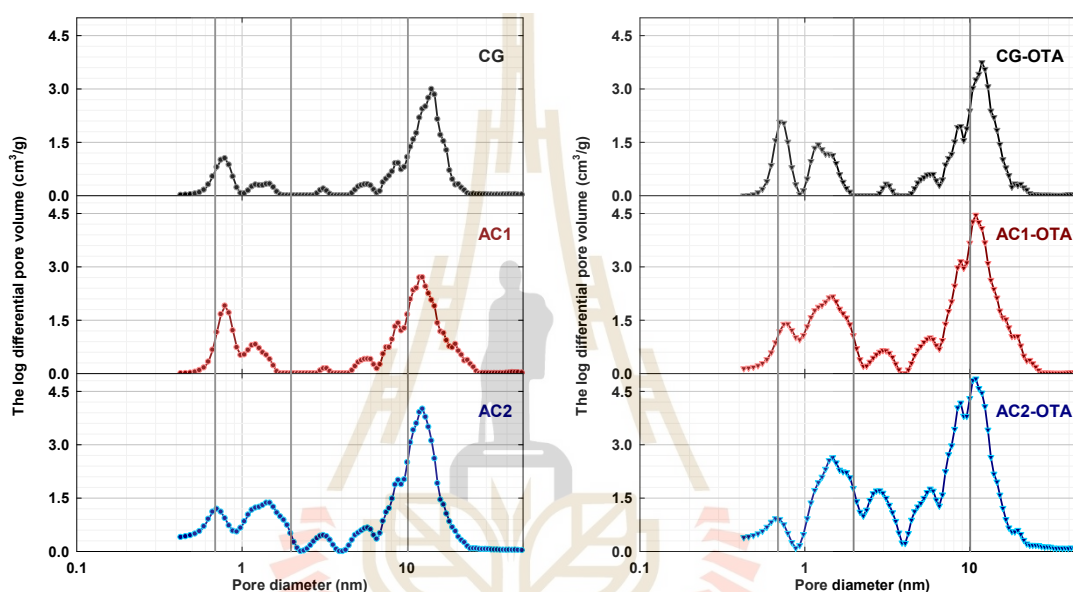


Figure 6.7 Pore size distributions of carbon samples obtained by using the NLDFT method.

Table 6.3 The calculated pore volume for each pore size range (NLDFT method)

Sample name	Micropores (cm ³ /g)		Mesopores (cm ³ /g)	
	0–0.7 nm	0.7–2 nm	2–10 nm	10–50 nm
CG	0.032 (3.4%)	0.162 (17.5%)	0.150 (16.2%)	0.564 (61.2%)
AC1	0.034 (2.9%)	0.338 (28.4%)	0.216 (18.1%)	0.596 (50.1%)
AC2	0.131 (7.6%)	0.445 (25.7%)	0.375 (21.6%)	0.760 (43.9%)
CG-OTA	0.096 (5.5%)	0.493 (28.0%)	0.388 (22.0%)	0.755 (42.9%)
AC1-OTA	0.078 (3.3%)	0.742 (31.1%)	0.666 (27.9%)	0.878 (36.8%)
AC2-OTA	0.136 (4.5%)	0.726 (23.9%)	1.229 (40.5%)	0.898 (29.6%)

6.4.5 Role of Surface Functional Groups in the OTA Method

The key success of the OTA method is the inclusion of oxidation and heat treatment steps prior to the final activation of the carbon. The oxidation step increases the amount of surface functional groups, while the following heat treatment removes such groups. Thus, a large number of active reaction sites for the subsequent activation step are produced that substantially help the improvement of the porous properties of the derived carbon. In this work, the amounts of oxygen-containing functional groups of the carbon samples were analyzed by a TPD (Temperature Programmed Desorption) method conducted under vacuum. Typical TPD spectra, which show the desorption rate of CO, CO₂, and H₂ as a function of temperature, of carbon samples collected after each step of the sequence of the OTA method, namely the initial carbon obtained through CO₂ activation for 1 h (AC), the air oxidized sample (AC-O), the sample after heat treatment (AC-OT), and the final reactivated carbon (AC-OTA) are shown in Figure 6.8. The total amounts of CO, CO₂, and H₂ desorbed from the samples in the unit of $\mu\text{mol/g}$ are presented in Table 6.4.

For the initial activated carbon (AC), the profile of CO₂ showed a maximum at around 340°C, while the profile of CO displayed a maximum at about 1000°C. In the literature, the CO₂ peak at low temperatures is usually attributed to carboxylic groups, while CO₂ desorption above 400°C is assigned to acid anhydrides, and lactones (Ishii & Kyotani, 2016). CO desorption is ascribed to the decomposition of phenol, ethers, and carbonyls and the desorption temperature of carbonyls is higher than those of the others (Figueiredo et al., 1999; Ishii & Kyotani, 2016). For the air-oxidized carbon (AC-O), two sharp peaks appear in its CO₂ spectra which are at around 300°C for the smaller one and about 670°C for the larger one. The maximum CO desorption rate for the air-oxidized sample can be observed at around 700°C, which is thought to be due to the decomposition of phenolic groups (Zielke et al., 1996). However, it should be noted that larger amounts of CO₂ and CO desorbed from AC-O than from AC, by about 10 and 25 times, respectively. It is obvious that the air oxidation of activated carbon has led to the creation of large amounts of oxygen-containing functional groups on the graphene sheets which form the carbon.

After heating the oxidized carbon at 1000°C in an N₂ flow, the heat-treated sample (AC-OT) showed similar results to those of the initial activated carbon

(AC) for both the CO₂ and CO spectra but with lower amounts of emitted gases. This indicates that most of the oxygen-containing functional groups were removed from the heat-treated carbon, thus the number of unpaired electrons due to bond disruption was enhanced. Slightly larger amounts of gases were emitted from the carbon reactivated by CO₂ (AC-OTA) than from the heat-treated sample (AC-OT), which implies that functional groups are readily formed by CO₂ during the activation step. On the other hand, AC-OTA also showed similar spectra to the initial activated carbon (AC) but the amounts of emitted gases were slightly lower than those of the initial activated carbon. It could be possible that the CO₂ gasification reaction removes more of the reactive edge sites in the carbon structure, leading to fewer functional groups at the edge sites as well.

To investigate the influence of oxygen functional groups on the main role of the OTA method, the amount of each type of oxygen functional group was determined by peak separation of the TPD spectra of CO₂ and CO. The desorption temperature and full width at half-maximum of the oxygen-containing functional groups were determined based on previous work (Nagaishi et al., 2023). Table 6.5 presents the amount of oxygen-containing functional groups in the carbon samples. The order of oxygen-containing functional group content in the carbon sample after the oxidation step (AC-O) was as follows: phenol/ether > lactone > carbonyl > carboxylic > anhydride. These results indicate that air oxidation of carbon primarily led to the formation of phenol/ether groups. The acidic groups of the AC-OT sample were almost completely removed as compared to those of the oxidized carbons, with their amounts being slightly lower than those in the starting activated carbon (AC). On the other hand, after heat treatment, the carbonyl groups content was reduced to the value of about 50% as compared to that of the AC sample (0.128 vs 0.064 mmol/g), while the contents of other functional groups remained almost unchanged. Interestingly, the AC-OTA sample showed a slight increase in the functional groups formed by CO₂ during the activation step, except for the carbonyl groups which increased up to 95%. This suggests that the thermal destruction of the carbonyl groups during gasification could play a stronger role in the generation of reaction sites for gasification, and hence the pore development in activated carbon.

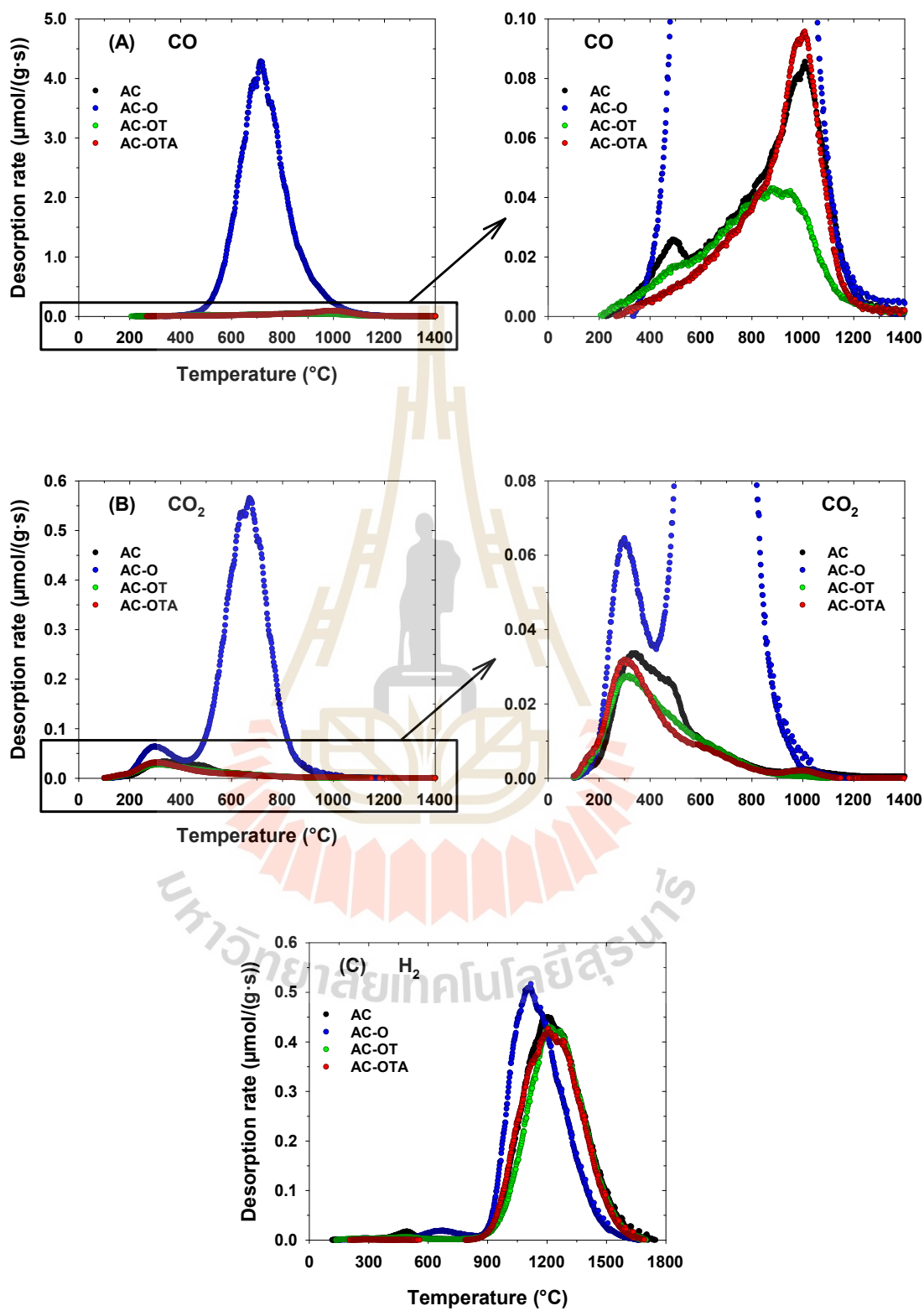


Figure 6.8 (A) CO (B) CO₂ and (C) H₂ desorption spectra of the OTA samples.

Table 6.4 Total amounts of CO₂, CO, and H₂ desorbed from the samples

Sample code	CO ₂	CO	H ₂
	(μmol/g)	(μmol/g)	(μmol/g)
AC	63.8	191	2026
AC-O	723	5520	1989
AC-OT	56.1	122	1805
AC-OTA	55.9	169	1887

Table 6.5 The amount of oxygen-containing functional groups of the samples

Sample code	Carboxylic	Anhydride	Lactone	Pheno/ether	Carbonyl
	(mmol/g)	(mmol/g)	(mmol/g)	(mmol/g)	(mmol/g)
AC	0.036	0.019	0.010	0.044	0.128
AC-O	0.072	0.000	0.651	4.987	0.532
AC-OT	0.034	0.012	0.009	0.035	0.064
AC-OTA	0.038	0.009	0.009	0.046	0.125

6.4.6 Determination of Carbon Reactivity Towards CO₂ Gasification

TGA analysis was employed to illustrate the importance of the OTA method in increasing the reactivity of active sites for CO₂ gasification. The carbon reactivity for CO₂ gasification (R_c) was defined here as the rate of fractional conversion according to Equation (6.3):

$$R_c = \frac{dX}{dt} \quad (6.3)$$

where X is the fractional conversion of carbon ($X = (W_0 - W_t) / (W_0 - W_\infty)$), and W_0 , W_t , and W_∞ are the initial weight of carbon before gasification, the weight of carbon at time t , and the remaining weight, respectively. The results calculated for the CO₂ gasification of AC and AC-OT at 1000°C are shown in Figure 6.9.

The carbon conversion data with respect to the gasification time are presented in Figure 6.9A. The results indicated that the carbon conversion of AC-OT increased at a much higher rate than that of AC, which can be observed from the steeper slope of the curve. This could be associated with the larger number of reactive sites available during the activation step. Figure 6.9B shows the effect of carbon conversion on carbon reactivity. The reactivity curve of AC showed a relatively constant rate, while the AC-OT curve stayed above the AC curve and showed a characteristic of continuous rising with the increase in the fractional conversion, meaning higher reactivity at all degrees of carbon conversion. The rising trend of the reactivity curve is attributed to the increase in surface area with increasing carbon conversion that provided more reactive sites for the gasification, leading to a higher reaction rate. As mentioned above, the reactivity of carbon from the OTA method was higher than that derived through the conventional activation method, as observed from the comparison between the curves of AC and AC-OT at the same carbon conversion (X). These results support the fact that the OTA method is capable of increasing the number of active sites for the gasification reaction by CO₂, resulting in the rapid development of pores and the corresponding increase in surface area.

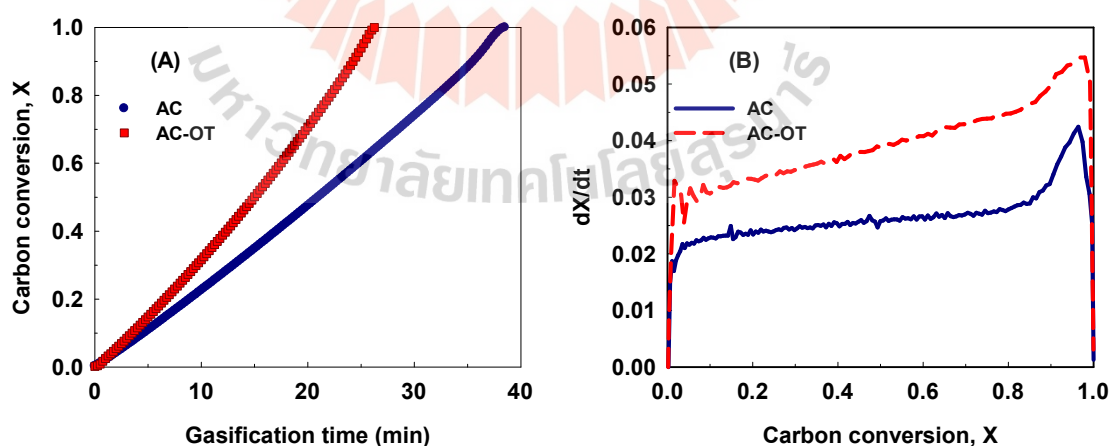


Figure 6.9 (A) the carbon conversion profiles for CO₂ gasification at 1000°C of the activated carbons prepared by conventional activation (AC) and by the OTA method (AC-OT) and (B) the effect of carbon conversion on the carbon reactivity towards CO₂ gasification.

6.4.7 Electrochemical performances

In this study, the electrochemical performances of activated carbons prepared under the same activation conditions by the conventional activation method (AC2) and the OTA method (AC1-OTA) were compared. Figure 6.10 displays the cyclic voltammetry curves of AC2 and AC1-OTA measured in a 1 M H_2SO_4 solution at a sweeping rate of 2 mV/s using a three-electrode cell. The cyclic voltammetry curves showed a rectangular shape, indicating that the charge-discharge process was purely a physical process that involved the formation of an electrical double-layer (EDL) at the interface, where there are no redox reactions observed during the charge and discharge processes (Wu et al., 2021). The specific capacitances of AC2 and AC1-OTA were calculated from the cyclic voltammetry curves and were found to be 140.8 F/g and 152.2 F/g, respectively. The capacitance was observed to increase when the OTA method was applied. The charge-discharge curves of AC2 and AC1-OTA were also analyzed for the capacitance at a current density in the range of 0.5–10 A/g, as shown in Figure 6.11. It was observed that increased almost linearly with time during charging and linearly decreased during discharging period. This confirms that the charge-discharge processes of both AC2 and AC1-OTA proceeded through a physical process of adsorption and desorption of electrolyte ions, which was in line with the results obtained from cyclic voltammetry measurements.

The specific capacitances of AC2 and AC1-OTA were examined at a current density range of 0.5–10 A/g to investigate the effect of the pore size of carbon on the rate performance, the results of which were depicted in Figure 6.12. According to the calculated pore volume in Table 6.3, the supermicropores (0.7–2 nm), lower-size mesopores (2–10 nm), and upper-size mesopores (10–50 nm) of the AC1-OTA had higher values than those of AC2 by about 66.7%, 77.6%, and 15.5%, respectively. This indicates that supermicropores contributed to an increase in surface area, while lower-size mesopores played a significant role in facilitating the diffusion of the electrolytes in the activated carbon gels. Upon examination of Figure 6.12, it was noted that AC1-OTA exhibited a higher specific capacitance ($C = 155\text{--}226$ F/g) than that of AC2 ($C = 140\text{--}169$ F/g) at current densities below 2 A/g. The results suggest that the presence of supermicropores and lower-size mesopores could enhance the rate performance even at low current densities. Moreover, the activated carbon gels in this work showed a higher specific capacitance compared to the

ordered hierarchical mesoporous/microporous carbons (OHMMC), even with comparable porous properties (i.e. $S_{\text{BET}} = 1950 \text{ m}^2/\text{g}$, $V_{\text{T}} = 1.34 \text{ cm}^3/\text{g}$ with 58% mesopore volume of OHMMC, providing a specific capacitance of 145 F/g, at the current density of 0.5 A/g) (Zhou et al., 2013). Additionally, at the highest current density of 10 A/g, the specific capacitance of AC1-OTA ($C = 48 \text{ F/g}$) was found to be twofold higher than that of AC2 ($C = 21 \text{ F/g}$). At this current density, the presence of lower-size mesopores (2–10 nm) is thought to facilitate the efficient mass transport of the electrolytes, leading to improved capacitance at high current densities. However, the ion diffusion process within the mesopores is primarily governed by the pore packing defects, rather than by variations in pore size distribution (Wang et al., 2006). Overall, the findings suggest that to achieve high capacitance and good rate performance, the design of porous carbon materials should balance the specific surface area and mesopores by utilizing carbons with lower-size mesopores that enable rapid mass transport of electrolyte ions and sufficient volume of supermicropores that provide a moderately high specific surface area, without significantly reducing the electrical conductivity.

In summary, the OTA method is a modified technique of the conventional physical activation method for producing mesoporous activated carbon with high porous properties by incorporating two consecutive steps of air oxidation and thermal destruction of the developed functional groups before CO_2 gasification. Mesopores are created not only by the coalescence of micropores at a high degree of carbon burn-off but also as a result of micropore widening caused by the increasing surface reactivity of micropores for CO_2 gasification. Therefore, when the OTA method is used, small mesopores can be formed within the carbon nanoparticles at any level of carbon burn-off, while the overall structure of the activated carbon gels remains stable throughout the activation process, as observed in the surface images of AC2 and AC1-OTA obtained by a field scanning electron microscopy (FE-SEM; JEOL, Ltd., JSM-6600F) at 50K magnification (Figure 6.13). With the OTA method, the activated carbon possesses a high specific surface area due to the increase in the supermicropores. In addition, the mesopores is present not only in the interparticle spaces but also within the nanoparticles.

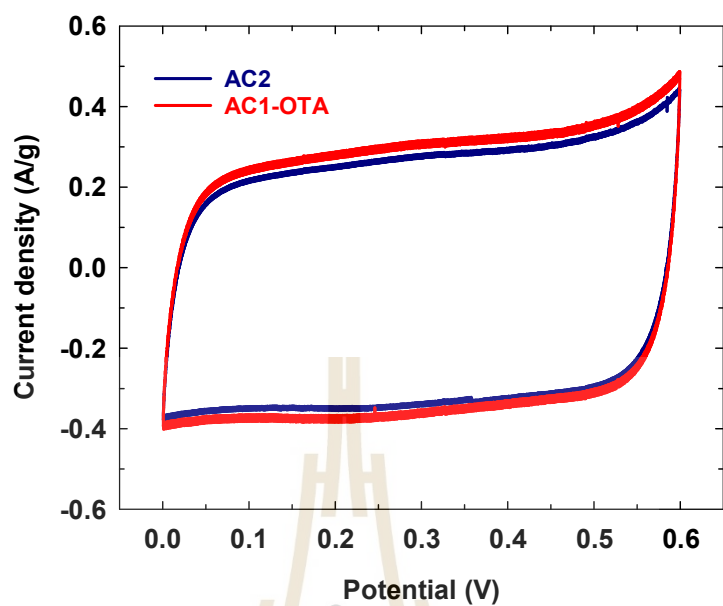


Figure 6.10 Cyclic voltammetry curves of AC2 (blue) and AC1-OTA (red) at a scan rate of 2 mV/s.

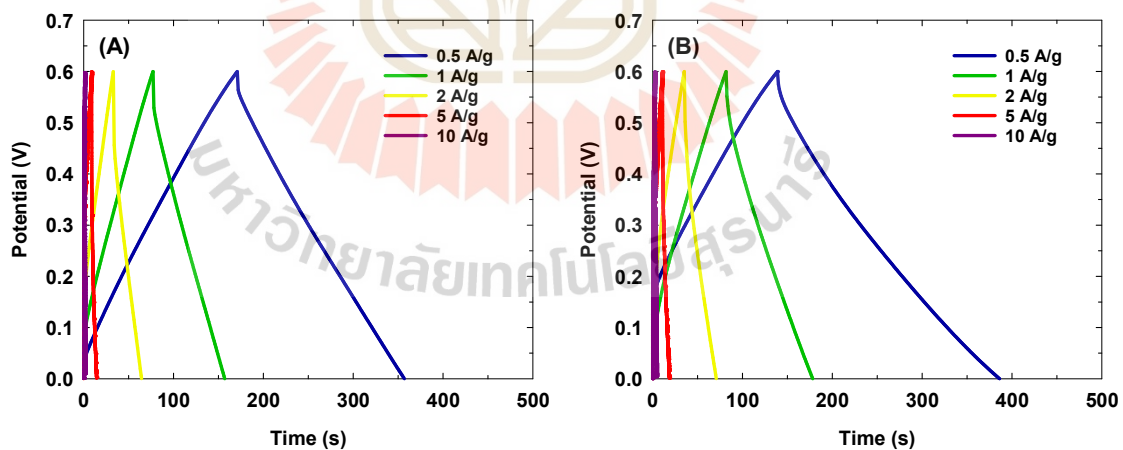


Figure 6.11 Charge-discharge curves of (A) AC2 and (B) AC1-OTA at various current densities.

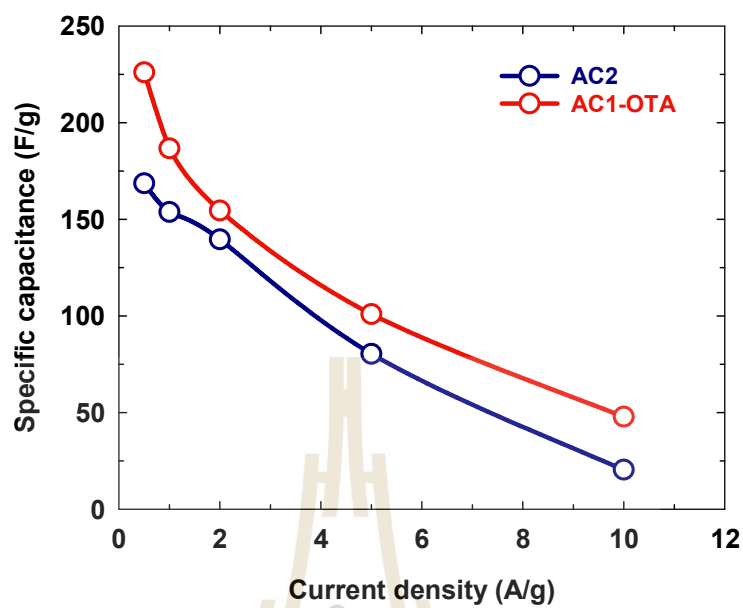


Figure 6.12 The effect of current density on specific capacitances of (A) AC2 and (B) AC1-OTA.

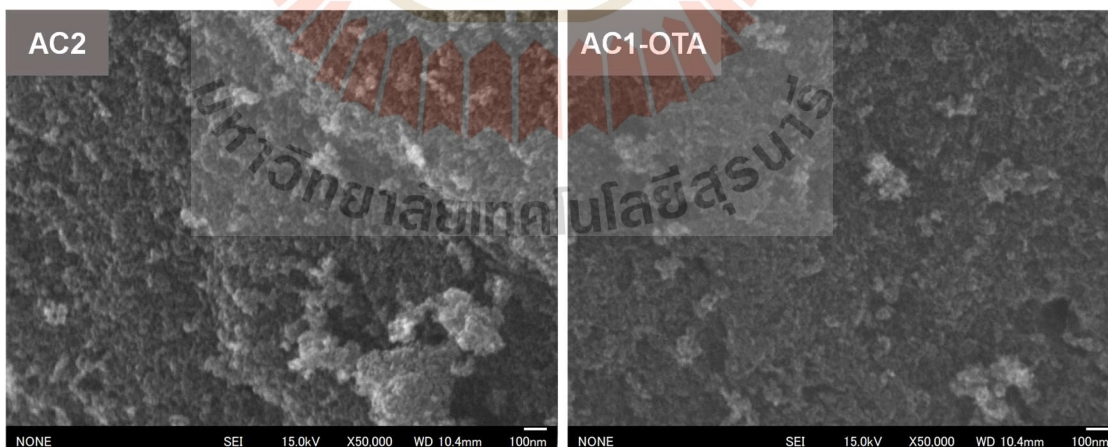


Figure 6.13 FE-SEM micrographs of AC2 (left) and AC1-OTA (right).

6.5 Conclusions

Carbon gels were used as precursors for the synthesis of microporous-mesoporous activated carbon by the OTA method. It was found that the activated carbons derived from the OTA procedure provided large improvement in porous properties as compared with those prepared through the traditional activation method under the same activation conditions or the same carbon burn-off level. The maximum values of the porous properties of activated carbon gel obtained by the OTA method in this work were 2,920 m²/g, 3.03 cm³/g, 1.19 cm³/g, and 1.81 cm³/g for the BET surface area, total pore volume, micropore volume, and mesopore volume, respectively. The superiority of the OTA method lies in its ability to generate a larger number of reaction sites for CO₂ gasification, which results from the bond disruption of the created surface functional groups. The produced activated carbon had a larger volume of mesopores as compared to that of micropores, which reflects the highly porous nature of the carbon gel. Furthermore, increasing the activation time tended to decrease the percentage of mesopores and a corresponding increase in the volume percent of micropores. It is also evident that the upper-size mesopores (10–50 nm) are probably formed outside the carbon particles in the carbon gel, while the lower-size mesopores (2–10 nm) and micropores (< 2 nm) are created inside the particles.

The study also compared the electrochemical performances of activated carbons prepared using the conventional activation and the OTA methods at the same activation conditions. The results showed that the capacitance increased when the OTA method was used, indicating that introducing supermicropores and lower-size mesopores could enhance the rate performance, even at low current densities. Activated carbons prepared by the OTA method showed higher specific capacitance than the ordered hierarchical mesoporous/microporous carbons, despite having comparable porous properties. The findings suggested that the design of porous carbon materials should take into consideration the balance between the magnitude of specific surface area and mesopores by utilizing carbons with lower-size mesopores for rapid mass transport of electrolyte ions and an optimum volume of supermicropores for a moderately high specific surface area to achieve high capacitance and good rate performance.

6.6 References

- Al-Muhtaseb, S. A., & Ritter, J. A. (2003, 2003/01/16). Preparation and Properties of Resorcinol–Formaldehyde Organic and Carbon Gels. *Advanced Materials*, 15(2), 101-114.
- Alegre, C., Sebastián, D., Gálvez, M. E., Moliner, R., & Lázaro, M. J. (2016, 2016/09/05/). Sulfurized carbon xerogels as Pt support with enhanced activity for fuel cell applications. *Applied Catalysis B: Environmental*, 192, 260-267.
- Arenillas, A., Menéndez, J. A., Reichenauer, G., Celzard, A., Fierro, V., Hodar, F. J. M., Bailón-García, E., & Job, N. (2019). *Organic and Carbon Gels: From Laboratory Synthesis to Applications*. Springer.
- Brunauer, S., Emmett, P. H., & Teller, E. (1938, 1938/02/01). Adsorption of Gases in Multimolecular Layers. *Journal of the American Chemical Society*, 60(2), 309-319.
- Calvo, E. G., Juárez-Pérez, E. J., Menéndez, J. A., & Arenillas, A. (2011, 2011/05/15/). Fast microwave-assisted synthesis of tailored mesoporous carbon xerogels. *Journal of Colloid and Interface Science*, 357(2), 541-547.
- Canal-Rodríguez, M., Menéndez, J. A., & Arenillas, A. (2017). Carbon Xerogels: The Bespoke Nanoporous Carbons. In *Porosity-Process, Technologies and Applications* (pp. 69-89). IntechOpen London, UK.
- Celzard, A., Fierro, V., & Amaral-Labat, G. (2012). Chapter 7 - Adsorption by Carbon Gels. In J. M. D. Tascón (Ed.), *Novel Carbon Adsorbents* (pp. 207-244). Elsevier.
- Czakkel, O., Nagy, B., Dobos, G., Fouquet, P., Bahn, E., & László, K. (2019, 2019/07/05/). Static and dynamic studies of hydrogen adsorption on nanoporous carbon gels. *International Journal of Hydrogen Energy*, 44(33), 18169-18178.
- Dollimore, D., & Heal, G. R. (1964). An improved method for the calculation of pore size distribution from adsorption data. *Journal of Applied Chemistry*, 14(3), 109-114.

- Dubinin, M. M. (1975). Physical Adsorption of Gases and Vapors in Micropores. In D. A. Cadenhead, J. F. Danielli, & M. D. Rosenberg (Eds.), *Progress in Surface and Membrane Science* (Vol. 9, pp. 1-70). Elsevier.
- ElKhatat, A. M., & Al-Muhtaseb, S. A. (2011, 2011/07/12). Advances in Tailoring Resorcinol-Formaldehyde Organic and Carbon Gels. *Advanced Materials*, 23(26), 2887-2903.
- Figueiredo, J. L., & Pereira, M. F. R. (2013, 2013/03/01/). Synthesis and functionalization of carbon xerogels to be used as supports for fuel cell catalysts. *Journal of Energy Chemistry*, 22(2), 195-201.
- Figueiredo, J. L., Pereira, M. F. R., Freitas, M. M. A., & Órfão, J. J. M. (1999, 1999/01/01/). Modification of the surface chemistry of activated carbons. *Carbon*, 37(9), 1379-1389.
- Ganesamoorthy, R., Vadivel, V. K., Kumar, R., Kushwaha, O. S., & Mamane, H. (2021, 2021/12/20/). Aerogels for water treatment: A review. *Journal of Cleaner Production*, 329, 129713.
- Gómez-Cápiro, O., Hinkle, A., Delgado, A. M., Fernández, C., Jiménez, R., & Arteaga-Pérez, L. E. (2018). Carbon Aerogel-Supported Nickel and Iron for Gasification Gas Cleaning. Part I: Ammonia Adsorption. *Catalysts*, 8(9), 347.
- Guo, H., Si, D.-H., Zhu, H.-J., Li, Q.-X., Huang, Y.-B., & Cao, R. (2022, 2022/05/01/). Ni single-atom sites supported on carbon aerogel for highly efficient electroreduction of carbon dioxide with industrial current densities. *eScience*, 2(3), 295-303.
- Isaacs Páez, E., Haro, M., Juárez-Pérez, E. J., Carmona, R. J., Parra, J. B., Leyva Ramos, R., & Ania, C. O. (2015, 2015/06/01/). Fast synthesis of micro/mesoporous xerogels: Textural and energetic assessment. *Microporous and Mesoporous Materials*, 209, 2-9.
- Ishii, T., & Kyotani, T. (2016). Chapter 14 - Temperature Programmed Desorption. In M. Inagaki & F. Kang (Eds.), *Materials Science and Engineering of Carbon* (pp. 287-305). Butterworth-Heinemann.

- Job, N., Panariello, F., Marien, J., Crine, M., Pirard, J.-P., & Léonard, A. (2006, 2006/01/01/). Synthesis optimization of organic xerogels produced from convective air-drying of resorcinol-formaldehyde gels. *Journal of Non-Crystalline Solids*, 352(1), 24-34.
- Job, N., Pirard, R., Marien, J., & Pirard, J.-P. (2004, 2004/01/01/). Porous carbon xerogels with texture tailored by pH control during sol-gel process. *Carbon*, 42(3), 619-628.
- Kakunuri, M., & Sharma, C. S. (2018). Resorcinol-formaldehyde derived carbon xerogels: A promising anode material for lithium-ion battery. *Journal of Materials Research*, 33(9), 1074-1087.
- Kang, F., Inagaki, M., & Itoi, H. (2021). *Porous Carbons: Syntheses and Applications*. Elsevier Science.
- Kiciński, W., Dyjak, S., & Tokarz, W. (2021, 2021/11/30/). Carbon gel-derived Fe-N-C electrocatalysts for hydrogen-air polymer electrolyte fuel cells. *Journal of Power Sources*, 513, 230537.
- Lawtae, P., & Tangsathitkulchai, C. (2021a). A New Approach for Controlling Mesoporosity in Activated Carbon by the Consecutive Process of Air Oxidation, Thermal Destruction of Surface Functional Groups, and Carbon Activation (the OTA Method). *Molecules*, 26(9), 2758.
- Lawtae, P., & Tangsathitkulchai, C. (2021b). The Use of High Surface Area Mesoporous-Activated Carbon from Longan Seed Biomass for Increasing Capacity and Kinetics of Methylene Blue Adsorption from Aqueous Solution. *Molecules*, 26(21), 6521.
- Lin, C., & Ritter, J. A. (2000, 2000/01/01/). Carbonization and activation of sol-gel derived carbon xerogels. *Carbon*, 38(6), 849-861.
- Majedi Far, H., Rewatkar, P. M., Donthula, S., Taghvaei, T., Saeed, A. M., Sotiriou-Leventis, C., & Leventis, N. (2019, 2019/01/01). Exceptionally High CO₂ Adsorption at 273 K by Microporous Carbons from Phenolic Aerogels: The Role of Heteroatoms in Comparison with Carbons from Polybenzoxazine and Other Organic Aerogels. *Macromolecular Chemistry and Physics*, 220(1), 1800333.

- Marsh, H., & Rodríguez-Reinoso, F. (2006). *Activated carbon*. Elsevier Science Ltd.
- Mishra, S., Yadav, A., & Verma, N. (2017, 2017/10/15/). Carbon gel-supported Fe-graphene disks: Synthesis, adsorption of aqueous Cr(VI) and Pb(II) and the removal mechanism. *Chemical Engineering Journal*, 326, 987-999.
- Mohaddespour, A., Atashrouz, S., & Ahmadi, S. J. (2017, 2017/05/31). Nanostructured Carbon Xerogels by Super-Fast Carbonization. *Industrial & Engineering Chemistry Research*, 56(21), 6213-6220.
- Moreno, A. H., Arenillas, A., Calvo, E. G., Bermúdez, J. M., & Menéndez, J. A. (2013, 2013/03/01/). Carbonisation of resorcinol-formaldehyde organic xerogels: Effect of temperature, particle size and heating rate on the porosity of carbon xerogels. *Journal of Analytical and Applied Pyrolysis*, 100, 111-116.
- Mori, T., Iwamura, S., Ogino, I., & Mukai, S. R. (2019, 2019/05/01/). Cost-effective synthesis of activated carbons with high surface areas for electrodes of non-aqueous electric double layer capacitors. *Separation and Purification Technology*, 214, 174-180.
- Nagaishi, S., Iwamura, S., Ishii, T., & Mukai, S. R. (2023, 2023/01/25). Clarification of the Effects of Oxygen Containing Functional Groups on the Pore Filling Behavior of Discharge Deposits in Lithium-Air Battery Cathodes Using Surface-Modified Carbon Gels. *The Journal of Physical Chemistry C*.
- Pekala, R., & KONG, F.-M. (1989). A synthetic route to organic aerogels-mechanism, structure, and properties. *Le Journal de Physique Colloques*, 50(C4), C4-33-C34-40.
- Pekala, R. W. (1989). *Aerogels and xerogels from organic precursors*.
- Pekala, R. W. (1989, 1989/09/01). Organic aerogels from the polycondensation of resorcinol with formaldehyde. *Journal of Materials Science*, 24(9), 3221-3227.
- Pekala, R. W., & Schaefer, D. W. (1993, 1993/09/01). Structure of organic aerogels. 1. Morphology and scaling. *Macromolecules*, 26(20), 5487-5493.
- Pillai, A., & Kandasubramanian, B. (2020, 2020/05/14). Carbon Xerogels for Effluent Treatment. *Journal of Chemical & Engineering Data*, 65(5), 2255-2270.

- Rey-Raap, N., Angel Menéndez, J., & Arenillas, A. (2014, 2014/09/01/). RF xerogels with tailored porosity over the entire nanoscale. *Microporous and Mesoporous Materials*, 195, 266-275.
- Rey-Raap, N., Arenillas, A., & Menéndez, J. A. (2016, 2016/03/15/). A visual validation of the combined effect of pH and dilution on the porosity of carbon xerogels. *Microporous and Mesoporous Materials*, 223, 89-93.
- Song, Z., Miao, L., Ruhlmann, L., Lv, Y., Zhu, D., Li, L., Gan, L., & Liu, M. (2022, 2022/11/01). Lewis Pair Interaction Self-Assembly of Carbon Superstructures Harvesting High-Energy and Ultralong-Life Zinc-Ion Storage. *Advanced Functional Materials*, 32(48), 2208049.
- Soni, R. U., Edlabadkar, V. A., Greenan, D., Rewatkar, P. M., Leventis, N., & Sotiriou-Leventis, C. (2022, 2022/06/14). Preparation of Carbon Aerogels from Polymer-Cross-Linked Xerogel Powders without Supercritical Fluid Drying and Their Application in Highly Selective CO₂ Adsorption. *Chemistry of Materials*, 34(11), 4828-4847.
- Taylor, S. J., Haw, M. D., Sefcik, J., & Fletcher, A. J. (2014, 2014/09/02). Gelation Mechanism of Resorcinol-Formaldehyde Gels Investigated by Dynamic Light Scattering. *Langmuir*, 30(34), 10231-10240.
- Thommes, M., Kaneko, K., Neimark, A. V., Olivier, J. P., Rodriguez-Reinoso, F., Rouquerol, J., & Sing, K. S. (2015). Physisorption of gases, with special reference to the evaluation of surface area and pore size distribution (IUPAC Technical Report). *Pure and Applied Chemistry*, 87(9-10), 1051-1069.
- Tsuchiya, T., Mori, T., Iwamura, S., Ogino, I., & Mukai, S. R. (2014, 2014/09/01/). Binderfree synthesis of high-surface-area carbon electrodes via CO₂ activation of resorcinol-formaldehyde carbon xerogel disks: Analysis of activation process. *Carbon*, 76, 240-249.
- Velez, V., Ramos-Sánchez, G., Lopez, B., Lartundo-Rojas, L., González, I., & Sierra, L. (2019, 2019/06/01/). Synthesis of novel hard mesoporous carbons and their applications as anodes for Li and Na ion batteries. *Carbon*, 147, 214-226.

- Wang, D.-W., Li, F., Fang, H.-T., Liu, M., Lu, G.-Q., & Cheng, H.-M. (2006, 2006/05/01). Effect of Pore Packing Defects in 2-D Ordered Mesoporous Carbons on Ionic Transport. *The Journal of Physical Chemistry B*, 110(17), 8570-8575.
- Wang, E., Shao, C., Qiu, S., Chu, H., Zou, Y., Xiang, C., Xu, F., & Sun, L. (2017). Organic carbon gel assisted-synthesis of $\text{Li}_{1.2}\text{Mn}_{0.6}\text{Ni}_{0.2}\text{O}_2$ for a high-performance cathode material for Li-ion batteries. *RSC Advances*, 7(3), 1561-1566.
- Wei, G., Miao, Y.-E., Zhang, C., Yang, Z., Liu, Z., Tjiu, W. W., & Liu, T. (2013, 2013/08/14). Ni-Doped Graphene/Carbon Cryogels and Their Applications As Versatile Sorbents for Water Purification. *ACS Applied Materials & Interfaces*, 5(15), 7584-7591.
- Wu, Q., He, T., Zhang, Y., Zhang, J., Wang, Z., Liu, Y., Zhao, L., Wu, Y., & Ran, F. (2021). Cyclic stability of supercapacitors: materials, energy storage mechanism, test methods, and device. *Journal of Materials Chemistry A*, 9(43), 24094-24147.
- Yan, J., Miao, L., Duan, H., Zhu, D., Lv, Y., Li, L., Gan, L., & Liu, M. (2022, 2022/05/01/). High-energy aqueous supercapacitors enabled by N/O codoped carbon nanosheets and "water-in-salt" electrolyte. *Chinese Chemical Letters*, 33(5), 2681-2686.
- Yoo, J., Yang, I., Kwon, D., Jung, M., Kim, M.-S., & Jung, J. C. (2021, 2021/04/01). Low-Cost Carbon Xerogels Derived from Phenol-Formaldehyde Resin for Organic Electric Double-Layer Capacitors. *Energy Technology*, 9(4), 2000918.
- Zheng, X., Miao, L., Song, Z., Du, W., Zhu, D., Lv, Y., Li, L., Gan, L., & Liu, M. (2022). In situ nanoarchitecturing of conjugated polyamide network-derived carbon cathodes toward high energy-power Zn-ion capacitors. *Journal of Materials Chemistry A*, 10(2), 611-621.
- Zhou, D.-D., Du, Y.-J., Song, Y.-F., Wang, Y.-G., Wang, C.-X., & Xia, Y.-Y. (2013). Ordered hierarchical mesoporous/microporous carbon with optimized pore structure for supercapacitors. *Journal of Materials Chemistry A*, 1(4), 1192-1200.
- Zielke, U., Hüttinger, K. J., & Hoffman, W. P. (1996, 1996/01/01/). Surface-oxidized carbon fibers: I. Surface structure and chemistry. *Carbon*, 34(8), 983-998.

CHAPTER VII

CONCLUSIONS AND RECOMMENDATIONS

7.1 Conclusions

In this research work, a novel method called the OTA method was proposed for preparing activated carbon with a large surface area and a high percentage of mesopore volume from longan seed biomass. The OTA method consisted of three consecutive steps, including air oxidation, thermal destruction of surface functional groups, and physical activation to produce and control the volume of mesopores. Compared to the conventional two-step activation method, the OTA method yielded microporous-mesoporous activated carbon with better and more precise control of mesopore development. The microporous-mesoporous activated carbon obtained through the OTA method showed promising results for removing methylene blue (MB) from aqueous solutions due to its high adsorption equilibrium capacity and rapid kinetics. Moreover, the present work incorporated a fundamental study of pore development in activated carbon based on the defect surface model using a computer simulation technique. Furthermore, the OTA method had also been applied to the carbon gel precursor, which provided further insights into the pore development during the OTA process. From another perspective, the OTA method could be applied to other carbon materials, representing its flexibility and adaptability applied to various materials. Overall, these results offered important insights into the development of mesopores in activated carbon and its potential applications in the field of adsorption. The results of these studies have led to the following conclusions.

The OTA method was a simple and effective approach for producing activated carbon from longan seed biomass via based purely on physical activation, with the advantage of allowing precise control of mesopore development. A cycle of the OTA method comprised three consecutive steps, including air oxidation for the formation of surface oxygen functional groups, the thermal destruction of functional groups to enhance surface reactivity by increasing the number of defects, and the reactivation of activated carbon by CO₂. This led to the enlargement of the pre-existing micropores to form mesopores as well as the formation of new micropores.

The OTA method produced activated carbon with a high proportion of mesopores, resulting in a significant increase in the total specific surface area when compared to the conventional two-step activation method. The results showed that the porous properties of activated carbon synthesized by both methods improved with increasing activation time and temperature. However, the OTA method outperformed the conventional method, with a maximum mesopore volume of $0.474 \text{ cm}^3/\text{g}$ accounting for 44.1% of the total pore volume, and a maximum BET surface area of $1773 \text{ m}^2/\text{g}$ by utilizing three cycles of the OTA method at the activation temperature of 850°C and the activation time of 1 h for each treatment cycle. For comparison, the conventional activation method produced the maximum mesopore volume and surface area of $0.270 \text{ cm}^3/\text{g}$ and $1,421 \text{ m}^2/\text{g}$, respectively, under activation conditions of 900°C and 4 h. Overall, the OTA method offered a promising approach for producing activated carbon with tailored mesopore properties.

The adsorption performance of activated carbon prepared by the conventional two-step activation method and by the OTA method for the removal of methylene blue (MB) from an aqueous solution provided the following results. The adsorption kinetics was best described by the pseudo-second-order model, followed by the pore-diffusion model and the pseudo-first-order model. The average pore size was found to have a profound effect on the model rate constants and pore diffusivity. The activated carbon prepared by the OTA method exhibited a significantly higher average pore diffusivity compared to that of the activated carbon prepared by the conventional two-step activation method. The activated carbon with the highest surface area yielded the maximum MB adsorption capacity of 1000 mg/g . The initial pH of the MB solution had no significant effect on the adsorption capacity or the removal efficiency of MB dyes. An increase in the adsorption temperature resulted in an increase in the amount of MB adsorbed, indicating that the adsorption process was endothermic. Overall, this study demonstrated that longan seed-based activated carbon prepared by the OTA method was an excellent adsorbent for the removal of MB dyes from aqueous solutions.

The following conclusions can be drawn from the analysis of gas adsorption and pore development of microporous-mesoporous activated carbon based on GCMC simulation and a surface defect model. Simulated isotherms were generated for N_2 adsorption (77 K) and CO_2 adsorption (273 K) in carbon slit pores of various pore widths

ranging from 0.65 to 4 nm. These isotherms showed a continuous pore-filling mechanism for pore widths less than 0.85 nm. Capillary condensation was observed for N₂ adsorption for pore widths larger than 1.7 nm, while this phenomenon was not observed for CO₂ adsorption. The isotherms for N₂ adsorption on defective surfaces showed a similar pattern to the perfective surface, with a consistent pattern of continuous pore filling for pore widths less than 0.85 nm, resulting in a maximum adsorbed density for each pore size. However, smaller size defects exhibited lower adsorbed density for single-layer adsorption, while larger defects showed higher adsorbed density. This suggested that the size and distribution of defects significantly affect the adsorbed density. Additionally, it was found that the adsorption occurred initially at the defect pits before proceeding on the carbon surface, indicating that the stronger solid-fluid (SF) interaction at the defect pits initiated the adsorption process. Two contact layers formed adjacent to the walls due to the strong SF interaction near the pore wall. The pore size distribution (PSD) data obtained from N₂ and CO₂ adsorption isotherms indicated that the activated carbon samples primarily consisted of micropores and small mesopores, with a multimodal distribution covering the pore size range from 0.65 to 4 nm. The computed PSD from both N₂ and CO₂ isotherms revealed that the supermicropores (1.4–2 nm) were responsible for increasing the surface area of activated carbon, while the mesopores were predominantly distributed within the 2–3 nm range. The pore volume of the mesopores increased with the number of OTA cycles. This demonstrated that the use of the OTA method increased the mesopore volume not only by the coalescence of micropores at a high carbon burn-off but also by micropore widening caused by the increased surface reactivity of micropores for subsequent CO₂ gasification. It should be noted that the total pore volume determined from CO₂ adsorption were slightly higher than those obtained from N₂ adsorption due to the faster diffusion rate of CO₂ through carbon pores and its ability to access smaller pores.

In addition to the development of the OTA method, a facile pre-oxidation technique for increasing CO₂ gasification rates in longan-seed chars was also investigated in the study. It was observed that the char reactivity was increased with the increase of oxidation temperature between 250 to 300°C. The increase in char reactivity was attributed to an increase in the number of reaction sites, which resulted from the bond disruption of functional groups formed during air oxidation at high

gasification temperatures between 850–950°C. The gasification kinetic data obtained from the TGA were tested using four commonly used kinetic models, and the modified volume reaction model (MVRM) was found to provide the best prediction capability. The average rate constant of the MVRM over the course of the reaction (k_m) was employed as a measure of char reactivity and was found to increase with the increase of oxidation temperature, similar to the case of the gasification rate. By fitting the k_m data with the Arrhenius equation, the activation energy of the gasification reaction was found to vary in the range from 156.87–218.98 kJ/mol.

In the final section of this research work, the OTA method was applied to improve the porous properties of the activated carbon gels. The activated carbons produced from the OTA procedure showed significantly improved porous properties when compared to those prepared through the traditional activation method under the same activation conditions or at the same carbon burn-off level. The maximum porous properties of the activated carbon gel produced via the OTA method were 2,920 m²/g, 3.03 cm³/g, 1.19 cm³/g, and 1.81 cm³/g for the BET surface area, total pore volume, micropore volume, and mesopore volume, respectively. The OTA method was found to be superior to the traditional activation method due to its ability to produce a greater number of reaction sites for CO₂ gasification resulting from the disruption of the bonds of the created surface functional groups. The carbon gel produced had a larger volume of mesopores than that of micropores, which confirmed the highly porous nature of the carbon gel. Additionally, increasing the activation time resulted in a decrease in the percentage of mesopores and a corresponding increase in the volume percent of micropores. The formation of upper-size mesopores (10–50 nm) outside the carbon particles in the carbon gel and lower-size mesopores (2–10 nm) and micropores (< 2 nm) inside the particles was evident. With the OTA method, the resulting activated carbon possessed a high specific surface area due to the increase in the amounts of supermicropores, and pore size distribution analysis confirmed the presence of mesopores not only in the interparticle spaces but also within the nanoparticles. The electrochemical performance testing suggested that the rapid mass transport of electrolyte ions could be achieved with lower-size mesopores and the micropore volume distributed in supermicropores ranges could yield a high capacitance characteristic. These notable porous properties of activated carbon gel are highly advantageous for its application as an electrode material in supercapacitors.

7.2 Recommendations

7.2.1 Investigation of other biomass sources

In addition to longan seed biomass, other biomass precursors such as wood coconut shells, sawdust, and sugarcane bagasse could be studied for their potential to produce activated carbon with desired mesoporous structures using the OTA technique. This could be helpful to achieve more information on the effect of biomass structure on mesopore development by the OTA method and more options for selecting suitable biomass precursors based on their abundance, availability, and cost-effectiveness.

7.2.2 Optimization of the OTA preparation method

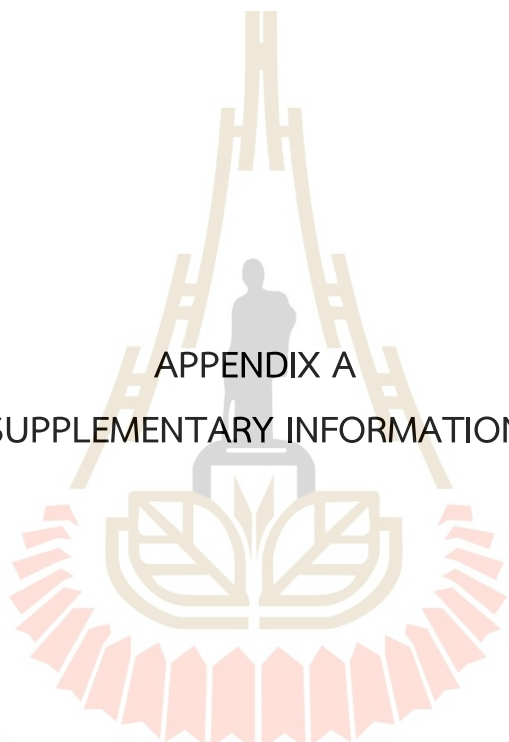
The OTA method involves various activation parameters such as temperature, time, and concentration of the activating agent. Further investigation could be performed to optimize these parameters for achieving the desired mesoporous structure. For instance, the effect of different concentrations of the activating agent on the development of mesopores could be studied to find the optimal concentration that yields the highest mesoporosity.

7.2.3 Comparison of CO₂ activation with other methods

The OTA method could be compared with other activation methods such as steam activation, and microwave activation. This would be helpful to improve the controlling strategy of mesoporosity development via the OTA method. The comparison could be based on the mesoporous structure, surface area, pore size distribution, and adsorption capacity of the activated carbon produced by each method. This would provide a comprehensive understanding of the advantages and limitations of different activation methods.

7.2.4 Adsorption studies on other pollutants

In addition to dyes, the adsorption efficiency of activated carbon produced by the OTA method could be tested on other pollutants such as heavy metals, organic compounds, and pharmaceuticals. This would broaden the applicability of the produced activated carbon for different environmental remediation applications.



APPENDIX A
SUPPLEMENTARY INFORMATION

มหาวิทยาลัยเทคโนโลยีสุรนารี

Chapter III THE CONSECUTIVE PROCESS OF AIR OXIDATION, THERMAL DESTRUCTION OF SURFACE FUNCTIONAL GROUPS, AND CARBON ACTIVATION (THE OTA METHOD)

Non-isothermal gasification of logan-seed char (C500-90) under CO_2 atmosphere in a thermogravimetric analyzer (TGA)

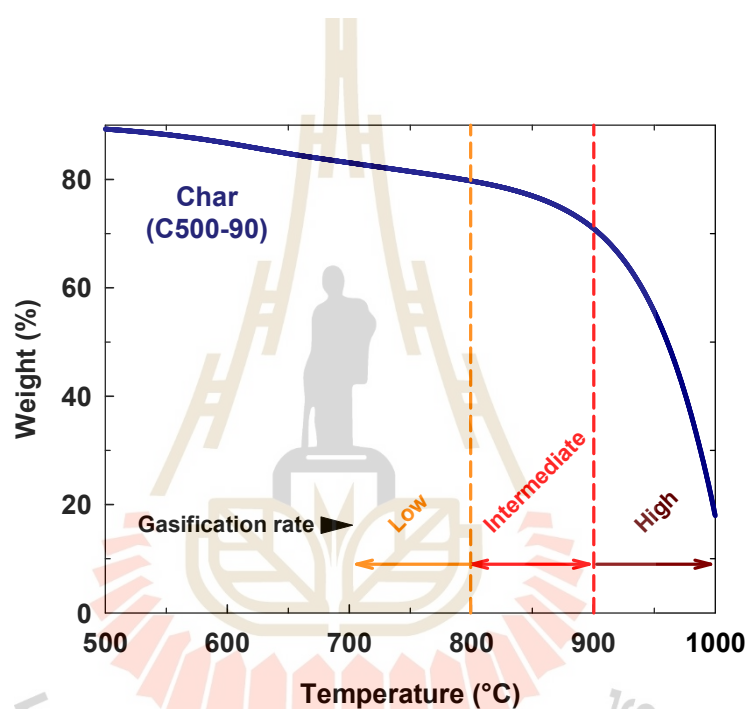


Figure S1 TGA data of logan-seed char by heating in CO_2 from room temperature to the final temperature of 1000°C, using the heating rate of 10°C/min.

Effect of the thermal treatment step of the OTA method on carbon reactivity

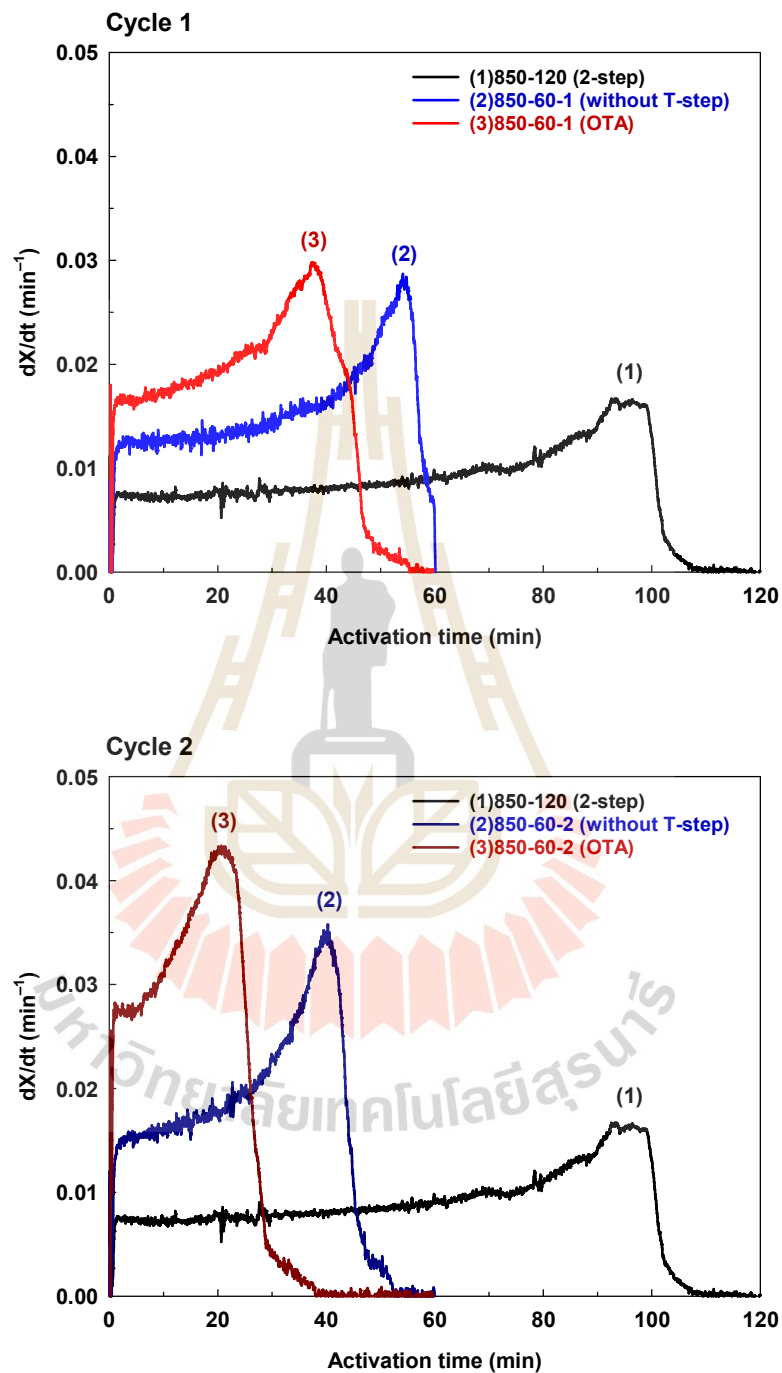


Figure S2 Effect of reaction time on the gasification rates (dx/dt) of activated carbon prepared by the two-step activation (1, black line), the OTA method without the heat treatment (T) step (2, blue line), and the OTA method (3, red line).

Chapter III THE USE OF ACTIVATED CARBON FROM LONGAN SEED BIOMASS FOR
INCREASING CAPACITY AND KINETICS OF METHYLENE BLUE
ADSORPTION FROM AQUEOUS SOLUTION

Table S1 Data for methylene blue standard curve

MB concentration (mg/L)	Absorbance at 665 nm			
	1	2	3	average
0	0	0	0	0
0.2	0.006	0.007	0.007	0.007
0.5	0.046	0.047	0.049	0.047
1	0.139	0.137	0.138	0.138
2	0.282	0.281	0.280	0.281
3	0.386	0.386	0.387	0.386
4	0.511	0.512	0.515	0.513
6	0.765	0.766	0.765	0.765
7	0.934	0.932	0.933	0.933

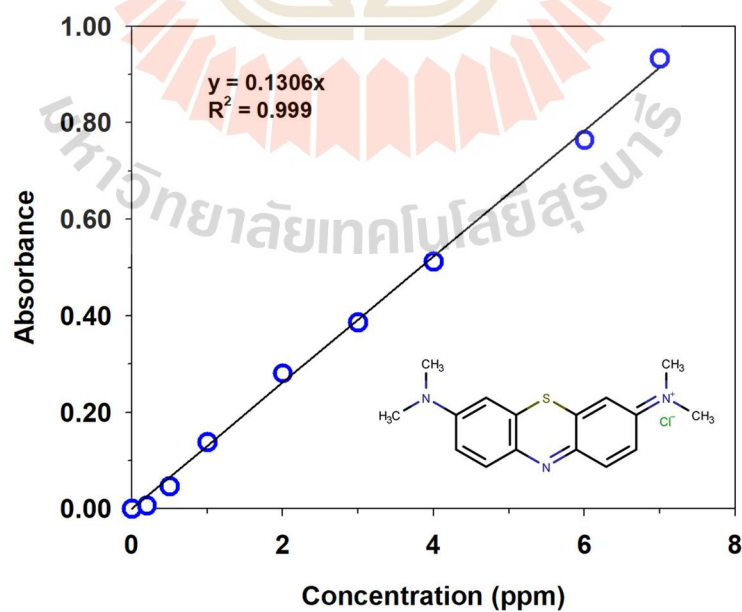


Figure S3 Standard methylene blue curve with concentrations ranging from 0 to 7 ppm at ambient temperature.

Chapter IV ANALYSIS OF GAS ADSORPTION AND PORE DEVELOPMENT IN
ACTIVATED CARBON BASED ON SURFACE DEFECT MODEL

Snapshots of N₂ adsorption at 77 K and 0.1 MPa on the defect-free surface

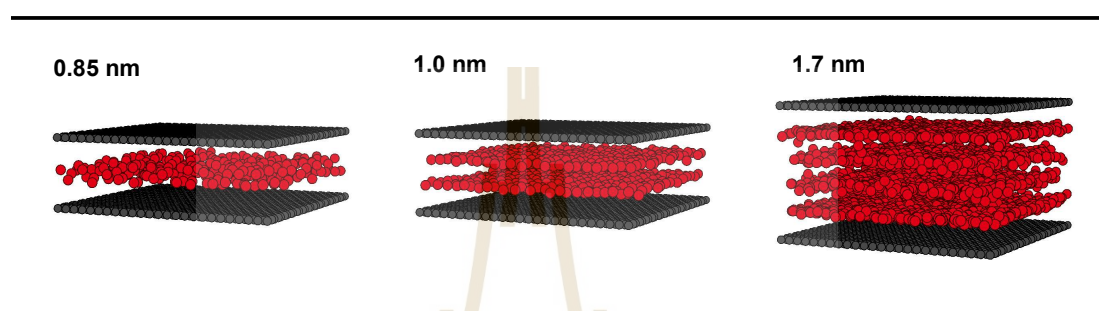


Figure S4 Snapshots of N₂ adsorption at 77 K in pore width of 0.85 nm, 1.0 nm, and 1.7 nm at 0.1 MPa on the carbon surface with defect-free.

Degree of a surface defect by holding a constant effective radius (R_c)

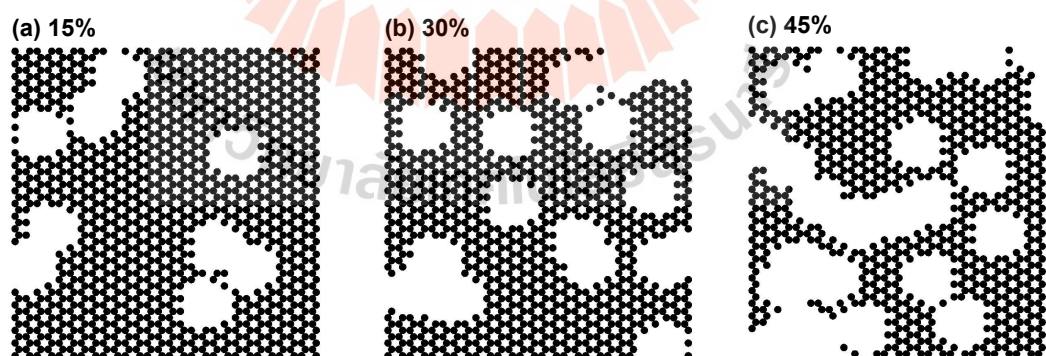


Figure S5 Solid configuration of one graphene layer with an effective radius of 0.492 nm and percentage defects of (a) 15%, (b) 30%, and (c) 45%. The black spheres represent carbon atoms of the graphene layer and the spaces represent the defect area.

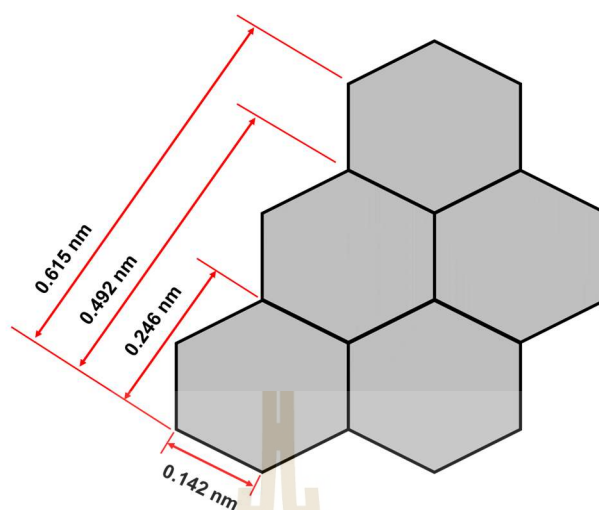


Figure S6 The structure of hexagonal graphite with trigonal planar bonding within the graphene layers.

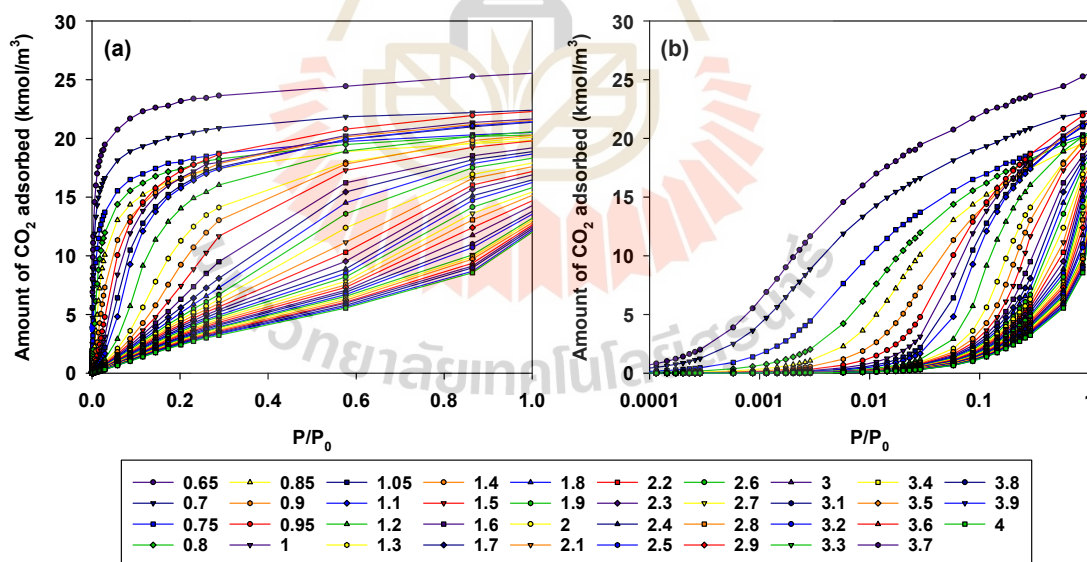


Figure S7 Simulated adsorption isotherms of CO_2 at 273 K in carbon slit pores with a pore width ranging from 0.65 to 4 nm. The plots in (a) are presented in a linear scale, while (b) are shown in a semi-log scale.

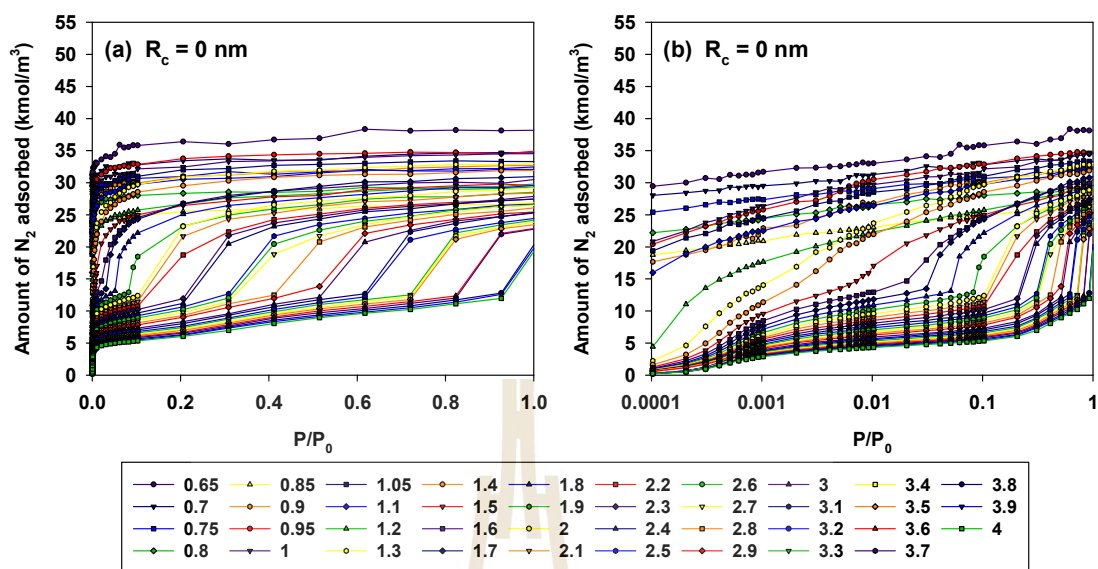


Figure S8 Simulated adsorption isotherms of N_2 at 77 K in carbon slit pores with a pore width ranging from 0.65 to 4 nm (perfective surface). The plots in (a) are presented in a linear scale, while (b) are shown in a semi-log scale.

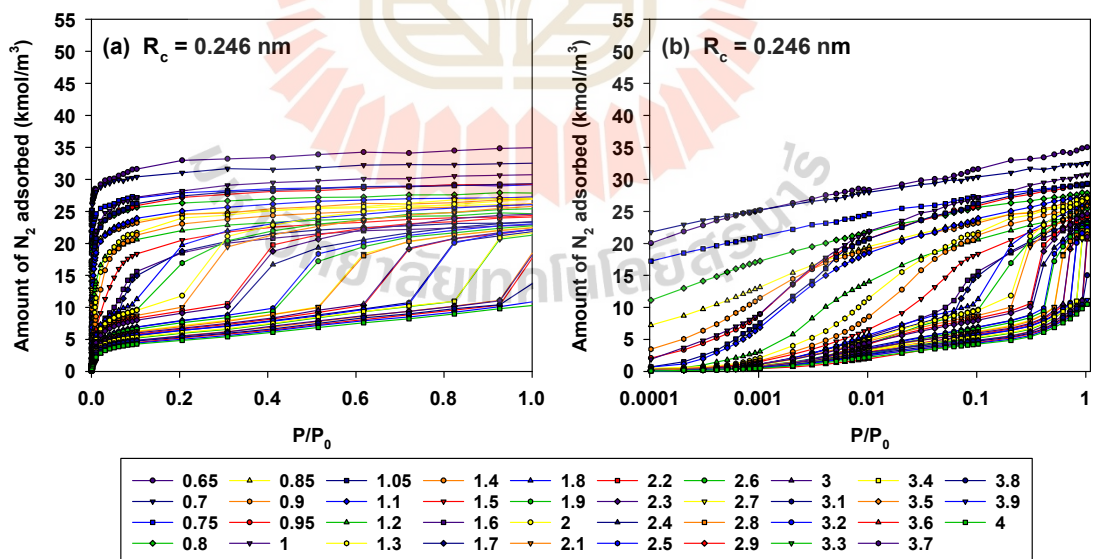


Figure S9 Simulated adsorption isotherms of N_2 at 77 K in carbon slit pores with 30% defects and an effective radius of 0.246 nm. The plots in (a) are presented in a linear scale, while (b) are shown in a semi-log scale.

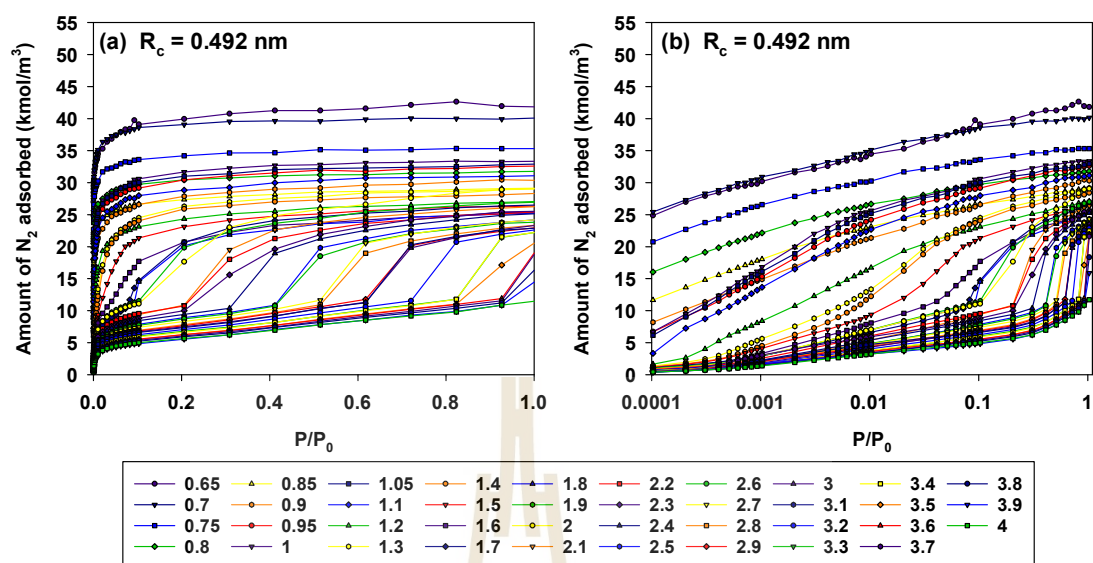


Figure S10 Simulated adsorption isotherms of N_2 at 77 K in carbon slit pores with 30% defects and an effective radius of 0.492 nm. The plots in (a) are presented in a linear scale, while (b) are shown in a semi-log scale.

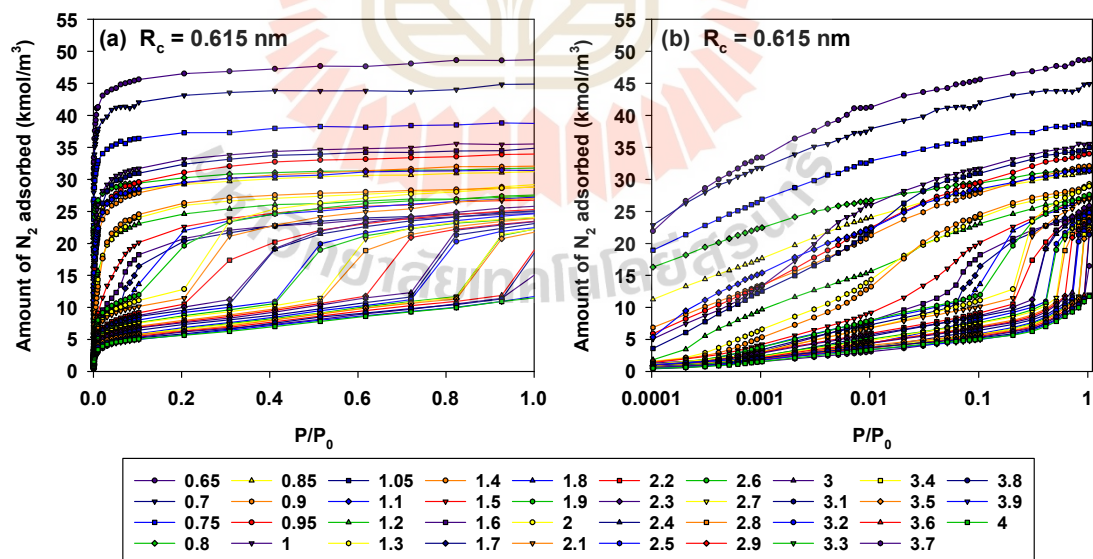


Figure S11 Simulated adsorption isotherms of N_2 at 77 K in carbon slit pores with 30% defects and an effective radius of 0.615 nm. The plots in (a) are presented in a linear scale, while (b) are shown in a semi-log scale.

Chapter V A SIMPLE PRE-OXIDATION TECHNIQUE FOR INCREASING CO₂
GASIFICATION RATES IN LONGAN-SEED CHAR

Activation Energy (E) and Pre-Exponential Factor (k₀)

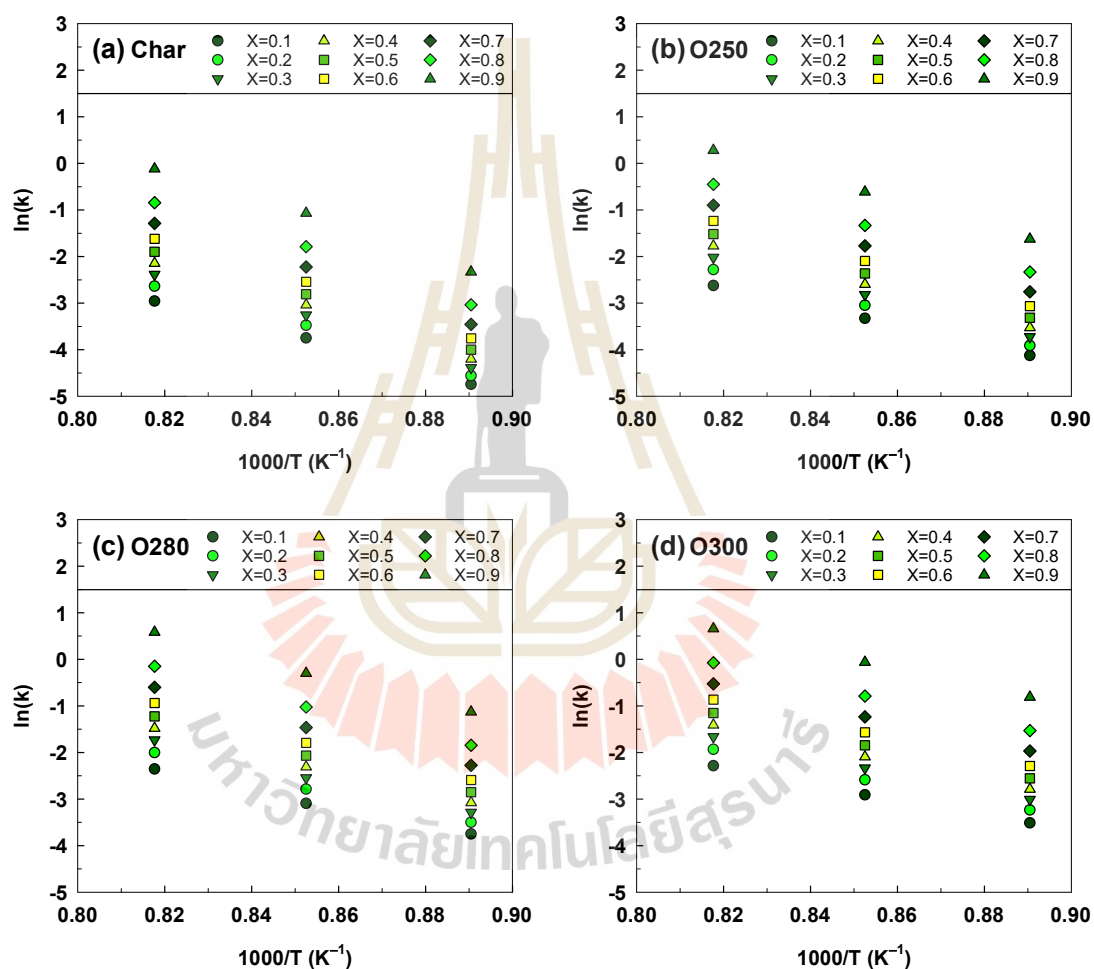


Figure S12 Arrhenius plot between $\ln(k)$ versus $1/T$ for various oxidized longan-seed chars.

Table S2 Activation energy and pre-exponential factor values of char gasification for various oxidized longan-seed chars

X	Activation energy, E (kJ/mol)				Pre-exponential factor, k_0 (min^{-1})			
	Char	O250	O280	O300	Char	O250	O280	O300
0.10	204.35	171.35	159.12	139.74	2.85E+07	1.52E+06	5.79E+05	9.32E+04
0.20	219.78	185.95	170.59	148.55	1.80E+08	8.98E+06	2.54E+06	3.16E+05
0.30	228.80	194.48	177.29	153.70	5.63E+08	2.71E+07	6.45E+06	6.90E+05
0.40	235.20	200.54	182.05	157.36	1.34E+09	6.29E+07	1.32E+07	1.27E+06
0.50	240.17	205.24	185.74	160.20	2.81E+09	1.29E+08	2.47E+07	2.18E+06
0.60	244.23	209.08	188.76	162.51	5.53E+09	2.49E+08	4.41E+07	3.64E+06
0.70	247.66	212.32	191.30	164.47	1.08E+10	4.80E+08	7.96E+07	6.21E+06
0.80	250.63	215.13	193.51	166.17	2.26E+10	9.92E+08	1.55E+08	1.15E+07
0.90	253.25	217.61	195.46	167.67	6.07E+10	2.63E+09	3.91E+08	2.78E+07

Chapter VI IMPROVING POROUS PROPERTIES OF ACTIVATED CARBON GEL BY THE OTA METHOD

Synthesis of Resorcinol (R)-Formaldehyde (F) Gels

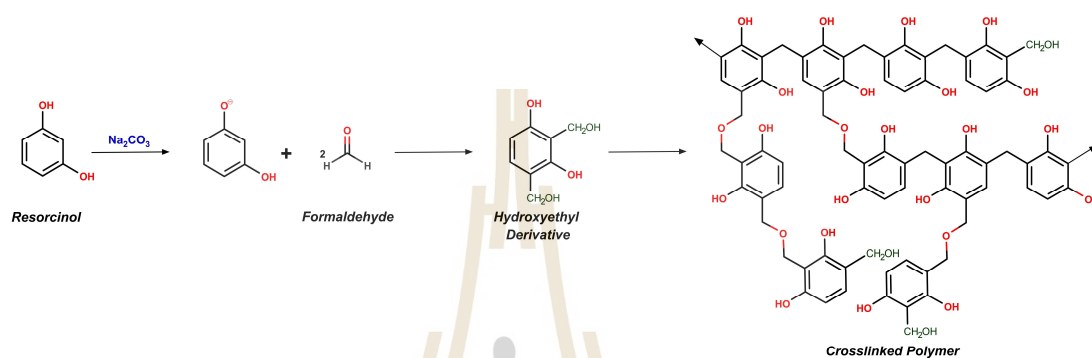


Figure S13 Polymerization process for the synthesis of RF gels.

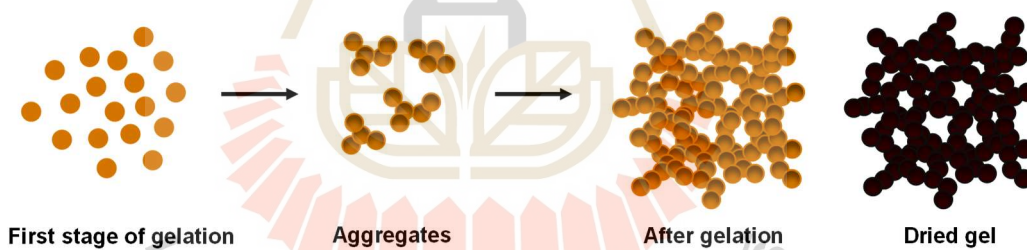


Figure S14 Schematic for cluster formation and growth process in RF gel synthesis.

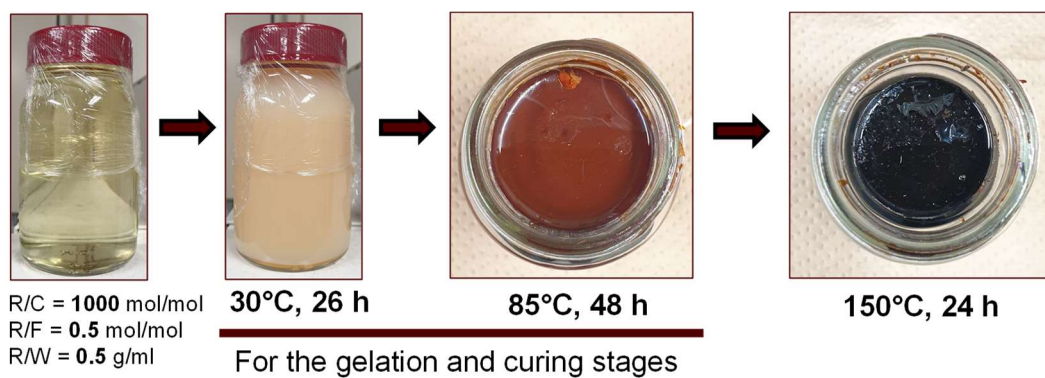


Figure S15 Stages for the synthesis process of RF gels.

TGA data of carbon gel produced at a carbonization temperature of 800°C

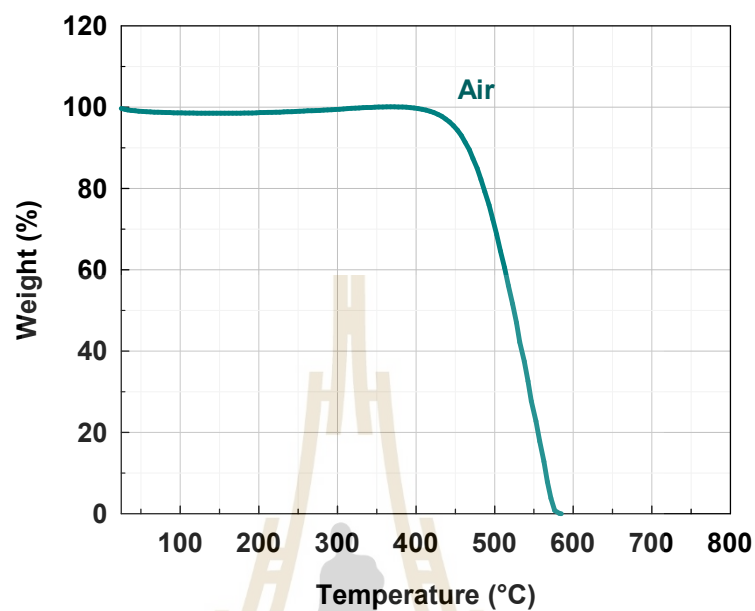


Figure S16 TG curve for the non-isothermal heating of the carbon gel under air in the TGA, using the heating rate of 5°C/min

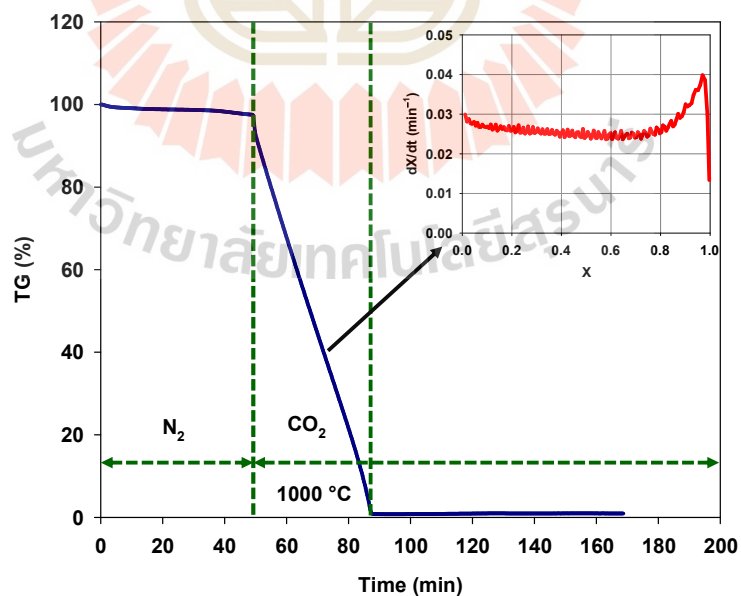


Figure S17 TGA data of carbon gel by heating in N₂ from room temperature to the final gasification temperature of 1000°C in CO₂

Effect of activation time (h) on the BET surface area (m^2/g)

$$S_{BET,AC} = -66.324t^2 + 658.2t + 601.91; \quad dS/dt = -132.65t + 658.2$$

$$S_{BET,OTA} = -223.35t^2 + 1298.3t + 642.09; \quad dS/dt = -446.70t + 1298.3$$

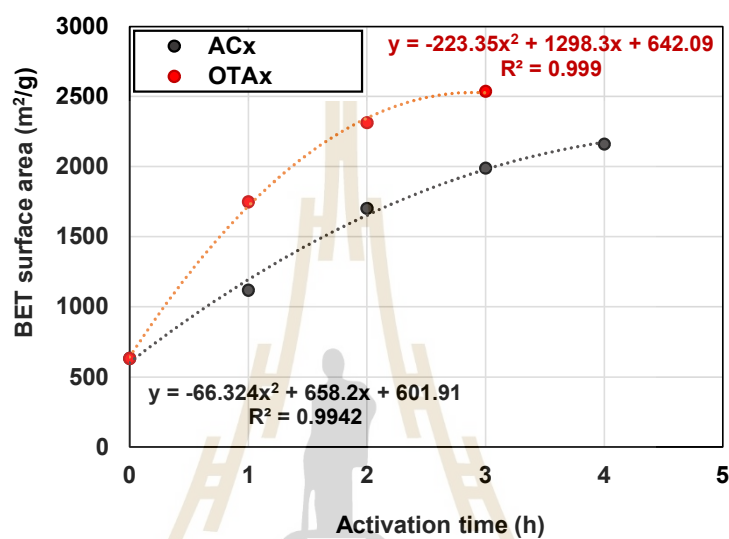


Figure S18 Second-order polynomial function of the BET surface area (m^2/g) vs the activation time (h) of the AC series and OTA series.

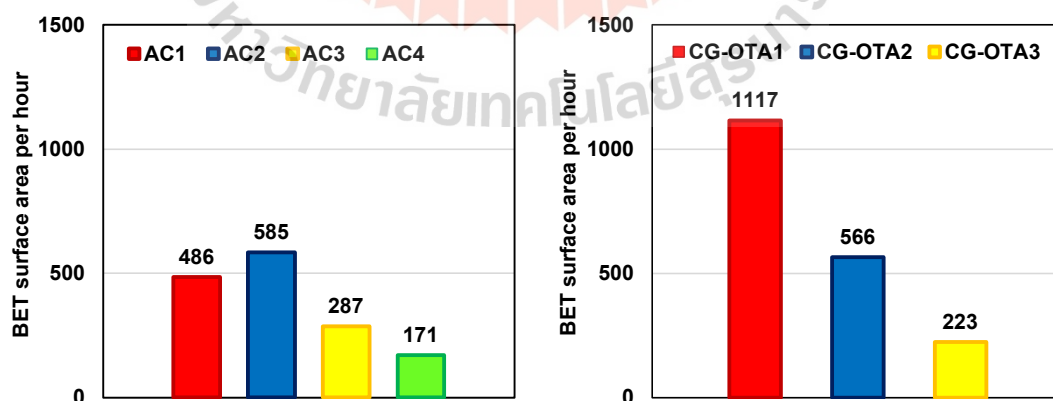


Figure S19 The increase in BET surface area (m^2/g) per hour by CO_2 gasification of AC series and OTA series.

Peak Separation of TPD Analysis

To estimate the amount of each type of oxygen-containing functional group, the peak separation of the TPD spectra of CO and CO₂ was carried out. The desorption temperature and full width at half maximum (FWHM) were determined based on the literature (Ishii et al., 2014; Ishii & Ozaki, 2020; Li et al., 2011). Peak separation from the obtained TPD spectra was conducted using the conditions shown in Table S3, and the peak fitting results are presented in Figure S12.

Table S3 Peak separation conditions of CO and CO₂ TPD spectra

Functional groups	Desorption gas	Peak temperature (°C)	FWHM (°C)
Carboxylic #1	CO ₂	240	150
Carboxylic #2	CO ₂	340	150
Anhydride	CO ₂ + CO	490	130
Lactone#1	CO ₂	600	130
Lactone#2	CO ₂	700	130
Phenol/Ether#1	CO	550	125
Phenol/Ether#2	CO	640	125
Phenol/Ether#3	CO	750	150
Carbonyl#1	CO	900	150
Carbonyl#2	CO	1030	100
Carbonyl#3	CO	1125	150

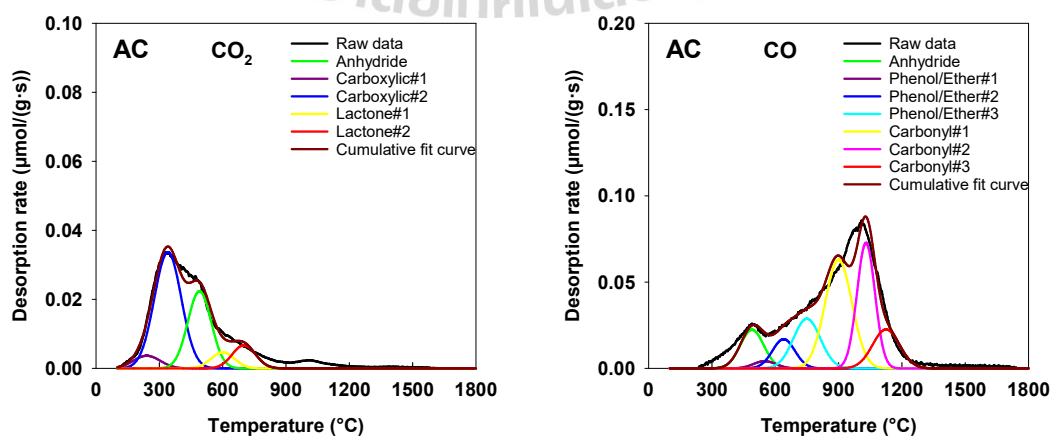


Figure S20 Cont.

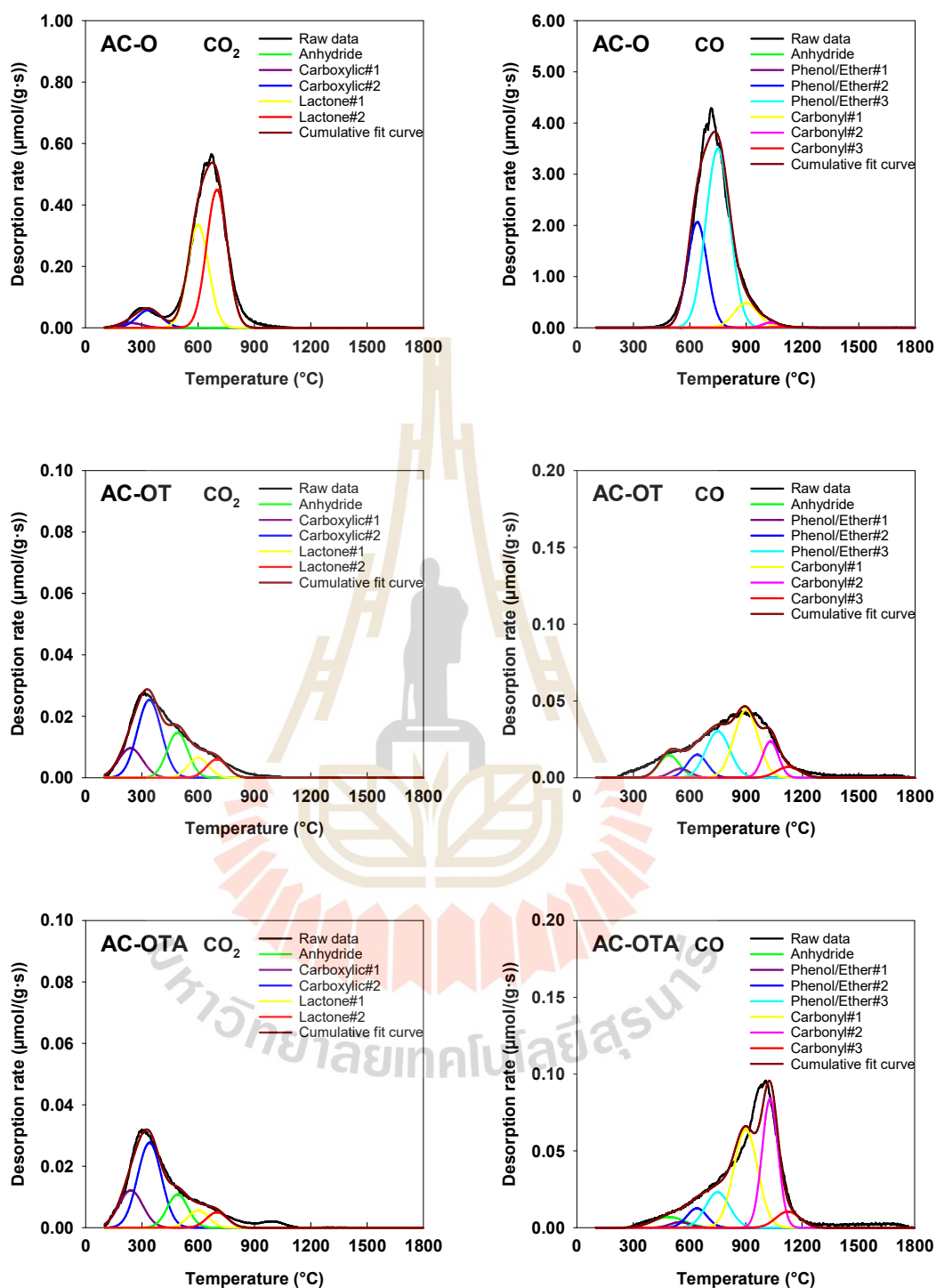


Figure S20 Peak fitting results of TPD profiles for activated carbon gels using a Gaussian function. The black lines represent the TPD experimental data, and the colored lines show the fitting profiles optimized by the Levenberg-Marquardt method.

Cyclic Voltammetry (CV) Curve

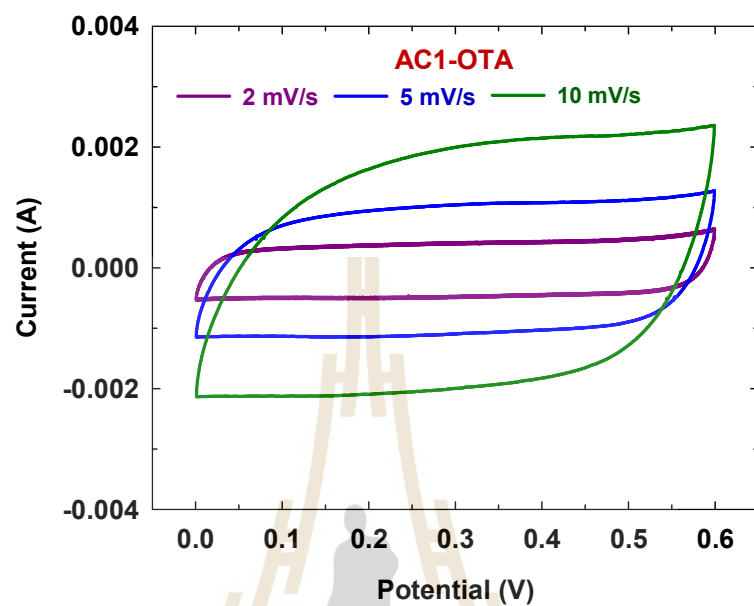


Figure S21 Cyclic voltammetry curves of AC1-OTA at different scan rates.

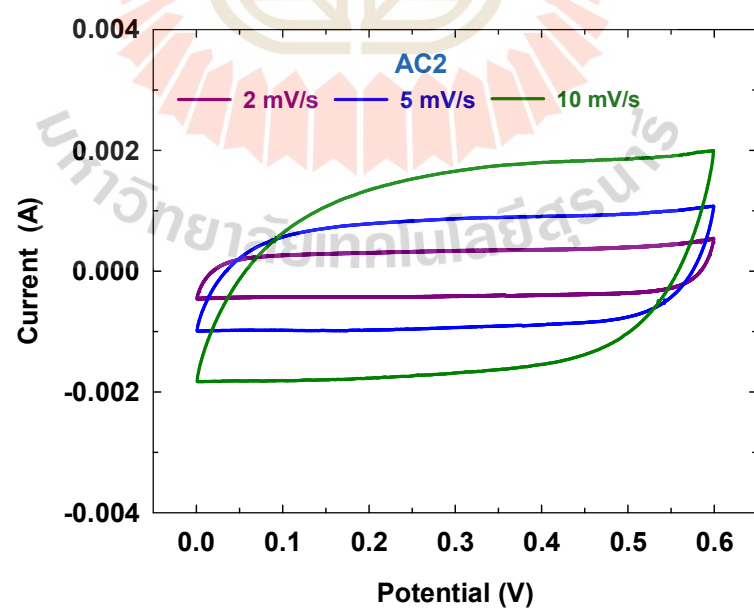


Figure S22 Cyclic voltammetry curves of AC2 at different scan rates.

From cyclic voltammetry curves, the specific capacitance of the electrode was calculated using the following equation.

$$C = \frac{A}{2 \times v \times m \times \Delta V} \quad (\text{S.1})$$

where C (F/g) is the specific capacitance of the electrode, A is the area under the cyclic voltammetry curve, v is the potential scan rate (mV/s), m is the active mass of the electrode materials, and ΔV is the potential window (V).

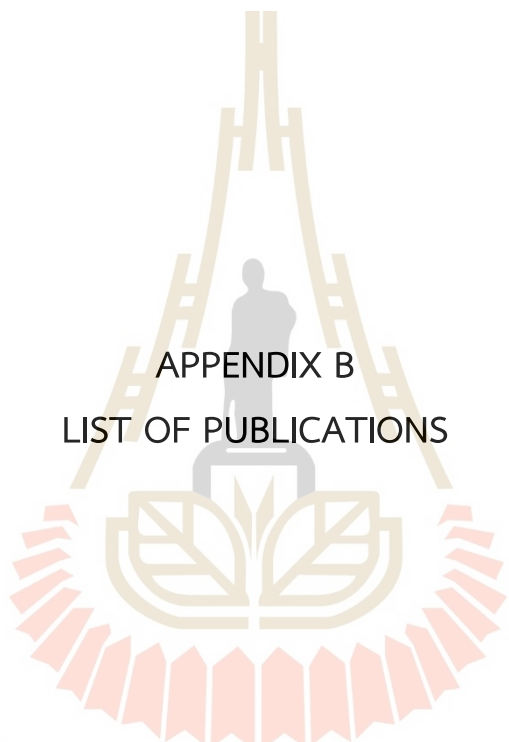
Table S4 Specific capacitance from cyclic voltammetry (CV) of AC2 and AC1-OTA

Scanning rate (mV/s)	Specific capacitance (F/g)	
	AC2	AC1-OTA
2	140.8	152.2
5	127.8	139.6
10	109.7	121.6

References

- Ishii, T., Kashihara, S., Hoshikawa, Y., Ozaki, J.-i., Kannari, N., Takai, K., Enoki, T., & Kyotani, T. (2014, 2014/12/01/). A quantitative analysis of carbon edge sites and an estimation of graphene sheet size in high-temperature treated, non-porous carbons. *Carbon*, 80, 135-145.
- Ishii, T., & Ozaki, J.-i. (2020, 2020/05/01/). Understanding the chemical structure of carbon edge sites by using deuterium-labeled temperature-programmed desorption technique. *Carbon*, 161, 343-349.
- Li, N., Ma, X., Zha, Q., Kim, K., Chen, Y., & Song, C. (2011, 2011/12/01/). Maximizing the number of oxygen-containing functional groups on activated carbon by using ammonium persulfate and improving the temperature-programmed desorption characterization of carbon surface chemistry. *Carbon*, 49(15), 5002-5013.



The logo of Sakon Nakhon Rajabhat University is a circular emblem. At the top, there is a stylized golden structure resembling a traditional Thai roof or a tiered stupa. Below this, a grey silhouette of a person stands on a pedestal. Underneath the person is a golden lotus flower with five petals. The entire emblem is surrounded by a decorative border of red and orange scalloped shapes. The university's name in Thai is written in a grey, curved font at the bottom of the emblem.

APPENDIX B
LIST OF PUBLICATIONS

มหาวิทยาลัยเทคโนโลยีสุรนารี

LIST OF PUBLICATIONS

1. International Publications

Lawtae, P., Tangsathitkulchai, C. (2021). A New Approach for Controlling Mesoporosity in Activated Carbon by the Consecutive Process of Air Oxidation, Thermal Destruction of Surface Functional Groups, and Carbon Activation (the OTA Method). *Molecules*. 26(9): 2758.

Lawtae, P., Tangsathitkulchai, C (2021). The Use of High Surface Area Mesoporous-Activated Carbon from Longan Seed Biomass for Increasing Capacity and Kinetics of Methylene Blue Adsorption from Aqueous Solution. *Molecules*. 26(21): 6521.

Lawtae, P., Nagaishi, S., Tangsathitkulchai, C., Iwamura, S., and Mukai, S. R., (2023). Improving porous properties of activated carbon from carbon gel by the OTA method. *RSC Advances*. 13(21): 14065-14077.

Lawtae, P., Phothong, K., Tangsathitkulchai, C., and Wongkoblaph, A. Analysis of gas adsorption and pore development of microporous-mesoporous activated carbon based on GCMC simulation and a surface defect model. *Journal of Porous Materials*. (Accepted for publication)

Lawtae, P., Tangsathitkulchai, C., Phothong, K., and Wongkoblaph, A. Increasing CO₂ gasification rates of longan-seed char by a technique of char pre-oxidation. *Bioresource Technology Reports*. (Accepted for publication)

2. Conference Abstract

Lawtae, P., C., Tangsathitkulchai. (2019). Control of mesoporosity in physically activated carbon from longan seed biomass using a novel repeated oxidation/activation method. The 1st Thailand Biorefinery Conference. Nakhon Ratchasima, Thailand.

BIOGRAPHY

Panuwat Lawtae was born on December 8, 1994, in Buriram. After graduating from Lahansai Ratchadapisek School in 2013, he received a scholarship from Suranaree University of Technology (SUT), Nakhon Ratchasima, Thailand. With his dedication and enthusiasm, he was awarded the degree of Bachelor of Engineering (Chemical Engineering) with First Class Honours in June 2017. Thereafter, he earned a scholarship from the Royal Golden Jubilee Ph.D. program (RGJ-Ph.D.) through the National Research Council of Thailand (NRCT) and Thailand Research Fund (TRF) to pursue a Doctor of Philosophy (Ph.D.) in Chemical Engineering at SUT under the thesis supervision of Prof. Dr. Chaiyot Tangsathitkulchai. He worked diligently on his thesis and developed a new technique for increasing and controlling mesopore volume in activated carbon. As part of the RGJ funding program, he had short-term research training at an overseas university to strengthen his research capability. He spent over ten months (May 2022 to February 2023) in the Graduate School of Engineering, Division of Applied Chemistry, Hokkaido University, under the supervision of Prof. Dr. Shin R. Mukai, conducting research on the synthesis of mesoporous carbons with high surface area. In June 2023, he successfully defended his doctoral dissertation, showcasing his expertise in the synthesis and application of porous carbon materials.

มหาวิทยาลัยเทคโนโลยีสุรนารี